
Electronic Thesis and Dissertation Repository

3-28-2018 2:00 PM

High Performance Optical Computed Tomography for Accurate Three-Dimensional Radiation Dosimetry

Kurtis Hendrik Dekker
The University of Western Ontario

Supervisor
Jordan, Kevin J.
The University of Western Ontario Joint Supervisor
Battista, Jerry J.
The University of Western Ontario

Graduate Program in Medical Biophysics
A thesis submitted in partial fulfillment of the requirements for the degree in Doctor of Philosophy
© Kurtis Hendrik Dekker 2018

Follow this and additional works at: <https://ir.lib.uwo.ca/etd>



Part of the [Medical Biophysics Commons](#)

Recommended Citation

Dekker, Kurtis Hendrik, "High Performance Optical Computed Tomography for Accurate Three-Dimensional Radiation Dosimetry" (2018). *Electronic Thesis and Dissertation Repository*. 5264.
<https://ir.lib.uwo.ca/etd/5264>

This Dissertation/Thesis is brought to you for free and open access by Scholarship@Western. It has been accepted for inclusion in Electronic Thesis and Dissertation Repository by an authorized administrator of Scholarship@Western. For more information, please contact wlsadmin@uwo.ca.

Abstract

Optical computed tomography (CT) imaging of radiochromic gel dosimeters is a method for truly three-dimensional radiation dosimetry. Although optical CT dosimetry is not widely used currently due to previous concerns with speed and accuracy, the complexity of modern radiotherapy is increasing the need for a true 3D dosimeter. This thesis reports technical improvements that bring the performance of optical CT to a clinically useful level. New scanner designs and improved scanning and reconstruction techniques are described.

First, we designed and implemented a new light source for a cone-beam optical CT system which reduced the scatter to primary contribution in CT projection images of gel dosimeters from approximately 25% to approximately 4%. This design, which has been commercially implemented, enables accurate and fast dosimetry.

Second, we designed and constructed a new, *single-ray, single-detector* parallel-beam optical CT scanner. This system was able to very accurately image both absorbing and scattering objects in large volumes (15 cm diameter), agreeing within $\sim 1\%$ with independent measurements. It has become a reference standard for evaluation of optical CT geometries and dosimeter formulations.

Third, we implemented and characterized an iterative reconstruction algorithm for optical CT imaging of gel dosimeters. This improved image quality in optical CT by suppressing the effects of noise and artifacts by a factor of up to 5.

Fourth, we applied a fiducial-based ray path measurement scheme, combined with an iterative reconstruction algorithm, to enable optical CT reconstruction in the case of refractive index mismatch between different media in the scanner's imaged volume. This improved the practicality of optical CT, as time-consuming mixing of liquids can be avoided.

Finally, we applied the new laser scanner to the difficult dosimetry task of small-field measurement. We were able to obtain beam profiles and depth dose curves for 4 fields ($\leq 3 \times 3$

cm²) using one 15 cm diameter dosimeter, within 2 hours. Our gel dosimetry depth-dose curves agreed within ~1.5% with Monte Carlo simulations.

In conclusion, the developments reported here have brought optical CT dosimetry to a clinically useful level. Our techniques will be used to assist future research in gel dosimetry and radiotherapy treatment techniques.

Keywords: Cancer, Radiation Therapy, Radiation Dosimetry, Small-field Dosimetry, Computed Tomography, Optical Imaging, Stray Light, Laser Scanning

Co-Authorship Statement

Chapter 2 is adapted from a manuscript published as “Stray light in cone beam optical computed tomography: II. Reduction using a convergent light source” by Kurtis H. Dekker, Jerry J. Battista and Kevin J. Jordan, *Physics in Medicine and Biology*, 61, 2910-2925 (2016). KHD designed the study, performed experiments and analysis, and wrote and edited the manuscript. KJJ and J²B supervised, provided input on study design and analysis, and edited the manuscript.

Chapter 3 is adapted from a manuscript published as “Scanning laser optical computed tomography system for large volume 3D dosimetry” by Kurtis H. Dekker, Jerry J. Battista and Kevin J. Jordan, *Physics in Medicine and Biology*, 62, 2636-2657 (2017). KHD designed the study, performed experiments and analysis, and wrote and edited the manuscript. KJJ and J²B supervised, provided input on study design and analysis, and edited the manuscript.

Chapter 4 is adapted from a manuscript published as “Technical Note: Evaluation of an iterative reconstruction algorithm for optical CT radiation dosimetry” by Kurtis H. Dekker, Jerry J. Battista and Kevin J. Jordan, *Medical Physics*, 44, 6678-6689. KHD designed the study, performed experiments and analysis, and wrote and edited the manuscript. KJJ and J²B supervised, provided input on study design and analysis, and edited the manuscript.

Chapter 5 is adapted from a manuscript published as “Optical CT imaging of solid radiochromic dosimeters in mismatched refractive index solutions using a scanning laser and large area detector” by Kurtis H. Dekker, Jerry J. Battista and Kevin J. Jordan, *Medical Physics*, 43, 4585-4597 (2016). KHD designed the study, performed experiments and analysis, and wrote and edited the manuscript. KJJ and J²B supervised, provided input on study design and analysis, and edited the manuscript.

Chapter 6 describes gel dosimetry experiments performed at the London Regional Cancer Program. Experiments were performed by Kurtis H. Dekker, Sydney Bell, and Kevin J.

Jordan. KHD performed optical CT imaging and analysis, assisted in irradiations, and authored the chapter. SB manufactured gel dosimeters and performed irradiations. KJJ supervised experiments, manufactured gel dosimeters, performed irradiations and edited the chapter. Jerry J. Battista also edited the chapter manuscript.

Appendix A is adapted from a technical note published as “Fixed, object-specific intensity compensation for cone beam optical CT radiation dosimetry” by Kurtis Hendrik Dekker, Rubin Hazarika, Matheus A. Silveira, and Kevin J. Jordan, *Physics in Medicine and Biology*, 63, 06NT02 (2018). KHD designed the study, supervised and performed experiments, and wrote and edited the manuscript. RH and MAS performed experiments and edited the manuscript. KJJ provided input on study design, supervised, and edited the manuscript.

Acknowledgements

First, I would like to thank my supervisors, Drs. Kevin Jordan and Jerry Battista, whose guidance and passion for medical physics enabled and inspired my development as a researcher. I also wish to thank my advisory committee members, Drs. Tim Scholl and George Hajdok, for volunteering their time and insights in my (*very* infrequent) committee meetings. I am also grateful to the examiners for volunteering their time to review this dissertation.

I wish to thank the staff in the Department of Medical Biophysics office for their help with various administrative details. I would also like to extend my gratitude to the Department of Physics and Engineering at the London Regional Cancer Program. In particular: Barb Barons, for administrative support; George De Waele, for machining various components; the engineering group, for help with the linear accelerators; and the physicists and physics associates, for their guidance and knowledge of clinical radiotherapy physics. Additionally, I thank the co-op students I have worked with over the past five years.

I would also like to acknowledge the sources of funding that contributed to my dissertation, including the London Regional Cancer Program and the Department of Medical Biophysics at the University of Western Ontario. In addition, funding for the project was provided by the Ontario Research Challenge Fund (OCAIRO project) and a grant from the Plunkett foundation in London, Ontario. My graduate studies have also been supported by scholarships from the Ontario Ministry of Training, Colleges, and Universities and from the Natural Sciences and Engineering Research Council of Canada (NSERC).

I thank all of my friends, both in the department here and outside of it. Finally, I thank my brother, Lukas; my parents, Ron and Teresa; and my fiancée, Erin, for their support.

Contents

Abstract	ii
Co-Authorship Statement	iv
Acknowledgements	vi
Table of Contents	vii
List of Figures	xiii
List of Tables	xx
List of Appendices	xxii
List of Abbreviations	xxiii
List of Symbols	xxv
1 General Introduction	1
1.1 Cancer Basics	1
1.1.1 Cancer in Canada	1
1.2 Radiation Therapy	2
1.2.1 Radiation therapy process	4
1.2.2 Advances in external beam radiotherapy	6
1.3 Radiotherapy Quality Assurance	9
1.4 Radiation Dosimeters	9
1.4.1 Properties of dosimeters	10
1.4.2 Comparison of common dosimeters	13
1.5 The Case for 3D Dosimeters	13
1.6 3D Chemical Dosimeters	17
1.6.1 Gel dosimeters	17
1.6.1.1 Gel dosimeter basics	17
1.6.1.2 Condensed history of gel dosimetry	18
1.6.2 Non-gel 3D chemical dosimeters	19
1.6.3 3D chemical dosimeter readout	20
1.7 Optical Computed Tomography	21
1.7.1 Computed tomography basics	21

1.7.1.1	Attenuation	21
1.7.1.2	Projections	23
1.7.1.3	The Fourier Slice Theorem and tomographic reconstruction	24
1.7.1.4	Backprojection-based reconstruction techniques	26
1.7.1.5	Algebraic / Iterative reconstruction algorithms	27
1.7.2	Optical CT scanners	28
1.8	Motivation of Research	30
1.8.1	Stray light effects	30
1.8.1.1	Stray light in attenuation measurements	31
1.8.1.2	Stray light in optical CT	32
1.8.1.3	Stray light reduction in optical CT	35
1.8.2	Large volume dosimetry	35
1.8.3	Optical artifacts and image reconstruction	36
1.9	Research Hypothesis	36
1.10	Specific Objectives	37
1.11	References	37
2	Stray Light Reduction in Cone-beam Optical CT	46
2.1	Introduction	46
2.2	Materials and Methods	48
2.2.1	Fresnel modified optical CT scanner	48
2.2.2	Vertical slot array	51
2.2.3	Test solutions	51
2.2.4	Phantoms	53
2.2.4.1	Uniform solution in Vista10 vessel	53
2.2.4.2	FEP finger phantom	56
2.2.5	Experimental setups	57
2.2.5.1	Fan beam vs. narrow beam geometry	57
2.2.5.2	Fan beam vs. cone beam - uniform phantom	58
2.2.5.3	Fan beam vs. cone beam - finger phantom	58
2.2.5.4	Gelatin finger phantom imaging	58
2.2.5.5	Source spot size optimization	59
2.3	Results and Discussion	60
2.3.1	Stray light	60
2.3.1.1	Fan beam vs. narrow beam geometry	60
2.3.1.2	Uniform phantom	61
2.3.1.3	Fan beam vs. cone beam - finger phantom	62
2.3.1.4	Gelatin finger phantom	63
2.3.2	Image artifacts and source spot size optimization	65
2.4	Conclusion	68
2.5	References	69
3	Large-volume Scanning Laser Optical CT	72
3.1	Introduction	72
3.1.1	Optical CT dosimetry	72

3.1.2	Large-volume 3D dosimetry	73
3.1.3	Optical CT scanners	74
3.1.4	Stray light effects in optical CT	74
3.1.5	Study objectives and outline	75
3.2	Scanner Design	76
3.2.1	Choice of scanner geometry	78
3.2.2	Optical CT aquarium	79
3.2.2.1	Lens-shaped acylindrical aquarium	79
3.2.2.2	Importance of asymmetric design	80
3.2.3	Detector collimation and flood-field uniformity	80
3.2.4	CT sampling and reconstruction	81
3.3	Initial Characterization Tests	83
3.3.1	Detector linearity	83
3.3.2	Noise and stability	84
3.3.3	Parallel beam geometry verification	85
3.3.4	Spatial resolution in projection images	86
3.3.5	Summary of specifications	87
3.4	Optical CT scanning experiments	88
3.4.1	Phantoms	88
3.4.2	Optical CT scan parameters	88
3.4.3	Large-volume uniform absorbing phantom	89
3.4.4	Large-volume uniform scattering phantom	90
3.4.5	Small absorbing finger phantom in gel-like scattering medium	90
3.4.6	Small absorbing finger phantom in highly scattering medium - opposing sinogram reconstructions	91
3.5	Results and Discussion	93
3.5.1	Large-volume uniform absorbing phantom	93
3.5.2	Large-volume scattering phantom	95
3.5.3	Absorbing finger phantom in gel-like scattering medium	97
3.5.4	Small absorber in highly scattering medium - opposing sinogram reconstructions	99
3.5.5	Summary of results and current limitations	101
3.6	Conclusion	102
3.7	Appendix: Ray Tracing for Aquarium Design	103
3.8	References	104
4	Iterative Reconstruction in Optical CT: Noise and Artifact Reduction	108
4.1	Introduction	108
4.1.1	Optical CT dosimetry	108
4.1.2	Effects of image noise and artifacts on dosimetric analysis	109
4.1.3	Iterative CT reconstruction	111
4.2	Methods	112
4.2.1	Optical CT scanner	112
4.2.2	Optical CT datasets	112
4.2.2.1	Phantom datasets	113

4.2.2.2	Gel dataset	114
4.2.3	Image reconstruction	114
4.2.3.1	Filtered backprojection (FBP)	114
4.2.3.2	Ordered subsets convex algorithm with total variation minimization (OSC-TV)	115
4.2.4	Image reconstruction details	117
4.2.4.1	OSC-TV iteration stopping conditions	118
4.2.5	Image analysis	119
4.2.5.1	Mean and standard deviation	119
4.2.5.2	Contrast to artifact + noise ratio (CANR)	119
4.2.5.3	Gradient Preservation	119
4.3	Results and Discussion	120
4.3.1	Uniform solution phantom (Phantom A)	120
4.3.2	Finger Phantom (Phantom B)	123
4.3.2.1	Contrast to artifact + noise ratio	123
4.3.2.2	Gradient sharpness	123
4.3.3	Gel dosimeter with small fields (Phantom C)	125
4.3.3.1	Contrast to artifact + noise ratio	125
4.3.3.2	Gradient sharpness	126
4.3.3.3	Field central attenuation coefficient value	128
4.3.4	Investigation of mean central value drop-off	129
4.4	Discussion and Conclusion	130
4.5	Appendix: Calculation of Total Variation Gradient	132
4.6	References	133

5 Iterative Reconstruction in Optical CT: Mismatched Refractive Index Scanning 137

5.1	Introduction	137
5.1.1	Optical computed tomography (CT) for three-dimensional (3D) ra- diation dosimetry	137
5.1.2	PRESAGE® solid dosimeters	138
5.1.3	Intentionally mismatched refractive index	140
5.1.4	Study outline	141
5.2	Methods	142
5.2.1	Scanning laser optical CT system	142
5.2.1.1	Scanning wavelengths	144
5.2.2	Ray path measurement	144
5.2.2.1	Mathematical description	144
5.2.2.2	Implementation in optical CT iterative reconstruction process	146
5.2.3	Aquarium liquid selection	147
5.2.4	CT scanning and reconstruction	148
5.2.5	Validation of technique with a uniform solution phantom	149
5.2.6	PRESAGE® experiments	150
5.2.6.1	Irradiation setup	150

5.2.6.2	PRESAGE [®] experiment 1 - uniform dose	150
5.2.6.3	PRESAGE [®] experiment 2 - step dose pattern	151
5.3	Results and Discussion	152
5.3.1	Phantom experiment	152
5.3.2	PRESAGE [®] experiments	154
5.3.2.1	PRESAGE [®] experiment 1 - uniform dose	154
5.3.2.2	PRESAGE [®] experiment 2 - step-pattern irradiation	157
5.3.2.3	PRESAGE [®] reconstruction artifacts and non-uniformity	160
5.3.3	Effects of geometric errors	161
5.3.4	Mathematical framework for 3D ray paths	163
5.4	Discussion and Conclusion	164
5.5	Appendix	167
5.5.1	PRESAGE [®] dose response non-uniformity	167
5.5.2	PRESAGE [®] optical activity	170
5.6	References	172
6	Applications of Optical CT: Small Field Dosimetry	176
6.1	Background: Small Field Dosimetry	176
6.1.1	Measuring small fields with gels	178
6.2	Small Field Dosimetry Experiment	179
6.2.1	Gel preparation	179
6.2.2	Irradiation	180
6.2.3	Optical CT imaging	181
6.3	Small Fields Analysis	181
6.3.1	Measured field size	182
6.3.2	Relative dose factors (RDFs)	183
6.3.3	Field profiles and percent depth dose curves	184
6.4	Gel Preparation Insights	187
6.5	Discussion and Conclusions	189
6.6	References	190
7	Conclusions and Future Direction	192
7.1	Summary of Contributions and Limitations	192
7.1.1	Stray light reduction: new optical CT scanner designs	192
7.1.2	Iterative CT reconstruction: Noise reduction and refractive index mismatched optical CT	194
7.1.3	Utility of optical CT dosimetry: Small field measurements	195
7.1.4	Summary of results	195
7.2	Remaining Limitations and Future Directions in Optical CT Dosimetry	196
7.2.1	Gel dosimeter vessels	197
7.2.2	Gel dosimeter chemistry	197
7.2.3	Clinical applications and developments	199
7.3	References	200
	Appendix A Fixed intensity compensation for cone beam optical CT	202

A.1	Introduction	202
A.1.1	Optical CT Dosimetry	202
A.1.2	Intensity compensation in cone beam optical CT	203
A.1.3	Study Outline	206
A.2	Materials and Methods	206
A.2.1	Optical CT Scanner	206
A.2.2	Intensity Compensators	207
A.2.2.1	Transmission vs. grayscale value	207
A.2.2.2	Parabolic grayscale profile compensator	208
A.2.2.3	Object-specific compensator	208
A.2.3	Solution phantom imaging with compensated source	209
A.3	Results and Discussion	210
A.3.1	Transmission of printed compensators	210
A.3.1.1	Relationship between grayscale value and transmission	210
A.3.1.2	Parabolic-profile compensators	211
A.3.2	Solution phantom with compensated source	213
A.4	Discussion and Conclusions	216
A.5	References	217
Appendix B Copyright Releases		220
B.1	Permission to reproduce content in Chapters 1-3	221
B.2	Permission to reproduce content in Chapter 4	222
B.3	Permission to reproduce content in Chapter 4	223
B.4	Permission to reproduce content in Chapter 4	224
B.5	Permission to reproduce content in Chapter 5	225
B.6	Permission to reproduce content in Appendix A	226
Appendix C Curriculum Vitae		227

List of Figures

1.1	Comparison of external beam radiation therapy treatment plans for an intraocular cancer. Axial, coronal, and sagittal planes through the planning CT volume are shown in the top, middle, and bottom rows for each treatment plan. a) Conformal Radiotherapy (CRT). b) Intensity Modulated Radiation Therapy (IMRT). c) Volume Modulated Arc Therapy (VMAT). Red indicates regions of high dose, while green and blue indicate regions of lower dose. Moving from CRT to IMRT and VMAT leads to increasingly uniform, conformal doses delivered preferentially to the targeted volume.	7
1.2	Attenuation of primary photons through a block of material.	22
1.3	Parallel beam (a), fan beam (b) and cone beam (c) CT projection geometries.	24
1.4	The Fourier Slice Theorem. The 1D Fourier transform of a projection $P(\theta, t)$ at angle θ is equal to the “spoke” of the 2D Fourier transform of the object at the same angle in the spatial frequency domain.	25
1.5	Measuring the absorption of a small attenuator within a scattering medium using a broad-beam transmission measurement. Stray light pollutes the measurement of primary ray transmission.	31
1.6	(a) - (d) Top view ray diagrams illustrating the origins and relative magnitude of stray light in an optical CBCT scanner with a diffuse light source used to image a two finger phantom. Horizontal line profiles on the right side illustrate relative contributions of non-primary rays (stray light) . (e) Horizontal line profile of a transmission image.	34
2.1	Top view schematics of (a) the entire Fresnel-modified optical CBCT scanner (Vista10, Modus Medical Devices Inc., London, Canada). Roman numerals depict the locations of the isotropic source (i), Fresnel lens (ii), entrance aperture (iii), exit aperture (iv) and camera (v). (b) The light source, consisting of LED, lens, bandpass filter, and diffuser. The source is set up to achieve an approximately 2 mm diameter spot at the entrance side (LED side) of the diffuser. The circuit powering the LED is not shown.	49

2.2	Single cone-beam projection images of solution-filled PETE vessel. (a) 7.5% propylene glycol (by volume) inside and outside the vessel, with the original diffuser light source. (b) water inside and outside the vessel, with the Fresnel source, illustrating the lack of signal toward the vessel periphery. (c) 7.5% by volume propylene glycol inside the vessel, water outside, demonstrating improved signal capture through intentional refractive index mismatch. Note the appearance of vessel features, including seams, in (b) and (c), which are not visible in (a), indicating high contrast performance of the Fresnel system. (d) central horizontal axis intensity profiles (jar seam rotated out of view) for cases (b) (dashed black) and (c) (solid grey). Vessel wall edges can be seen as the sharp edges in profiles near 2.2 and 11.8 cm. Note the better signal coverage through a wider extent of the vessel for intentional refractive index mismatching.	55
2.3	Central-line profiles (solid black) through reconstructions from full cone beam data of the 5 uniform attenuating solutions (#4-8 in Table 2.2, numbered above profiles in figure). The dashed, gray horizontal lines mark the mean values measured from four $12.5 \times 12.5 \times 2.5 \text{ mm}^3$ ROIs located just off the rotation axis (see Table 2.2). Note that spikes appearing near the edges of profiles are associated with missing projection data very near the vessel wall and mechanical error in the alignment between pre- and post-scans.	62
2.4	Central horizontal axis line profiles: (a) uniform reference phantom (5% gelatin), (b) carbon black finger gel. Composite open field (solid black) and stray light component (solid gray) are shown. Within the vessel, stray light contributes less than 4% of the total signal.	64
2.5	(a) A reconstruction slice (window = 0.3 cm^{-1} , level = 0.12 cm^{-1}), of the FEP finger phantom filled with attenuating water based solution (solution #10), acquired with the full cone beam and reconstructed with 0.25 mm voxels on a 512^3 grid. The bright edges of the finger are due to mechanical misalignment between reference and data scans. (b) A reconstruction slice of the attenuating, 7.5% propylene glycol, carbon black solution (solution #6) (window = 0.05 cm^{-1} , level = 0.12 cm^{-1}) acquired with the full cone beam and reconstructed with 0.5 mm voxels on a 256^3 grid. Note the appearance of streaking through the center of the reconstruction, associated with the seams of the PETE vessel, as well as artifacts near the vessel walls associated with unique wall features and missing data. (c) A reconstruction slice (window = 0.05 cm^{-1} , level = 0.12 cm^{-1}) of the uniformly attenuating carbon black 7.5% propylene glycol solution scanned with the larger LED source. Note that the appearance of artifacts is reduced compared to (b), due to stray light blurring and filling in near-wall missing data.	67

3.1	Top-view schematic of the scanning-laser system. The rotating galvanometer mirror and detector module are mounted on synchronized vertical translation stages. The curvature of the aquarium was designed by ray-tracing simulation to generate parallel-beam geometry through the interior of the dosimeter volume. The axis of rotation and points 7.5 cm away in each of the 4 cardinal directions are indicated by letters A-E, and correspond to points where spatial resolution was measured using a knife edge test (See Section 3.3.4).	78
3.2	Photomultiplier vs. Photodiode measurement of laser intensity, demonstrating the linearity of the detector used in the scanner. Error bars are included but are similar in size to the data markers.	84
3.3	Top view photograph (brightness and contrast enhanced) of scattering Intralipid solution with laser beam directed along the diameter. The white line indicates the central plane through the dosimeter. The attenuation of the primary beam due to scatter can be seen, with the conical “bloom” of scattered light clearly visible, showing the three-dimensional distribution of scattered light.	92
3.4	Reconstruction of the 15 cm phantom containing a uniform absorbing liquid (a) Central axial slice. (b) horizontal profile through the axial slice, (c) vertical (z) profile from top to bottom of the phantom.	95
3.5	Central slice profiles across reconstruction slices of the uniform 15 cm scattering phantom. Reconstructions are flat within 3%, indicating a lack of cupping artifacts.	96
3.6	Reconstruction slice (a) and profile across finger (b) for the FEP tube phantom experiment (liquid A12 in table 3.5). The profile location in (b) is indicated by the white line in (a). Dashed vertical lines in (b) indicate the actual diameter of the phantom. Asymmetry in the profile, particularly evident in the baseline outside the cylinder, is caused by a slight mechanical displacement between pre- and post-scans introduced when changing the liquids within the phantom.	98
3.7	Profiles across the finger phantom reconstructions from the “front” and “back” half of the sinogram, for the case of 2% transmission (a) and 50% transmission (b) scattering solution surrounding the finger. In (a) there is approximately 3% difference between the central attenuation coefficients, while in (b) there is only a 0.5% difference.	100

3.8	Schematic for ray-tracing lens profile generation. The algorithm starts at position A , and minimizes Δy_{SAD} for each y_{step} by applying Snell's law of refraction and varying the angle of the aquarium wall interface. The x coordinate of point A is set by the user, and the x coordinates of the subsequent minimization steps are calculated by computing a linear segment of the air-water interface profile, with a y step size of 0.01 mm. This generates the profile of the aquarium wall, to create an acylindrical lens aquarium.	104
4.1	Axial slices of phantoms used in the study. Reconstructions shown are performed with Hamming-filtered FBP. a) Phantom A: uniform 15 cm diameter liquid absorber (window/level = 0.3 / 0.0 cm^{-1}). b) Phantom B: finger phantom (window/level = 2.0 / 0.0 cm^{-1}). c) Phantom C: small radiation fields (window/level = 1.2 / 0.0 cm^{-1}).	113
4.2	Results from the uniform absorbing solution phantom. a) reconstruction slices (window = 0.25, level = 0.125 cm^{-1}) from FBP with Hamming filter (left) and OSC-TV with $c = 0.5$ (right), showing the reduction in streak artifacts associated with vessel imperfections. b) profiles across reconstruction slices, showing the reduction in noise. For visibility, only a subset of profiles are plotted. Almost all OSC-TV profiles overlap throughout the center of the profile. c) mean and standard deviation measured within a $10 \times 10 \times 1 \text{ mm}^3$ region of interest in each reconstruction.	122
4.3	Contrast to artifact + noise ratios for reconstructions of the finger phantom (Phantom B).	123
4.4	Central profiles across the finger phantom (phantom B) reconstructions. For visibility, only a subset of reconstructions are plotted. OSC-TV reconstructions with $c < 2.0$ show almost perfect overlap. b) profiles plotted as % differences from the $c = 0.5$ OSC-TV reconstruction.	124
4.5	Contrast to artifact + noise ratios for the small-field gel dosimetry reconstructions.	125
4.6	a) single line profiles through the 4 field sizes in each reconstruction. For visibility, only a subset of profiles are plotted. b) profiles plotted as % differences from the $c = 0.5$ reconstruction.	127
4.7	Relative mean central attenuation coefficient values for small-field reconstructions (normalized to the FBP-ramp reconstruction).	128
4.8	Relative mean central attenuation coefficient for a $0.6 \times 0.6 \text{ cm}$ square field in the digital phantom simulation, with and without 1% Gaussian noise added to projection data.	130

5.1	Optical CT projection acquired with a scanning laser cone-beam CT with a viscous refractive index matching liquid in the aquarium. This image is the ratio of the post-irradiation projection over the pre-irradiation projection (i.e. post-scan / pre-scan). In the aquarium liquid, Schlieren bands are clearly visible, resulting in unacceptable variable signal levels (+/- 10%) through the reference liquid. These patterns change with time and therefore are different in each projection.	139
5.2	Ray-tracing simulation of refracted fan-beam light rays through an 11 cm diameter PRESAGE [®] solid dosimeter ($n = 1.5$) placed within a purposely mismatched refractive index media ($n = 1.41$). The plastic dosimeter acts as a converging lens.	141
5.3	Scanning laser CT schematic, top view. A helium neon laser beam is filtered and raster-scanned in cone-beam geometry across the aquarium and dosimeter. The primary ray strikes a planar diffuser screen, which causes forward scattering of light. A fraction of this light is detected by a photomultiplier tube (PMT), and this intensity is assigned to the ray's path determined by a fiducial marker placed on the side of the dosimeter.	143
5.4	Schematic of fiducial-based ray path measurement technique. A primary ray is occluded by a fiducial marker at its entry (a) and exit (b) from the dosimeter at two different rotation angles. (c) The fiducial's sinogram trajectory, with the rotation angles corresponding to (a) and (b). By finding the intersection point between vertical "ray index lines" and the fiducial spot trajectory, the angles θ_{entry} and θ_{exit} , and thus the actual ray paths through the dosimeter, can be calculated.	146
5.5	Results from the liquid phantom experiment. (a) Re-binned parallel-beam sinogram projection. Dashed vertical lines mark the edge of the completely-sampled region used in the iterative reconstruction algorithm. (b) CT reconstruction of axial slice. A ring artifact appears at the boundary between fully sampled and under-sampled radii. (c) Horizontal profile across the image in (b). The solid and dashed horizontal lines show the mean $\pm 1\sigma$ for the reference Beer-Lambert law central axis value determined along the diametric path.	153
5.6	Uniformly irradiated PRESAGE [®] sample (9.0 Gy nominal dose). (a) Reconstructed axial slice. (b) Central profile. The reconstruction shows agreement with the central axis Beer-Lambert value (mean $\pm 1\sigma$ shown as horizontal solid and dashed lines in (b)).	155
5.7	Two-level irradiation PRESAGE [®] experiment results (a) 0.32 mm pixel resolution reconstruction of axial slice. (b) Central line profiles from the 0.32 mm resolution reconstruction (dashed gray) and the 1 mm resolution reconstruction (solid black).	158

5.8	Profiles across the gradient generated by the lead block, measured by PRESAGE® (solid black), EBT3 film (dashed grey), and A1SL ion chamber (cross symbols). The readouts from each dosimeter (PRESAGE®: attenuation coefficient in cm^{-1} ; film: dose in cGy from optical density calibration data; ion chamber: charge in nC) were normalized in the center of the high dose plateau. Optical CT, film, and ion chamber measurements show good agreement in the gradient region.	159
5.9	Sketch of the fiducial layout needed for ray path measurement in 3D. The z dependence of the angular separation is known.	164
5.10	Central profiles (1 mm pixel resolution) through reconstructions of four uniformly irradiated PRESAGE® dosimeters manufactured in different batches, with non-uniformity in response ranging from severe (top) to moderate (bottom). The dashed grey lines in the plots indicate uniform attenuation. There is a substantial non-uniformity in some dosimeters, up to 20% difference from central to maximum response. The non-uniformity is inconsistent from batch to batch. The best dosimeters, used in the main experiments in this paper, exhibit approximately 5% non-uniformity (minimum to maximum response).	169
5.11	Central profile (1 mm pixel resolution) through a PRESAGE® dosimeter irradiated to a nominal dose of 2.2 Gy. (a) raw attenuation profile. (b) calibrated dose profile using a “pre-irradiation” of 1.1 Gy to create a spatial dose response map. Note that the calibrated dose profile is flat within the fully sampled region (the “spikes” in (b)), but the calibration fails outside of it. This dosimeter exhibited fairly severe non-uniformity in response. . .	170
5.12	(a) Schematic of apparatus used to examine optical activity in PRESAGE® dosimeters. If the dosimeter is optically active, the camera will detect signal, otherwise the image will be dark. (b,c) Transmission images acquired using a single polarizer (b) and crossed polarizers (c). With crossed polarizers there is no transmission through the glycerol, indicating that it is not optically active. However, fringe patterns of transmission are visible in the light transmitted through the PRESAGE® dosimeter, indicating structured optical activity.	171
6.1	Small-field gel dosimetry dataset. Axial (10 cm depth), sagittal and coronal slices of the reconstruction (OSC-TV) are shown. Reconstruction matrix size was $512 \times 512 \times 400$ voxels (0.33 mm isotropic). Window/level = 0.25/0.5 cm^{-1} . The red square outlined in the left panel (side length = 10 mm) is a region of interest used to measure background auto-oxidation. . .	182
6.2	Gel and Monte Carlo beam profiles at 10 cm depth for small fields (Varian 21iX, 6MV, jaw-defined fields). Profiles plotted here are normalized to the <i>gel</i> . For visibility, error bars are not included.	185

6.3	Gel and Monte Carlo Percent Depth Dose curves for small fields (Varian 21iX, 6MV, jaw-defined fields). Doses have been normalized at the field center at 5 cm depth. Large spikes in the magnitude of error bars correspond to ring artifacts in the reconstruction.	186
6.4	3×3 cm ² field percent depth dose curves obtained from Monte Carlo simulation and 3 iterations of the small field gel dosimetry experiment with different gel storage times. Doses have been normalized at 5 cm depth (the most trustworthy region of the gel). For visibility, error bars on gel measurements have not been included.	188
A.1	Top view schematic of the modified Vista TM optical CT scanner. The positions of the light source (i), intensity compensator (ii), Fresnel lens (iii), aquarium entrance aperture (iv), aquarium exit aperture (v) and camera (vi) are shown. Positions of the light source and compensator were adjustable, so only approximate distances are provided in this figure. A convergent cone of image forming primary rays is generated by the Fresnel lens focusing the light from the small LED + diffuser source.	207
A.2	a) Average transmission values (averaged over 1 cm \times 5 cm ROI) of laser-printed test strips on overhead transparencies, measured at the scanner's rotation axis (in focus). The transmission of the base film (no printing) is also shown (solid gray line). b) Central horizontal profiles across bitmap image files used to print the parabolic (solid black) and object-specific (dashed gray) compensators.	211
A.3	Transmission (air reference) images of laser-printed parabolic-profile compensators. a) large compensator located at scanner rotation axis (in focus). b) small compensator located 6cm from light source (out of focus). c) indicated profiles through (a) and (b), as well as the expected transmission profile for (a). Note that the compensator in (b) is slightly offset from the center of the field of view; this was corrected prior to performing optical CT imaging experiments.	213
A.4	a) Horizontal profiles across single projection images of the reference solution phantom with no compensator, object-specific, 2-layer object-specific, and parabolic compensators. Note that the signal value in the "no compensator" profile reaches approximately 6×10^4 in the regions outside the vessel, which has been cut off in this plot. Also note that the vessel was rotated such that the seam was not visible in the latter 2 profiles. b) Reconstruction slice (OSC-TV, 0.25 mm voxels) of the solution phantom scanned using the parabolic compensator. c) Central horizontal profiles (FDK and OSC-TV) across the reconstructions, along line indicated in (b).	215

List of Tables

1.1	Dosimetric properties of commonly used radiation detectors.	14
2.1	Comparison of narrow-beam experiment and Fan beam CT attenuation coefficient. Narrow beam attenuations were calculated using the Beer-Lambert law. CT measurements were averaged over four $12.5 \times 12.5 \times 2.5$ mm ³ ROIs located just off the rotation axis and away from between-seam artifacts.	60
2.2	Comparison of Fresnel source cone beam optical CT (CBCT) and Fresnel source fan beam optical CT (FBCT) measurements of the 7.5% propylene glycol, carbon black micelle solutions. CT scans were performed with the full cone beam as well as with the 1 cm fan beam aperture. The average reconstructed linear attenuation coefficients were calculated by averaging over four $12.5 \times 12.5 \times 2.5$ mm ³ ROIs located just off the rotation axis and away from between-seam artifacts.	61
2.3	Comparison of Fresnel source cone beam optical CT (CBCT) and Fresnel source fan beam optical CT (FBCT) attenuation measurements of the carbon black micelle solutions inside the FEP tubes of the finger phantom, with no PETE vessel in the scanner. CT scans were performed with the full cone beam as well as with the 1 cm fan beam aperture. The average reconstructed attenuation coefficients were averaged over a cylindrical region of interest (6 mm diameter, 4 mm height) in the center of the finger.	63
3.1	Horizontal MTF50% and MTF10% resolutions for various positions measured by knife edge test. The vertical direction MTF values were similar but showed no variation across the horizontal field of view, since the curvature of the aquarium is only in the horizontal direction. Locations are indicated by the letters in Figure 3.1, and correspond to the scanner's rotation axis and points 7.5 cm away in the cardinal directions.	86
3.2	Summary of initial characterization test results for scanning laser system. .	87
3.3	Parameters used for optical CT scan acquisition and reconstruction.	89

3.4	Optical CT and Beer-Lambert (10 cm cell) attenuation coefficients measured in the 15 cm phantom containing absorbing liquids (A1-A7). μ_{CT} is reported as the mean and standard deviation within a $5 \times 5 \times 5 \text{ mm}^3$ ROI located 1 cm off the rotation axis in the central axial plane. The fraction of voxels within the vessel which have values that lie within 2%, 3%, and 5% of the mean value was also quantified for each reconstruction. $\mu_{cuvette}$ uncertainty is taken from three repeated trials of the spectrometer assessment, with samples re-positioned between each measurement.	94
3.5	Optical CT and Beer-Lambert (10 cm cell) attenuation coefficients measured in the uniform solution phantom experiment for scattering liquids (S1-S5). μ_{CT} is reported as the mean and standard deviation within a $5 \times 5 \times 5 \text{ mm}^3$ ROI located 1 cm off the rotation axis in the central axial plane. $\mu_{cuvette}$ uncertainty is taken from three repeated trials of the spectrometer assessment, with samples re-positioned between each measurement.	96
3.6	Optical CT and absorption spectrometer attenuation coefficients measured in the 12.5 mm (inner diameter) finger phantom placed within a 15 cm vessel containing the gelatin-simulating Intralipid solution. The finger contained absorbing Nigrosin-dyed liquids (A8-A15). $\mu_{cuvette}$ measurement uncertainty is derived from three repeated trials where the cuvettes were removed and re-positioned in the spectrometer on each trial.	98
5.1	Summary of laser wavelengths used for experiments in the study.	144
5.2	Reconstructed attenuation coefficients (μ_{CT}) measured from eleven $2 \times 2 \text{ mm}^2$ ROIs equally spaced every 4 mm within the central, fully sampled region compared to those calculated using the Beer-Lambert law along the central axis of the dosimeter ($\mu_{Beer-Lambert}$), for the nominal doses delivered to a PRESAGE [®] dosimeter.	156
6.1	Measured FWHM field sizes (10 cm depth) and relative dose factors (vs. 3×3 field) for small fields (6 MV).	183
6.2	Relative Dose Factors (3×3 reference) for 6MV photons, measured at SSD = 90 cm and $d = 10$ cm. Results from 3 trials of the gel dosimetry experiment, performed using different batches of LCV-SDS, are included (bold font). External study results have been calculated from reported output factors for 3×3 , 2×2 , and $1 \times 1 \text{ cm}^2$ field sizes, where available.	183

List of Appendices

- A. Fixed intensity compensation for cone beam optical CT 202
- B. Copyright Releases 220
- C. Curriculum Vitae 227

List of Abbreviations

2D	two-dimensional
3D	three-dimensional
AAPM	American Association of Physicists in Medicine
ADU	analog-digital units
CCD	charge coupled device
CANR	contrast to artifact + noise ratio
CNR	contrast to noise ratio
CT	computed tomography
CTV	clinical target volume
DTA	distance to agreement
EBRT/XBRT	external beam radiation therapy
FBP	filtered backprojection
FT	Fourier transform
FWHM	full width at half maximum
FX	ferrous xlenol
GPU	graphics processing unit
GTV	gross tumour volume
He-Ne	helium-neon
kVCT	kilovoltage computed tomography
ICRU	International Commission on Radiological Units
IGRT	image guided radiation therapy
IMRT	intensity modulated radiation therapy
IROC	Imaging and Radiation Oncology Core
ITV	internal target volume
LCV	leuco crystal violet
LED	light emitting diode
MLC	multileaf collimator
MRI	magnetic resonance imaging
MU	monitor unit

MV	megavoltage
OAR	organ at risk
OBI	on-board imaging
OD	optical density
OSC-TV	ordered subsets convex algorithm with total variation minimization
OSLD	optically stimulated luminescence dosimeter
PDD	percent depth dose
PETE	polyethylene terephthalate
PMMA	polymethyl methacrylate
PTV	planning target volume
QA	quality assurance
RDF	relative dose factor
ROF	relative output factor
ROI	region of interest
RTAP	resolution, time, accuracy, precision
SNR	signal to noise ratio
SPR	scatter to primary ratio
TAR	tissue to air ratio
TG-XX	AAPM Task Group #XX
TLD	thermoluminescent dosimeter
TPR	tissue to phantom ratio
TPS	treatment planning system
VMAT	volumetric modulated arc therapy

List of Symbols

λ	wavelength
D	absorbed dose
d_{max}	depth of maximum dose
μ	attenuation coefficient
I	light intensity
V	voltage

Chapter 1

General Introduction

1.1 Cancer Basics

Cancer, at the fundamental level, is a group of over 100 diseases characterized by genetic mutations resulting in abnormal, uncontrolled cell growth. This leads to the formation of malignant tumours that have the ability to invade tissues and spread to other parts of the body [1]. The symptoms of cancer are caused by the inhibition of normal tissue and organ functions as a result of tumours. Thus, symptoms vary depending on the disease location and type, and will only appear once a cancerous tumour is growing. There are a multitude of known (and suspected) environmental, pathogen, and hereditary causes and risk factors for different types of cancer [2], and some cancers appear to develop randomly, without any known cause.

1.1.1 Cancer in Canada

The Canadian Cancer Society estimates that in 2017, there were approximately 200 000 new cases of cancer diagnosed in Canada (excluding non-melanoma skin cancers), and approximately 81 000 cancer deaths. This incidence corresponds to approximately 0.5% of the total population of Canada being newly diagnosed with some form of the disease in

a single year alone. It is estimated that 1 in 2 Canadians will develop cancer during their lifetime, and that 1 in 4 Canadians will die from the disease. Cancer is the leading cause of death in Canada, and was responsible for approximately 30% of total deaths in 2012 [3].

1.2 Radiation Therapy

According to the US National Cancer Institute [4], about half of all newly diagnosed cancer patients *should* receive radiation therapy at some point during their treatment. Approximately 60% of radiotherapy patients are treated with the aim of curing the disease, with the rest treated as palliative patients; alleviating symptoms associated with tumour masses to improve quality of life. In Ontario, as of 2012, the radiation treatment utilization rate (the proportion of cancer patients who receive at least one course of radiation during their lifetime) was only 37%, which is below the Cancer Care Ontario target rate of 48% [5], due to capacity and geographic access limitations. Cancer Care Ontario projects that additional new treatment units will be required to reach a utilization rate of 42% by 2020 [5]. Regardless, it is clear that a very large minority of cancer patients require radiation therapy.

Radiation therapy, or radiotherapy, is generally divided into internal radiotherapy, also known as brachytherapy, and external beam radiotherapy (EBRT). Brachytherapy involves bringing a radioactive source within close proximity of the tumour, through either the implantation of radioactive seeds or the temporary insertion of a radioactive source within a catheter inserted by a needle. External beam radiotherapy involves delivering a beam of ionizing radiation (high-energy x-rays or charged particles) into the patient from the outside. Generally, the type (and dose) of therapy given will depend on the size and location of the tumour being treated. A combination of both external beam radiotherapy and brachytherapy can also be used in some circumstances. Radiotherapy can also be combined with chemotherapy treatments, where the chemotherapy is used to either enhance the

treatment of the local disease, or to kill cancer cells in other parts of the body [6].

Ionizing radiation kills cells by damaging DNA, which leads to cell death through a variety of pathways, including apoptosis or failure to successfully divide due to improper DNA repair (chromosomal aberrations). With an increase in absorbed radiation doses (the energy absorbed per unit mass, usually given in units of Gray, $1 \text{ Gy} = 1 \text{ J/kg}$ absorbed), the amount of DNA damage is increased, and so too is the probability that a lethal chromosomal aberration will occur. DNA damage in radiation therapy occurs by either *direct* interactions between the radiation particles (photons, electrons, protons etc.) and the DNA molecule, or by *indirect* interactions, wherein the ionizing radiation interacts with water to create free radicals (highly reactive molecules) that subsequently interact with the DNA. In photon and electron beam treatments, most radiation damage is delivered through the indirect interactions [7–9]. Radiation kills both healthy and cancerous cells. However, radiotherapy plans are spatially optimized to preferentially deposit dose in cancerous tissue and spare healthy tissue. Accurate three-dimensional measurement of such dose distributions is the focus of this thesis.

In addition to spatial optimization, cancer cells are generally undifferentiated and have a reduced capacity to repair sub-lethal DNA damage compared to healthy cells [8]. To exploit this, radiation therapy is often delivered in a set of time-separated fractions, which provides time for DNA repair between doses. Healthy tissue will repair more sub-lethal damage than cancer cells, resulting in a therapeutic advantage. In addition, the time gap allows for reoxygenation of hypoxic tumour regions and re-organization of cells in the reproduction cycle. These effects can enhance cell killing, however they must be balanced against the tumour's repopulation / growth rate and DNA repair rate. Usually, radiotherapy fractions are delivered once per day, 5 days a week over several weeks (which may allow concurrent tumour cell repopulation). A typical fractionated treatment plan may consist of 60 Gy of dose delivered to the target over 30 treatment visits, in fractions of 2 Gy.

1.2.1 Radiation therapy process

After diagnosis and recommendation for radiotherapy, a cancer patient will be referred to a radiation oncologist who will determine and oversee their treatment. For external beam radiation therapy patients, the process will begin with the acquisition of a “planning CT”, which is an x-ray computed tomography (CT) imaging study performed with the patient set up in the posture in which they will later be treated. Additional studies, for example contrast CT or magnetic resonance imaging (MRI) may also be acquired in this preparatory stage, in order to aid the radiation oncologists and radiation therapists in targeting the diseased volume and avoiding nearby normal structures.

The planning CT data is imported into a Treatment Planning System (TPS), a software package in which radiation treatment planners delineate both the tumour and surrounding organs at risk (OARs) that must be considered when planning the radiation delivery. Tumour volumes are expanded from the gross tumour volume (GTV) with additional margins to account for less visible microscopic extension of the disease (the “clinical target volume” or CTV), tumour motion such as that due to respiration (the “internal target volume”, or ITV), and patient set-up uncertainty on treatment days (the “planning target volume” or PTV) [10]. Once all the important structures have been contoured, the radiation oncologist prescribes a radiation dose to the target volume. The prescription dose is chosen based on clinical protocols and prior experience with similar cases. Additionally, the OARs have associated dose-limiting constraints (e.g. maximum dose to any point, maximum volume receiving more than a certain dose, etc) that are chosen to avoid normal tissue complications as much as possible. Dose prescriptions and OAR limits are informed by the results of various clinical trials, and refinements to protocols are always ongoing.

In addition to contoured volumes and dose constraints, a map of electron density (electrons per cm^3) is required for dose calculation and treatment planning. The electron density map is obtained by applying a calibration curve to the CT image data, which assigns a given

electron density based on the CT number (or Hounsfield Units, HU) of different tissues in the reconstructed scan.

The electron density map, contours, and dose constraints are then used to plan the treatment. Depending on the treatment type and software package, this optimization stage may require some degree of user intervention. The planning software iteratively modifies the treatment plan's radiation beams in an effort to achieve coverage of the target volume while minimizing dose to OARs (or at least staying below threshold values). This is done through an optimization process that minimizes a cost function based on the dose to target and doses to OARs. Once the optimized treatment plan has been approved by the radiation oncologist, verified dosimetrically, and reviewed by a medical physicist, the patient's treatment course can begin in earnest. Depending on the treatment fractionation scheme, this can occur over one day (single fraction radiosurgery) to several weeks (conventional fractionated radiotherapy).

On a treatment day, the patient is set up in the treatment pose on the couch of the linear accelerator. Often, an image guidance cone-beam CT (CBCT) is acquired (in some cases, 2D planar x-ray imaging alone, or in conjunction with CBCT, may be used). By looking at the alignment of the bony anatomy in the planning CT compared to the cone-beam CT scan of the day, radiation therapists can correct for positional shift between images by moving the linear accelerator couch. The couch can be translated in the 3 coordinate directions (vertical, lateral, longitudinal), and (on newer treatment units) even rotated about all 3 coordinate axes to bring the target back to the planned location. The cone-beam CT scan can also be used to assess anatomical changes in the patient, due to tumour progression/response or other anatomical changes (typically weight loss). If these changes are substantial, the treatment may need to be re-planned, since the doses delivered will no longer be appropriate. Re-planning is done in much the same way as the initial planning, with a new planning CT and dose calculation performed. Additionally, there is ongoing research in the field

of *adaptive* radiotherapy, which is the ongoing modification of a treatment plan based on feedback from various biological and anatomical measurements [11, 12]. These approaches have the potential to improve radiotherapy outcomes by providing better tumour control as well as fewer or less severe normal tissue complications.

1.2.2 Advances in external beam radiotherapy

Modern radiation therapy techniques are increasingly good at maximizing the dose delivered to the cancer, while minimizing the dose delivered to organs at risk. Over the last several decades, linear accelerators (linacs) producing megavoltage (MV) X-rays have supplanted cobalt-60 irradiators as the standard for delivery of external beam therapy in North America. Megavoltage accelerators provide higher energy photons than the gamma rays from cobalt-60 decay. This allows them to more effectively deliver dose to deep tumours, due to an increase in the depth at which they deposit maximum dose. More recently, the multi-leaf collimator (MLC) has been developed. This device consists of many narrow, movable tungsten leaves that can sculpt a radiation field into a prescribed shape [13], which increases the degrees of freedom that can be used to achieve a conformal dose distribution in the patient.

The MLC's development enabled the advent of modern, inverse-planned treatment techniques such as Intensity Modulated Radiation Therapy (IMRT) [14, 15] and Volumetric Modulated Arc Therapy (VMAT) [16]. In IMRT, beams are delivered from a discrete number of gantry angles, with radiation fields for each angle shaped by moving MLC leaves either dynamically with the beam on ("sliding window" IMRT) or by turning the beam off during MLC movements ("step and shoot" IMRT). The superposition of the doses deposited by each field creates a tightly conformal dose distribution in the target, while sparing more normal tissue than was previously achievable with conventional or conformal radiotherapy. VMAT is essentially the dynamic beam angle form of IMRT. Here, the

gantry of the treatment unit is continuously rotating while the MLC concurrently shapes the radiation field. This can achieve similarly conformal dose distributions in the target volume as IMRT, usually with a faster treatment. The main differences between IMRT and VMAT plans are in the surrounding normal tissue; VMAT plans deliver a lower average dose to a larger volume of healthy tissue than IMRT plans. Figure 1.1 shows planned dose distributions for a conformal, IMRT and VMAT treatment plan. The improved conformity of the inverse-planned treatments is evident from the dose colour maps, as is the enhanced normal tissue sparing.

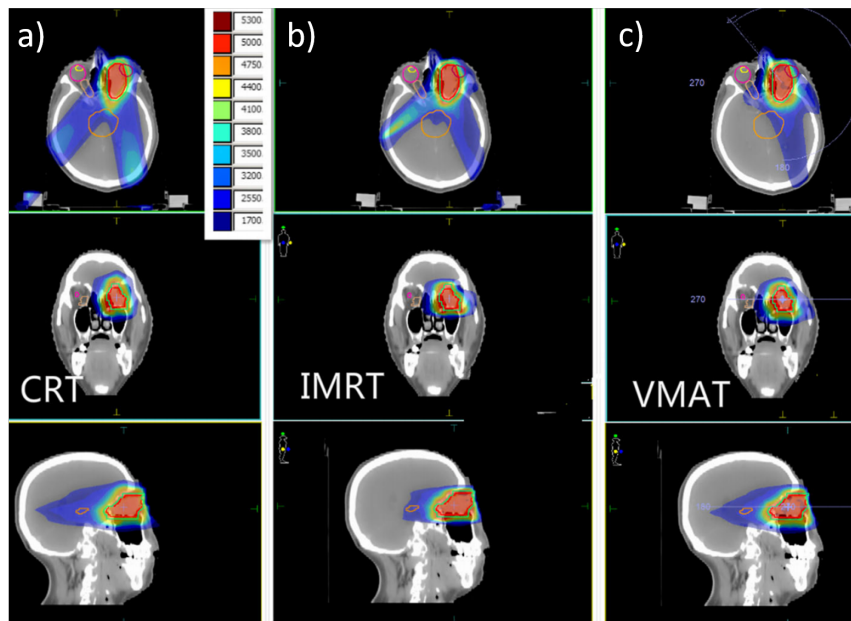


Figure 1.1: Comparison of external beam radiation therapy treatment plans for an intraocular cancer. Axial, coronal, and sagittal planes through the planning CT volume are shown in the top, middle, and bottom rows for each treatment plan. a) Conformal Radiotherapy (CRT). b) Intensity Modulated Radiation Therapy (IMRT). c) Volume Modulated Arc Therapy (VMAT). Red indicates regions of high dose, while green and blue indicate regions of lower dose. Moving from CRT to IMRT and VMAT leads to more uniform, conformal doses delivered preferentially to the targeted volume. Figure reproduced from Deng *et al.* [17] under the Creative Commons Attribution 4.0 License¹.

¹©Deng *et al.* 2017. Available for use under the Creative Commons Attribution License (CC-BY) (<http://creativecommons.org/licenses/by/4.0/>). Figure modified to add labels.

While IMRT and VMAT were developed for cone-beam linear accelerators, an alternative technology known as tomotherapy was also developed [18]. Tomotherapy treatment ma-

chines deliver a fan beam of MV x-rays, shaped by a simpler binary MLC. The fan beam rotates continuously around the patient while the MLC shapes the fan beam. In helical tomotherapy, the patient is translated through the beam continuously, causing the source to have a helical trajectory in the patient's frame of reference.

For the most part, advances in radiotherapy have been made while keeping to the principle that dose should be uniformly delivered to target volumes. However, the notion that tumours are homogeneous in a biological sense (radiosensitivity, oxygenation, proliferation) is known to be false. Uniform target prescriptions have been used both for practical purposes (consistency in clinical trials, for example) and because the actual distribution of radiation sensitivity and biological activity within tumours was previously difficult to discern. Advances in functional imaging, with an improving understanding of tumour biology and radiobiology, are driving research into prescribing different doses to sub-volumes of targets. Concepts such as sub-volume boosting [19] and “dose painting” [20] are being investigated to improve tumour response in hyposensitive regions of hypoxia [21] or to deliver higher doses to regions that are expected to be at higher risk of progression [22–24].

Finally, the conventional dose fractionation schemes for radiotherapy are also being challenged to achieve even better temporal optimization. Stereotactic radiosurgery (SRS) techniques are based on a hypofractionation scheme, delivering a high dose in 1-5 fractions rather than 10-30 [25–27]. These types of treatments are normally reserved for small tumours or isolated metastatic lesions, and because of the small sizes, high doses, and small number of fractions, require more stringent geometric and dosimetric tolerances than standard therapies.

1.3 Radiotherapy Quality Assurance

The benefits of modern, precise radiation therapy will not come easily. The complexity of treatments, in terms of planned dose distributions as well as the technical control of delivery, has increased considerably over time. As treatment plans become more conformal, with sharper dose gradients between targets and normal tissue or OARs, the importance of accurately hitting the target is amplified, as a geographic miss could lead to severe underdosing of tumours and over-dosing of organs at risk. Therefore, a critical part of the operation of a radiotherapy physics team is quality assurance (QA). Quality Assurance, as defined by the International Organization for Standardization (ISO) is the set of “planned and systematic actions necessary to provide adequate confidence that a product or process will satisfy given requirements for quality” [28]. For radiation therapy, the required accuracy of dose delivery to a reference point in a patient is $\pm 5\%$, with a spatial accuracy within 5 mm (each at the 95% statistical confidence level) [29, 30]. These requirements refer to the end point of the radiation therapy sequence. As there are uncertainties associated with each part of radiotherapy procedures (e.g. beam calibration, dose calculations, patient setup) prior to the actual radiation delivery, the goals for accuracy in the delivery step for standard treatments are $\pm 3\%$ and 3 mm - rather stringent demands for treating an anatomy that changes over time.

1.4 Radiation Dosimeters

Radiation dosimeters are used to measure the amount of energy absorbed per unit mass of matter (the absorbed dose). Dose is measured in units of Gray ($1 \text{ Gy} = 1 \text{ J/kg}$). Dosimeters come in myriad forms, and are used for many different tasks in the fields of radiation therapy and radiation safety. Recent reviews by Seco *et al.* and Kron *et al.* give a good overview of dosimeters and specific dosimetry applications in radiotherapy [31, 32].

1.4.1 Properties of dosimeters

The various radiation dosimeters each come with their own strengths and shortcomings. Below are some of the important characteristics that can be used to evaluate and compare different dosimeters for different applications [30, 31, 33]:

Absolute vs. Relative: An absolute dosimeter can be used to directly measured the absorbed dose (in units of Gy) with no calibration, whereas a relative dosimeter's signal must be characterized as a function of known doses, usually measured by a secondary dosimeter traceable to a national standards lab. In other words, relative dosimeters require cross-calibration of their output signal.

Integrating vs. Differential: An integrating dosimeter measures the accumulated dose absorbed in the sensitive volume over a given exposure time. This type of dosimeter is most commonly used in quality assurance tests. Conversely, a differential dosimeter provides a measure of the instantaneous rate at which dose is being absorbed in a volume, which may be useful in situations where temporal fluctuations in dose rate are expected to be observed.

Tissue / Water Equivalence: Many clinical dosimetry and commissioning tasks are performed in a water medium, to mimic the absorption and scattering of radiation in the human body. Having a dosimeter that has similar absorption and scattering characteristics as water or tissue, for the type of particles being used to irradiate, makes interpretation of dosimetric results more direct, without introducing additional uncertainties due to cross-material conversion factors.

Accuracy: Accuracy refers to how closely a dosimeter agrees with the true value of the absorbed dose. In dosimetry, it is usually defined based on comparison against a "gold standard" dosimeter, which is typically an ion chamber measurement traceable to a national lab standard.

Precision: Precision is related to the reproducibility of measurements, and is expressed in terms of the standard deviation of a set of repeated measurements. Precision is limited by noise in the dosimeter or its associated readout system.

Sensitivity: Sensitivity is the rate of change in the dosimeter's readout signal with respect to an increasing dose. Graphically, it is the slope of a dosimeter's Readout Signal *versus* Dose curve.

Linearity: A dosimeter whose reading increases linearly with absorbed dose is easier to calibrate than a non-linear dosimeter.

Energy Independence: It is important that a dosimeter's sensitivity exhibits little to no dependence on the energy of incoming radiation, because the energy spectrum of treatment photon beams is broad and changes with depth in tissue (beam hardening). In other words, calibration of a dosimeter at the incident beam energy will not guarantee accuracy for measurements within an absorber, unless the dosimeter response is energy-independent.

Dose Rate Independence: For an integrating dosimeter it is *critical* that the response is not dependent on the rate at which dose is absorbed. If this is not the case, the reading from the dosimeter must be corrected using additional information, because the dose rate at different points in an absorber for a delivered radiation beam varies significantly.

Temporal Stability: Temporal stability refers to the stability of the dosimeter reading as a function of time after irradiation. For example, some radiochromic gel dosimeters exhibit an auto-oxidation or fading that may need to be corrected at readout time. In general, for an integrating dosimeter we want the dosimeter's response to radiation to be stable for at least the delay before readout and during readout (unless the readout involves "erasing" the dose signal). A lack of temporal stability may sometimes be misdiagnosed as a dose rate dependence in the dosimeter during very long exposures.

Fractionation Independence: A concept that is related to temporal stability and dose rate independence is fractionation independence. For example, a single exposure of 10 Gy should result in the same total reading as that obtained from two 5 Gy exposures separated by a time gap similar to that which may be present in a clinical dose delivery (e.g. delay between IMRT beams)

Dose Range: Ideally, a dosimeter can be used for any dose level, within the range of interest. Many dosimeters, however, exhibit a saturation level, or a threshold below which the response is not measurable. This limited range may be due to the dosimeter response itself, or the accompanying readout systems.

Dimensionality: The dimensionality (D) refers to the ability of the dosimeter to map dose *distributions* within a volume in a single radiation exposure. We can classify dosimeters as point (0D), line (1D), planar (2D) and volume (3D) dosimeters. 3D dosimetry is attractive as it could save time and reduce error by removing the need to move the dosimeter and spatially align many measurements to produce a multi-dimensional map.

Spatial Resolution: The true spatial resolution of a dosimeter is the smallest volume in which meaningful dosimetric information can be provided. This is linked to the size of the sensitive volume for point dosimeters, and is tied to the image noise and readout spatial resolution for integrating 2D and 3D dosimeters (films and gels).

Environmental Conditions: Ideally, the ambient temperature (or pressure) within the sensitive volume should not have an effect on the response. In practice, this is almost never the case. For example, ion chambers are sensitive to temperature and pressure, and the reactions involved in many chemical dosimeters are generally temperature dependent. It is good practice to avoid unnecessary temperature variations during irradiation and readout of the dosimeter.

Ease of Use and Speed: A large number of measurements are made by clinical physics

staff during quality assurance procedures, commissioning of new hardware, and research. Therefore, a dosimeter should be as easy to use and as fast as possible.

Cost effectiveness and Re-usability: Cost effectiveness is governed not only by the absolute monetary figure, but also by the application for which it is used, the human resources it requires, and the quality of the data it provides.

1.4.2 Comparison of common dosimeters

Table 1.1 provides a comparison of the dosimetric properties of a variety of radiation detectors. No single dosimeter provides all the desired qualities, so clinical physics departments make use of an array of different devices, and must choose the one most suited to the specific clinical or research task at hand.

1.5 The Case for 3D Dosimeters

Dosimetry tools that are readily available in the clinic include ion chambers, thermoluminescent and optically stimulated luminescent dosimeters (TLDs and OSLDs), and diodes for point measurements. Diode arrays provide sparse sampling of 2D surfaces or 3D volumes. Radiochromic film provides very high spatial resolution when making 2D measurements. However, due to the advances in delivery techniques, treatment plans are now more conformal to target volumes than ever before, and therefore dose distributions are taking on increasingly complicated 3D shapes with sharp fall-off gradients in multiple directions. The ability to verify 3D dose distributions directly has not kept pace, which has led to a high degree of variability in the quality of radiotherapy from institution to institution [34]. This is reflected in data from the Imaging and Radiation Oncology Core (IROC) group (formerly the Radiological Physics Center, RPC), which is responsible for certifying cancer centers for participation in clinical trials funded by the National Cancer Institute (NCI)

	Ion Chamber	OSL	Radiochromic Film	Diode Array	Polymer Gel	FX gel	LCV Gel	Radiochromic Plastic
Dimensionality	0D	0D typically, 2D/3D in works	2D	2D / 3D (sparse)	3D	3D	3D	3D
Accuracy (%)	0.5	5	2 - 4	0.5	5	2 - 3 (laser CT)	1 - 2 (laser CT)	1 - 2 (laser CT)
Precision (%)	0.5	≈ 5	2	0.5	5	1 - 2	1 - 2	1 - 2
Linearity	linear	linear	non-linear	linear	linear (except low dose and saturation regions)	linear	linear	linear
Energy Dependence	yes (< 30 kV)	no (MV range)	yes (< 100 kV)	yes	no	yes (< 100 kV)	no	yes (< 100 kV)
Dose Rate Dependence	no	no	no	(1% between 100-400 cGy/min)	some formulations, but can be minimized			
Fractionation Dependence	no	no	no	no	no	yes	no	no
Dose Range (Gy)	0+	0 - 50	0 - 10	0+	0 - 10	0 - 4	0 - 100	0 - 100s
Tissue Equivalence	no	no	no	no	yes	yes	yes	ok in MV range
Spatial Resolution	≈ 0.5 cm	≈ 3 mm	readout-dependent	poor (diode spacing ≈ 5 mm)	readout-dependent	readout-dependent	readout-dependent	readout-dependent
Temperature Dependence	yes	0.5% /C	yes	no	yes	yes	yes	yes
Temporal Stability	good	2% fading over 2.5 days	good	time drift	good	poor (diffusion)	good	very good
References	[37]	[38, 39]	[37, 40-47]	[48-50]	[51]	[52, 53]	[54-56]	[57-60]

Table 1.1: Dosimetric properties of commonly used radiation detectors.

in the United States. IROC's head and neck credentialing process involves an anthropomorphic head and neck phantom that is sent to a candidate institution and undergoes the radiotherapy process as if it were a real patient. The phantom contains a set of thermoluminescent dosimeters (TLDs) for point measurements as well as 2 planar film inserts (GAFChromic[®] EBT-3 film). The exposed TLDs are read out by IROC, and the films are evaluated following the procedure outlined in the American Association of Physicists in Medicine (AAPM) Task Group 55 report [35]. The current IROC acceptance criteria are that TLD doses should agree within $\pm 7\%$ of the planning system's absolute dose calculation, and that gamma analysis (a method for simultaneously incorporating dose difference and spatial offsets into dose comparisons, see [36]) of the film dosimetry measurements results in $\geq 85\%$ of pixels "passing" ($\gamma < 1.0$) with 7% dose difference and 4 mm distance to agreement (DTA) thresholds. It is noteworthy that these thresholds are not as stringent as the recommendations of the International Commission on Radiation Units and Measurements (ICRU), which states that dose delivery should be accurate to within $\pm 5\%$ in radiotherapy [29].

Even with the relaxed IROC criteria, only 66% of institutions were able to pass the credentialing for the head and neck phantom in 2001. Over the past ≈ 15 years, the annual pass rate for credentialing has improved to approximately 90%, which is certainly encouraging and reflects a growing competency in complex treatment delivery and dose verification. However, when dosimetric analyses are performed with more stringent criteria, pass rates drop substantially. In 2015, only 37% of institutions surveyed by IROC were able to pass the credentialing with the gamma criteria of 3% dose difference and 3 mm distance to agreement needed to conform to the ICRU's recommendation that the *overall* required accuracy for patient treatments is within $\pm 5\%$ and 5 mm [29], indicating that there is still substantial room for improvement [34].

The main problem in performing quality assurance of complex radiotherapy using point

and planar dosimeters is that it provides only a very sparse sampling of the 3D dose distribution, which may not capture regions of steep dose gradients where the uncertainty about the treatment is actually the highest. 2D film and diode array dosimeters can only detect errors in a specific plane or surface. It has been shown that 2D dosimetric evaluations of a select plane in a treatment generally do not correlate with 3D evaluations for IMRT and VMAT plans [61]. Additionally, “per-beam” evaluation of IMRT fields using 2D dosimeters has been found *not* to predict clinically-relevant dose errors in anatomical regions of interest [62]. To address these issues, pseudo-3D dosimeters using arrays of ion chambers or diodes have been developed commercially, including OCTAVIUS (PTW, Freiburg, Germany) [63], Delta⁴ (ScandiDos, Uppsala, Sweden) [48, 64], and ArcCheck (Sun Nuclear Corporation, Melbourne, Florida, USA) [65, 66]. These phantoms come with automated evaluation software, providing an easy to use dosimetry test. Unfortunately, considerable discrepancies between planned and measured dose distributions have been observed when using these devices in regions with steep dose gradients [49, 50]. Given that the point detectors in these phantoms are spaced by several millimetres (5-10 mm center to center) this is not surprising. The electronic portal imaging device (EPID) has also been used for 3D dosimetry, by inversely calculating patient dose using the planning CT and the exit fluence maps as measured by the EPID [67–69]. This approach relies on the assumption that patient setup/motion and machine performance are all within expected ranges. Another technique makes use of the linear accelerator log files and the patient’s planning CT to recalculate dose [70–72], but this too makes assumptions about positioning and performance of the linear accelerator, and thus is not an independent “dosimetry” procedure. These techniques also cannot be used to make basic dosimetry measurements such as depth dose curves or beam profiles in water. 3D dosimetry using liquid scintillators [73, 74] has also been presented in recent years. Additionally, Cherenkov emission based dosimetry has been described [75]. These methods allow for 3D differential (real-time) dosimetry in specific phantoms.

1.6 3D Chemical Dosimeters

There are several different types of dosimeters that are actively being developed for comprehensive, integrating 3D measurement of radiation dose. These 3D chemical dosimeters are generally based on either a gel, plastic, or silicone matrix, with some form of radiation sensitive material incorporated. Below, we briefly describe these materials.

1.6.1 Gel dosimeters

The earliest, and perhaps still the most well known of the 3D chemical dosimeters is the hydrogel dosimeter, which exists in a variety of different formulations. Typically, hydrogel dosimeters are nearly tissue-equivalent, since they are primarily composed of water and a gel-forming material (e.g. gelatin). A small quantity of radiosensitive material provides the actual dose-measuring capability, and the gel maintains the spatial integrity for mapping the dose deposition. Additional chemicals are often included to increase dose sensitivity or reduce the diffusion rate in the gel.

1.6.1.1 Gel dosimeter basics

Gel dosimeter response is primarily the result of the radiolysis of water, creating free radicals [9, 76]. These will react with either each other (recombination) or with other substances present in the medium. The reaction of radicals with some type of reporter molecule forms the basis for gel dosimetry. The rate of radiolysis is proportional to the rate of dose absorption, and so the concentration of radicals reacting with the reporter molecule will be proportional to dose.

In radiochromic gels, a dye molecule is contained within the gelatin matrix which undergoes a change in absorption at a specific wavelength when free radicals from water radioly-

sis interact with it. Examples of radiochromic gels include the iron-based Ferrous Xylenol Orange gels (FXG, based on Fricke gels with an additional reporter molecule) [52, 53], Leuco Malachite Green gels (LMG) [77] and Leuco Crystal Violet gels (LCV) [54–56].

Polymer gels [51] consist of a gelatin matrix doped with a monomer and crosslinker molecule. In these gels, radiolytic products interact with a monomer, which initiates a polymerization chain reaction. As the polymer chains grow and cross-link, the optical scattering of the gel increases locally. Additionally, the diffusion is greatly reduced by the polymerization, thus preserving the spatial integrity of the dose distribution.

1.6.1.2 Condensed history of gel dosimetry

Various different gel dosimeter formulations and readout techniques have been developed over the past two decades. Many of these have been presented in peer reviewed publications such as the *Physics in Medicine and Biology* and *Medical Physics* journals. In addition, a biennial conference on gel and other 3D dosimetry techniques has been held on nine occasions since 1999 (The International Conference on Three-Dimensional Dosimetry, IC3DDose), most recently in 2016 [78]. The proceedings of these meetings contain thorough reviews on gel dosimeters and readout systems [79–84]. In this section, we provide a very brief outline of the history of gel dosimetry.

The concept of 3D gel dosimetry was perhaps first proposed in 1950 by Day and Stein [85], who noted colour change in a variety of dye-containing gels when exposed to radiation. Even at this early stage, prior to the development of magnetic resonance (MR) and computed tomography (CT) imaging, these researchers noted that they were trying to develop a “system that would enable three-dimensional distributions of absorbed energy to be demonstrated”. However, the field of 3D gel dosimetry was generally inactive until the mid-1980s, when Gore *et al.* demonstrated that a Fricke gel (a gel form of the well known iron based Fricke solution dosimeter [86]) could be probed by MRI imaging [87].

In 1998, Kelly *et al.* reported on the addition of xylenol orange and benzoic acid solution to Fricke gels, which both reduced the diffusion rate of iron ions (preserving spatial information) and generated a radiation-induced change in optical attenuation with a broad peak around 540 nm, which could therefore be read out using a green helium-neon laser [52]. Later studies phased out the benzoic acid component, resulting in the Ferrous-Xylenol Orange Gelatin (FXG) dosimeter which has been used for clinically-relevant dosimetry tasks [53, 88, 89]. However, due to the diffusion of ferric ions, these gels lost spatial integrity relatively quickly, making it difficult to accurately measure steep dose gradients, which showed measurable loss of sharpness (requiring correction) within minutes after irradiation [90]. This prompted the development of low-diffusion radiochromic gels such as Leuco Crystal Violet (LCV) gels [54], which originally made use of surfactant micelles to limit the diffusion rate. Recent work in our lab seems to practically eliminate diffusion effects in LCV gels [91], at least for typical dose gradients delivered using clinical photon beams.

In response to the problem of losing spatial information in Fricke gels due to diffusion, polymer gel dosimeters were also developed and first reported by Maryanski *et al.* [92]. Polymer gels can be imaged with optical, magnetic resonance, x-ray or ultrasound techniques [51]. However, there are practical challenges in fabrication and disposal due to the toxicity of the materials. Additionally, the optical readout of polymer gels is complicated by optical scattering and by radiation-induced changes in refractive index [93].

1.6.2 Non-gel 3D chemical dosimeters

The most well-documented of the non-gel 3D chemical dosimeters is PRESAGE[®], a commercially available plastic product. This dosimeter is composed of a clear polyurethane matrix which is doped with radiochromic leuco dyes such as Leuco Malachite Green [57]. In this dosimeter, it is *not* the radiolysis of water that leads to products which interact with

the radiochromic dye. Rather, the dosimeter also includes halogenated compounds that release free radicals when irradiated [58]. PRESAGE® is read out using optical imaging techniques such as optical CT, and has been shown to exhibit excellent dose response linearity, no dose rate dependence, minimal energy dependence in the megavoltage range, and virtually no diffusion [57, 58]. Since the dosimeter is a solid plastic, it requires no dosimeter vessel and can be machined to any shape. PRESAGE® has been used for a variety of dosimetry applications [60, 94].

Silicone-based 3D radiochromic dosimeters have also been recently presented [95–97]. These dosimeters, like PRESAGE®, do not rely on water radiolysis, but on other molecules to release free radicals when irradiated. A silicone based dosimeter that uses optically stimulated luminescence, rather than a radiochromic leuco dye, is also in development [98].

The advantage of plastic dosimeters is that they can be made to be flexible or deformable, and do not require a container. However, a disadvantage of these materials is that they can be quite expensive compared to gels, mostly due to the considerably higher concentrations of radiosensitive materials, in particular leuco dyes (by mass, 1-2 % in PRESAGE® vs. ~ 0.05 % in gels). Because of the cost of these materials, it is likely that non-gel 3D dosimeters would need to be made re-usable (through signal fading or photo-bleaching) in order to be economically feasible. Additionally, the reproducibility of PRESAGE® dosimeters within and between batches, and the spatial uniformity of the dosimeter's response, are concerns that need to be addressed [99–101]

1.6.3 3D chemical dosimeter readout

While certain gel dosimeters can be probed using x-ray (polymer gels), ultrasound (polymer gels), or MRI techniques (Fricke and polymer gels), access to this type of equipment is not always possible in many settings, and the signal to noise ratio in some of these methods

is quite low. On the other hand, a dedicated optical readout technique can be constructed for a relatively low cost, and optical attenuation signal in gels is comparatively higher. A dedicated, robust, and fast on-site optical technique to read gel dosimeters would enable acceptance of gel dosimetry techniques in clinical settings. Therefore, the focus of this thesis is the use of optical imaging, specifically optical computed tomography (CT), to read *radiochromic* gel dosimeters.

1.7 Optical Computed Tomography

Optical computed tomography (CT) is the visible-light analogue to x-ray CT, which is a ubiquitous technology in healthcare. It was first introduced for radiation dosimetry in the 1990s [52, 102], but implementations had been described earlier for air quality measurements [103, 104] and imaging of fluid jets [105]. A functionally equivalent technology, Optical Projection Tomography, has also been described for imaging of biological specimens [106–108]. Typically, optical projection tomography is performed at finer spatial resolution and much smaller fields of view than optical CT radiation dosimetry.

1.7.1 Computed tomography basics

The mathematics of computed tomography have been well described in literature. In particular, the textbook by Kak and Slaney [109] provides an excellent explanation. Thus, we only briefly outline the principles here.

1.7.1.1 Attenuation

Consider a beam of photons travelling through a block of material. Within the material, some of the photons will interact with atoms. The nature of these reactions will depend

on the photon energy (visible range, x-ray, megavoltage x-ray, etc) as well as the nature of the material (absorption spectrum, etc), but in general we can say that some of the incident photons will be either absorbed or scattered away from the direction of the primary beam. This loss of primary photons is called *attenuation*. The fraction of incident photons removed from a narrow, monoenergetic beam per unit thickness of the medium is referred to as the *linear attenuation coefficient* (μ) of that material, and is usually expressed in units of cm^{-1} . If we have N_0 photons initially incident on a material of thickness L and having a linear attenuation coefficient of μ , then we can calculate the number of photons N leaving the material using the Beer-Lambert law:

$$N = N_0 e^{-\mu L} \quad (1.1)$$

Inverting Equation 1.1 allows us to solve for the linear attenuation coefficient of a uniform material of known thickness if we measure the transmission N/N_0 . Also, when we make experimental measurements, we normally do not directly count the number of photons, but measure the intensity of the radiation, which we usually denote using I and I_0 . So, we have:

$$\mu = -\frac{1}{L} \ln \left(\frac{I}{I_0} \right) \quad (1.2)$$

Now, consider the case where the material is not uniform, but has a linear attenuation coefficient that varies as a function of position s along the beam, as shown in Figure 1.2.

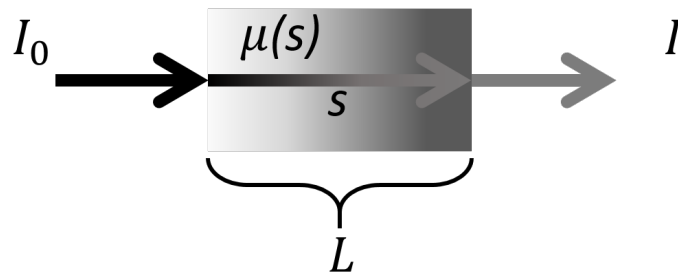


Figure 1.2: Attenuation of primary photons through a block of material.

Here, the intensity of the transmitted beam is determined by the line integral of the linear attenuation coefficient along the beam path:

$$I = I_0 e^{-\int_0^L \mu(s) ds} \quad (1.3)$$

and thus from a single transmission measurement we can only solve for either the net attenuation through the material (or for an *average* linear attenuation coefficient):

$$\int_0^L \mu(s) ds = -\ln\left(\frac{I}{I_0}\right). \quad (1.4)$$

In a real experiment, I_0 is a measured reference intensity, to which subsequent I values are compared after changing something in the sample. In absorption spectroscopy, one often computes “ μ relative to water”. In optical gel dosimetry, I_0 represents the detected intensity of a ray travelling through the gel prior to irradiation.

1.7.1.2 Projections

In the context of tomography, a *projection* is defined as a set of line-integrals (as in Equation 1.3) through an object at a particular view angle. The simplest case is a parallel-beam projection, which is a set of line integrals taken at the same angle. Parallel beam projection is also known as Radon transformation [110]. Slightly more complicated is the fan-beam projection, which would be obtained from a single source point coupled with a line or arc of detectors. Extending to 3D, a cone-beam projection is obtained by a single source point coupled with a 2D array of detectors. Parallel, fan, and cone-beam projection geometry are shown in Figure 1.3.

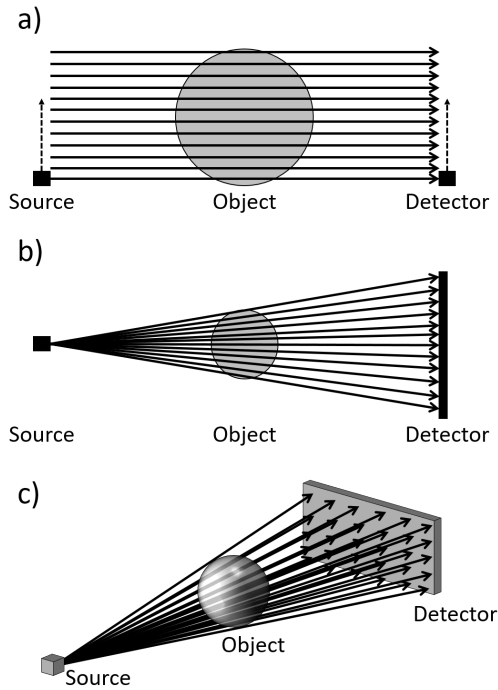


Figure 1.3: Parallel beam (a), fan beam (b) and cone beam (c) CT projection geometries.

1.7.1.3 The Fourier Slice Theorem and tomographic reconstruction

The fundamental mathematical result needed to understand CT image reconstruction is the Fourier Slice Theorem. This theorem states that the one-dimensional Fourier transform of a parallel-beam projection (set of line integrals) at a given angle through a two-dimensional function is equal to the values of the two-dimensional Fourier transform along a line at the same angle through the center of the 2D Fourier transform space, as sketched in Figure 1.4.

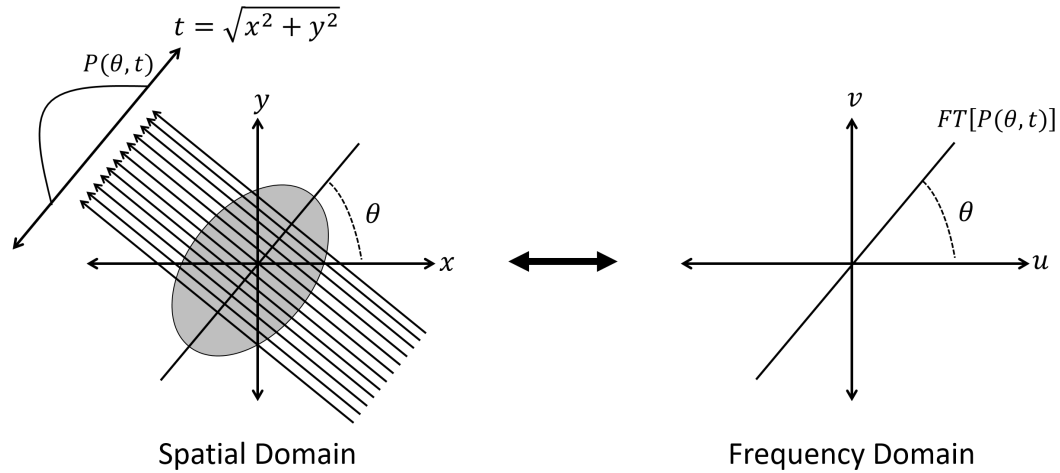


Figure 1.4: The Fourier Slice Theorem. The 1D Fourier transform of a projection $P(\theta, t)$ at angle θ is equal to the “spoke” of the 2D Fourier transform of the object at the same angle in the spatial frequency domain.

From this it follows that if we obtain a set of parallel-beam projection views from many angles around the object, we can fill in the 2D Fourier space “spoke-by-spoke” by taking the 1D Fourier transform of each projection. Then, performing the inverse 2D Fourier transform domain recovers the object. Furthermore, if our projection data are actually transmission data (Equation 1.3), then we can take the natural logarithm to transform them into the set of line integrals of the linear attenuation coefficient, and thus reconstruct the distribution of μ values within the object. This provides a *tomographic* image (from the Greek *tomos*, “slice”). The mathematics behind this technique, known as “direct Fourier reconstruction” were first proven by Radon in 1917 [110]; however, the first application of Fourier-based reconstruction appears to have been in radio astronomy work by Bracewell in 1956 [111].

In practice, the direct Fourier method is not used to reconstruct medical CT images. The reasons for this are both mathematical and practical. First, in real applications a discrete number of projections (and therefore “spokes” in the frequency domain) are acquired. That is to say, the 2D Fourier domain is filled in polar coordinates, while the desired object should be reconstructed in Cartesian coordinates. Interpolation from the polar to Cartesian

coordinates directly is challenging. Secondly, in the early days of CT scanners, computation time was an issue. The 2D inverse Fourier transform used to reconstruct the image was a computationally demanding task that could only be performed after the full scan data was acquired. Therefore, CT images are typically reconstructed using a backprojection algorithm, which allows image reconstruction concurrent with acquisition.

1.7.1.4 Backprojection-based reconstruction techniques

If one “backprojects” measured parallel-beam projection data into the image volume for each acquisition angle, the net result is a representation of the object convolved with a 2D blurring function $1/r$, where r represents radial distance from the origin ($r = \sqrt{x^2 + y^2}$). Intuitively this can be understood by considering backprojection akin to “smearing” the measured projection back across the image grid at the given projection angle. The sum of this “smearing” from all angles results in a radial blur surrounding the imaged point. To correct for this blurring, one can apply a deconvolution filter to remove the expected blur. Then, since convolution in the spatial domain corresponds to multiplication in the spatial frequency domain, and since the blurring function $1/r$ has a 2D Fourier transform that is well behaved ($1/\rho$, where ρ represent spatial frequency in the radial direction), one can perform this easily in the Fourier domain. The procedure to reconstruct the image could be to first backproject, then calculate the 2D FT, multiply by the filter $|\rho|$ to remove the blurring, and then take the inverse 2D FT. This approach is known as “backproject and filter”, or “BPF”.

Since the operations of back-projection and filtering are linear, the order in which one performs them does not matter. Therefore, one can *first* filter, then backproject projection data. This is the Filtered Backprojection (FBP) reconstruction technique. The advantage of FBP is that the reconstruction can be started as soon as the first projection is acquired, and no 2D FT calculations are required. *Filtered backprojection has been the standard recon-*

struction algorithm for medical (and optical) CT scanners since they were first introduced commercially.

Because the ramp filter used to remove the radial blurring from images amplifies high spatial frequencies, it also amplifies noise. To reduce this, the ramp filter is often multiplied by another windowing function, such as a Hamming window. This reduces the image noise at the cost of some spatial resolution. In medical CT, filters, usually called kernels, are chosen in an application-specific manner. For example, a “smooth” kernel (less amplification of high spatial frequencies) is usually used for brain imaging to reduce noise and enhance low contrast lesion detectability, whereas “sharper” kernels (more amplification of high spatial frequencies) are used to enhance edge imaging of bony structures with better spatial resolution.

1.7.1.5 Algebraic / Iterative reconstruction algorithms

Non-Fourier based reconstruction algorithms can also be used to reconstruct CT images. In simple terms, these algorithms involve making incremental adjustments to an estimated distribution of linear attenuation coefficients, guided by the measured projection data. This is done by iteratively computing simulated forward projections through the image estimate, comparing them to the measured projections from the CT scanner, and calculating and applying correction terms to refine the estimate of the image [112]. In addition to the actual reconstruction step, most iterative reconstruction algorithms also involve some form of regularization process, which acts to reduce noise. Iterative algorithms are much more computationally demanding than filtered backprojection, but they can offer improved image quality for the same input data. With the rise of parallel computing, especially the use of Graphics Processing Units (GPUs), iterative reconstruction techniques are now becoming increasingly popular for medical CT imaging [113]. In this thesis, we make use of iterative reconstruction algorithms in Chapters 4 and 5.

1.7.2 Optical CT scanners

The development of optical CT scanners has roughly imitated that of x-ray CT generations. Early scanners were based on the “1st-generation”, or “translate-rotate” design, featuring a laser source and small detector (e.g. photodiode) that translated synchronously across the field of view of the system [52, 102]. A commercial laser CT scanner using this geometry is available for research applications (OCTOPUS, MGS Research Inc., Madison, Connecticut, USA). Fan beam scanners utilizing line sources and linear detector arrays have also been presented [114, 115]. Finally, with the advent of charge coupled device (CCD) cameras, broad-beam geometries have become very common in optical CT imaging. Broad-beam optical CT scanners operate in an “inverse cone beam” geometry [116, 117] or a telecentric geometry [118–120]. Commercial cone beam optical CT scanners are available from Modus Medical Devices, Inc. (London, Ontario, Canada) for both radiation dosimetry research (VistaTM) as well as CT imaging education (DeskCATTM). In Chapter 2, a modification to the VistaTM optical CT scanner light source is described, which improved its quantitative accuracy.

There are a few key differences between optical CT and x-ray CT. First, in optical CT, it is possible to achieve very nearly mono-energetic beams, through the use of light emitting diodes (LEDs) with bandpass filters, or using lasers. This virtually eliminates the “beam hardening” artifact seen in x-ray CT, which is caused by the filtration of lower-energy x-rays by the object being imaged [121]. Second, the refractive index of different materials varies greatly at optical wavelengths, when compared to the variations seen at x-ray energies. For this reason, it is necessary to image dosimeters within an aquarium filled with a medium having a refractive index that is optimized for the dosimeter and its container. In this context, “optimized” refractive index refers to a value that allows standard CT geometry (fan, cone, or parallel-beam) to be achieved throughout the imaging field of view. This refractive index is dependent on the dosimeter material as well as the dosimeter vessel

wall material and thickness. Third, at optical wavelengths, lenses and mirrors are readily available (another consequence of the large refractive index variations between materials at these energies). This enables the use of typical digital cameras (CCD or CMOS sensors) for imaging, and allows the imaging light sources to be focused. In this thesis, we explore the use of focused / directional light sources to reduce non-primary signal detection (Chapters 2 and 3).

In radiochromic or scattering (polymer gel) optical CT dosimeters, the attenuation coefficient, μ , increases as a function of dose. Thus, the measurement of interest is actually the *change* in μ after irradiation, $\Delta\mu = f(D)$. To measure $\Delta\mu$, we perform an optical CT scan before and after irradiation (“pre-” and “post-scans”) and reconstruct from transmission projections relative to the pre-scan [82]. This process “removes” the initial dosimeter and vessel wall attenuation from datasets. However, it is sensitive to mechanical error in re-positioning dosimeter samples, especially if vessel walls contain optical imperfections, as shown in Chapter 2.

It should be noted that there is some inconsistency in the optical CT literature regarding the units used. First, many authors report pixel values in reconstructions not as attenuation coefficients, but as Optical Density (OD) values per unit length (e.g. OD / cm). However, by definition, optical density is a unitless quantity described by the following equation:

$$OD = -\log_{10}\left(\frac{I}{I_0}\right), \quad (1.5)$$

where I_0 and I represent initial and final intensity values. When authors report OD/cm values in CT reconstruction pixels, they are actually reporting a “decadic” attenuation coefficient, μ_{10} , which is related to the traditional exponential attenuation coefficient μ (Equation 1.2) by a simple change of logarithm base:

$$\mu_{10} = \frac{\mu}{\ln 10}. \quad (1.6)$$

It is important to keep this inconsistency in mind when comparing the dose sensitivity of different gel dosimeters in the optical CT literature.

A second common occurrence in optical CT literature is that although $\Delta\mu$ is what is actually measured, many authors simply use μ . In this dissertation, we use μ to represent the change in attenuation coefficient from pre- to post-scan, or the “attenuation with respect to the initial conditions”.

1.8 Motivation of Research

The overarching purpose of my dissertation work was to improve optical CT imaging to the point where 3D gel dosimetry demonstrated sufficient accuracy, precision, and utility to be implementable in a clinical physics setting. This required my work to focus on reducing stray light contamination in optical CT projection images, and reducing image artifacts in reconstructions. We approached these problems through both instrumentation improvements (scanner design) and data processing techniques (reconstruction algorithms). Our advances in these areas also enabled accurate imaging of larger dosimeter volumes than what had previously been possible, which is a desirable result for clinical dosimetry tasks.

1.8.1 Stray light effects

Generally speaking, the move from “1st-generation” (pencil beam, small detector) to broad-beam (CCD-based) optical CT scanners increases scan speed at the cost of an increased non-primary signal contribution in CT projection imaging. At the start of my doctorate, previous work in our lab had shown that stray light (i.e. any light following paths through

the system other than that assumed in image reconstruction) perturbed the accuracy of dosimetry using the existing version of the VistaTM optical CT scanner. Specifically, an under-estimate of dose near the center of dosimeters, was particularly evident when imaging small regions of dose (e.g. small field dosimetry) [90]. Additionally, Olding *et al.* [117] reported a limited range of attenuation coefficients over which the scanner remained linear and unperturbed by stray light related artifacts. In this section, we briefly explain how stray light perturbs the accuracy of optical CT imaging.

1.8.1.1 Stray light in attenuation measurements

The exponential attenuation described in Equations 1.1 - 1.4 pertains to the *primary* beam, that is, photons travelling along the line shown in Figure 1.2 from the light source to the detector. If the only light detected in an experiment travelled along that path, then the detected intensity will be governed by the Beer-Lambert law. However, consider the case of trying to measure the attenuation of a small object within a medium that scatters light, using a transmission measurement obtained using a broad beam illumination and non-infinitesimal detector, as shown in Figure 1.5.

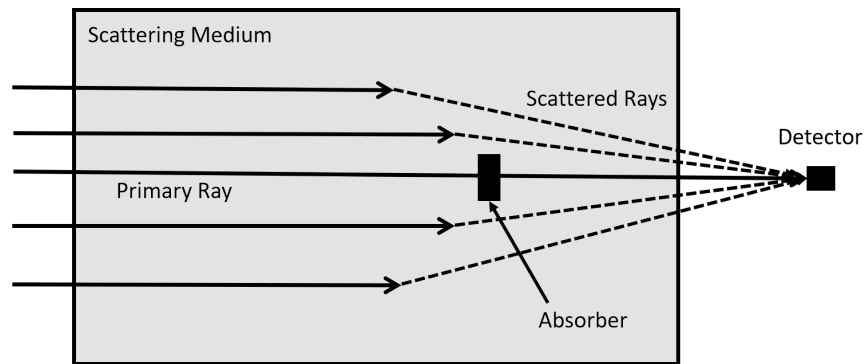


Figure 1.5: Measuring the absorption of a small attenuator within a scattering medium using a broad-beam transmission measurement. Stray light pollutes the measurement of primary ray transmission.

Here, we have signal contributions from both primary and scattered (“stray”) light. Therefore, our detected intensities can be written as:

$$I = I_{primary} + I_{stray} \quad (1.7)$$

$$I_0 = I_{primary,0} + I_{stray,0} \quad (1.8)$$

where $I_{primary}$ and I_{stray} represent primary and stray light signals. Only the primary signal, $I_{primary}$ will undergo Beer-Lambert governed attenuation along the primary ray track, while I_{stray} will undergo attenuation along a *different* path through the sample. Thus, if we were to calculate attenuation coefficients using I and I_0 , we would introduce error. The magnitude of the error depends on the transmission of the sample ($I_{primary}/I_{primary,0}$) as well as the magnitude of the stray light contributions to each measurement.

In the case of optical CT imaging, each individual pixel in each projection image will have its own unique I_{stray} contribution, which will depend on not only the optical imaging system but also the object being scanned. In some cases, scattered light signal will undergo very similar attenuation conditions to that of the primary rays, reducing the magnitude of errors introduced. On the other hand, correcting for scattered light signal in cases where objects with steep gradients and small objects are imaged is difficult to do correctly. To improve the accuracy and reproducibility of optical CT imaging, it is best to reduce the scatter to primary ratio (SPR) in detected signals as much as possible.

1.8.1.2 Stray light in optical CT

The sources of stray light in a broad, cone-beam optical CT scanner are shown in Figure 1.6. Work was done in our lab to measure the magnitude of non-primary light signal associated with the different components of the scanner [122]. A method to measure and subtract stray light signal using beam blocker arrays was described, which revealed that up to 25% of the signal detected by the camera when imaging radiochromic gel dosime-

ters was non-primary illumination. The main issue with the original Vista scanner design was the use of a diffuser-based light source to illuminate the object being imaged. With this source, which can be roughly considered as a planar array of an infinite number of isotropic point sources, almost all of the light entering the system was not travelling along the desired image forming rays. This non-primary illumination can scatter within the gel, reflect off the vessel wall, or reflect within the imaging lens to ultimately reach the detector, disturbing the transmission measurements (see Figure 1.6) and giving rise to the artifact observed by Babic *et al.* [123] when measuring small radiation fields. Unlike the scatter measurements in x-ray CT imaging [124], the “stray light image” recorded for optical CT imaging contains high spatial frequency structures due to reflection and refraction of light. Therefore, to fully correct for scatter and other stray light in an optical CT scan requires a separate measurement of the stray light signal for every position in the projection, for both the pre-irradiation and post-irradiation images of the gel [122].

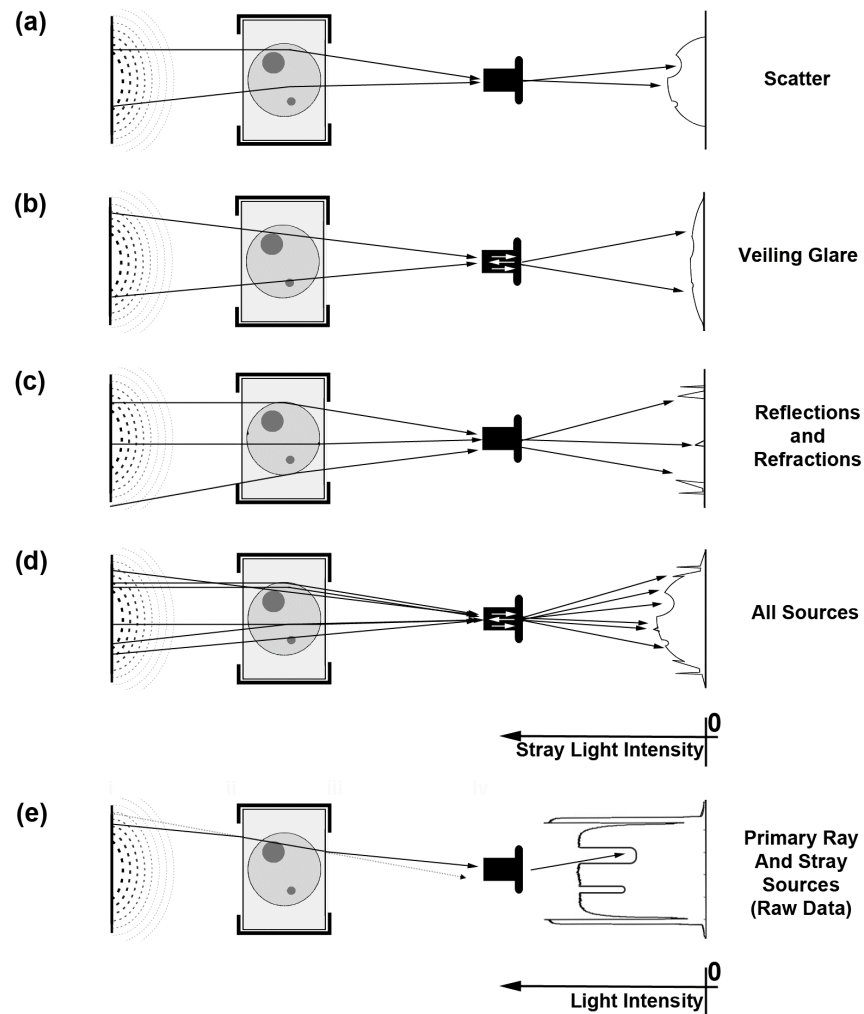


Figure 1.6: (a) - (d) Top view ray diagrams illustrating the origins and relative magnitude of stray light in an optical CBCT scanner with a diffuse light source used to image a two finger phantom. Horizontal line profiles on the right side illustrate relative contributions of non-primary rays (stray light). (e) Horizontal line profile of a transmission image. Figure reproduced with permission from Granton *et al.* 2016 [122]².

²© Institute of Physics and Engineering in Medicine. Reproduced by permission of IOP Publishing. All rights reserved. Refer to Appendix B

1.8.1.3 Stray light reduction in optical CT

In our lab, an initial re-design of the diffuser source for the cone beam optical CT scanner was implemented, increasing the distance between the diffuser and the camera. This, coupled with slot array based scatter subtraction, enabled quantitatively accurate imaging to be performed at the cost of doubling the length, width, and height of the scanner and tripling the scan time (as 3 scans were needed to completely remove scatter signal) [122]. Subsequently in this dissertation, an alternative source design is presented for CCD-based cone-beam scanning (Chapter 2), wherein the diffuser source is replaced with a convergent-cone light source which achieved even further stray light reduction.

To even further reduce stray light in optical CT, we ultimately moved away from cone-beam, CCD-based scanning and back towards “1st-generation” geometry, implementing a single-ray, small area detector scanning laser system. This geometry has very low stray light perturbation, as only a single pencil beam illuminates the gel at any given moment, and the detector has a small acceptance angle. We present a new optical CT scanner with this geometry in Chapter 3. Our scanner achieves excellent stray light rejection while maintaining practical scan speeds.

1.8.2 Large volume dosimetry

External beam radiation therapy is inherently a large-volume dosimetry problem. Even if the targeted tumour is small, there is a large region of surrounding normal tissue that receives a low dose of radiation. Additionally, there is increasing interest in multi-focal therapies, in particular for brain metastases (or surgical beds post-operatively) as an alternative to whole brain radiotherapy [125–127]. Such treatments require a large dosimeter to capture the net effect of the entire treatment. Therefore, one of the goals of my dissertation was to enable large volume gel dosimetry (cylindrical volumes up to 15 cm in diameter).

As the volume of gel increases, the effects of stray light become more pronounced due to longer path lengths through the dosimeter, and so the importance of minimizing production and acceptance of non-primary illumination rises.

1.8.3 Optical artifacts and image reconstruction

Optical CT artifacts are similar to those seen in x-ray CT. For example, bad detector elements lead to ring artifacts and highly attenuating objects lead to streaking in images. In optical CT, however, refractive index mismatch between different media can also generate artifacts. Additionally, as stray light is reduced in projection images, artifacts due to optical imperfections in the dosimeters or vessels become more evident. Therefore, a portion of my dissertation was devoted to improvements in image reconstruction techniques to reduce image noise and ring/streak artifacts through iterative CT reconstruction (Chapter 4). In addition, we examined the use of iterative reconstruction algorithms to enable reconstruction in the case of refractive index mismatches (Chapter 5), which makes the use of solid plastic dosimeters more practical.

1.9 Research Hypothesis

New, low stray light optical CT scanner designs and improved image reconstruction techniques will enable three-dimensional radiation dosimetry at clinically useful accuracy, precision, volume, resolution, and speed.

1.10 Specific Objectives

The overall goal of this dissertation was to improve upon the imaging aspects of optical CT dosimetry such that the technique would have clinical appeal. This was done by improving on the accuracy of optical CT scanners (by reducing stray light detection) and by implementing advanced reconstruction techniques to improve image quality and enable non-standard imaging geometries. With this goal in mind, the specific objectives of chapters 2 - 6 are:

Chapter 2: To design, implement, and characterize a new light source for camera-based cone beam optical CT scanning to improve accuracy by reducing stray light effects.

Chapter 3: To design, build, and characterize a scanning-laser optical CT system that images large volume dosimeters with very high accuracy (low stray light acceptance) while maintaining practical scan speeds.

Chapter 4: To demonstrate the improvement in optical CT image quality achieved through the use of an iterative reconstruction algorithm.

Chapter 5: To demonstrate the use of iterative CT reconstruction algorithms to enable accurate dosimetry in the case of refractive index mismatch (non-standard CT imaging geometry), improving the practicality of optical CT imaging.

Chapter 6: To demonstrate the use of a high performance optical CT scanner (Chapter 3) and iterative reconstruction algorithm (Chapter 4) to perform the difficult and clinically important dosimetry task of small field measurement.

1.11 References

1. Canadian Cancer Society. *What is cancer?* <http://www.cancer.ca/en/cancer-information/cancer-101/what-is-cancer> (2017).

2. National Cancer Institute. *Risk Factors* <https://www.cancer.gov/about-cancer/causes-prevention/risk> (2017).
3. Canadian Cancer Society's Advisory Committee on Cancer Statistics. *Canadian Cancer Statistics 2017* (Canadian Cancer Society, Toronto, ON, 2017).
4. National Cancer Institute. *Radiation Therapy and You* <https://www.cancer.gov/publications/patient-education/radiation-therapy-and-you> (2017).
5. Cancer Care Ontario. *Radiation Treatment Capital Investment Strategy* (Apr. 2012), 27.
6. Canadian Cancer Society. *Chemotherapy and other drug therapies - Canadian Cancer Society* [www.cancer.ca. http://www.cancer.ca/en/cancer-information/diagnosis-and-treatment/chemotherapy-and-other-drug-therapies/?region=on](http://www.cancer.ca/en/cancer-information/diagnosis-and-treatment/chemotherapy-and-other-drug-therapies/?region=on) (2018).
7. Johns, H. E. & Cunningham, J. R. *The physics of radiology* Google-Books-ID: 7TprAAAAMAAJ. 824 pp. (Charles C. Thomas, 1983).
8. Hall, E. J. & Giaccia, A. J. *Radiobiology for the Radiologist* Google-Books-ID: 6HhjwRyqBzgC. 566 pp. (Lippincott Williams & Wilkins, 2006).
9. Khan, F. M. & Gibbons, J. P. *The Physics of Radiation Therapy* Fifth edition. 624 pp. (LWW, Philadelphia, PA, Apr. 17, 2014).
10. Burnet, N. G. Defining the tumour and target volumes for radiotherapy. *Cancer Imaging* **4**, 153–161 (2004).
11. Yan, D., Vicini, F., Wong, J. & Martinez, A. Adaptive radiation therapy. *Physics in Medicine and Biology* **42**, 123 (Jan. 1997).
12. Li, X. A. *Adaptive Radiation Therapy* 404 pp. (CRC Press, Jan. 27, 2011).
13. Bortfeld, T. R., Kahler, D. L., Waldron, T. J. & Boyer, A. L. X-ray field compensation with multileaf collimators. *International Journal of Radiation Oncology*Biophysics* **28**, 723–730 (Feb. 1994).
14. Webb, S. The physical basis of IMRT and inverse planning. *The British Journal of Radiology* **76**, 678–689 (Oct. 2003).
15. *Image-Guided IMRT* (eds Bortfeld, T., Schmidt-Ullrich, R., De Neve, W. & Wazer, D. E.) DOI: 10.1007/3-540-30356-1 (Springer Berlin Heidelberg, Berlin, Heidelberg, 2006).
16. Otto, K. Volumetric modulated arc therapy: IMRT in a single gantry arc: Single arc radiation therapy. *Medical Physics* **35**, 310–317 (Dec. 26, 2007).
17. Deng, Z. *et al.* Dosimetric advantage of volumetric modulated arc therapy in the treatment of intraocular cancer. *Radiation Oncology* **12**, 83 (May 10, 2017).
18. Mackie, T. R. *et al.* Tomotherapy: A new concept for the delivery of dynamic conformal radiotherapy. *Medical Physics* **20**, 1709–1719 (Nov. 1, 1993).
19. Tome, W. A. & Fowler, J. F. Selective boosting of tumor subvolumes. *International Journal of Radiation Oncology*Biophysics* **48**, 593–599 (Sept. 2000).
20. Kim, Y. & Tome, W. A. Dose-painting IMRT optimization using biological parameters. *Acta Oncologica* **49**, 1374–1384 (Nov. 2010).
21. Popple, R. A., Ove, R. & Shen, S. Tumor control probability for selective boosting of hypoxic subvolumes, including the effect of reoxygenation. *International Journal of Radiation Oncology*Biophysics* **54**, 921–927 (Nov. 2002).

22. Kim, Y. & Tome, W. A. Risk-adaptive optimization: Selective boosting of high-risk tumor subvolumes. *International Journal of Radiation Oncology*Biophysics* **66**, 1528–1542 (Dec. 2006).
23. Kim, Y. & Tome, W. A. Is it beneficial to selectively boost high-risk tumor subvolumes? A comparison of selectively boosting high-risk tumor subvolumes versus homogeneous dose escalation of the entire tumor based on equivalent EUD plans. *Acta oncologica (Stockholm, Sweden)* **47**, 906 (2008).
24. Hardcastle, N. & Tome, W. A. Risk-Adaptive Volumetric Modulated Arc Therapy Using Biological Objective Functions for Subvolume Boosting in Radiotherapy. *Computational and Mathematical Methods in Medicine* **2012** (June 27, 2012).
25. Onishi, H. *et al.* Stereotactic hypofractionated high-dose irradiation for stage I non-small cell lung carcinoma. *Cancer* **101**, 1623–1631 (Oct. 1, 2004).
26. Timmerman, R. *et al.* Stereotactic Body Radiation Therapy for Inoperable Early Stage Lung Cancer. *JAMA* **303**, 1070–1076 (Mar. 17, 2010).
27. Phillips, M. H., Stelzer, K. J., Griffin, T. W., Mayberg, M. R. & Winn, H. R. Stereotactic radiosurgery: a review and comparison of methods. *Journal of Clinical Oncology* (Sept. 21, 2016).
28. International Organization for Standardization (ISO). *Quality management systems-Fundamentals and vocabulary (ISO 9000: 2005)* (2005).
29. International Commission on Radiation Units and Measurements. Report 24. *Journal of the International Commission on Radiation Units and Measurements* **13** (Sept. 15, 1976).
30. *Radiation oncology physics: a handbook for teachers and students* (eds Podgorsak, E. B. & International Atomic Energy Agency) (International Atomic Energy Agency, Vienna, 2005). 657 pp.
31. Seco, J., Clasié, B. & Partridge, M. Review on the characteristics of radiation detectors for dosimetry and imaging. *Physics in Medicine and Biology* **59**, R303 (Sept. 17, 2014).
32. Kron, T., Lehmann, J. & Greer, P. B. Dosimetry of ionising radiation in modern radiation oncology. *Physics in Medicine and Biology* **61**, R167–R205 (July 21, 2016).
33. Attix, F. H. *Introduction to radiological physics and radiation dosimetry* 607 pp. (Wiley, New York, 1986).
34. Carson, M. E. *et al.* Examining credentialing criteria and poor performance indicators for IROC Houston’s anthropomorphic head and neck phantom: IROC Houston head and neck phantom failure analysis. *Medical Physics* **43**, 6491–6496 (Nov. 11, 2016).
35. Niroomand-Rad, A. *et al.* Radiochromic film dosimetry: Recommendations of AAPM Radiation Therapy Committee Task Group 55. *Medical Physics* **25**, 2093–2115 (Nov. 1998).
36. Low, D. A., Harms, W. B., Mutic, S. & Purdy, J. A. A technique for the quantitative evaluation of dose distributions. *Medical Physics* **25**, 656–661 (May 1, 1998).
37. Metcalfe, P., Kron, T. & Hoban, P. *The Physics of Radiotherapy X-Rays And Electrons* Upd Rev edition. 905 pp. (Medical Physics Pub Corp, Madison, Wis, July 15, 2007).

38. Yukihiro, E. G. & McKeever, S. W. S. Optically stimulated luminescence (OSL) dosimetry in medicine. *Physics in Medicine and Biology* **53**, R351–R379 (Oct. 21, 2008).
39. Wouter, C., Dirk, V., Paul, L. & Tom, D. A reusable OSL-film for 2D radiotherapy dosimetry. *Physics in Medicine & Biology* **62**, 8441–8454 (Oct. 19, 2017).
40. Soares, C. G. New developments in radiochromic film dosimetry. *Radiation Protection Dosimetry* **120**, 100–106 (Sept. 1, 2006).
41. Fuss, M., Sturtewagen, E., Wagter, C. D. & Georg, D. Dosimetric characterization of GafChromic EBT film and its implication on film dosimetry quality assurance. *Physics in Medicine and Biology* **52**, 4211–4225 (July 21, 2007).
42. Devic, S. *et al.* Precise radiochromic film dosimetry using a flat-bed document scanner. *Medical Physics* **32**, 2245–2253 (July 1, 2005).
43. Rink, A., Lewis, D. F., Varma, S., Vitkin, I. A. & Jaffray, D. A. Temperature and hydration effects on absorbance spectra and radiation sensitivity of a radiochromic medium. *Medical Physics* **35**, 4545–4555 (Oct. 1, 2008).
44. Buchauer, K., Hillbrand, E. & de Vries, A. GAFCHROMIC® EBT photospectral dose response dependence on temperature and implications for flat bed scanning. *Medical Physics* **36**, 5044–5051 (Nov. 1, 2009).
45. Borca, V. C. *et al.* Dosimetric characterization and use of GAFCHROMIC EBT3 film for IMRT dose verification. *Journal of Applied Clinical Medical Physics* **14**, 158–171 (Mar. 1, 2013).
46. Grams, M. P., Gustafson, J. M., Long, K. M. & de los Santos, L. E. F. Technical Note: Initial characterization of the new EBT-XD Gafchromic film: EBT-XD Gafchromic. *Medical Physics* **42**, 5782–5786 (Sept. 14, 2015).
47. Yao, T., Luthjens, L. H., Gasparini, A. & Warman, J. M. A study of four radiochromic films currently used for (2D) radiation dosimetry. *Radiation Physics and Chemistry* **133**, 37–44 (Apr. 2017).
48. Nilsson, G. SU-FF-T-135: Delta4 - A New IMRT QA Device. *Medical Physics* **34**, 2432–2432 (June 1, 2007).
49. Pavord, D. SU-GG-T-210: A Comparison of Dosimetry Devices. *Medical Physics* **35**, 2773 (2008).
50. Penn, S. T. & Xue, T. SU-GG-T-170: Using a 3D Diode Array System to Perform Routine IMRT Machine QA. *Medical Physics* **35**, 2765 (2008).
51. Baldock, C. *et al.* Polymer gel dosimetry. *Physics in Medicine and Biology* **55**, R1–R63 (Mar. 7, 2010).
52. Kelly, R. G., Jordan, K. J. & Battista, J. J. Optical CT reconstruction of 3D dose distributions using the ferrous-benzoic-xylene (FBX) gel dosimeter. *Medical Physics* **25**, 1741 (1998).
53. Babic, S., Battista, J. & Jordan, K. An apparent threshold dose response in ferrous xylene-orange gel dosimeters when scanned with a yellow light source. *Physics in Medicine and Biology* **53**, 1637–1650 (Mar. 21, 2008).
54. Babic, S., Battista, J. & Jordan, K. Radiochromic leuco dye micelle hydrogels: II. Low diffusion rate leuco crystal violet gel. *Physics in Medicine and Biology* **54**, 6791–6808 (Nov. 21, 2009).

55. Nasr, A. T., Alexander, K., Schreiner, L. J. & McAuley, K. B. Leuco-crystal-violet micelle gel dosimeters: I. Influence of recipe components and potential sensitizers. *Physics in Medicine and Biology* **60**, 4665 (June 21, 2015).
56. Nasr, A. T., Alexander, K. M., Olding, T., Schreiner, L. J. & McAuley, K. B. Leuco-crystal-violet micelle gel dosimeters: II. Recipe optimization and testing. *Physics in Medicine and Biology* **60**, 4685 (June 21, 2015).
57. Guo, P., Adamovics, J. & Oldham, M. A practical three-dimensional dosimetry system for radiation therapy. *Medical Physics* **33**, 3962 (2006).
58. Gorjiara, T. *et al.* Investigation of radiological properties and water equivalency of PRESAGE dosimeters. *Medical Physics* **38**, 2265–2274 (Apr. 1, 2011).
59. Thomas, A., Newton, J., Adamovics, J. & Oldham, M. Commissioning and benchmarking a 3D dosimetry system for clinical use. *Medical Physics* **38**, 4846–4857 (Aug. 2011).
60. Jackson, J., Juang, T., Adamovics, J. & Oldham, M. An investigation of PRESAGE 3D dosimetry for IMRT and VMAT radiation therapy treatment verification. *Physics in Medicine and Biology* **60**, 2217 (Mar. 21, 2015).
61. Kim, J.-i. *et al.* Correlation analysis between 2D and quasi-3D gamma evaluations for both intensity-modulated radiation therapy and volumetric modulated arc therapy. *Oncotarget* (Jan. 16, 2017).
62. Nelms, B. E., Zhen, H. & Tomé, W. A. Per-beam, planar IMRT QA passing rates do not predict clinically relevant patient dose errors. *Medical Physics* **38**, 1037–1044 (Feb. 1, 2011).
63. Van Esch, A., Clermont, C., Devillers, M., Iori, M. & Huyskens, D. P. On-line quality assurance of rotational radiotherapy treatment delivery by means of a 2D ion chamber array and the Octavius phantom. *Medical Physics* **34**, 3825–3837 (Oct. 1, 2007).
64. Nilsson, J., Hauer, A. K. & Back, A. IMRT patient-specific QA using the Delta4 dosimetry system and evaluation based on ICRU 83 recommendations. *Journal of Physics: Conference Series* **444**, 012048 (June 26, 2013).
65. Létourneau, D., Publicover, J., Kozelka, J., Moseley, D. J. & Jaffray, D. A. Novel dosimetric phantom for quality assurance of volumetric modulated arc therapy. *Medical Physics* **36**, 1813–1821 (May 1, 2009).
66. Yan, G., Lu, B., Kozelka, J., Liu, C. & Li, J. G. Calibration of a novel four-dimensional diode array. *Medical Physics* **37**, 108–115 (Jan. 1, 2010).
67. Wendling, M. *et al.* Accurate two-dimensional IMRT verification using a back-projection EPID dosimetry method. *Medical Physics* **33**, 259–273 (Feb. 1, 2006).
68. Van Elmpt, W. *et al.* A literature review of electronic portal imaging for radiotherapy dosimetry. *Radiotherapy and Oncology* **88**, 289–309 (Sept. 2008).
69. Bawazeer, O., Herath, S., Sarasanandarajah, S. & Deb, P. in *World Congress on Medical Physics and Biomedical Engineering, June 7-12, 2015, Toronto, Canada* DOI: 10.1007/978-3-319-19387-8_135, 553–556 (Springer, Cham, 2015).
70. Luo, W. *et al.* Monte Carlo based IMRT dose verification using MLC log files and R/V outputs: Log file based Monte Carlo IMRT QA. *Medical Physics* **33**, 2557–2564 (June 26, 2006).

71. Teke, T. *et al.* Monte Carlo based, patient-specific RapidArc QA using Linac log files: Monte Carlo RapidArc QA using Linac log files. *Medical Physics* **37**, 116–123 (Dec. 4, 2009).
72. Barbeiro, A. R. *et al.* 3D VMAT Verification Based on Monte Carlo Log File Simulation with Experimental Feedback from Film Dosimetry. *PLOS ONE* **11**, e0166767 (Nov. 21, 2016).
73. Goulet, M. *et al.* Novel, full 3D scintillation dosimetry using a static plenoptic camera. *Medical Physics* **41**, n/a–n/a (Aug. 1, 2014).
74. Beaulieu, L. & Beddar, S. Review of plastic and liquid scintillation dosimetry for photon, electron, and proton therapy. *Physics in Medicine and Biology* **61**, R305–R343 (Oct. 21, 2016).
75. Glaser, A. K., Andreozzi, J. M., Zhang, R., Pogue, B. W. & Gladstone, D. J. Optical cone beam tomography of Cherenkov-mediated signals for fast 3D dosimetry of x-ray photon beams in water. *Medical Physics* **42**, 4127–4136 (July 1, 2015).
76. Spinks, J. W. T. & Woods, R. J. *An Introduction to Radiation Chemistry* Third edition. 592 pp. (Wiley-Interscience, New York, May 24, 1990).
77. Jordan, K. & Avvakumov, N. Radiochromic leuco dye micelle hydrogels: I. Initial investigation. *Physics in Medicine and Biology* **54**, 6773 (Nov. 21, 2009).
78. 9th International Conference on 3D Radiation Dosimetry. *Journal of Physics: Conference Series* **847**, 011001 (2017).
79. Oldham, M. Radiochromic 3D Detectors. *Journal of Physics: Conference Series* **573**, 012006 (Jan. 12, 2015).
80. Doran, S. J. Imaging and 3-D dosimetry: top tips for MRI and optical CT. *Journal of Physics: Conference Series* **250**, 012086 (Nov. 1, 2010).
81. Doran, S. J. The history and principles of chemical dosimetry for 3-D radiation fields: Gels, polymers and plastics. *Applied Radiation and Isotopes* **67**, 393–398 (Mar. 2009).
82. Doran, S. J. How to perform an optical CT scan: an illustrated guide. *Journal of Physics: Conference Series* **444**, 012004 (2013).
83. Doran, S. J. Dosimetry using MRI: can it really be that difficult? *J. Phys.: Conf. Ser.* **847**, 012051 (2017).
84. Jordan, K. J., Hilt, M. & Jirasek, A. Optical and X-ray computed tomography scanning of 3D dosimeters. *J. Phys.: Conf. Ser.* **847**, 012019 (2017).
85. Day, M. J. & Stein, G. Chemical Effects of Ionizing Radiation in some Gels. *Nature* **166**, 146–147 (July 22, 1950).
86. Fricke, H. & Morse, S. The action of X-rays on ferrous sulphate solutions. *The London, Edinburgh, and Dublin Philosophical Magazine and Journal of Science* **7**, 129–141 (Jan. 1, 1929).
87. Gore, J. C., Kang, Y. S. & Schulz, R. J. Measurement of radiation dose distributions by nuclear magnetic resonance (NMR) imaging. *Physics in Medicine and Biology* **29**, 1189–1197 (Oct. 1, 1984).
88. Babic, S., Battista, J. & Jordan, K. Three-Dimensional Dose Verification for Intensity-Modulated Radiation Therapy in the Radiological Physics Centre Head-and-Neck Phantom Using Optical Computed Tomography Scans of Ferrous

- Xylenol-Orange Gel Dosimeters. *International Journal of Radiation Oncology - Biology - Physics* **70**, 1281–1291 (Mar. 15, 2008).
89. Olding, T., Darko, J. & Schreiner, L. J. Effective Management of FXG Gel Dosimetry. *Journal of Physics: Conference Series* **250**, 012028 (Nov. 1, 2010).
 90. Babic, S., McNiven, A., Battista, J. & Jordan, K. Three-dimensional dosimetry of small megavoltage radiation fields using radiochromic gels and optical CT scanning. *Physics in Medicine and Biology* **54**, 2463–2481 (Apr. 21, 2009).
 91. Jordan, K. J., Lindenmaier, T. & Dekker, K. H. Non-diffusing radiochromic leuco-crystal violet hydrogel dosimeter. *Journal of Physics: Conference Series* **847**, 012009 (May 2017).
 92. Maryanski, M. J., Gore, J. C., Kennan, R. P. & Schulz, R. J. NMR relaxation enhancement in gels polymerized and cross-linked by ionizing radiation: a new approach to 3D dosimetry by MRI. *Magnetic Resonance Imaging* **11**, 253–258 (1993).
 93. Campbell, W. G., Wells, D. M. & Jirasek, A. Radiation-induced refraction artifacts in the optical CT readout of polymer gel dosimeters. *Medical Physics* **41**, 112102 (Nov. 2014).
 94. Sakhalkar, H., Sterling, D., Adamovics, J., Ibbott, G. & Oldham, M. Investigation of the feasibility of relative 3D dosimetry in the Radiologic Physics Center Head and Neck IMRT phantom using Presage/optical-CT. *Medical Physics* **36**, 3371–3377 (July 1, 2009).
 95. De Deene, Y., Skyt, P. S., Hil, R. & Booth, J. T. FlexyDos3D: a deformable anthropomorphic 3D radiation dosimeter: radiation properties. *Physics in Medicine and Biology* **60**, 1543 (Feb. 21, 2015).
 96. Hoyer, E. M. *et al.* Chemically tuned linear energy transfer dependent quenching in a deformable, radiochromic 3D dosimeter. *Physics in Medicine and Biology* **62**, N73–N89 (Feb. 21, 2017).
 97. Kaplan, L. P. *et al.* Determining the mechanical properties of a radiochromic silicone-based 3D dosimeter. *Physics in Medicine and Biology* (May 3, 2017).
 98. Sadel, M. *et al.* Three-dimensional radiation dosimetry based on optically-stimulated luminescence. *Journal of Physics: Conference Series* **847**, 012044 (May 2017).
 99. Dekker, K. H., Battista, J. J. & Jordan, K. J. Optical CT imaging of solid radiochromic dosimeters in mismatched refractive index solutions using a scanning laser and large area detector. *Medical Physics* **43**, 4585–4597 (Aug. 1, 2016).
 100. Mein, S., Rankine, L., Adamovics, J., Li, H. & Oldham, M. Development of a 3D remote dosimetry protocol compatible with MRgIMRT. *Medical Physics* (Sept. 6, 2017).
 101. Costa, F. *et al.* Investigating the effect of a magnetic field on dose distributions at phantom-air interfaces using PRESAGE® 3D dosimeter and Monte Carlo simulations. *Physics in Medicine & Biology* **63**, 05NT01 (2018).
 102. Gore, J. C., Ranade, M., Maryanski, M. J. & Schulz, R. J. Radiation dose distributions in three dimensions from tomographic optical density scanning of polymer gels: I. Development of an optical scanner. *Physics in Medicine and Biology* **41**, 2695 (1996).

103. Byer, R. L. & Shepp, L. A. Two-dimensional remote air-pollution monitoring via tomography. *Optics letters* **4**, 75–77 (1979).
104. Bennett, K. & Byer, R. L. Optical tomography: experimental verification of noise theory. *Optics letters* **9**, 270–272 (1984).
105. Faris, G. W. & Byer, R. L. Three-dimensional beam-deflection optical tomography of a supersonic jet. *Applied Optics* **27**, 5202–5212 (1988).
106. Brown, C. S., Burns, D. H., Spelman, F. A. & Nelson, A. C. Computed tomography from optical projections for three-dimensional reconstruction of thick objects. *Applied Optics* **31**, 6247 (Oct. 10, 1992).
107. Sharpe, J. *et al.* Optical Projection Tomography as a Tool for 3D Microscopy and Gene Expression Studies. *Science* **296**, 541–545 (Apr. 19, 2002).
108. Wong, M. D., Dazai, J., Walls, J. R., Gale, N. W. & Henkelman, R. M. Design and Implementation of a Custom Built Optical Projection Tomography System. *PLoS ONE* **8**, e73491 (Sept. 4, 2013).
109. Kak, A. C. & Slaney, M. *Principles of Computerized Tomographic Imaging* Google-Books-ID: Z6RpVjb9_lwC. 335 pp. (SIAM, Jan. 2001).
110. Radon, J. Über die Bestimmung von Funktionen durch ihre Integralwerte längs gewisser Mannigfaltigkeiten. *Berichte der Sächsischen Akademie der Wissenschaft* **69**, 262–277 (1917).
111. Bracewell, R. Strip Integration in Radio Astronomy. *Australian Journal of Physics* **9**, 198 (1956).
112. Zeng, G. L. *Medical image reconstruction: a conceptual tutorial* OCLC: 845614149. 198 pp. (Higher Education Press, Beijing, 2010).
113. Geyer, L. L. *et al.* State of the Art: Iterative CT Reconstruction Techniques. *Radiology* **276**, 339–357 (July 23, 2015).
114. Campbell, W. G., Rudko, D. A., Braam, N. A., Wells, D. M. & Jirasek, A. A prototype fan-beam optical CT scanner for 3D dosimetry. *Medical Physics* **40**, 061712 (June 1, 2013).
115. Papadakis, A. E. *et al.* Technical Note: A fast laser-based optical-CT scanner for three-dimensional radiation dosimetry. *Medical Physics* **38**, 830 (2011).
116. Wolodzko, J. G., Marsden, C. & Appleby, A. CCD imaging for optical tomography of gel radiation dosimeters. *Medical Physics* **26**, 2508 (1999).
117. Olding, T., Holmes, O. & Schreiner, L. J. Cone beam optical computed tomography for gel dosimetry I: scanner characterization. *Physics in Medicine and Biology* **55**, 2819–2840 (May 21, 2010).
118. Krstajic, N. & Doran, S. J. Characterization of a parallel-beam CCD optical-CT apparatus for 3D radiation dosimetry. *Physics in Medicine and Biology* **52**, 3693 (July 7, 2007).
119. Sakhalkar, H. S. & Oldham, M. Fast, high-resolution 3D dosimetry utilizing a novel optical-CT scanner incorporating tertiary telecentric collimation. *Medical Physics* **35**, 101–111 (Jan. 2008).
120. Thomas, A. & Oldham, M. Fast, large field-of-view, telecentric optical-CT scanning system for 3D radiochromic dosimetry. *Journal of Physics: Conference Series* **250**, 012007 (Nov. 1, 2010).

121. Brooks, R. A. & Chiro, G. D. Beam hardening in X-ray reconstructive tomography. *Physics in Medicine and Biology* **21**, 390–398 (May 1, 1976).
122. Granton, P. V., Dekker, K. H., Battista, J. J. & Jordan, K. J. Stray light in cone beam optical computed tomography: I. Measurement and reduction strategies with planar diffuse source. *Physics in Medicine and Biology* **61**, 2893 (2016).
123. Babic, S., McNiven, A., Battista, J. & Jordan, K. Three-dimensional dosimetry of small megavoltage radiation fields using radiochromic gels and optical CT scanning. *Physics in Medicine and Biology* **54**, 2463–2481 (Apr. 21, 2009).
124. Gao, H. *et al.* Scatter correction method for x-ray CT using primary modulation: Phantom studies. *Medical Physics* **37**, 934 (2010).
125. Brown, P. D. *et al.* Whole-Brain Radiotherapy for Brain Metastases: Evolution or Revolution? *Journal of Clinical Oncology*, JCO.2017.75.9589 (Dec. 22, 2017).
126. Brown, P. D. *et al.* Postoperative stereotactic radiosurgery compared with whole brain radiotherapy for resected metastatic brain disease (NCCTG N107C/CEC-3): a multicentre, randomised, controlled, phase 3 trial. *The Lancet Oncology* **18**, 1049–1060 (Aug. 1, 2017).
127. Li, J. & Brown, P. D. The Diminishing Role of Whole-Brain Radiation Therapy in the Treatment of Brain Metastases. *JAMA Oncology* **3**, 1023–1024 (Aug. 1, 2017).

Chapter 2

Stray light reduction in optical cone-beam computed tomography using a convergent light source

This chapter is adapted from a manuscript published as “Stray light in cone beam optical computed tomography: II. Reduction using a convergent light source” by Kurtis Hendrik Dekker, Jerry J. Battista and Kevin J. Jordan, *Physics in Medicine and Biology*, 61, 2910-2925 (2016)¹. Permission to reproduce this article was granted by IOP Publishing, and is provided in Appendix B.

2.1 Introduction

Optical CT scanning has been developed for 3D gel dosimetry, with designs ranging from scanning laser systems [1–5] to broad-beam cone-beam [6, 7] and parallel-beam [8–11] designs. The transition from laser pencil beams to large diffuse light illumination in cone-beam optical CT has introduced considerable stray light contamination, degrading the accuracy of attenuation coefficient measurements. Stray light causes an underestimation of CT reconstructed attenuation coefficients, as well as non-uniform reconstructions of uni-

¹© Institute of Physics and Engineering in Medicine. Reproduced by permission of IOP Publishing. All rights reserved.

form attenuators in the form of “cupping” and “bowing” artifacts, which limit the accuracy of dosimetric results [7, 12–14]. The effects are similar to those seen in X-ray cone beam CT [15] when compared to fan beam or pencil beam scanners. Efforts have been made to correct for stray light through the use of partial beam-stop arrays [16] as has been demonstrated for X-ray systems [17, 18]. The profile of detected scattered radiation in X-ray CT projections does not contain sharp features and can be interpolated. However, in optical CT systems, scattered fluence exhibits steep gradients and features due to reflection and refraction by the dosimeter vessel, so interpolation between measurement points in a beam-pass array becomes more complicated. Thomas *et. al.* [19] were able to use a spatially-invariant point spread function to correct for stray light in a bi-telecentric optical CT system used to scan the PRESAGE® dosimeter. However, this was only possible because the telecentric lens arrangement rejected the reflections and refractions generated by the dosimeter, and the remaining stray light was mostly generated by the optical elements of the scanner itself. In the cone-beam system described in this paper, this is not the case. In the accompanying study (Granton *et al.* 2016 [20]), we demonstrate a stray-light correction strategy using a movable vertical slot array and multiple CT scans to correct each individual projection image obtained with a commercially-available cone beam scanner (Vista10™, Modus Medical Devices, London, Canada). This method is effective, but impractical due to the time-consuming acquisition of multiple scans that are combined to form composite projection images. As an alternate approach to measurement and correction of scatter, we consider reducing the stray light originating at the light source itself. The system’s light emitting diode (LED) lightbox provides diffuse illumination, and much of the light emitted “sprays” into the scanned volume. The diffuser can be modeled as an array of isotropic point sources. The majority of the light does not follow image-forming primary ray paths assumed in CT reconstruction. We hypothesize that a convergent cone of image-forming rays will reduce stray light contributions “at source”. It should be noted that when we say “convergent” here we are actually referring to the forward propagation of light rays from a

large source towards a point, unlike in SPECT imaging where it refers to the “cone-beam collimator” [21]. We achieve our convergent light source by replacing the planar diffuse light source with a small source and a large diameter Fresnel lens. This forms a dual-optic system, which uses the Fresnel lens to focus light through the system into an imaging lens attached to a CCD camera. Dual optic systems have previously been used in some parallel-beam optical CT designs [9, 11]. Here, we present results from scanning large uniform phantoms and small finger phantoms to demonstrate the reduced stray light contributions achieved with the modified scanner. This modification will improve the accuracy of optical CT for radiation dosimetry applications.

2.2 Materials and Methods

2.2.1 Fresnel modified optical CT scanner

A top view schematic of the modified Vista10 scanner with Fresnel lens is shown in Figure 2.1a. The system consists of a small light source (Figure 2.1b) and Fresnel lens to provide convergent illumination, an aquarium to contain refractive index matching fluid to minimize image distortion, a sample stage to rotate the object being scanned, and a camera. The camera (DR2-BW, Point Grey Research, Inc., Canada), which captures projection images of 640×480 pixels through a $2/3''$ diameter, 16 mm focal length lens (HF 16HA-1B, Fujinon Corporation, China) was set to an aperture setting of $f/4$. The 12 bit images from the camera (4096 gray levels) are saved in a 16 bit format, with pixel values reported in analog to digital units (ADU) ranging from 0 to 65535.

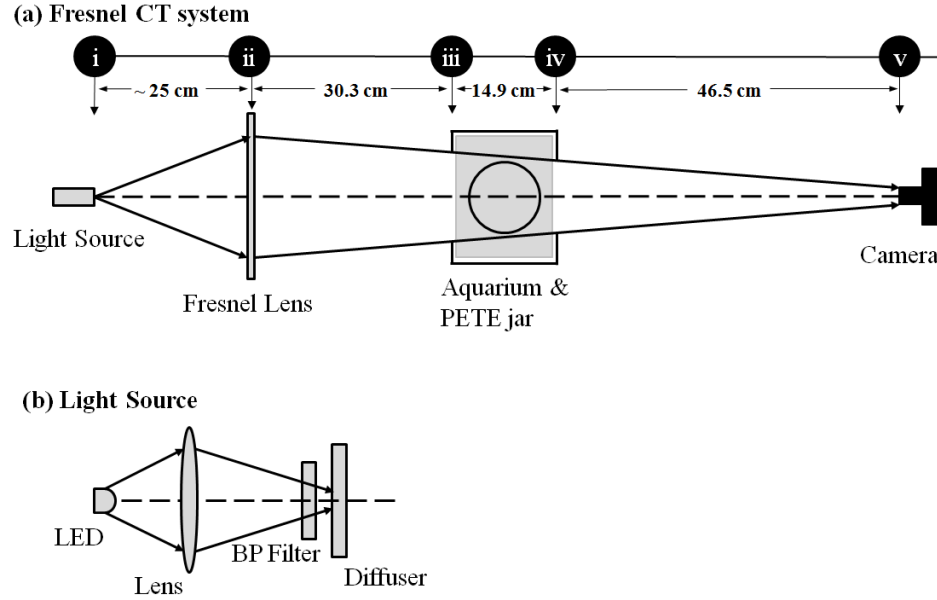


Figure 2.1: Top view schematics of (a) the entire Fresnel-modified optical CBCT scanner (Vista10, Modus Medical Devices Inc., London, Canada). Roman numerals depict the locations of the isotropic source (i), Fresnel lens (ii), entrance aperture (iii), exit aperture (iv) and camera (v). (b) The light source, consisting of LED, lens, bandpass filter, and diffuser. The source is set up to achieve an approximately 2 mm diameter spot at the entrance side (LED side) of the diffuser. The circuit powering the LED is not shown.

The lightbox and diffuser screen of the original Vista10 system was removed, and replaced with the new light source shown in Figure 2.1b. The new source consists of a single LED (TLYE17T, Toshiba Corporation, Japan) with a central wavelength of 590 nm, connected in series with a $1\text{ k}\Omega$ resistor and an adjustable power supply (Harrison 6206B DC Power Supply, Hewlett-Packard Company, USA). A multimeter (Fluke 77 Digital Multimeter, Fluke Corporation, USA) is used to monitor the current in the LED, which was held fixed at 5.9 mA. Light emitted by the LED is focused by a converging lens and passes through a bandpass filter with nominal central wavelength of 590 nm and bandwidth of 10 nm (590-10, TFI Technologies, USA), after which it strikes the “entrance side” (LED side) of a diffuser plate made from Teflon tape wrapped around a glass microscope slide. The lens was positioned to achieve a spot size of approximately 2 mm at the entrance side of the diffuser. This creates a nearly isotropic, point-like source at the exit side of the diffuser. This apparatus is enclosed in black construction paper to prevent extraneous light leakage into the

optical system. The Fresnel lens (Edmund Optics, cat # 32-595, 26.42 cm diameter, 20.32 cm focal length) focuses light emitted from the source down onto the camera lens. With the lens positioned against the baseplate of the Vista10 scanner (i.e. as close as possible to the aquarium without cutting the baseplate), the source position was adjusted until the entire field of view of the camera was illuminated and the intensity profile appeared Gaussian and centered on the optic axis. The camera focus was adjusted until transparent rulers placed at the entrance (source-side) and exit (camera-side) windows of the aquarium both appeared in focus. To calibrate the geometric parameters of the system, these rulers were also placed at the entrance and exit window of the water-filled aquarium, in both vertical and horizontal orientations. The magnification from entrance to exit was used to determine the scanner's effective Source to Axis Distance and beam angles. Reconstructions of the linear attenuation coefficient were performed using the VistaReconTM software (Modus Medical Devices Inc., London, Canada) shipped with the scanner, which implements the Feldkamp filtered backprojection algorithm [22]. Measurement of attenuation coefficients within regions of interest (ROIs) of reconstructed images was performed in Microview 2.1.2 software (GE Healthcare, UK). Unlike in X-ray CT, where transmission is calculated relative to air, in optical CT the transmission is usually determined relative to a "reference scan". The object scanned as a reference is the vessel containing the media (gel or solution) before any attenuation change is introduced by additives or irradiation. This procedure accounts for the unique optical properties of the vessel. In gel dosimetry applications a reference scan is acquired of the gel prior to irradiation, and is often called a "pre-scan". This is analogous to the procedure used in absorption spectrometry, where transmission is measured relative to a reference fluid within the same cuvette. When performing scans in this study, the camera integration time and frame rate were chosen such that the central region of reference scan projection images were just beginning to show a few saturated pixels; this maximizes the dynamic range achievable. Scans were performed using the open cone beam geometry (CBCT) as well as with a 1 cm high fan beam aperture (FBCT), made from black construc-

tion paper, positioned at the entrance window (Figure 2.1a, position iii.) near the optic axis to reduce out-of-plane stray light contribution. In X-ray CT, the magnitude of stray light effects has been shown to be much higher for large cone beam angles than for smaller-angle cone beam or fan beam images [15]. This effect is also present in optical CT, and therefore the comparison of reconstructed attenuation coefficients between cone beam and fan beam data provides information about the impact of stray light in the cone beam system.

2.2.2 Vertical slot array

To further characterize the stray light contribution, the vertical slot array method described previously by Jordan *et al.* [23] and used in the accompanying study (Granton *et al.* 2016 [20]) was used to generate primary and stray light signal images for a single cone beam projection for each phantom using one slot array (a series alternating open and blocked 1 cm wide regions, blocking 50% of beam in total) cut from opaque film and positioned at the entrance window. Three images were acquired, with the array shifted horizontally by 7 mm between each image. The open and blocked portions of the 3 images were combined to form composite open and shadow (stray light) images. Subtracting the shadow image from the open image creates the primary signal image.

2.2.3 Test solutions

To prepare the test liquids scanned in the study, carbon black (CB) (Aldrich, cat # 633100), with average particle size of 30 nm, was dispersed in a dilute Triton®-X 100 (Sigma Aldrich Ltd, Oakville, Canada) emulsion, in order to form a black liquid [24]. Carbon black is useful for optical CT tests because of its relatively smooth absorption spectrum, facilitating comparisons between CT and other measurements without significant dependence on wavelength of the light source. The spectrum is also relatively insensitive to pH,

and carbon black is chemically inert. The CB + Triton®-X 100 liquid was added, drop-by-drop, to either distilled water (finger phantom) or a 7.5% by volume propylene glycol solution (uniform phantom) . During experiments, it was unexpectedly found that the attenuation coefficients obtained from CT reconstruction of uniform attenuating phantoms reported consistently higher than those obtained on a spectrometer (Model 139, Hitachi Perkin-Elmer) for the test solutions. On average, there was an approximately 5% discrepancy between fan beam CT and spectrometer in the range of attenuations used in this study. Narrow-beam measurements (described in Section 2.2.5.1) showed similar disagreement with the spectrometer. Therefore we instead used a narrow-beam experiment (Section 2.2.5.1) as a reference point for attenuation measurements, and used the spectrometer only to confirm that solutions were stable throughout the duration of the experiment. Experiments comparing the CB solutions to solutions based on water-soluble Nigrosin stain (Fisher Scientific, USA) showed that the spectrometer and CT disagreement was specific to the CB solutions. Optical scattering from surfactant micelles was ruled out as a possible cause. Thus, we suspect that scattering from the suspended carbon black nanoparticles themselves is the cause of the difference. The spectrometer and the optical CT system have different acceptance angles, which causes different amounts of scattered light to be collected in the detectors of the two systems. The fact that the optical CT measurements are higher indicates a smaller acceptance angle, which is consistent with the longer source to detector distance compared to the spectrometer. This discrepancy between the optical CT and spectrophotometer was not observed previously [20], likely because stray light from the diffuse light source was masking the effect.

2.2.4 Phantoms

2.2.4.1 Uniform solution in Vista10 vessel

The first phantom in the study was a uniformly attenuating cylinder. This consisted of a 0.9 L Vista10 polyethylene terephthalate (PETE) vessel (outer diameter 96 +/- 1 mm) filled with carbon black solutions of various concentrations. Preliminary work performed in the study showed that if the aquarium fluid and fluid inside the PETE vessel had the same refractive index, there was considerable loss of signal towards the periphery of the vessel in the projection images, as seen in Figure 2.2b, which was not observed when acquiring images with the original diffuse light source (Figure 2.2a). This effect arises because the cylindrical jar acts as a diverging lens, causing primary rays to be rejected by the camera lens. At the periphery of the vessel in projection images (Figure 2.2b), the incident angles and effective wall thickness (as a fraction of the ray's total path length through the dosimeter) increase rapidly, and the divergence is more pronounced than near the centre of the image. Reconstructed data from these projections exhibit noise and artifacts due to missing data in this region. Therefore, in order to capture more primary signal in the periphery of the vessel, an intentional refractive index mismatch was introduced in the system. By experimentation, it was found that a 7.5% by volume mixture of propylene glycol (Sigma-Aldrich Ltd, Oakville, Canada) inside the vessel (refractive index ≈ 1.34 , similar to 4% gelatin gel dosimeters), with water in the aquarium (refractive index = 1.33) provided an improvement in the signal capture towards the periphery of the vessel, as shown in Figure 2.2c and 2.2d. Similar effects have been observed in parallel beam laser [1, 25] and CCD-based [10] systems. To characterize the expected impact of this mismatch, ray-tracing code written in MATLAB (The Mathworks Inc., Natick, MA, USA) was used to simulate a fan beam CT acquisition using the refractive indices of the aquarium (1.33), propylene glycol solution (1.34) and PETE vessel (1.56) and the geometry of the Vista10 system. Similar ray-tracing simulations have been reported by Doran *et al.* [10] to study vessel wall effects,

and by Oldham *et al.* to simulate scanning of the PRESAGE® solid dosimeter [26, 27]. The simulation showed that such a refractive index mismatch actually counteracts some of the distortion caused by the vessel wall, leading to a more accurate image reconstruction. This was consistent with work done with the system by Olding *et al.* [28], who reported that the amount of radial compression in reconstructed images is minimized for an aquarium liquid with a refractive index about 0.5% below that of the medium within the vessel. It is important to note that it is the mismatch between aquarium and in-vessel refractive indices that counteracts the effects of the PETE vessel and provides good signal throughout. Had we used the 7.5% propylene glycol inside and outside the vessel, we would obtain projection images very similar to those seen in Figure 2.2b for water. When scanning the uniform solutions, the non-attenuating 7.5% propylene glycol liquid was used as the reference scan, and the carbon black dye was then added to the fluid to create uniform phantoms of varying attenuation. Adding the dye directly to the phantom after acquiring a reference scan minimized the creation of air bubbles on the walls of the Vista10 vessel from pouring fluids into the jar, avoiding CT image artifacts.

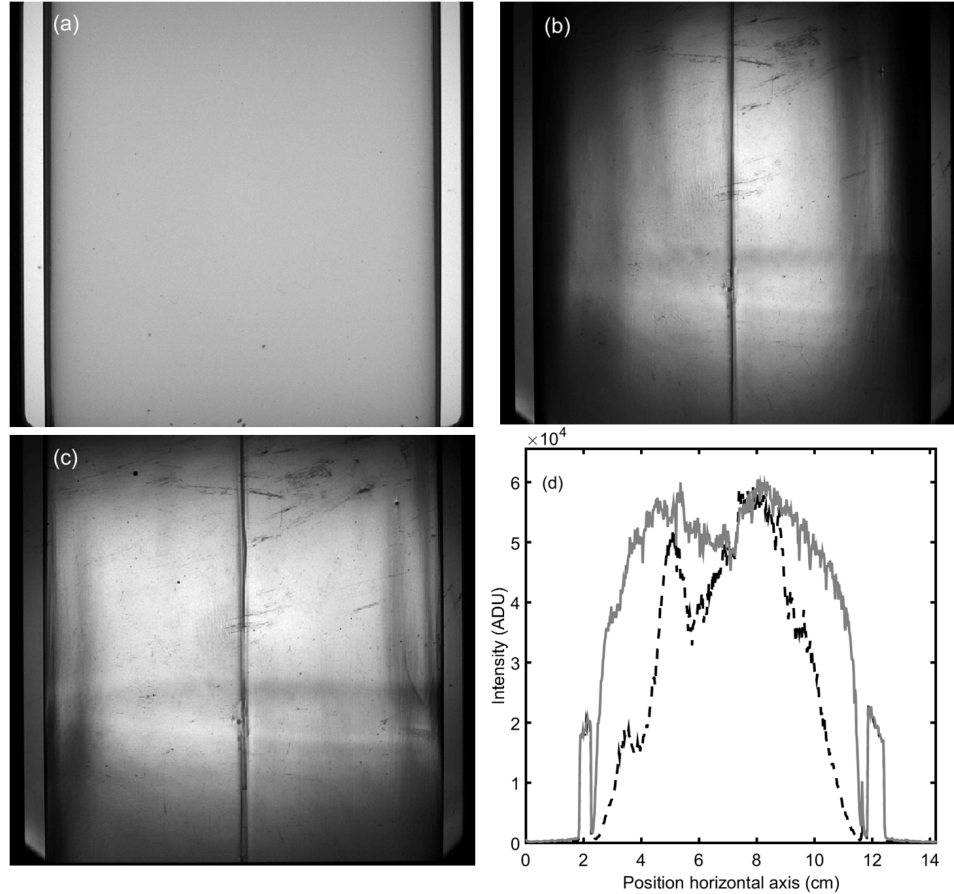


Figure 2.2: Single cone-beam projection images of solution-filled PETE vessel. (a) 7.5% propylene glycol (by volume) inside and outside the vessel, with the original diffuser light source. (b) water inside and outside the vessel, with the Fresnel source, illustrating the lack of signal toward the vessel periphery. (c) 7.5% by volume propylene glycol inside the vessel, water outside, demonstrating improved signal capture through intentional refractive index mismatch. Note the appearance of vessel features, including seams, in (b) and (c), which are not visible in (a), indicating high contrast performance of the Fresnel system. (d) central horizontal axis intensity profiles (jar seam rotated out of view) for cases (b) (dashed black) and (c) (solid grey). Vessel wall edges can be seen as the sharp edges in profiles near 2.2 and 11.8 cm. Note the better signal coverage through a wider extent of the vessel for intentional refractive index mismatching.

Comparing Figure 2.2a to Figures 2.2b and 2.2c also provides some insight into the effect of stray light in the original diffuser-source system. In both the diffuser and Fresnel source case, the same type of vessel is used. Also, the vessel's seams are rotated to be in the center of the image in both cases. However, when using the large diffuse source (Figure 2.2a), the vessel seams, as well as many other scratches and other optical features, are not seen. This is due to the considerable stray light in the system, which masks these features. It is clear from the comparison of Figure 2.2a and 2.2c that the Fresnel source system provides much better contrast than the original design.

2.2.4.2 FEP finger phantom

The second phantom used in the study was a simple “finger phantom”, used to test the scanner's performance in the case of a small absorbing object with sharp boundaries in a bright background. This is a severe test of the imaging performance because transmission measurements through the finger object can be corrupted by inward-scattered light from the surrounding medium. Similarly, small-field irradiation patterns have been used to commission optical CT systems [29].

The phantom consisted of a fluorinated ethylene propylene (FEP) cylinder of inner diameter 12.5 mm, outer diameter 13.5 mm (heat-shrink tubing, Newark, SKU#92N6000), suspended from a Vista10 jar lid. The finger was positioned slightly away from the axis of rotation, and a fill hole in the lid enabled the interior fluid to be changed without moving the aquarium or removing the phantom from the aquarium. This reduced possible confounding effects due to mechanical misalignment between reference and data scans. To eliminate several reflection and refraction artifacts, scans were performed without any Vista10 PETE vessel (i.e. Finger is suspended from the lid into the aquarium medium). The reference scans were performed using distilled water inside the finger and in the aquarium, and data scans were performed using water-based attenuating solutions described in Section 2.2.2.

Optimizing the refractive indices in the same way as was done for the PETE vessels (Section 2.2.3.1) was attempted, but it was found that water-based solutions provided projections with very little missing data, and a more optimal refractive index mismatch was not found.

2.2.5 Experimental setups

2.2.5.1 Fan beam vs. narrow beam geometry

As discussed in Section 2.2.3, spectrometer-measured attenuation was not a valid reference point for CT-measured attenuation, likely due to different acceptance angles between the systems. Instead, two 1 cm² apertures were placed at the center of the entrance and exit windows of the aquarium (Figure 2.1a, positions iii and iv.) to create narrow-beam geometry. To measure attenuation, solutions were put into a Vista10 jar and single reference (no dye added) and data (dyed solution) images were captured with the camera. The inner diameter of the Vista10 jar (94 +/- 1 mm) was used in the Beer-Lambert law to calculate the attenuation coefficient. To demonstrate the equivalence of attenuation coefficients measured by 1 cm fan beam CT and the narrow-beam system described above, a sequence of three uniform solution phantoms (Section 2.2.4.1) were measured using the narrow beam geometry above and then scanned using the fan beam aperture. For CT scans, 512 equally spaced projections about 360° were acquired and reconstructed on a 256³ grid with voxel size 0.5 × 0.5 × 0.5 mm³ using a Hamming filter prior to backprojection. This voxel size was considered adequate for imaging large uniform objects, and the number of projections was chosen to satisfy the Nyquist sampling criterion. The CT reconstructed attenuation coefficient was measured by averaging over four 12.5 × 12.5 × 2.5 mm³ ROIs located slightly off the centre in the reconstructed image. This was done to avoid image artifacts located at the rotation axis and between the vessel seams. The measured fan beam CT attenuation coefficient was then compared to the narrow-beam calculation.

2.2.5.2 Fan beam vs. cone beam - uniform phantom

A series of five uniform phantoms of increasingly greater attenuation was scanned using both the fan beam aperture and the full cone beam. CT scan and reconstruction parameters, as well as reconstructed attenuation measurement methods, were the same as in Section 2.2.5.1. Independent spectrometer measurements were taken during the CT scan and approximately 1 hour after the experiment to confirm that the attenuation of the solutions did not significantly change during the trials.

2.2.5.3 Fan beam vs. cone beam - finger phantom

The fan beam aperture and full cone beam were used to scan a sequence of 4 water-based attenuating solutions within the FEP finger phantom (Section 2.2.4.2). CT Scans were performed using 1024 equally spaced projections around a full 360° , and reconstructed on a 512^3 grid with voxel size $0.25 \times 0.25 \times 0.25 \text{ mm}^3$. The smaller voxel size here was chosen in order to resolve the sharp boundaries of the fingers, and the increase in grid size necessitated the larger number of projections. The mean and standard deviation of the reconstructed attenuation coefficient were measured inside a cylindrical ROI (6 mm diameter, 5 mm height) located at the centre of the finger. Independent spectrometer measurements taken during the CT scans and 24 hours later confirmed that the attenuation of solutions was stable.

2.2.5.4 Gelatin finger phantom imaging

The gelatin finger phantom used in the companion study (Granton *et al.* 2016 [20]) was also imaged in a water-filled aquarium for comparison to that work. This phantom was manufactured using 4.5% gelatin by weight, and closely approximates the optical scattering properties of gelatin-based dosimeters. Because this phantom actually consisted of two

parts, a blank reference phantom and a finger phantom made using carbon black in gelatin [30], the unique features of the different Vista10 vessel walls became a problem. As seen in Figure 2.2b, the vessel itself displays many optical features, which were not visible with the original diffuse light source, but are accentuated with the convergent source. Using a different vessel for reference and data scans causes severe artifacts in the CT reconstructed image due to mismatching features of each unique vessel. However, the vertical slot array (Section 2.2.2) was used to generate the primary and stray-light images for a single projection, for comparison to the previous work done with the diffuse source (Granton *et al.* 2016 [20]). To confirm that the vertical slot array provides a good estimate of the stray light contribution along the optic axis, the narrow-beam geometry described in Section 2.2.5.1 was used to acquire a single image. The mean pixel values in the narrow-beam aperture region were compared to the mean pixel values in the same location of an open-field image (no apertures set up) with the same camera settings and light source intensity. This comparison provides an estimate of the stray light contribution from the full cone beam to the central region of the projection image.

2.2.5.5 Source spot size optimization

Altering the size of the focal spot on the entrance side of the diffuser (Figure 2.1b) changes the amount of stray light that enters the optical system. Increasing the amount of stray light slightly by increasing the spot size reduces the system’s sensitivity to the unique optical features of the jar walls, and reduces the effects of refractive index mismatches leading to missing CT projection data at the vessel periphery. This should result in CT reconstructions that look visually “better”, with fewer artifacts than those obtained with a smaller spot size. The trade-off is a marginal increase in stray light effects that slightly reduce the accuracy of CT reconstructed attenuation coefficients. To examine the effect of an increased source size, we modified the light source shown in Figure 2.1b using a larger LED (Luxeon III 3W,

LXHL-ML1D) operating at a current of 7.0 mA. The converging lens was removed, and the LED was positioned just behind the bandpass filter, providing a spot size of approximately 5 mm at the LED side of the diffuser. We performed a single uniform phantom experiment in the manner described in Section 2.2.5.2, in order to perform a visual examination of CT artifacts seen using the two different spot sizes, and to compare the fan and cone beam reconstructions numerically to characterize stray light contribution.

2.3 Results and Discussion

2.3.1 Stray light

2.3.1.1 Fan beam vs. narrow beam geometry

Table 2.1 contains attenuation coefficients of uniformly attenuating solutions within the Vista10 jar measured using the narrow-beam apertures and from CT reconstructions of data acquired using the 1 cm width fan beam aperture. The values are in excellent agreement, indicating that the effect of stray light is minimal when moving from a narrow-beam to fan beam geometry. In the remaining experiments, the comparison used to demonstrate the effect of stray light is henceforth that between fan beam and cone beam CT.

Carbon Black Solution	Narrow-beam μ (cm ⁻¹)	Fan Beam CT μ (cm ⁻¹)	% Difference
1	0.073 \pm 0.001	0.073 \pm 0.001	0 \pm 2
2	0.191 \pm 0.002	0.192 \pm 0.002	1 \pm 2
3	0.400 \pm 0.004	0.400 \pm 0.005	0 \pm 2

Table 2.1: Comparison of narrow-beam experiment and Fan beam CT attenuation coefficient. Narrow beam attenuations were calculated using the Beer-Lambert law. CT measurements were averaged over four $12.5 \times 12.5 \times 2.5$ mm³ ROIs located just off the rotation axis and away from between-seam artifacts.

2.3.1.2 Uniform phantom

Table 2.2 contains the CT reconstructed attenuation coefficients for the uniform solution phantom experiments. In this case, the agreement between fan and cone beam is very strong, with mean discrepancies of 1% or less. As expected, the cone beam still produces slightly lower values than the fan beam data, consistent with an increased stray-light contribution in cone beam CT. We find agreement between fan and cone beam data for attenuating fluids with attenuation coefficient between 0.036 and 0.43 cm^{-1} , corresponding to transmission values from 75% down to 1%. This doubles the optimum range reported by Olding *et al.* [14] of 0.06 to 0.18 cm^{-1} for the original diffuser source.

Carbon Black Solution	CBCT Fresnel $\mu \text{ (cm}^{-1}\text{)}$	FBCT Fresnel $\mu \text{ (cm}^{-1}\text{)}$	% Difference
4	0.036 ± 0.001	0.036 ± 0.001	0 ± 3
5	0.071 ± 0.001	0.072 ± 0.001	1 ± 2
6	0.112 ± 0.001	0.113 ± 0.001	1 ± 1
7	0.234 ± 0.002	0.236 ± 0.001	1 ± 1
8	0.430 ± 0.004	0.433 ± 0.004	1 ± 1

Table 2.2: Comparison of Fresnel source cone beam optical CT (CBCT) and Fresnel source fan beam optical CT (FBCT) measurements of the 7.5% propylene glycol, carbon black micelle solutions. CT scans were performed with the full cone beam as well as with the 1 cm fan beam aperture. The average reconstructed linear attenuation coefficients were calculated by averaging over four $12.5 \times 12.5 \times 2.5 \text{ mm}^3$ ROIs located just off the rotation axis and away from between-seam artifacts.

The cone beam reconstructions were also examined for uniformity. Central line profiles (Figure 2.3) appear flat. We do not see substantial cupping or bowing artifacts for highly attenuating liquids. Missing data near the wall and wobbling during scans can also lead to non-flat profiles, so we expect that better mechanical precision and thinner vessel walls would further improve this result. To quantitatively examine flatness, the mean attenuation coefficient within concentric cylindrical shells with thickness of 1 mm and height of 5 mm was computed for reconstructions of solutions within the studied attenuation range. We found that cone beam reconstructions remained flat within 2% over 85% of the vessel's

inner diameter.

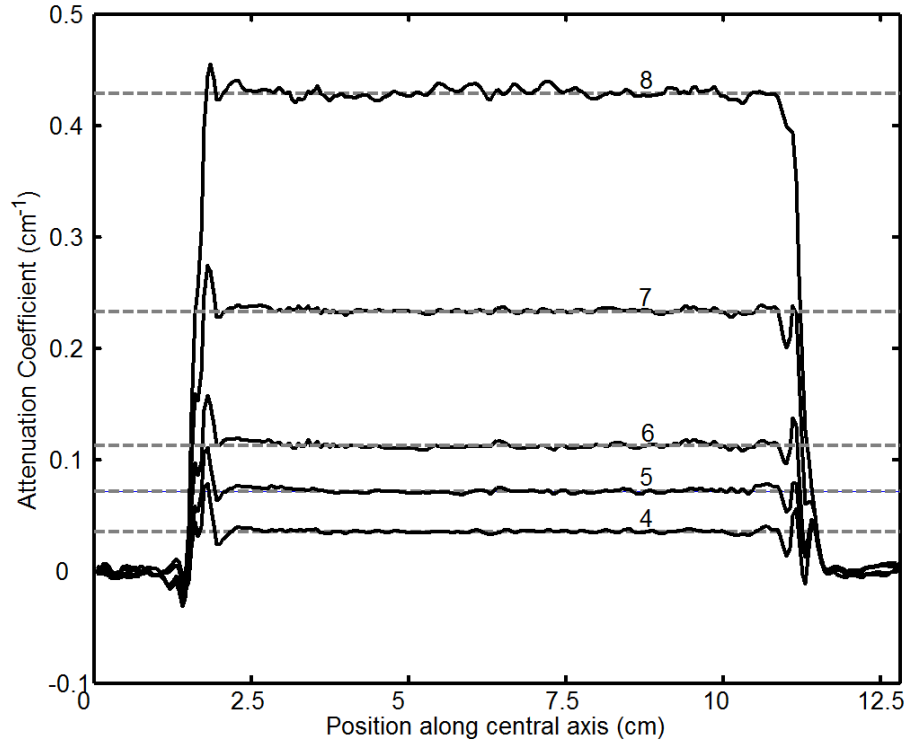


Figure 2.3: Central-line profiles (solid black) through reconstructions from full cone beam data of the 5 uniform attenuating solutions (#4-8 in Table 2.2, numbered above profiles in figure). The dashed, gray horizontal lines mark the mean values measured from four $12.5 \times 12.5 \times 2.5 \text{ mm}^3$ ROIs located just off the rotation axis (see Table 2.2). Note that spikes appearing near the edges of profiles are associated with missing projection data very near the vessel wall and mechanical error in the alignment between pre- and post-scans.

2.3.1.3 Fan beam vs. cone beam - finger phantom

Table 2.3 contains the CT reconstructed attenuation coefficients for four water-based carbon black solutions poured into the FEP finger phantom. Cone beam acquisition results in attenuation coefficients that are consistently lower than those from the fan beam acquisition. It should be noted that the FEP walls of the phantom cause considerable scattering, which may explain some of the difference between fan and cone beam results. However the values agree within 4% of each other even for the worst case of the darkest solution (solution 12). This is a marked improvement over previous work done with the original diffuse source,

where a difference of about 10% has been seen for a finger of comparable size [20]. These results indicate that the Fresnel light source is highly effective in removing the contribution of stray light. This finding was further supported by the vertical slot array measurement of scatter contribution, which showed that the stray light made up less than 4% of the overall signal passing through the FEP finger on a single projection (figure not shown).

Carbon Black Solution	CBCT Fresnel μ (cm ⁻¹)	FBCT Fresnel μ (cm ⁻¹)	% Difference
9	0.095 \pm 0.004	0.097 \pm 0.005	2 \pm 7
10	0.180 \pm 0.003	0.184 \pm 0.003	2 \pm 3
11	0.330 \pm 0.004	0.342 \pm 0.005	4 \pm 2
12	0.450 \pm 0.004	0.469 \pm 0.005	4 \pm 1

Table 2.3: Comparison of Fresnel source cone beam optical CT (CBCT) and Fresnel source fan beam optical CT (FBCT) attenuation measurements of the carbon black micelle solutions inside the FEP tubes of the finger phantom, with no PETE vessel in the scanner. CT scans were performed with the full cone beam as well as with the 1 cm fan beam aperture. The average reconstructed attenuation coefficients were averaged over a cylindrical region of interest (6 mm diameter, 4 mm height) in the center of the finger.

2.3.1.4 Gelatin finger phantom

Figure 2.4 shows central plane profiles through single projection images of the blank and carbon black finger gelatin phantoms, acquired by combining open field and shadow images from the slot array images at the three different positions. Near the walls, the overall signal drops well below 10% of the camera's maximum pixel value, and a large fraction of this signal is made up of stray light. This is another illustration of the loss of primary signal that was described in Section 2.2.4.1 and shown in Figure 2.2. Throughout the central region, where the measured intensity is above 10% of the camera's maximum pixel value, the stray light contribution does not exceed 4% of the overall signal, indicating that the level of stray light in the useful region of the vessel is low. The stray light estimate obtained by comparing pixel values between open-field and narrow-beam geometry was also approximately 4%, confirming that the vertical slot array provided a good estimate of

stray light near the center of images. The measured stray light level of about 4% represents a considerable improvement over the results obtained using the original diffuser system, where the stray light contribution measured was on the order of 20 to 25% of the total signal in the central region of the vessel (See Granton *et al.* 2016 [20]).

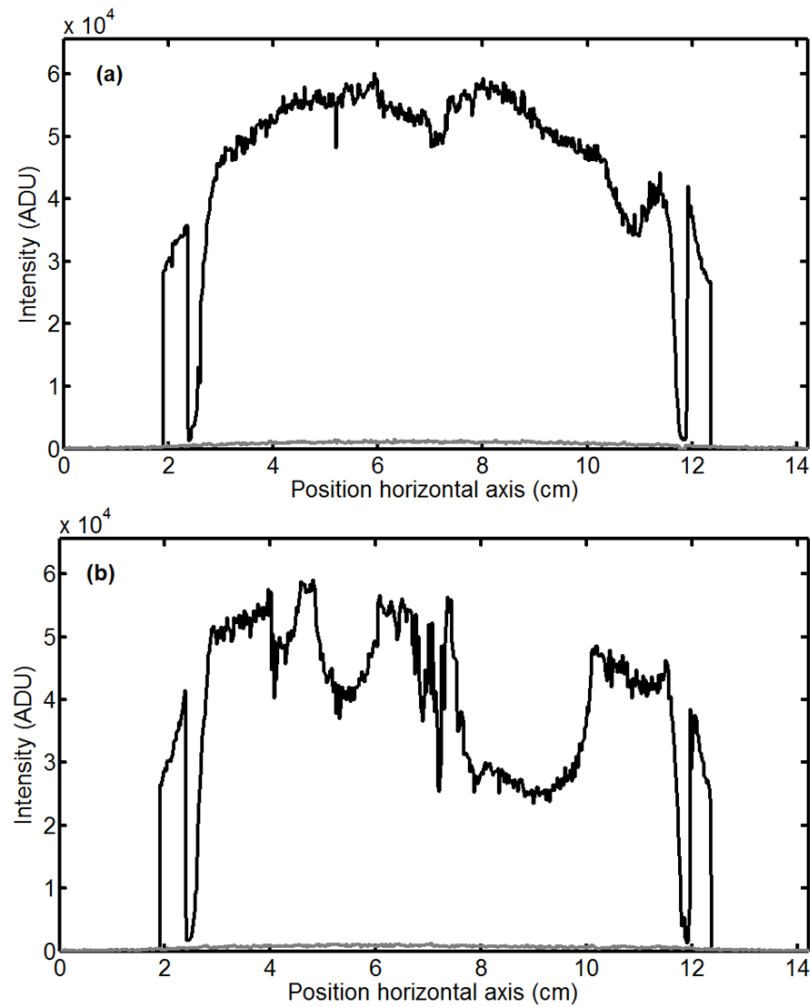


Figure 2.4: Central horizontal axis line profiles: (a) uniform reference phantom (5% gelatin), (b) carbon black finger gel. Composite open field (solid black) and stray light component (solid gray) are shown. Within the vessel, stray light contributes less than 4% of the total signal.

2.3.2 Image artifacts and source spot size optimization

Figure 2.5 shows examples of reconstructions of the FEP finger phantom and uniform solution phantom examined in the study, for qualitative analysis. The finger phantom (Figure 2.5a) shows a bright edge on one side and a dark edge on the other side of the finger, as well as some streaks through the image that originate from these locations. This artifact is associated with mechanical misalignment of rotations between reference and data scan acquisitions. This phantom represents the worst case scenario for such an artifact, as the attenuating FEP walls, which are small and very sharp-edged, are present in both reference and data scans. The uniform solution phantom, when imaged with the 2 mm source (Figure 2.5b), shows several artifacts associated with the Vista10 polyethylene terephthalate vessel. Streaks that appear to originate at the vessel's seams are visible throughout the image. These are most pronounced through the center of the image, because the seams lie directly opposite each other, but are also visible at other locations, fanning outward from each seam. At or near the location of the wall, a dark and adjacent bright ring is seen in the reconstruction. These artifacts have been seen in previous optical CT work [25, 31], and are caused by missing information close to the vessel wall as well as a mechanical misalignment between reference and data scans. Visually, the reconstructions obtained using the convergent light source and the Vista10 vessel appear to be of poorer quality than those obtained with the diffuse light source, exhibiting increased noise and artifacts. With a small spot size at the diffuser (Figure 2.1b), the system is very sensitive to refraction and to unique optical features of the Vista10 vessels. These effects create artifacts in the CT reconstructed image. While it may in principle be possible to correct for these artifacts with post-processing of CT reconstructions, it would be preferable to eliminate the need. Increasing the size of the spot formed at the entrance to the diffuser allows a slightly increased amount of stray light into the system, thereby reducing the sensitivity to these features. A reconstruction slice of a uniform phantom, imaged using the larger spot size of approximately 5 mm, is shown in

Figure 2.5c. In this reconstruction the appearance of streaking and near-wall artifacts is reduced in comparison to Figure 2.5b. The numerical values of reconstructions, measured in the same way as the uniform phantom experiments described in Section 2.2.4.2, are $0.118 \pm 0.002 \text{ cm}^{-1}$ for the fan beam aperture, and $0.117 \pm 0.002 \text{ cm}^{-1}$ for the full cone beam, a difference of $(1 \pm 2) \%$ in mean values. The maintained agreement between fan and cone beam data indicates that changes in the attenuation-suppressing effects of stray light are minimal when moving from a 2 mm focal spot to a 5 mm spot. Later, this was further validated by a narrow-beam experiment using a 2 mm diameter hole aperture. Central axis Beer-Lambert law calculations using an open field and the 2 mm aperture agreed within 1% (0.310 ± 0.004 vs. 0.312 ± 0.006). This result confirms that the modified light source design has removed most of the effects of stray light from the system.

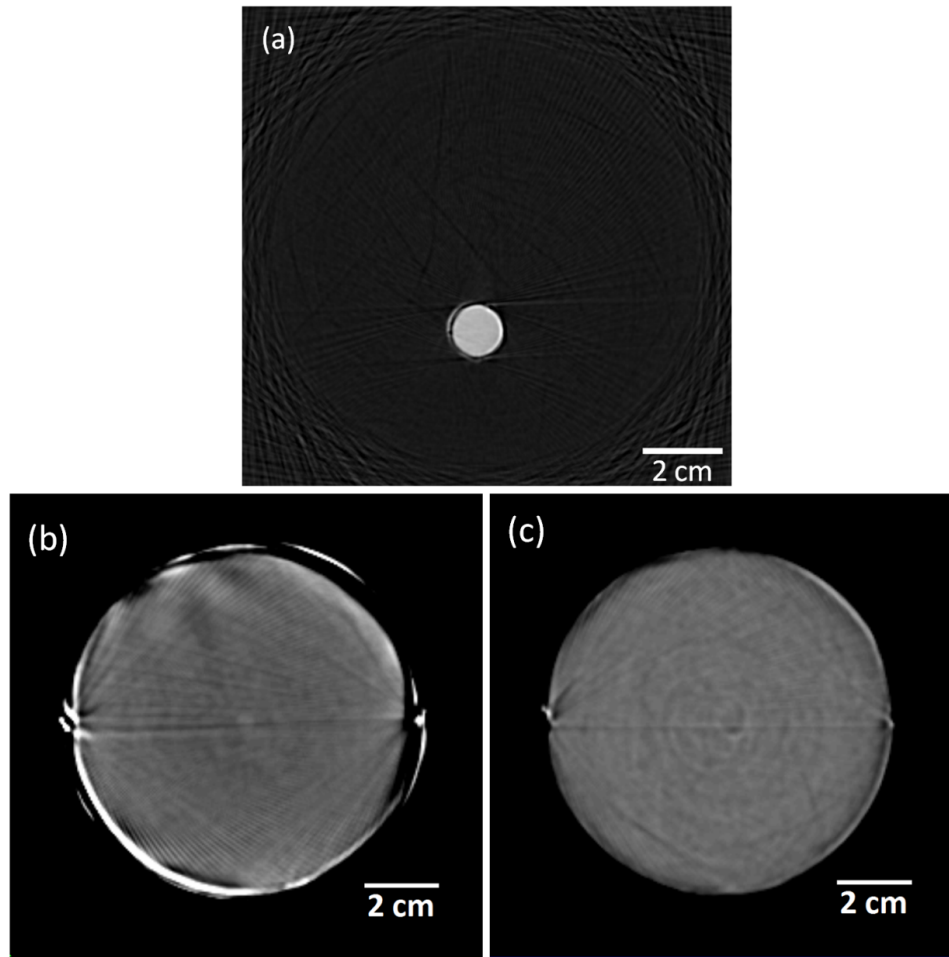


Figure 2.5: (a) A reconstruction slice (window = 0.3 cm^{-1} , level = 0.12 cm^{-1}), of the FEP finger phantom filled with attenuating water based solution (solution #10), acquired with the full cone beam and reconstructed with 0.25 mm voxels on a 512^3 grid. The bright edges of the finger are due to mechanical misalignment between reference and data scans. (b) A reconstruction slice of the attenuating, 7.5% propylene glycol, carbon black solution (solution #6) (window = 0.05 cm^{-1} , level = 0.12 cm^{-1}) acquired with the full cone beam and reconstructed with 0.5 mm voxels on a 256^3 grid. Note the appearance of streaking through the center of the reconstruction, associated with the seams of the PETE vessel, as well as artifacts near the vessel walls associated with unique wall features and missing data. (c) A reconstruction slice (window = 0.05 cm^{-1} , level = 0.12 cm^{-1}) of the uniformly attenuating carbon black 7.5% propylene glycol solution scanned with the larger LED source. Note that the appearance of artifacts is reduced compared to (b), due to stray light blurring and filling in near-wall missing data.

2.4 Conclusion

We have presented a practical method of performing cone beam optical CT scans with very low stray light contribution through the use of a Fresnel lens generated convergent cone light source on a Vista10 system. Fan beam and cone beam acquisitions were performed on a uniformly attenuating phantom containing 7.5% by volume propylene glycol solutions within a Vista10 vessel, and on FEP finger phantoms filled with uniformly attenuating water-based solutions. Good agreement between fan and cone beam reconstructed attenuation coefficients was found, with a maximum discrepancy of $(4 \pm 2) \%$ for the FEP finger phantom for attenuations between 0.097 and 0.469 cm^{-1} and $(1 \pm 2) \%$ for the uniform solutions between 0.036 and 0.433 cm^{-1} . This corresponds to transmission values from 1-75% along the diameter of the vessel. Cone beam reconstructions of uniform solutions in this attenuation range were flat within 2% for upwards of 85% of the vessel's inner radius, showing no cupping or bowing artifacts. For a gelatin phantom with similar scattering properties to a gel dosimeter, the stray light contribution, as measured in a single cone beam projection using a vertical slot array, did not exceed 4% of the total signal. These results are considerable improvements over those obtained with the original LED array with a diffuser plate, where stray light corresponded to up to 25% of the total signal in the default configuration, and was only reduced to 6% by extending the source distance, at the cost of doubling the length, width, and height of the scanner [20]. Imaging with the convergent source highlights newly seen artifacts associated with the Vista10 PETE vessels. In particular, the vessel seams and unique optical features of each vessel can create significant CT image artifacts if there is any error in repositioning between reference and data scan. With improved mechanical positioning it should be possible to minimize these effects. However, the seams create streaking artifacts that appear throughout the reconstructed volume, and are worst along the central axis between them. Imaging with the new source also demonstrates an increased sensitivity to refractive index mismatching, as

non-optimal index tuning between in-jar and aquarium fluids results in significant missing data and creates noisy, inaccurate reconstructions. Increasing the light source spot size at the entrance side of the diffuser can reduce the sensitivity of the system to optical imperfections. In this study we found that increasing the spot from 2 to approximately 5 mm resulted in improved CT reconstructions while still maintaining 1% agreement between fan and cone beam attenuation coefficients in a uniform sample. In future work, the source spot size will be optimized to obtain the best quality image reconstructions and quantitative attenuation measurements. Additionally, dynamic range of the system can be improved by inserting apertures to create fluence patterns specific to the scanning task, similar to the use of bowtie filters in x-ray CT. Most importantly, alternative dosimeter vessels with thinner walls will be investigated. The optimum vessel has not yet been identified, but will likely be custom-made using thin sheets of plastic, and will enable high-quality data for gel dosimetry applications.

2.5 References

1. Gore, J. C., Ranade, M., Maryanski, M. J. & Schulz, R. J. Radiation dose distributions in three dimensions from tomographic optical density scanning of polymer gels: I. Development of an optical scanner. *Physics in Medicine and Biology* **41**, 2695 (1996).
2. Maryanski, M. J. & Ranade, M. K. *Laser microbeam CT scanning of dosimetry gels* in *Medical Imaging 2001* (International Society for Optics and Photonics, 2001), 764–774.
3. Krstajic, N. & Doran, S. J. Fast laser scanning optical-CT apparatus for 3D radiation dosimetry. *Physics in Medicine and Biology* **52**, N257 (June 7, 2007).
4. Van Doorn, T., Bhat, M., Rutten, T. P., Tran, T. & Costanzo, A. A fast, high spatial resolution optical tomographic scanner for measurement of absorption in gel dosimetry. *Australasian Physics & Engineering Sciences in Medicine* **28**, 76–85 (June 2005).
5. Kelly, R. G., Jordan, K. J. & Battista, J. J. Optical CT reconstruction of 3D dose distributions using the ferrous-benzoic-xylene (FBX) gel dosimeter. *Medical Physics* **25**, 1741 (1998).
6. Wolodzko, J. G., Marsden, C. & Appleby, A. CCD imaging for optical tomography of gel radiation dosimeters. *Medical Physics* **26**, 2508 (1999).

7. Jordan, K. & Battista, J. Linearity and image uniformity of the VistaTM optical cone beam scanner. *Journal of Physics: Conference Series* **56**, 217 (Dec. 1, 2006).
8. Sakhalkar, H. S. & Oldham, M. Fast, high-resolution 3D dosimetry utilizing a novel optical-CT scanner incorporating tertiary telecentric collimation. *Medical Physics* **35**, 101–111 (Jan. 2008).
9. Thomas, A. & Oldham, M. Fast, large field-of-view, telecentric optical-CT scanning system for 3D radiochromic dosimetry. *Journal of Physics: Conference Series* **250**, 012007 (Nov. 1, 2010).
10. Doran, S. J. *et al.* A CCD-based optical CT scanner for high-resolution 3D imaging of radiation dose distributions: equipment specifications, optical simulations and preliminary results. *Physics in Medicine and Biology* **46**, 3191 (2001).
11. Krstajic, N. & Doran, S. J. Characterization of a parallel-beam CCD optical-CT apparatus for 3D radiation dosimetry. *Physics in Medicine and Biology* **52**, 3693 (July 7, 2007).
12. Bosi, S., Naseri, P., Puran, A., Davies, J. & Baldock, C. Initial investigation of a novel light-scattering gel phantom for evaluation of optical CT scanners for radiotherapy gel dosimetry. *Physics in Medicine and Biology* **52**, 2893–2903 (May 21, 2007).
13. Babic, S., McNiven, A., Battista, J. & Jordan, K. Three-dimensional dosimetry of small megavoltage radiation fields using radiochromic gels and optical CT scanning. *Physics in Medicine and Biology* **54**, 2463–2481 (Apr. 21, 2009).
14. Olding, T., Holmes, O. & Schreiner, L. J. Cone beam optical computed tomography for gel dosimetry I: scanner characterization. *Physics in Medicine and Biology* **55**, 2819–2840 (May 21, 2010).
15. Siewerdsen, J. H. & Jaffray, D. A. Cone-beam computed tomography with a flat-panel imager: Magnitude and effects of x-ray scatter. *Medical Physics* **28**, 220 (2001).
16. Olding, T., Holmes, O. & Schreiner, L. J. Scatter corrections for cone beam optical CT. *Journal of Physics: Conference Series* **164**, 012031 (May 1, 2009).
17. Zhu, L., Xie, Y., Wang, J. & Xing, L. Scatter correction for cone-beam CT in radiation therapy. *Medical Physics* **36**, 2258–2268 (June 1, 2009).
18. Gao, H. *et al.* Scatter correction method for x-ray CT using primary modulation: Phantom studies. *Medical Physics* **37**, 934 (2010).
19. Thomas, A., Pierquet, M., Jordan, K. & Oldham, M. A method to correct for spectral artifacts in optical-CT dosimetry. *Physics in Medicine and Biology* **56**, 3403–3416 (June 7, 2011).
20. Granton, P. V., Dekker, K. H., Battista, J. J. & Jordan, K. J. Stray light in cone beam optical computed tomography: I. Measurement and reduction strategies with planar diffuse source. *Physics in Medicine and Biology* **61**, 2893 (2016).
21. Gullberg, G. T. *et al.* Review of convergent beam tomography in single photon emission computed tomography. *Physics in Medicine and Biology* **37**, 507 (1992).
22. Feldkamp, L. A., Davis, L. C. & Kress, J. W. Practical cone-beam algorithm. *JOSA A* **1**, 612–619 (1984).

23. Jordan, K., Snir, J. & Battista, J. Multiple slot array collimator to minimize stray light in optical cone beam CT. *Journal of Physics: Conference Series* **250**, 012062 (Nov. 1, 2010).
24. Jordan, K. & Battista, J. A stable black-refractive-index-matching liquid for optical CT scanning of hydrogels. *Journal of Physics: Conference Series* **164**, 012045 (May 1, 2009).
25. Oldham, M. & Kim, L. Optical-CT gel-dosimetry II: Optical artifacts and geometrical distortion. *Medical Physics* **31**, 1093 (2004).
26. Oldham, M. ScanSim: A tool for simulating optical-CT imaging. *Journal of Physics: Conference Series* **250**, 012064 (Nov. 1, 2010).
27. Rankine, L. & Oldham, M. On the feasibility of optical-CT imaging in media of different refractive index. *Medical Physics* **40**, 051701 (2013).
28. Olding, T., Holmes, O. & Schreiner, L. J. Cone beam optical computed tomography for gel dosimetry I: scanner characterization. *Physics in Medicine and Biology* **55**, 2819–2840 (May 21, 2010).
29. Thomas, A., Newton, J., Adamovics, J. & Oldham, M. Commissioning and benchmarking a 3D dosimetry system for clinical use. *Medical Physics* **38**, 4846–4857 (Aug. 2011).
30. Jordan, K. & Battista, J. A transparent black non-diffusing micelle gel for optical CT performance evaluation phantoms. *Journal of Physics: Conference Series* **164**, 012046 (May 1, 2009).
31. Campbell, W. G., Rudko, D. A., Braam, N. A., Wells, D. M. & Jirasek, A. A prototype fan-beam optical CT scanner for 3D dosimetry. *Medical Physics* **40**, 061712 (June 1, 2013).

Chapter 3

Scanning laser optical computed tomography system for large volume three-dimensional dosimetry

This chapter is adapted from a manuscript published as “Scanning laser optical computed tomography system for large volume 3D dosimetry” by Kurtis Hendrik Dekker, Jerry J. Battista and Kevin J. Jordan, *Physics in Medicine and Biology*, 62, 2636-2657 (2017)¹. Permission to reproduce this article was granted by IOP Publishing, and is provided in Appendix B.

3.1 Introduction

3.1.1 Optical CT dosimetry

Optical computed tomography (CT) can be used to perform true three-dimensional (3D) radiation dosimetry by measuring the distribution of optical attenuation induced in radiosensitive gels or plastics. Two main varieties of gel dosimeters exist: polymer gels [1] and radiochromic gels [2]. The two are similar in that they are mostly water, with a gelatin

¹© Institute of Physics and Engineering in Medicine. Reproduced by permission of IOP Publishing. All rights reserved.

matrix ($\approx 5\%$ by weight) and a radiation-sensitive molecule. In polymer gels, ionizing radiation induces a polymerization chain reaction, increasing optical scattering. In contrast, radiochromic gels rely on absorbance and hence change colour when irradiated. The solid dosimeter, PRESAGE®, similarly makes use of a radiochromic dye within a clear polyurethane plastic instead of gel [3]. The result in all types of optical CT dosimeters is a localized change in attenuation coefficient, caused by either scattering or absorbance, as a function of absorbed dose. The distribution of optical attenuation can then be mapped using computed tomography techniques.

3.1.2 Large-volume 3D dosimetry

Even if a target volume is small in external beam radiotherapy, there is still a large volume of irradiated normal tissue of interest surrounding the primary disease site. Confidence in dosimetric verification of a treatment plan is improved as the volume that can be measured increases, motivating the use of larger dosimeters. Additionally, there is interest in treating multiple small tumours in a single radiotherapy session. One example is brain metastases and post-operative surgical beds treated with stereotactic radiosurgery at several isocentres [4, 5]. These treatment plans exhibit high localized doses, with steep dose gradients, to several small targets distributed over a large volume. Large 3D dosimeters with high spatial resolution would enable a “one-step” verification of these deliveries rather than sparsely sampling dose distributions with multiple point or planar dosimeters with data that needs to be “stitched” together for a quasi-3D assessment. Therefore, the goal of this study is to build an optical CT scanner capable of quantitative 3D imaging of large dosimeters.

3.1.3 Optical CT scanners

Optical CT is the visible-light analogue of x-ray CT. Transmission measurements are taken from many projection angles around the object of interest and images are reconstructed using filtered backprojection or iterative CT reconstruction techniques [6]. Optical CT has also been described for air quality measurements [7, 8], and 3D Schlieren imaging of flames [9] and jets [10]. Optical Projection Tomography, used for imaging of biological specimens, is functionally similar but typically images much smaller volumes at finer spatial resolutions than what is needed in radiation dosimetry [11–14].

The development of optical CT for gel dosimetry parallels that of x-ray CT for medical imaging, beginning with “1st generation” translate-rotate scanners using a pencil beam of light (e.g. laser) and small area detector [15–17] and culminating in fast, broad-beam scanners [18–21] which make use of digital cameras to quickly acquire 2D projection images. Fan-beam scanning has also been described using a linear source [22–24] which reduces the illuminated volume during imaging compared to broad beam, thus reducing stray light production.

3.1.4 Stray light effects in optical CT

As in x-ray CT, the progression to broad-beam scanners has resulted in an increase in the effects of “stray” light (light that does not follow a primary ray path through the optical system), leading to an underestimation of measured attenuation coefficients and ‘cupping’ artifacts in dose image reconstructions. These effects are particularly problematic when imaging scatter-based dosimeters, but even the gelatin component of radiochromic hydrogel can cause problems. The accuracy of attenuation coefficients from broad-beam scanners that illuminate with diffuse light sources has been shown to be substantially degraded by scattered light [25–27]. The effects become worse as dosimeter volume increases, due to

longer path lengths through the scattering media. Previously, we described a modification to an existing cone beam scanner, whereby replacing the diffuse light source with a more directional beam greatly improved the accuracy of camera-based optical CT imaging [28]. However, this approach does not achieve the minimum level of stray light rejection possible using a laser scanning system, where only a single pencil beam illuminates the object at any given moment during the scan. In this case, a single transmission measurement can only be perturbed by the paraxial cone of scattered light emitted along that single beam. Furthermore, if a small-area detector is used, a considerable fraction of this cone of scatter can be effectively rejected. This motivates a return to single-ray, single-detector geometries with a small area detector to enhance scatter rejection. Scanning laser systems based on mechanically translating the beam have typically been too slow for practical application to clinical 3D dosimetry, with scan times on the order of minutes per slice [15, 17, 29]. Scanners based on deflecting the beam using rotating mirrors (e.g. galvanometer mirrors) are faster. Van Doorn et al. [30] presented a laser scanner that acquired 144 projections of size $10\text{ cm} \times 7\text{ cm}$ at 1 mm resolution in 3 minutes. The system described by Krstajić and Doran [31] acquired 400 projections of a $12\text{ cm} \times 12\text{ cm}$ field of view (FOV) at 1 mm resolution in 20 minutes. Xu and Wu [32] reported a modification to the commercial OCTOPUS-10X scanner (MGS Research Inc., Madison, CT, USA) which could acquire 400 projections of a $20\text{ cm} \times 10\text{ cm}$ FOV at 1 mm resolution in 50 minutes. The scanner described in this paper can acquire 1024 projections with an $18\text{ cm} \times 12\text{ cm}$ FOV at 0.25 mm nominal resolution in approximately 30 minutes.

3.1.5 Study objectives and outline

The purpose of this study was to build an optical CT system which enables accurate 3D dosimetry in large 15 cm diameter radiochromic gel dosimeters, at sufficient speed for clinical dosimetry ($< 1\text{ hr}$ for a 3D scan). Briefly, this means designing an optical transmis-

sion imaging platform which minimizes the production and detection of stray light while maintaining scan speed. In this report, we describe the imaging system and present quantitative results obtained using both absorbing and scattering phantoms to characterize the stray-light minimization. Phantoms in the study simulate the optical CT imaging challenges that are encountered in a range of dosimetry problems, from large uniform irradiations (i.e. simplest case) to small field dosimetry (i.e. the most challenging scenario).

This report is organized as follows: Section 3.2 describes the design and construction of the optical CT scanner. Section 3.3 reports experiments and results concerning the fundamental performance in terms of detector linearity, spatial resolution, signal to noise ratio and CT geometry. Sections 3.4 and 3.5 describe the optical CT phantom imaging experiments. The ability to accurately image these phantoms without artifacts indicates that the scanner is effective in rejecting stray light and therefore suitable for large volume 3D dosimetry.

3.2 Scanner Design

A top-view schematic of the fan-beam system is shown in Figure 3.1. A 594 nm Helium-Neon laser (Model 1677P, JDS Uniphase Corporation, USA) is attenuated to approximately $80\ \mu\text{W}$ (to prevent detector saturation and dosimeter photochromic reactions), bandpass filtered (10 nm bandwidth, to block plasma discharge), and directed to a galvanometer scanning mirror (Model 6210H, Cambridge Technologies Inc., Bedford, MA, USA) mounted on a vertical translation stage (250 mm eTrack Linear Stage, Newmark Systems Inc., Rancho Santa Margarita, CA, USA). To reduce the beam width and thus improve spatial resolution, a 75 cm focal length lens is mounted on the translation stage, prior to the galvanometer mirror. The detector consists of a photomultiplier (PMT) module (Model H10492-013, Hamamatsu Corporation, Bridgewater, NJ, USA) mounted on a second, synchronized vertical stage, with a small diffuser (1 cm high \times 5 cm wide rectangle) placed 3 cm in front

of the PMT. The photomultiplier is operated with a tube voltage of approximately 300 V. When scanning, the laser beam strikes the diffuser and is scattered into a forward cone, a fraction of which is detected by the photomultiplier, providing an intensity measurement. The PMT outputs a current, which a preamplifier within the module converts to a voltage signal that is sampled by a data acquisition (DAQ) card (USB 6351mx, National Instruments Corporation, Austin, TX, USA) at a rate of 1 MHz. The DAQ has a resolution of 16 bits and is operated with a detection voltage range of -5 V to 5 V.

A projection image is formed as follows: The beam is raster-scanned in a horizontal fan pattern by rotating the galvanometer mirror. The mirror swivels back and forth, controlled by a voltage waveform with a frequency of 200Hz, sweeping the beam across the entrance face of the aquarium. Simultaneously, the paired vertical translation stages move vertically. Mirror rotation and PMT signal sampling are simultaneously triggered by a signal output from the linear motion stage controller when the stage passes user-defined positions that set the vertical extent of the imaging field of view (FOV). The vertical translation stages move at constant speed during data acquisition, and the PMT voltage signal is continuously sampled. The detected voltage at a given sample time is assigned to a ray path based on the instantaneous mirror angle and vertical translation stage position. In this way, a 2D image is constructed from the continuous time series sampling of the PMT voltage. In practice, this scanner represents a “general” optical transmission imaging platform, as the sampling locations and rates can be programmed. This flexibility enhances the scope of possible applications, as imaging of some objects may be improved by using a customized scanning pattern. The following sections describe the design of the scanner as applied specifically to large volume gel dosimetry.

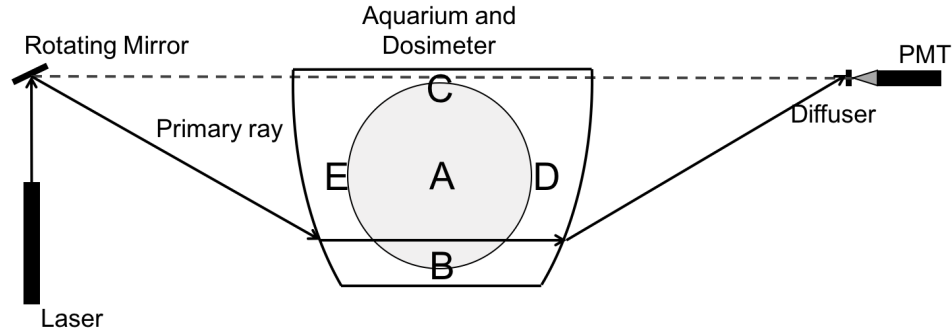


Figure 3.1: Top-view schematic of the scanning-laser system. The rotating galvanometer mirror and detector module are mounted on synchronized vertical translation stages. The curvature of the aquarium was designed by ray-tracing simulation to generate parallel-beam geometry through the interior of the dosimeter volume. The axis of rotation and points 7.5 cm away in each of the 4 cardinal directions are indicated by letters A-E, and correspond to points where spatial resolution was measured using a knife edge test (See Section 3.3.4).

3.2.1 Choice of scanner geometry

While some optical CT scanners have operated in a cone-beam geometry, either with broad beam [18, 26] or scanning laser [33], the common Feldkamp-Davis-Kress (FDK) algorithm for cone beam reconstruction [34] is limited in accuracy to a range of central axial planes. Slices near the vertical limits of a cone-beam scanner's field of view are only sparsely traversed by divergent rays and are thus poorly sampled and not well reconstructed. When scanning cylindrical dosimeters, it is not possible to acquire data spanning the full vertical extent of the sample, as the highly divergent light rays are intercepted at either the air-water interface or floor of the aquarium. This represents wasted dosimeter volume, and is crucially important when trying to examine, for example, the buildup region of a radiation beam delivered from the top of a long cylinder, or the effects of an air interface (i.e. oxygen effects or electron disequilibrium). Therefore, it was important to design a system that could acquire data in all planes of the cylindrical dosimeter, leading to the use of a planar fan-beam scan and vertical translation stages. A galvanometer mirror was used to deflect the beam as it is faster and more reproducible than a stepper motor. With the current arrangement, the scanner can acquire 1024 projections with a field of view of approximately

18 cm (horizontal) by 12 cm (vertical), at a nominal resolution (pixel size) of 0.25 mm in approximately 30 minutes.

3.2.2 Optical CT aquarium

3.2.2.1 Lens-shaped acylindrical aquarium

An aquarium is needed in optical CT to maintain straight-line ray paths through the imaging volume, thus enabling complete radial sampling of the dosimeter volume. In this scanner, the aquarium is designed to have an acylindrical lens shape. The idea of incorporating a lens-like design into the optical CT aquarium itself has been recently presented for broad-beam systems [35] in an effort to reduce optical CT system costs. Other related approaches include “in-air” scanning using the gel dosimeter itself as a lens [36], or using a thick-walled vessel that generates parallel-beam geometry within the gel [37].

In this scanner, the lens-shaped aquarium serves to 1) generate parallel-beam rays within the scanned object, 2) refocus the beams down towards a small detector after passage through the sample, 3) avoid interference fringes associated with air-plastic interfaces perpendicular to the incident laser beam, and 4) reduce the number and cost of optical elements in the system by avoiding large glass lenses. The acylindrical lens-shaped curvature of the aquarium was determined through a ray-tracing optimization algorithm described in Section 3.7. The curve was exported to guide a tool path on a numerically controlled milling (CNC) machine, which was used to cut slots in the top and bottom plates of the aquarium. The curved walls, made from 2 mm thick polymethyl methacrylate (PMMA) were inserted into these slots and secured with silicone caulking. A plastic platform is mounted to a vertical drive shaft which connects, through a water-seal, to a rotation stage (RT-2D-22, Newmark Systems Inc., Rancho Santa Margarita, CA, USA) mounted beneath the aquarium.

3.2.2.2 Importance of asymmetric design

An initial prototype aquarium was manufactured using a design which was symmetrical about the optic axis. However, when projection images were acquired, it was found that interference fringes appeared near the center of images, which created substantial ring artifacts near the center of reconstructed CT images, a region of considerable dosimetric importance. These fringes were found to be related to the air-plastic interface orthogonal to the entering laser beam. To avoid this issue, an asymmetric design was therefore conceived, wherein the perpendicular interface was shifted to the edge of the field of view. With this design, the interference fringes fall outside of the projection space of dosimeters and therefore do not perturb the image reconstruction. An alternate approach is to build the aquarium symmetrically but with antireflective coated plastic material.

3.2.3 Detector collimation and flood-field uniformity

In a previous cone-beam design [33], a large area diffuser and stationary PMT was used. This prevented the use of collimators to reject stray light, and resulted in intensity variations of a factor of 5-10 across flood-field images of a water filled aquarium, due to the large changes in the relative positions of the laser beam and the detector during projection acquisition. In the present scanner design, the aquarium focuses all the exit pencil beams down to a small region, subject to imperfections of the aquarium walls. This allows for a much smaller diffuser to be used, which is advantageous for rejection of scattered light [38]. It also generates a more uniform signal intensity across the entire field of view in flood-field images, which improves the signal to noise ratio in the periphery of the field of view.

Due to some imperfections in the aquarium construction, the diffuser was required to be an approximately 1 cm high by 5 cm wide slot to capture all incoming rays, and flood-field im-

ages displayed intensity variations of only 20% across 75% of the horizontal field of view before falling off by a factor of 2 toward the edges. Better uniformity (<10% variation) was observed over the vertical direction in flood field projection images. Specifically, the wall on the detector side of the aquarium is slightly bowed outward (in the vertical plane), leading to the spot's vertical wandering at the detector plane. The horizontal wandering of the spot at the detector is less than 2 cm when scanning within the central 15 cm of the horizontal field of view, but outside this range the beam exhibits more horizontal wandering, which is caused by the wall curvature being slightly imperfect near the edges. The aquarium was made by inserting plastic walls into a baseplate and top plate with machined cutouts. In the future, aquarium construction may be improved by instead thermoforming the curved walls. Despite these fabrication limitations of the prototype aquarium, the uniformity of flood-field images represents a substantial improvement over our previous cone-beam scanning laser system [33]. Another source of intensity variation is that the diffuser face in the current design is flat, but incoming beam rays are incident at varying angles. A curved surface diffuser could be used in the future to improve uniformity of response during spot scanning.

3.2.4 CT sampling and reconstruction

If projections were acquired by turning the mirror at a constant angular speed and sampling at a constant temporal rate, projection scanlines would be obtained at constant angular intervals. Due to the lens-shaped aquarium, however, this would correspond to non-constant spacing between measured points in a parallel-beam projection line. This can be addressed by re-sampling the projection data onto a uniform grid whose spacing is set to the maximum spacing between samples (to avoid interpolation errors). However, with a galvanometer mirror, it is also possible to address the issue mechanically. The voltage waveform used to control the galvanometer can be experimentally calibrated (by imaging transparent grids)

to move the mirror at a non-constant angular speed, such that equally spaced temporal sampling corresponds to equally-spaced parallel-ray sampling within the aquarium. In the current study, this approach was used to acquire uniformly-spaced projection scanlines in a back-and-forth fashion.

To determine the galvanometer control waveform, a transparent ruler was placed in the center of the water-filled aquarium in a horizontal orientation, spanning the full field of view of the scanner. A profile across ruler gradations was acquired in a step-and-shoot fashion in order to obtain the absolute position of the beam in the rotation axis plane as a function of galvanometer voltage. A sixth-order polynomial function was fitted to this relationship of position versus voltage, and used to design a digital waveform to control the mirror motion. To account for mirror inertia and turnaround time at the ends of its rotational motion, an additional linear initialization ramp was added to the waveform at each reversal. When sampling during an actual scan, data outside the central 90% of each scanline is not used (fill fraction), which provides time for the mirror to settle onto its trajectory. Additionally, there is a delay lag of 135 microseconds between the voltage signal input to the galvanometer and the actual position of the mirror, which is accounted for when placing data into a 2D projection. This delay was measured using an oscilloscope connected to both the control voltage and the position output voltage pins of the galvanometer circuit board, and then fine-tuned by imaging a sharp edge and adjusting the value until the edge did not appear jagged. To ensure that the custom waveform did achieve equal ray spacing, a final image of the transparent ruler was acquired and the spacing between gradations (in pixel space) was measured to confirm equidistance. A useful resource on galvanometer scanning, detailing fill fraction and acquisition delays, is found on the ScanImage [39] wiki page² (Vidrio Technologies LLC). If the scan speed or field of view is changed, the fill fraction and acquisition delay should be re-calibrated by imaging a transparent grid.

A second CT sampling concern arises due to the constant vertical translation of the source

²<http://scanimage.vidriotechnologies.com/pages/viewpage.action?pageId=17400306>

and detector during acquisition as opposed to a “step and shoot” approach. At the current scan speeds, the stage moves 0.25 mm during a single scanline, and therefore data is acquired in a vertical “zig-zag” pattern. A uniform vertical spacing 2D projection can be interpolated from these measurements. In this study, it was found that when reconstructing at 0.33 mm voxels, there was minimal difference between image reconstructions of typical dosimetry samples done with this re-gridding and those performed while simply ignoring the sub-pixel vertical translation and assuming a fixed vertical position during a scanline. If samples with extreme vertical gradients are to be imaged, further testing and correction may be required.

3.3 Initial Characterization Tests

3.3.1 Detector linearity

The linearity of the detector chain was tested to verify that the photomultiplier tube (PMT) and amplifier maintain a linear response at the relatively low bias voltage used (-300 V). A set of neutral density filters (Melles-Griot) was used to attenuate the laser, and beam intensities were measured using the PMT as well as a calibrated photodiode (Model 818 UV Optical Power Meter, Newport Corporation, Irvine, California, USA). As shown in Figure 3.2, excellent linearity between PMT and photodiode was observed, with a linear regression resulting in $r^2 = 0.999$. This confirms that the detector is linear at least up to a detected voltage of 5 V, which is the maximum voltage that can be digitized by the DAQ card in its current configuration.

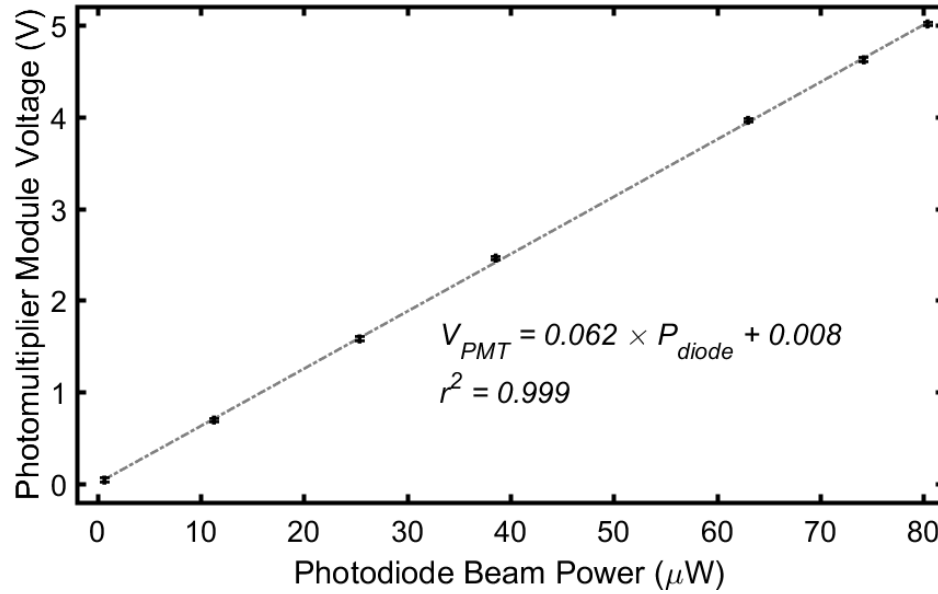


Figure 3.2: Photomultiplier vs. Photodiode measurement of laser intensity, demonstrating the linearity of the detector used in the scanner. Error bars are included but are similar in size to the data markers.

3.3.2 Noise and stability

Variations in detected intensity in this system may be caused by electronic noise (PMT, amplifier, power supply) as well as changes in incident laser brightness (laser noise, mode transitions). These fluctuations can occur at both very high frequencies (noise) and low frequencies (laser mode transitions). To assess the level of source and detector-related noise present in the system, the beam was held in place and 2250 samples were acquired from the detector at a rate of 1 MHz. This represents the number of samples acquired for a single horizontal scan-line in a 16.5 cm wide projection image. The mean and standard deviation were calculated, and used to determine the signal to noise ratio. This was repeated with a sequence of neutral density filters, ranging from 0.1 to 2.0 in optical density, placed in the beam. SNR drops to about 30 for a detected signal of about 0.045 V, approximately 1% of the maximum detection level (5 V). Above 10% of this value, the SNR remained above 100.

To assess long-timescale changes in signal, the mean value in a static region of interest

located outside the scanned object was measured in each projection during an optical CT scan, and compared to the value obtained from the initial projection. This quantifies the long-term “mode-sweeping” of the laser, where changes in resonant mode occur due to small thermal expansion and contraction of the cavity. We observed intensity variations of approximately 3%, which were not periodic but occurred on timescales of the order of minutes. In practice, we apply a normalization correction when reconstructing, by scaling each projection data set based on these measurements to remove the effect. This approach is similar to that used in LED-based broad-beam scanners [40].

3.3.3 Parallel beam geometry verification

To verify that the rays passing through the aquarium are in fact parallel and equally-spaced, transparent rulers were placed in a horizontal orientation at planes located ± 8 cm from the rotation axis plane within the water-filled aquarium. Using a calibrated galvanometer control voltage waveform, transmission images with a nominal field of view of 165×120 mm were acquired, with a nominal horizontal pixel size of 0.22 mm (horizontal) by 0.25 mm (vertical). Profiles through the 1 cm ruler divisions were taken from each image. The spacing between horizontal ruler gradations as a function of position within the projection images was found to be 45 ± 1 samples at both entrance and exit locations, verifying the horizontal pixel size of 0.22 mm. The same measurement was performed using vertical rulers to the vertical pixel size of 0.25 mm. These measurements demonstrate that the system achieves accurate parallel-beam geometry, with equally-spaced samples within each horizontal scanline of projection images. A second validation was performed using a cylindrical vessel with a fiducial marker to measure ray paths, a technique we have also used with the PRESAGE® dosimeter (Chapter 5)[41]. This fiducial test also confirmed the parallel-beam geometry of the scanner with the vessel and a solution of similar refractive index as the gels ($n \approx 1.34$).

3.3.4 Spatial resolution in projection images

The spatial resolution of projection images was evaluated by imaging a tilted knife-edge and measuring the edge response function [42]. This was used to calculate the modulation transfer function (MTF). The resolutions at which the MTF curve reached 50% and 10% (MTF50% and MTF10%) were reported, where MTF10% is often taken to correspond to the highest spatial frequency (i.e. sharpest feature) that can be resolved [43]. This test was repeated at various positions within the aquarium: the axis of rotation (Location A in Figure 3.1), 7.5 cm to the left and right of the axis of rotation (Locations B and C), and 7.5 cm towards the entrance and exit sides of the aquarium (Locations D and E), to test the depth of field of the scanner and uniformity of the resolution throughout the dosimeter volume. It was also repeated within a water-Intralipid solution inside a 15 cm diameter vessel to introduce scattered light. The Intralipid (Intralipid 20%, Fresenius Kabi AB, Uppsala, Sweden) solution was mixed to mimic the scattering conditions of a 5% gelatin gel dosimeter (approximately 50% transmission, relative to water, along central axis). The results of the edge response test are listed in Table 3.1. From these results, we see that a gel dosimeter-like scattering object results in only a small degradation in spatial resolution.

Position	MTF50% (mm)	MTF10% (mm)
Position A, no scatter solution	0.500	0.290
Position B, no scatter solution	0.550	0.325
Position C, no scatter solution	0.490	0.278
Position D, no scatter solution	0.489	0.278
Position E, no scatter solution	0.505	0.303
Position A, with gel-like scattering solution	0.501	0.298

Table 3.1: Horizontal MTF50% and MTF10% resolutions for various positions measured by knife edge test. The vertical direction MTF values were similar but showed no variation across the horizontal field of view, since the curvature of the aquarium is only in the horizontal direction. Locations are indicated by the letters in Figure 3.1, and correspond to the scanner’s rotation axis and points 7.5 cm away in the cardinal directions.

There is a change in the horizontal spatial resolution across the field of view (moving across positions A-C in Figure 3.1). The beam changes shape as a function of position due

to varying angle of incidence on the aquarium wall. For a circular beam (e.g. symmetric Gaussian) at normal incidence to the aquarium wall, the beam inside the aquarium will remain circular. However, at oblique incidence, the beam within the aquarium will become elliptical. This results in an asymmetric variation in horizontal spatial resolution across the field of view. In this case, the MTF10% resolution at all positions was finer than 0.33 mm, so when performing optical CT scans we reconstructed data using 0.33 mm cubic voxels. The vertical MTF values were similar to horizontal MTF values observed at position C, and did not exhibit variation, since the aquarium curvature is only in the horizontal direction. It should be noted that any scanning-laser system that uses beam deflection combined with a lens or lens-shaped aquarium wall to focus rays will exhibit a spatially varying resolution throughout the dosimeter.

3.3.5 Summary of specifications

Table 3.2 summarizes the results of initial performance testing. These experiments indicate that the scanner should be capable of imaging with a quasi-isotropic resolution of 0.33 mm, which was used in the subsequent scanning experiments.

Characterization Test	Key Result
Detector Linearity	PMT linear <i>w.r.t</i> photodiode ($r^2 = 0.999$)
Detector / Source Noise	SNR > 100 when above 10% of max signal
CT Geometry	Parallel-beam, confirmed by imaging rulers
Projection Spatial Resolution	MTF10% resolution < 0.33 mm within FOV

Table 3.2: Summary of initial characterization test results for scanning laser system.

3.4 Optical CT scanning experiments

3.4.1 Phantoms

Optical CT scanning experiments were designed using phantoms that mimic extreme cases in 3D gel dosimetry, from the simplest problem of large, uniform irradiations, to the challenging problem of small-field dosimetry. These tests were performed with solution phantoms consisting of either absorbing or scattering liquids loaded in either a large cylinder or a small “finger” phantom. The large phantom was a custom 15 cm diameter vessel with 0.25 mm thick walls made from polyester film. The finger phantom was made from a fluorinated ethylene propylene (FEP) cylinder (heat-shrink tubing, SKU#92N6000, Newark Corporation, Toronto, ON, Canada), with inner diameter 12.5 mm and outer diameter 13.5 mm.

3.4.2 Optical CT scan parameters

Table 3.3 lists the parameters used for optical CT scanning and image reconstruction. To account for variation in laser brightness, projection intensity values were renormalized, prior to reconstruction, to a peripheral region outside of the scanned vessel. Image reconstructions were performed *via* filtered backprojection [6] with a Hamming filter, using in-house GPU-accelerated functions programmed in the CUDA environment (NVIDIA Corporation, Santa Clara, California, USA). On a PC equipped with an Intel Core i7-2600 CPU (Intel Corporation) and an NVIDIA GTX 780 GPU, backprojection time is under 10 seconds for the full 3D volume, and total reconstruction time (including loading and pre-processing scan data) is less than one minute.

Parameter	Value
Projection FOV	165 mm (H) \times 120 mm (V)
Projection Pixel Size	0.22 mm (H) \times 0.25 mm (V)
Projection Size	750 \times 480 (pixels)
# of Projections	1024
Scan Rotation	360 $^{\circ}$
Reconstruction FOV	165 mm
Reconstruction Method	FBP – Hamming Filter
Reconstruction Resolution	0.33 mm (isotropic)
Reconstruction Axial Size	500 \times 500
Reconstruction Slices	364

Table 3.3: Parameters used for optical CT scan acquisition and reconstruction.

3.4.3 Large-volume uniform absorbing phantom

The large phantom (Section 3.4.1) was imaged with a series of increasingly dark absorbing liquids with limited scattering power. Test solutions were formed by dissolving carbon black (CB) nanoparticles in an aqueous solution containing liquid dish soap (Sunlight®, Sun Products Corporation, Wilton, CT, USA) to form a dark black ink [44]. This was added to a water-based liquid containing (by weight) 5% propylene glycol and 2% Triton-X 100 surfactant (Sigma-Aldrich, Oakville, ON, Canada). The aquarium was filled with pure water. The mismatched refractive index between aquarium and scanned object maintains straight-line ray paths through the cylindrical volume [26, 45].

The liquids in this experiment spanned the range from approximately 90% down to 2% transmission (relative to the liquid with no CB added) along the central axis of the phantom vessel (15 cm diameter). Attenuation coefficients were measured in a region of interest (ROI) of size $5 \times 5 \times 5 \text{ mm}^3$ located 1 cm away from the rotation axis. This was performed at the central slice as well as the ± 4 cm slices in the vertical (z) direction along the cylinder. These measurements were compared to Beer-Lambert law calculations performed using a 10 cm path length cell with the laser and calibrated photodiode (Model 818 UV Optical Power Meter, Newport Corporation, Irvine, California, USA). Reconstruction flatness was

quantified across the diameter of the vessel by measuring the mean attenuation coefficient inside concentric 2 mm wide, 5 mm high cylindrical shells located at the central axial plane. To evaluate uniformity in the vertical direction, the mean value within a $5 \times 5 \text{ mm}^2$ ROI, 1 cm away from the image center, was measured in each axial slice.

3.4.4 Large-volume uniform scattering phantom

The scanner's ability to image large volume uniformly scattering phantoms was evaluated. A series of 5% propylene glycol solutions with varying concentrations of Intralipid were scanned within the large vessel. 5% propylene glycol without Intralipid was used as the reference scan. In this experiment, Intralipid solutions spanned the range from approximately 50% down to 2% transmission along the 15 cm diameter of the vessel. As before, CT reconstructed attenuation coefficients were measured in ROIs ($5 \times 5 \times 5 \text{ mm}^3$) in the central and ± 4 cm slices and compared to Beer-Lambert law results from the photodiode setup. Reconstruction flatness was again quantified axially using 2 mm wide, 5 mm high concentric shells and vertically using $5 \times 5 \text{ mm}^2$ regions within each slice. Obtaining uniform reconstructions and agreement between optical CT and independent measurement re-affirms that the scanner is effective at rejecting scattered light.

3.4.5 Small absorbing finger phantom in gel-like scattering medium

One of the most challenging dosimetry problems in contemporary radiation therapy is the measurement of dose in small-fields ($\approx 1 \text{ cm}$) [46, 47]. These fields are used for radio-surgery, but can occur within intensity-modulated beam segments. Measuring small fields is required to commission or verify treatment planning software. Commissioning small fields has long been proposed as a unique application for optical CT dosimetry, and has been attempted using a variety of different dosimeters [48–50]. However, small fields also

represent a difficult optical imaging problem: accurately measuring the attenuation of a small absorber surrounded by a scattering medium. Therefore, a “finger” phantom experiment, using the FEP tube phantom (Section 3.4.1), was designed to test the scanner performance in such a stressed scenario.

The finger phantom was mounted within the large phantom vessel, approximately 3.5 cm from the rotation axis. The large vessel was filled with a scattering Intralipid – water solution representative of the scattering present in a gelatin-based radiochromic dosimeter (approximately 50% transmission along the diameter, relative to water). The tube was filled with absorbing solutions of Nigrosin (Fisher Scientific, USA) dissolved in water, to mimic a gel exposed to small beams of radiation. Pure water was used inside the tube for the reference scan. Eight solutions were used in this experiment, spanning a transmission range of approximately 90% down to 3% along the 12.5 mm inner diameter of the small FEP tube. The attenuation of the liquids was measured independently by absorption spectrometer and compared to a measurement within the reconstructed CT image (7 mm diameter, 5 mm height cylindrical region of interest located at the center of the finger).

3.4.6 Small absorbing finger phantom in highly scattering medium - opposing sinogram reconstructions

Figure 3.3 shows a photograph of a scattering Intralipid solution in the optical CT scanner, with a laser beam directed along the central axis.

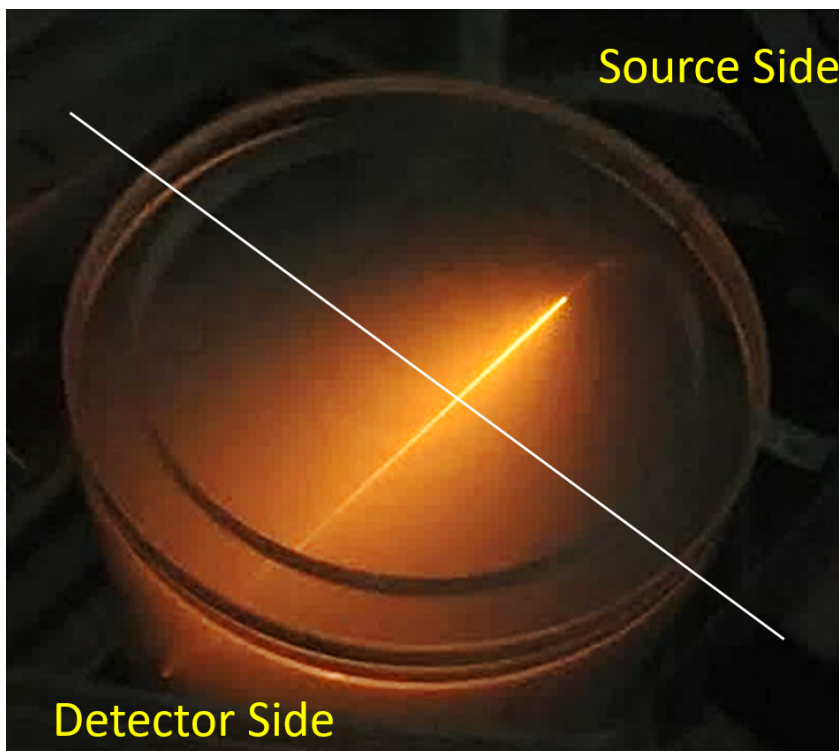


Figure 3.3: Top view photograph (brightness and contrast enhanced) of scattering Intralipid solution with laser beam directed along the diameter. The white line indicates the central plane through the dosimeter. The attenuation of the primary beam due to scatter can be seen, with the conical “bloom” of scattered light clearly visible, showing the three-dimensional distribution of scattered light.

The closer to the source that a small absorber is located within a scattering medium, the shorter the path length before the incoming pencil beam confronts that absorber, and therefore less scattering will occur prior to primary ray attenuation. If the system could perfectly reject scattered light, transmission measurements of a small absorber would be consistent regardless of its position along a ray within the scattering sample. Since the detector has a finite size and cannot discriminate between primary and scattered light, not all scatter is entirely rejected. This has implications when imaging a small object, because the fraction of the scattered radiation that encounters the absorber is dependent upon its position along the primary ray path, i.e. the solid angle subtended by the absorber governs how much of the scatter cone is occluded. Therefore, an absorber located at the detector side of the vessel will block less overall light (primary plus scatter cone) than one located at the entrance

side. Simply put, the apparent transmission of a small absorbing object depends not only on its intrinsic absorption coefficient, but also on the scatter coefficient of the surrounding medium and its position within that medium.

In the case of optical CT, this means that scatter perturbs each projection differently. To examine stray light effects, separate reconstructions of the finger phantom within Intralipid surrounding medium were performed, using two halves of the 360° parallel-beam sinogram: the “front 180°” (where the finger is on the source side of the rotation axis) and the “back 180°” (i.e. detector side). In parallel-beam geometry, these two datasets would be completely equivalent if no scattered light was detected, and therefore no difference in reconstructed attenuation coefficients would be observed. If, however, scatter is detected, then the “back 180°” reconstruction will have a lower attenuation coefficient. The opposing sinogram reconstructions were performed for a single Nigrosin finger phantom within an extremely scattering Intralipid solution (2% transmission along large vessel diameter), as well as within the gelatin-like scattering medium, for comparison. Reconstructed attenuation coefficients from the opposing sinograms were measured in each case.

3.5 Results and Discussion

3.5.1 Large-volume uniform absorbing phantom

Table 3.4 lists the CT and Beer-Lambert attenuation coefficients for the large uniform absorbing solution experiment. The values agreed within the standard deviation of the measurements for all cases. A linear regression shows near perfect agreement between the two measurement techniques, with a slope of 0.994 ± 0.004 and r^2 value of 0.9999. These results demonstrate the excellent accuracy of the scanner over a large range of transmission values ($\approx 90\%$ to 2% along the diameter). The mean values within concentric 2 mm wide, 5 mm high shells located at the central axial plane varied by less than 2%, confirming that

reconstructions were uniform across the vessel diameter. Reconstructed images were also flat within 2% along the vertical direction, measured within $5 \times 5 \text{ mm}^2$ ROIs in each slice. As a further test of overall uniformity, the fraction of voxels within the entire vessel (up to 1 mm from the inner diameter) having attenuation values lying within 2%, 3%, and 5% of the mean value was calculated for each absorbing liquid. Since the ROI-based measurements and pixel profiles (Figure 3.4) did not show a systematic non-uniformity, the low voxel fractions observed for lightly attenuating liquids are the result of artifacts (streaks and rings) and noise in the reconstruction. These voxel fractions increase with increasing attenuation coefficient, which suggests that there is a baseline noise present in the images. While the mean value is generally accurate, the precision of very low attenuation coefficients is limited unless a large region of interest (i.e. more pixels) is averaged. A sample reconstruction slice and profiles are shown in Figure 3.4, showing the uniformity. Some slight ring artifacts can be seen, which are likely the result of imperfections in the aquarium wall. Additionally, there is an asymmetry at the edges of the profile in Figure 3.4b which is likely due to a small mechanical misalignment between scans.

Fluid	$\mu_{CT} \text{ (cm}^{-1}\text{)}$	Fraction of voxels within 2% / 3% / 5% of mean	$\mu_{cuvette} \text{ (cm}^{-1}\text{)}$	% Difference μ_{CT} vs $\mu_{cuvette}$
A1	0.009 ± 0.001	0.07 / 0.12 / 0.21	0.009 ± 0.001	$(0 \pm 11) \%$
A2	0.036 ± 0.001	0.22 / 0.33 / 0.52	0.036 ± 0.001	$(0.0 \pm 2.7) \%$
A3	0.055 ± 0.001	0.46 / 0.64 / 0.86	0.055 ± 0.001	$(0.0 \pm 1.8) \%$
A4	0.098 ± 0.002	0.75 / 0.91 / 0.98	0.097 ± 0.002	$(1.0 \pm 2.1) \%$
A5	0.146 ± 0.002	0.84 / 0.81 / 0.98	0.145 ± 0.003	$(0.7 \pm 1.4) \%$
A6	0.193 ± 0.003	0.90 / 0.98 / 0.99	0.193 ± 0.003	$(0.0 \pm 1.5) \%$
A7	0.255 ± 0.004	0.97 / 0.99 / 0.99	0.257 ± 0.004	$(0.8 \pm 1.6) \%$
Linear Regression	slope = 0.994 ± 0.004 intercept = 0.0006 ± 0.0006 $r^2 = 0.9999$			

Table 3.4: Optical CT and Beer-Lambert (10 cm cell) attenuation coefficients measured in the 15 cm phantom containing absorbing liquids (A1-A7). μ_{CT} is reported as the mean and standard deviation within a $5 \times 5 \times 5 \text{ mm}^3$ ROI located 1 cm off the rotation axis in the central axial plane. The fraction of voxels within the vessel which have values that lie within 2%, 3%, and 5% of the mean value was also quantified for each reconstruction. $\mu_{cuvette}$ uncertainty is taken from three repeated trials of the spectrometer assessment, with samples re-positioned between each measurement.

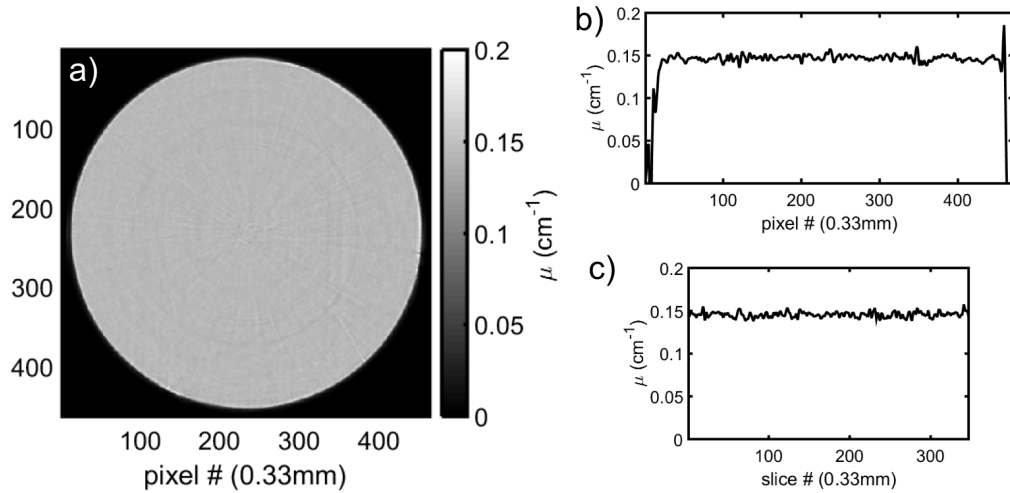


Figure 3.4: Reconstruction of the 15 cm phantom containing a uniform absorbing liquid (a) Central axial slice. (b) horizontal profile through the axial slice, (c) vertical (z) profile from top to bottom of the phantom.

3.5.2 Large-volume scattering phantom

Table 3.5 summarizes the optical CT and Beer-Lambert coefficients for the large-volume scattering experiment. Good agreement was found between the two measurements within the range of 50% down to 2% transmission along the vessel diameter. Linear regression between the two measurements results in a slope of 1.02 ± 0.02 and r^2 value of 0.9992, indicating a very good linear fit. The slope being 2% above unity appears to be mainly due to the comparatively large discrepancy seen for solution S5, which had approximately 2% transmission along the diameter of the large vessel. Differences in acceptance angle between the two measurement systems may become important at these elevated scatter conditions. However, reconstruction profiles for the 5 solutions (Figure 3.5) remain flat within 3% across the diameter, as well as along the vertical direction, demonstrating an absence of scatter-related cupping artifacts.

Fluid	$\mu_{CT} \text{ (cm}^{-1}\text{)}$	$\mu_{cuvette} \text{ (cm}^{-1}\text{)}$	% Difference
S1	0.047 ± 0.001	0.046 ± 0.001	$(2.2 \pm 2.2) \%$
S2	0.066 ± 0.002	0.067 ± 0.002	$(1.5 \pm 3.1) \%$
S3	0.124 ± 0.003	0.126 ± 0.002	$(1.6 \pm 2.4) \%$
S4	0.171 ± 0.003	0.172 ± 0.004	$(0.5 \pm 1.7) \%$
S5	0.267 ± 0.005	0.261 ± 0.004	$(2.2 \pm 1.5) \%$
Linear Regression	slope = 1.02 ± 0.02 intercept = -0.003 ± 0.003 $r^2 = 0.9992$		

Table 3.5: Optical CT and Beer-Lambert (10 cm cell) attenuation coefficients measured in the uniform solution phantom experiment for scattering liquids (S1-S5). μ_{CT} is reported as the mean and standard deviation within a $5 \times 5 \times 5 \text{ mm}^3$ ROI located 1 cm off the rotation axis in the central axial plane. $\mu_{cuvette}$ uncertainty is taken from three repeated trials of the spectrometer assessment, with samples re-positioned between each measurement.

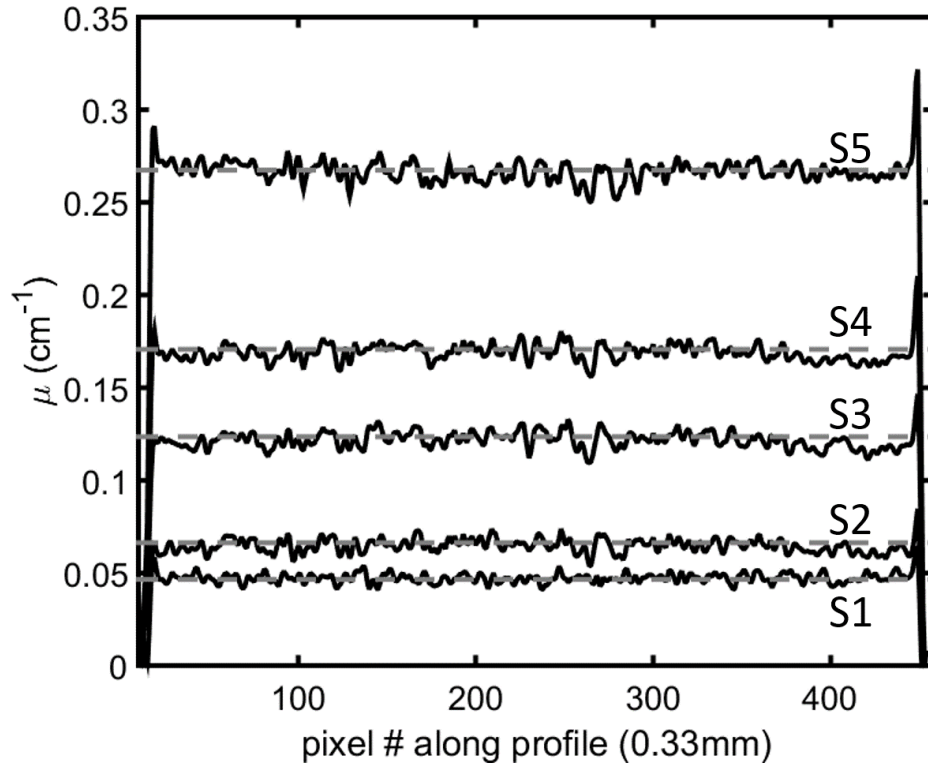


Figure 3.5: Central slice profiles across reconstruction slices of the uniform 15 cm scattering phantom. Reconstructions are flat within 3%, indicating a lack of cupping artifacts.

3.5.3 Absorbing finger phantom in gel-like scattering medium

Table 3.6 presents the CT and spectrometer attenuation coefficient measurements for the uniform Nigrosin solutions scanned inside the 1.25 cm finger phantom within the gel-like Intralipid solution phantom. Reconstructed images of the finger phantom were circular with the correct diameter, demonstrating the geometric fidelity of the scanner. Agreement within approximately 2% was observed for all liquids, spanning the attenuation range from 0.085 cm^{-1} to 2.9 cm^{-1} (transmission range: 90% down to 3% along the diameter of the finger). The maximum deviation between the two measurements was 2.4%, observed for the lightest fluid. A linear regression between the two measurement systems gives a slope of 0.99 ± 0.01 and r^2 value of 0.9992. Reconstructions of the finger appear uniform, with no evidence of artifacts related to scattered light. These results demonstrate that the system accurately measures attenuation in the case of a small attenuating object immersed within a medium representative of the scattering in typical gel dosimeters. A sample reconstruction slice and profile through the finger reconstruction is shown in Figure 3.6. Asymmetry in the profile is related to misalignment between pre- and post-scan data, due to a small movement of the finger phantom while changing the attenuating liquid.

Fluid	$\mu_{CT} \text{ (cm}^{-1}\text{)}$	$\mu_{cuvette} \text{ (cm}^{-1}\text{)}$	% Difference
A8	0.087 ± 0.002	0.085 ± 0.002	$(2.4 \pm 2.4) \%$
A9	0.174 ± 0.003	0.174 ± 0.002	$(0.0 \pm 1.7) \%$
A10	0.332 ± 0.003	0.338 ± 0.001	$(1.7 \pm 0.8) \%$
A11	0.530 ± 0.007	0.531 ± 0.006	$(0.1 \pm 1.3) \%$
A12	0.905 ± 0.005	0.925 ± 0.005	$(2.2 \pm 0.5) \%$
A13	1.487 ± 0.009	1.489 ± 0.006	$(0.1 \pm 0.6) \%$
A14	2.300 ± 0.010	2.255 ± 0.004	$(2.0 \pm 0.4) \%$
A15	2.850 ± 0.010	2.913 ± 0.013	$(2.1 \pm 0.3) \%$
Linear Regression	slope = 0.99 ± 0.01 intercept = 0.0030 ± 0.02 $r^2 = 0.9992$		

Table 3.6: Optical CT and absorption spectrometer attenuation coefficients measured in the 12.5 mm (inner diameter) finger phantom placed within a 15 cm vessel containing the gelatin-simulating Intralipid solution. The finger contained absorbing Nigrosin-dyed liquids (A8-A15). $\mu_{cuvette}$ measurement uncertainty is derived from three repeated trials where the cuvettes were removed and re-positioned in the spectrometer on each trial.

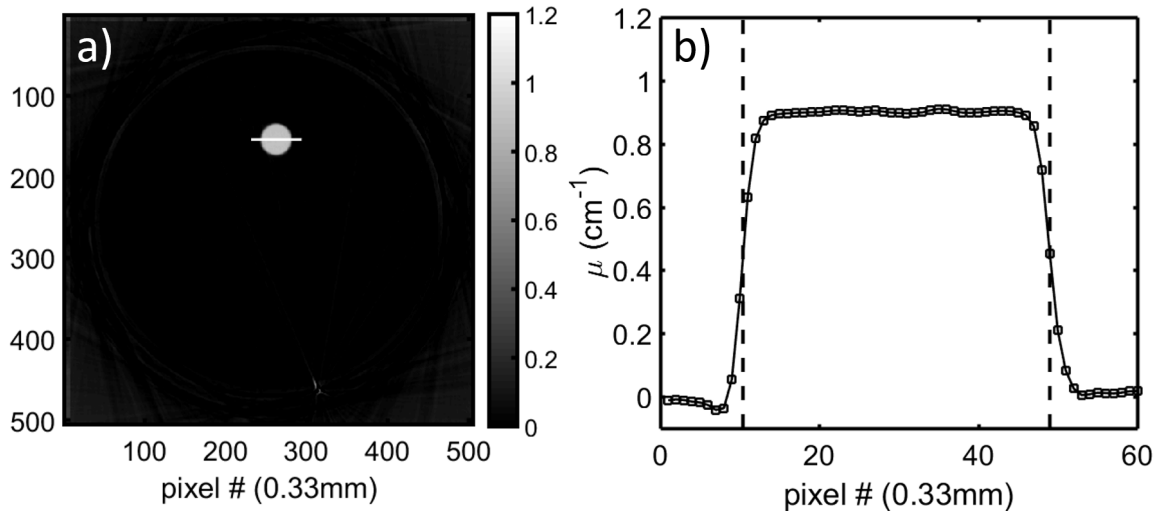


Figure 3.6: Reconstruction slice (a) and profile across finger (b) for the FEP tube phantom experiment (liquid A12 in table 3.5). The profile location in (b) is indicated by the white line in (a). Dashed vertical lines in (b) indicate the actual diameter of the phantom. Asymmetry in the profile, particularly evident in the baseline outside the cylinder, is caused by a slight mechanical displacement between pre- and post-scans introduced when changing the liquids within the phantom.

3.5.4 Small absorber in highly scattering medium - opposing sinogram reconstructions

In the case of the extremely scattering surrounding medium, reconstructing the finger phantom from the “back 180°” of the scan yielded an approximately 3% lower attenuation coefficient than reconstructing from the “front 180°” (Figure 3.7a). This result demonstrates that the scatter problem in optical CT is indeed a three-dimensional one. It would not be sufficient to simply subtract a constant value from measurements, as the scatter signal is dependent on the attenuation distribution of the object itself, which is unknown a priori. If extremely scattering dosimeters (such as polymer gels) are to be imaged, improved scatter rejection or measurement and subtraction using a secondary detector may be needed. As a first step, improving aquarium construction would allow for better primary ray focusing to an even smaller detector, which would improve stray light rejection.

The discrepancy between “front half” and “back half” reconstructions is reduced to less than 0.5% when imaging the finger within a 50% transmission Intralipid solution, which is more representative of typical gel dosimeters. Profiles through these reconstructions are shown in Figure 3.7b. The results of this experiment suggest that scattered light should have a relatively minor impact when imaging current gel dosimeters.

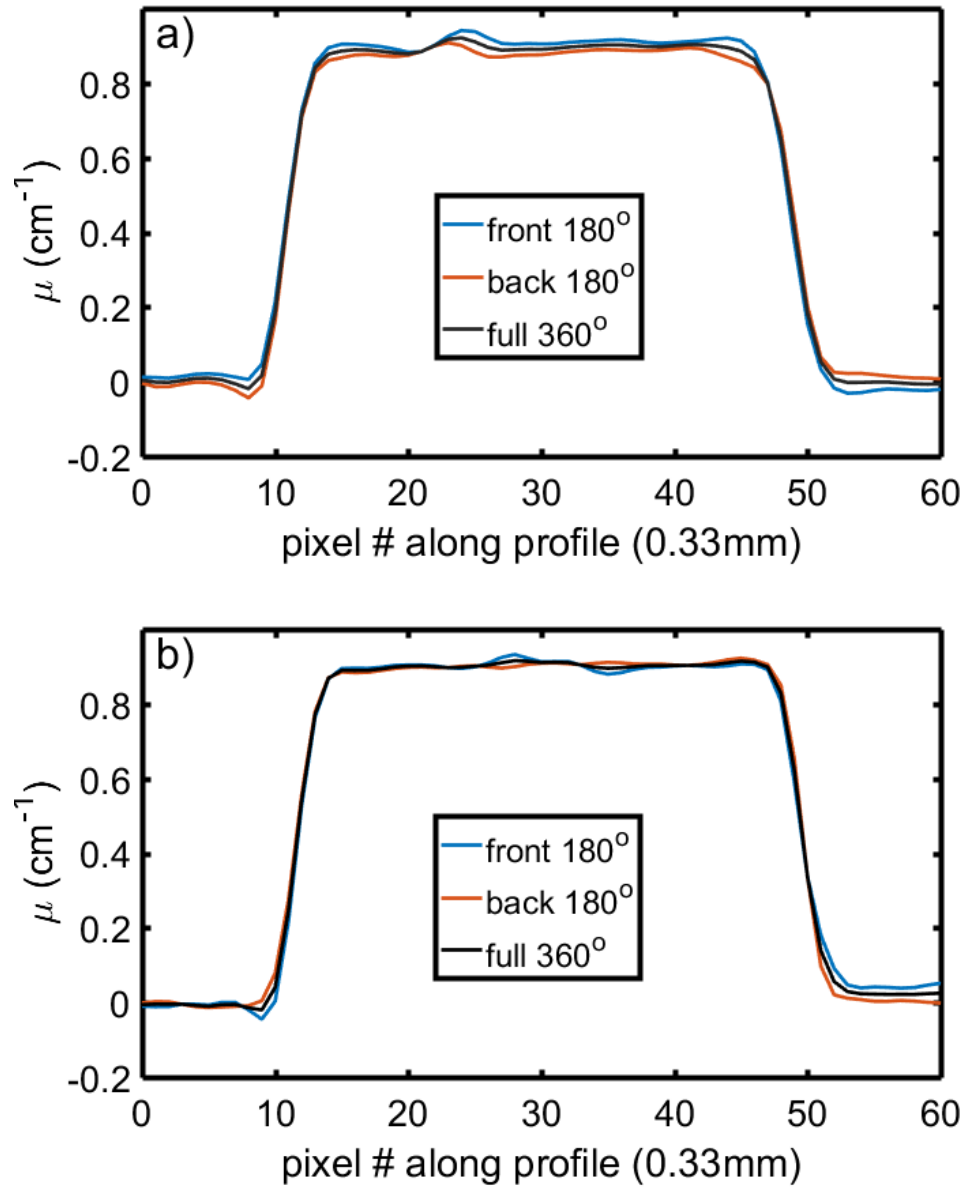


Figure 3.7: Profiles across the finger phantom reconstructions from the “front” and “back” half of the sinogram, for the case of 2% transmission (a) and 50% transmission (b) scattering solution surrounding the finger. In (a) there is approximately 3% difference between the central attenuation coefficients, while in (b) there is only a 0.5% difference.

3.5.5 Summary of results and current limitations

With the new scanner design, mean optical CT attenuation coefficients showed agreement with independent measurements within 1% for absorbing liquids imaged in a large 15 cm diameter vessel, within 2% for scattering liquids scanned in the same phantom, and within 2% for small 1.25 cm diameter absorbers scanned within a scattering liquid having similar scatter to that of typical gel dosimeters. More importantly, excellent linearity was observed over a very wide dynamic range (between 90% and 2% transmission). Reconstruction of finger phantom images from two “halves” of a 360° parallel-beam sinogram resulted in only a 0.5% difference in reconstructed attenuation coefficient for a gel dosimeter-like scattering background, which provides further evidence that scattered light should have a minimal effect on quantitative imaging of typical gels. When imaging a finger within a very highly scattering medium (2% transmission along 15 cm diameter), this discrepancy increased to 3%. However, this amount of scattering would not likely be encountered in currently available radiochromic gels.

The approach we describe in this study does have some limitations. The device is not as fast as some broad-beam scanners which use CCD detectors to acquire projection images at video frame rates. In this implementation, the movement of the vertical translation stages limits the achievable scan speed. This may become a limitation if gel dosimeters that exhibit high diffusion rates, such as Ferrous-Xylenol Orange gels [51], are to be imaged at high resolutions. Currently in our lab we are using a modified leuco crystal violet (LCV) dosimeter [52] with a diffusion rate low enough that we do not observe changes over the timespan of optical CT scanning. A second limitation is that there appears to be a noise baseline in the reconstructed images that will limit precision when measuring very small attenuation coefficients, as seen in the uniform absorbing phantom results. This should be considered when designing a dosimetry experiment, to ensure that the attenuation change in the gel dosimeter is large enough to overcome this noise level. Noise can be reduced by

reconstructing at a lower resolution (if the dosimetry task allows), or by reconstructing with a regularized iterative CT reconstruction algorithm. Iterative reconstruction may also help with gels with more diffusivity, as it may be possible to achieve the same image quality with fewer projection measurements, which would decrease scan time. The spatial resolution of this scanner is limited by the width of the laser beam within the region of interest that is imaged. Currently, the scanner is configured to have a uniform resolution across the large, 15 cm diameter field of view. The beam size can be decreased to improve spatial resolution, but unless advanced techniques such as depth of field multiplexing [53] are employed, this comes at the expense of the scanner's field of view. However, the current spatial resolution (0.33 mm voxels) should be adequate for most external beam radiation therapy dosimetry applications.

3.6 Conclusion

We have presented a scanning laser optical CT system design with a minimal level of scatter production and acceptance. It achieves excellent accuracy in attenuation measurement while still maintaining acceptable scan speed for 3D dosimetry. The instrument is easily configurable, as it is a single-ray, single-detector, planar scanner where the imaging geometry, sampling density/location, and detector collimation can all be adjusted for a given imaging task. In its current configuration, we image cylindrical volumes up to 15 cm in diameter and 12 cm in height at 0.33 mm resolution in approximately 30 minutes.

The optical scanning experiments reported here simulate a wide range of expected dosimetry problems, from uniformly irradiated gels to small-field dosimetry. The accuracy we have achieved in these phantom experiments gives confidence that this system is ready for clinical dosimetry applications using current radiochromic gel formulations. This is currently the best-performing optical CT scanner in our laboratory, and therefore we will use

it as a reference device when evaluating applications for which other faster or simpler designs (e.g. cone-beam) may be acceptable. Additionally, we will use this scanner to explore novel CT scanning patterns and new dosimeter formulations.

3.7 Appendix: Ray Tracing for Aquarium Design

In-house MATLAB (The MathWorks, Inc., Natick, MA, USA) code was used to generate the profile of the curved aquarium wall. The algorithm starts from the initial position A shown in Figure 3.8. The initial x position is specified based on the desired maximum dosimeter radius. The y -direction distance of a simulated light ray from the optic axis at the source-axis distance of the scanner (i.e. the focal length of the lens-aquarium) is minimized numerically by iterating over different wall angles and calculating ray paths using Snell's law. Once a minimum is found, a linear segment of the wall profile is calculated by stepping forward in y , using the angle to calculate the next x position. This process is repeated, stepping across the field of view, until a complete lens profile is generated. The step size in the y -direction is kept very small (0.01 mm), so that the approximation of constant wall angle over each y -step is appropriate. The angular step size in each minimization step is set to 0.001 radians. Many points ($\approx 20\,000$) are generated along the profile. However only 300 were used when cutting on the CNC machine, which used non-uniform B-spline interpolation (NURBS) between given points.

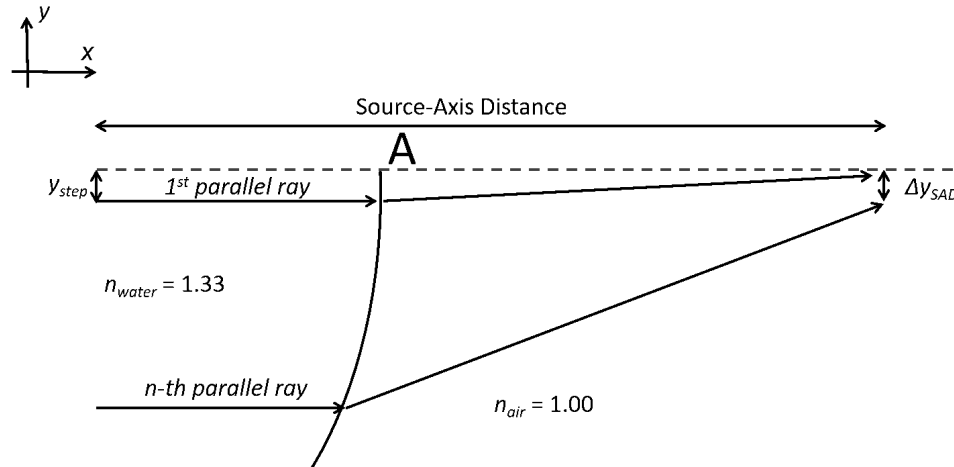


Figure 3.8: Schematic for ray-tracing lens profile generation. The algorithm starts at position **A**, and minimizes Δy_{SAD} for each y_{step} by applying Snell's law of refraction and varying the angle of the aquarium wall interface. The x coordinate of point **A** is set by the user, and the x coordinates of the subsequent minimization steps are calculated by computing a linear segment of the air-water interface profile, with a y step size of 0.01 mm. This generates the profile of the aquarium wall, to create an acylindrical lens aquarium.

3.8 References

1. Baldock, C. *et al.* Polymer gel dosimetry. *Physics in Medicine and Biology* **55**, R1–R63 (Mar. 7, 2010).
2. Oldham, M. Radiochromic 3D Detectors. *Journal of Physics: Conference Series* **573**, 012006 (Jan. 12, 2015).
3. Guo, P., Adamovics, J. & Oldham, M. A practical three-dimensional dosimetry system for radiation therapy. *Medical Physics* **33**, 3962 (2006).
4. Yamamoto, M. *et al.* Stereotactic radiosurgery for patients with multiple brain metastases (JLGK0901): a multi-institutional prospective observational study. *The Lancet Oncology* **15**, 387–395 (Apr. 2014).
5. Mahajan, A. *et al.* Postoperative Stereotactic Radiosurgery Versus Observation for Completely Resected Brain Metastases: Results of a Prospective Randomized Study. *International Journal of Radiation Oncology - Biology - Physics* **96**, S2 (Oct. 1, 2016).
6. Kak, A. C. & Slaney, M. *Principles of Computerized Tomographic Imaging* Google-Books-ID: Z6RpVjb9_lwC. 335 pp. (SIAM, Jan. 2001).
7. Byer, R. L. & Shepp, L. A. Two-dimensional remote air-pollution monitoring via tomography. *Optics letters* **4**, 75–77 (1979).
8. Bennett, K. & Byer, R. L. Optical tomography: experimental verification of noise theory. *Optics letters* **9**, 270–272 (1984).
9. Ishino, Y., Horimoto, K., Kato, T., Ishiguro, S. & Saiki, Y. 3D-CT Measurement of Premixed Flames Using a Multi-directional Quantitative Schlieren Optical System

- (Solo-measurement of Density and Combined-measurement of Density and Light-emission Distributions). *Procedia Engineering* **67**, 303–316 (Jan. 2013).
10. Faris, G. W. & Byer, R. L. Three-dimensional beam-deflection optical tomography of a supersonic jet. *Applied Optics* **27**, 5202–5212 (1988).
 11. Brown, C. S., Burns, D. H., Spelman, F. A. & Nelson, A. C. Computed tomography from optical projections for three-dimensional reconstruction of thick objects. *Applied optics* **31**, 6247–6254 (1992).
 12. Burns, D. H. Optical tomography for three-dimensional spectroscopy. *Applied spectroscopy* **48**, 12A–19A (1994).
 13. Sharpe, J. *et al.* Optical Projection Tomography as a Tool for 3D Microscopy and Gene Expression Studies. *Science* **296**, 541–545 (Apr. 19, 2002).
 14. Meyer, H. *et al.* Scanning laser optical tomography: a highly efficient volumetric imaging technique for mesoscopic specimens in *Proceedings of OSA Biomedical Optics - SPIE* **8797** (2013), 879706–879706–4.
 15. Gore, J. C., Ranade, M., Maryanski, M. J. & Schulz, R. J. Radiation dose distributions in three dimensions from tomographic optical density scanning of polymer gels: I. Development of an optical scanner. *Physics in Medicine and Biology* **41**, 2695 (1996).
 16. Maryanski, M. J., Zastavker, Y. Z. & Gore, J. C. Radiation dose distributions in three dimensions from tomographic optical density scanning of polymer gels: II. Optical properties of the BANG polymer gel. *Physics in Medicine and Biology* **41**, 2705 (1996).
 17. Kelly, R. G., Jordan, K. J. & Battista, J. J. Optical CT reconstruction of 3D dose distributions using the ferrous-benzoic-xyleneol (FBX) gel dosimeter. *Medical Physics* **25**, 1741 (1998).
 18. Wolodzko, J. G., Marsden, C. & Appleby, A. CCD imaging for optical tomography of gel radiation dosimeters. *Medical Physics* **26**, 2508 (1999).
 19. Krstajic, N. & Doran, S. J. Characterization of a parallel-beam CCD optical-CT apparatus for 3D radiation dosimetry. *Physics in Medicine and Biology* **52**, 3693 (July 7, 2007).
 20. Sakhalkar, H. S. & Oldham, M. Fast, high-resolution 3D dosimetry utilizing a novel optical-CT scanner incorporating tertiary telecentric collimation. *Medical Physics* **35**, 101–111 (Jan. 2008).
 21. Thomas, A. & Oldham, M. Fast, large field-of-view, telecentric optical-CT scanning system for 3D radiochromic dosimetry. *Journal of Physics: Conference Series* **250**, 012007 (Nov. 1, 2010).
 22. Cheng, H.-W. *et al.* Development of a novel optical CT employing a laser to create a collimated line-source with a flat-top intensity distribution. *Radiation Measurements* **46**, 1932–1935 (Dec. 2011).
 23. Papadakis, A. E. *et al.* Technical Note: A fast laser-based optical-CT scanner for three-dimensional radiation dosimetry. *Medical Physics* **38**, 830 (2011).
 24. Campbell, W. G., Rudko, D. A., Braam, N. A., Wells, D. M. & Jirasek, A. A prototype fan-beam optical CT scanner for 3D dosimetry. *Medical Physics* **40**, 061712 (June 1, 2013).

25. Bosi, S. G., Brown, S., Sarabipour, S., De Deene, Y. & Baldock, C. Modelling optical scattering artefacts for varying pathlength in a gel dosimeter phantom. *Physics in Medicine and Biology* **54**, 275–283 (Jan. 21, 2009).
26. Olding, T., Holmes, O. & Schreiner, L. J. Cone beam optical computed tomography for gel dosimetry I: scanner characterization. *Physics in Medicine and Biology* **55**, 2819–2840 (May 21, 2010).
27. Granton, P. V., Dekker, K. H., Battista, J. J. & Jordan, K. J. Stray light in cone beam optical computed tomography: I. Measurement and reduction strategies with planar diffuse source. *Physics in Medicine and Biology* **61**, 2893 (2016).
28. Dekker, K. H., Battista, J. J. & Jordan, K. J. Stray light in cone beam optical computed tomography: II. Reduction using a convergent light source. *Physics in Medicine and Biology* **61**, 2910 (2016).
29. Oldham, M., Siewerdsen, J. H., Kumar, S., Wong, J. & Jaffray, D. A. Optical-CT gel-dosimetry I: Basic investigations. *Medical Physics* **30**, 623–634 (Apr. 1, 2003).
30. Van Doorn, T., Bhat, M., Rutten, T. P., Tran, T. & Costanzo, A. A fast, high spatial resolution optical tomographic scanner for measurement of absorption in gel dosimetry. *Australasian Physics & Engineering Sciences in Medicine* **28**, 76–85 (June 2005).
31. Krstajic, N. & Doran, S. J. Fast laser scanning optical-CT apparatus for 3D radiation dosimetry. *Physics in Medicine and Biology* **52**, N257 (June 7, 2007).
32. Xu, Y. & Wu, C.-S. Optical computed tomography utilizing a rotating mirror and Fresnel lenses: operating principles and preliminary results. *Physics in Medicine and Biology* **58**, 479 (Feb. 7, 2013).
33. Jordan, K. J., Turnbull, D. & Battista, J. J. Laser cone beam computed tomography scanner geometry for large volume 3D dosimetry. *Journal of Physics: Conference Series* **444**, 012062 (June 26, 2013).
34. Feldkamp, L. A., Davis, L. C. & Kress, J. W. Practical cone-beam algorithm. *JOSA A* **1**, 612–619 (1984).
35. Miles, D., Yoon, S., Adamovics, J. & Oldham, M. TH-CD-201-05: Characterization of a Novel Light-Collimating Tank Optical-CT System for 3D Dosimetry. *Medical Physics* **43**, 3870–3870 (June 2016).
36. Maryanski, M. J. & Ranade, M. K. *Laser microbeam CT scanning of dosimetry gels in Medical Imaging 2001* (International Society for Optics and Photonics, 2001), 764–774.
37. Ramm, D., Rutten, T. P., Shepherd, J. & Bezak, E. Optical CT scanner for in-air readout of gels for external radiation beam 3D dosimetry. *Physics in Medicine and Biology* **57**, 3853–3868 (June 21, 2012).
38. Knoll, G. F. *Radiation Detection and Measurement* Google-Books-ID: 4vTJ7UDel5IC. 857 pp. (John Wiley & Sons, Aug. 16, 2010).
39. Pologruto, T. A., Sabatini, B. L. & Svoboda, K. ScanImage: Flexible software for operating laser scanning microscopes. *BioMedical Engineering OnLine* **2**, 13 (May 17, 2003).
40. Olding, T. & Schreiner, L. J. Cone-beam optical computed tomography for gel dosimetry II: imaging protocols. *Physics in Medicine and Biology* **56**, 1259 (Mar. 7, 2011).

41. Dekker, K. H., Battista, J. J. & Jordan, K. J. Optical CT imaging of solid radiochromic dosimeters in mismatched refractive index solutions using a scanning laser and large area detector. *Medical Physics* **43**, 4585–4597 (Aug. 1, 2016).
42. Samei, E., Flynn, M. J. & Reimann, D. A. A method for measuring the presampled MTF of digital radiographic systems using an edge test device. *Medical Physics* **25**, 102–113 (Jan. 1, 1998).
43. Friedman, S. N., Fung, G. S. K., Siewerdsen, J. H. & Tsui, B. M. W. A simple approach to measure computed tomography (CT) modulation transfer function (MTF) and noise-power spectrum (NPS) using the American College of Radiology (ACR) accreditation phantom. *Medical Physics* **40**, 051907 (May 1, 2013).
44. Jordan, K. & Battista, J. A stable black-refractive-index-matching liquid for optical CT scanning of hydrogels. *Journal of Physics: Conference Series* **164**, 012045 (May 1, 2009).
45. Dekker, K. H., Battista, J. J. & Jordan, K. J. Stray light in cone beam optical computed tomography: II. Reduction using a convergent light source. *Physics in Medicine and Biology* **61**, 2910 (2016).
46. Das, I. J., Ding, G. X. & Ahnesjo, A. Small fields: Nonequilibrium radiation dosimetry. *Medical Physics* **35**, 206–215 (Jan. 1, 2008).
47. Sharma, S. Challenges of small photon field dosimetry are still challenging. *Journal of Medical Physics* **39**, 131 (2014).
48. Babic, S., McNiven, A., Battista, J. & Jordan, K. Three-dimensional dosimetry of small megavoltage radiation fields using radiochromic gels and optical CT scanning. *Physics in Medicine and Biology* **54**, 2463–2481 (Apr. 21, 2009).
49. Clift, C. *et al.* Toward acquiring comprehensive radiosurgery field commissioning data using the PRESAGE/ optical-CT 3D dosimetry system. *Physics in Medicine and Biology* **55**, 1279–1293 (Mar. 7, 2010).
50. Shih, T.-Y. *et al.* Small-Field Measurements of 3D Polymer Gel Dosimeters through Optical Computed Tomography. *PLOS ONE* **11**, e0151300 (Mar. 14, 2016).
51. Babic, S., Battista, J. & Jordan, K. Three-Dimensional Dose Verification for Intensity-Modulated Radiation Therapy in the Radiological Physics Centre Head-and-Neck Phantom Using Optical Computed Tomography Scans of Ferrous Xylenol-Orange Gel Dosimeters. *International Journal of Radiation Oncology - Biology - Physics* **70**, 1281–1291 (Mar. 15, 2008).
52. Babic, S., Battista, J. & Jordan, K. Radiochromic leuco dye micelle hydrogels: II. Low diffusion rate leuco crystal violet gel. *Physics in Medicine and Biology* **54**, 6791–6808 (Nov. 21, 2009).
53. Maurer, C., Khan, S., Fassl, S., Bernet, S. & Ritsch-Marte, M. Depth of field multiplexing in microscopy. *Optics Express* **18**, 3023–3034 (Feb. 1, 2010).

Chapter 4

Iterative Reconstruction in Optical CT: Noise and artifact reduction in gel dosimetry

This chapter is adapted from a manuscript published as “Technical Note: Evaluation of an iterative reconstruction algorithm for optical CT radiation dosimetry” by Kurtis Hendrik Dekker, Jerry J. Battista and Kevin J. Jordan, *Medical Physics*, 44, 6678-6689¹. Permission to reproduce this article was granted by John Wiley and Sons, Inc., and is provided in Appendix B.

4.1 Introduction

4.1.1 Optical CT dosimetry

Optical computed tomography (CT) scanning of radiochromic gel dosimeters is a method for true 3D radiation dosimetry that can provide large-volume, fine-resolution measurement using a single radiation exposure. Various optical CT scanner designs exist, ranging from scanning-laser pencil beam systems [1–4] to CCD-based broad-beam systems

¹© 2017 American Association of Physicists in Medicine. Reproduced with permission.

[5–9]. Optical CT images are subject to similar artifacts as x-ray CT images, in terms of scatter-related attenuation suppression, rings, and streaking between highly attenuating structures. Additionally, optical CT is sensitive to the effects of refraction. As scatter production and detection is reduced in optical CT, systems become more sensitive to the effects of optical imperfections in dosimeters and dosimeter vessels [10], which deflect primary image-forming rays away from their intended path. These imperfections create considerable streaking artifacts when reconstructing datasets using filtered backprojection, which is currently the most common reconstruction algorithm used in gel dosimetry.

4.1.2 Effects of image noise and artifacts on dosimetric analysis

Measurement noise and uncorrected image artifacts have a detrimental effect on clinical dosimetry. For example, noise perturbs the results of gamma analysis [11], a standard clinical tool for comparing 2D or 3D dose distributions. Low and Dempsey [12] showed that adding noise to an evaluated dose distribution results in fewer pixels failing the gamma comparison to the reference distribution (Gamma values > 1.0 for given dose difference and distance to agreement thresholds) in steep dose regions compared to a no-noise case, as noise can result in locating points with spuriously agreeing dose values within the distance threshold. This effect was also reported by Huang et al. [13], in comparisons between film dosimetry and a treatment planning system. In an extreme example, they found that noise resulted in a plan that passed the overall gamma analysis QA threshold ($\geq 95\%$ of pixels passing) when it should have failed. These authors also found that plans which had a lower initial pass rate (i.e. worse agreement between measured and computed dose) had a greater artificial increase in pass rate upon introducing noise than those which had good original agreement.

The reason that noise in the evaluated dose distribution can inflate the pass rate is that at every point along the reference distribution, the entire evaluated distribution is used

to compute the local value of Gamma. Therefore, there is an asymmetry in the Gamma calculation; the result depends on the selection of reference and evaluated distributions. In a region where the two distributions truly overlap, noise that pushes one pixel in the evaluated distribution outside of the dose tolerance will not result in a local Gamma failure, as the calculation will simply locate a neighbouring point, as long as the resolution of the dose distributions is smaller than the chosen distance to agreement threshold. On the other hand, in regions where the true distributions do not agree, noise that pushes one pixel of the evaluated distribution into the dose tolerance will result in several nearby points in the reference distribution locating it as a point satisfying the criteria, resulting in an artificial increase in overall pass rate.

The effects of image artifacts on dosimetric analyses are more complicated. Image artifacts may mimic the effects of noise in some cases. For example, taking a profile across streak artifacts in CT will result in a “noisy” line. However, artifacts, such as the streaking shown in Figure 3.1, are spatially structured. The impact of these artifacts on tests such as the Gamma evaluation are hard to predict; they may lead to artificial inflation or suppression of passing rates depending on the dose distribution and true dosimetric / positional errors. Therefore, removing or reducing artifacts in imaging-based dosimeters, such as radiochromic film or gels, is important.

Overall, reducing the magnitude of image noise and artifacts while preserving the underlying shape of dosimetric data (i.e. preserving spatial resolution), will improve the validity of dosimetric analyses such as the gamma evaluation. In the context of optical CT, this improvement takes the form of reducing noise and artifacts in reconstructions. This can be accomplished through improvements in experimental apparatus and technique; however, it is virtually inevitable that there will be optical features associated with gel dosimeters and vessels that will create artifacts in images, degrading the quality of dosimetric tests. Therefore, in this study we examine the use of iterative CT reconstruction techniques to provide

artifact and noise suppression.

4.1.3 Iterative CT reconstruction

In general, most optical CT dosimetry has been performed using images reconstructed using the filtered backprojection (FBP) technique [14]. Iterative algorithms have been studied for reconstruction in the case of incomplete projection data due to refraction [15–17]. Additionally, noise reduction benefits have recently been demonstrated in phantoms [18] and in polymer gel dosimeters [19]. However, one of the challenges associated with iterative reconstruction algorithms is that they often contain one or more empirically determined constants that control either the weighting of correction terms made at each iteration, or the aggressiveness of the denoising performed. If these constants are set inappropriately, either the noise/artifact reduction will be sub-optimal, or there will be unacceptable losses in the spatial resolution of the reconstruction, causing blurring of edges. A suboptimal setting of these user-defined parameters may also lead to systematic or local inaccuracy in reconstructed attenuation coefficients.

The purpose of this study was to examine the utility of an iterative CT reconstruction algorithm for gel dosimetry using radiochromic gel dosimeters. The reconstruction method used was an ordered-subsets convex algorithm with total variation minimization regularization (OSC-TV), which was described by Matenine *et al.* [20]. This algorithm was chosen for its noise reduction and edge preserving capabilities as well as ease of implementation. Matenine *et al.* previously applied the algorithm to cone-beam optical CT scanning [21], but used projection data obtained using the DeskCAT scanner (Modus Medical Devices, Inc.). This is a dedicated educational system, which suffers from both stray light effects [22, 23] and refractive index mismatch between phantoms and surrounding media. Additionally, these authors did not examine the effects of varying the algorithm parameters on the value of reconstructed attenuation coefficients in different-sized image

structures. Therefore, further examination of the algorithm’s performance in gel dosimetry is required. In our experiment, we used OSC-TV to reconstruct images of three different objects scanned with an in-house scanning laser optical CT scanner: a large, uniform absorber (phantom A), a small absorbing finger phantom (phantom B), and a gel dosimeter irradiated with 4 small-field photon beams (phantom C). We performed reconstructions with a variety of total-variation regularization constants. Images were assessed in terms of contrast vs. artifact and noise, attenuation coefficient accuracy, and edge sharpness. From these experiments, we establish that OSC-TV greatly reduces image artifacts and noise, and therefore should improve the validity of dosimetric analysis.

4.2 Methods

4.2.1 Optical CT scanner

A scanning-laser, planar scanner was used to acquire the datasets used in this note. The system, described in Chapter 3 [24], performs full 3D parallel-beam CT imaging of large, 15 cm diameter by 14 cm height cylindrical dosimeters within 40-minute scan-times, while exhibiting very low stray light acceptance and thus excellent accuracy.

4.2.2 Optical CT datasets

Three experimental datasets were used in this reconstruction algorithm study. All datasets used the same 15 cm diameter, 14 cm height vessel. Each dataset contained both a “pre” and “post” scan of 1024 projections spanning 360° rotation, acquired with nominal pixel size of 0.22 mm (horizontal) by 0.25 mm (vertical). Since the MTF10% resolution of the optical CT scanner is roughly 0.33 mm, limited by the width of the scanning laser beam, datasets were downsampled to 0.33 mm resolution prior to reconstruction. Additionally, the mean

value in a region of interest outside the dosimeter vessel (in the water-filled aquarium) was measured in all projections and normalized to a constant, in order to correct for variation in the laser intensity. These scanning parameters represent a standard imaging protocol that is used for optical CT dosimetry in our lab. An axial slice of each dataset, reconstructed using filtered backprojection with the Hamming filter, is shown in Figure 4.1.

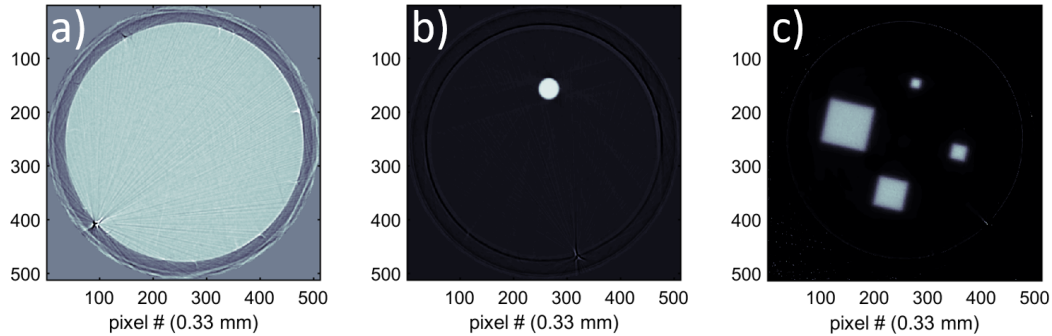


Figure 4.1: Axial slices of phantoms used in the study. Reconstructions shown are performed with Hamming-filtered FBP. a) Phantom A: uniform 15 cm diameter liquid absorber (window/level = 0.3 / 0.0 cm^{-1}). b) Phantom B: finger phantom (window/level = 2.0 / 0.0 cm^{-1}). c) Phantom C: small radiation fields (window/level = 1.2 / 0.0 cm^{-1}).

4.2.2.1 Phantom datasets

The first dataset (Phantom A) was a scan of a uniform absorbing liquid, made from carbon black nanoparticles dispersed with a surfactant (Triton-X 100) in a 5% propylene glycol solution. The second scanned object (Phantom B) was a small finger phantom (PFA heat shrink tubing, 13.5 mm outer diameter, 12.5 mm inner diameter, Newark, SKU: 92N6000) filled with an absorbing Nigrosin-water solution, scanned within an Intralipid-water solution that was mixed to have a scatter attenuation coefficient similar to that of typical gel dosimeters ($\mu_{scatter} \approx 0.05 \text{ cm}^{-1}$). This phantom presents a difficult optical CT imaging task, measuring the absorption of a small object within a scattering background, and simulates a small-field radiation dosimetry experiment. Details of the solution phantom experiments are found in a separate publication [24]. Together, these phantoms represent the extreme

imaging cases in optical CT, from the easiest problem of a uniform object to one of the most challenging problems, a small absorber located within a scattering medium. Similarly, they span the range of clinically relevant gel dosimetry problems, from a uniform dose distribution to small field commissioning.

4.2.2.2 Gel dataset

The final dataset (Phantom C) was the result of a small-field radiation dosimetry experiment. Small-field dosimetry via optical CT has previously been reported using radiochromic and polymer gels, as well as radiochromic plastics (references [25–27] and citations therein). In this experiment, we used a leuco crystal violet (LCV) gel dosimeter [28] which uses sodium dodecyl sulfate (SDS) as a surfactant to prevent diffusion. The details of this modified LCV dosimeter are reported elsewhere [29]. This gel dosimeter was already quite dark prior to irradiation as it had been previously irradiated, melted, and re-cast. The initial transmission along the central axis of the gel was approximately 1% relative to water. Therefore, this gel serves as an excellent stress-test of the scanner and reconstruction algorithm.

The gel was irradiated from the top (gel surface open to air, SSD = 90 cm) with 4 small fields, defined by the jaws of a Varian 21X linear accelerator. Nominal field sizes at SAD = 100 cm were 3.0×3.0 , 2.0×2.0 , 1.0×1.0 , and 0.6×0.6 cm². The dose at 10 cm depth in each beam was approximately 20 Gy.

4.2.3 Image reconstruction

4.2.3.1 Filtered backprojection (FBP)

Standard filtered backprojection reconstruction was performed using both a ramp filter and a Hamming filter, for comparison to the iterative algorithm. The Hamming filter results

in reduced noise, but also a loss of spatial resolution, compared to the ramp filter. Reconstructed attenuation coefficients from the FBP algorithm were considered as “true” (when averaging over regions of interest) for this study. We have previously demonstrated agreement within about 1-2 % between FBP and independent measurements for the solution phantoms [24]. For the gel dosimeter, “true” values are less available, as small field dosimetry is difficult to verify using point detectors. However, FBP is the current standard reconstruction algorithm used for optical CT dosimetry measurements.

4.2.3.2 Ordered subsets convex algorithm with total variation minimization (OSC-TV)

The ordered subsets convex iterative reconstruction algorithm, with total variation minimization [20], was implemented. Both ordered subsets and TV-minimization have been well described in literature [20, 30–36]. A thorough description of OSC-TV has been documented [20], so in this section we briefly summarized the approach and re-state the mathematical formulation. Our specific contribution is the exploration of the effects of the regularization parameter on the quantitative accuracy of gel dosimetry.

The algorithm can be broken into two distinct steps at each iteration: the Ordered Subsets Convex (OSC) reconstruction step, and the total variation (TV) minimization step.

First, the OSC step can be described by the equation:

$$\mu_{s+1}^n = \mu_s^n + \mu_s^n \frac{\sum_{i \in i_s} l_{ij} [y_i^s - Y_i]}{\sum_{i \in i_s} l_{ij} t_i^s y_i^s} \quad (4.1)$$

where μ_s^n represents the estimate of the image after processing the ‘*sth*’ subset of the ‘*nth*’ overall iteration, l_{ij} represents the path lengths for each of the i rays through each of the j voxels in the image, $t_i = \sum_j l_{ij} \mu_j$ is the line integral along each ray, and $y_i = d_i e^{-t_i}$ represents the estimate of detected intensities for each ray. In optical CT, a pre- and post-irradiation

scan are acquired, and it is the *change* in attenuation that is reconstructed. Therefore, in this case, d_i represents the pre-scan projection data, and Y_i the post-scan projection data.

The second component to the reconstruction is the regularization based on total variation minimization (TV-minimization), which is performed by a gradient descent method:

$$\mu_{i,j,k}^{q+1} = \mu_{i,j,k}^q - cd_A \frac{v_{i,j,k}^q}{\sqrt{\sum_{i,j,k} v_{i,j,k}^2}} \quad (4.2)$$

where q is the TV-minimization iteration index, c is a user-specified parameter, $v_{i,j,k}$ is the local value of the TV gradient [37, 38], and d_A is the norm of the difference between images at subsequent steps of the algorithm:

$$d_A = \sqrt{\sum_{i,j,k} (\mu_{i,j,k}^n - \mu_{i,j,k}^{n-1})^2} \quad (4.3)$$

The use of this quantity causes the image to be regularized proportionally to the magnitude of changes made by the latest OSC step, which helps to prevent over-regularization in later iterations of the overall algorithm. In our case, we used 20 iterations of the gradient descent step at each iteration of the overall algorithm. The parameter investigated in this study was the value of the empirical constant c , which affects the “aggressiveness” of the regularization. If c is set too high, then edges of objects can be blurred out and fine structure can be lost in the image. This can also suppress the central attenuation coefficient within a small object. On the other hand, if c is set very low, then the reconstructed image will not achieve the maximum noise reduction that was possible without sacrificing spatial integrity. The purpose of our experiments was to study the effects of this parameter on reconstructions, to achieve noise and artifact reduction without perturbing accuracy.

4.2.4 Image reconstruction details

Datasets were reconstructed with filtered backprojection using both ramp and Hamming filters, as well as OSC-TV with varying values for the regularization constant ($c = 0.05, 0.25, 0.35, 0.5, 0.75, 0.85, 1.0, 1.25, 1.5, 2.0$). For all iterative reconstructions, 10 iterations were used, with 64, 61, 57, 53, 49, 44, 39, 32, 24 and finally 4 subsets, respectively, following the subset number reduction suggested by Matenine *et al.* [20]. All reconstructions were performed using 0.33 mm isotropic voxels, and no pre-processing of input data or post-processing of output data was performed after the reconstruction. Image reconstruction was done using GPU-accelerated forward and back-projection operators written in the CUDA programming environment and called externally from MATLAB as mex files. In this case, a ray-driven forward projection was implemented using 3D texture memory to store the reconstructed image estimate, in order to take advantage of texture-based 3D linear interpolation to approximate Siddon's method [39]. Backprojection was implemented in a voxel-driven fashion using 2D texture memory on the GPU to store projections and perform bilinear interpolation [40]. It should be noted that this projector/backprojector pair is unmatched, which has been shown to sometimes be beneficial in reconstructions in terms of ring artifact reduction [40–42]. The gradient descent algorithm for total variation minimization was also performed on the GPU using a CUDA *mex* file.

A PC equipped with 32GB of RAM, an Intel Core i7-2600 quad-core CPU (Intel Corporation, Santa Clara, CA, USA), and an NVIDIA GTX 780 video card (NVIDIA Corporation, Santa Clara, CA, USA) with 3GB of video RAM was used for reconstruction. Both forward and back-projection times for a $512 \times 512 \times 424$ reconstruction, from 1024 projections of size 512×424 , were under 10 seconds, including data transfer to and from the GPU. The time required for the total variation minimization was approximately 2 seconds for a $512 \times 512 \times 424$ volume. Overall, including data loading (from a hard drive) and filtering, FBP reconstruction took approximately 1 minute. In this study, data transfers were not mini-

mized for the iterative reconstruction; the entire reconstruction volume was transferred to and from the GPU for every subset iteration of OSC-TV, which is not optimal. As a result, OSC-TV reconstruction time was approximately 20 minutes for 10 iterations. While maximizing the speed of our reconstruction was not the goal of this study, in the future we will improve speed by minimizing the number of GPU data transfers required.

4.2.4.1 OSC-TV iteration stopping conditions

Preliminary tests with OSC-TV for gel dosimetry images showed that reconstructed images changed very little after 10 iterations. Therefore, in the first part of this study we set the number of iterations to 10 and varied the value of the regularization constant c . As we describe in Section 4.3.3.3, we found that the mean attenuation value within very small structures diverges from the mean value reported by filtered backprojection at larger values of c , indicating an over-aggressive denoising. Because the value of the regularization constant impacts the convergence of the algorithm, we performed a second set of reconstructions for our gel dosimetry dataset, where we allowed the algorithm to continue iterating until either 1) the mean value measured within a region of interest defined within the smallest field agreed (within 0.5%) with that measured in the ramp-filtered FBP reconstruction, or 2) 50 iterations had been performed. For these reconstructions, subset number reduction was performed as before for the first 10 iterations, but any iterations beyond the 10th were performed using only 1 subset. The purpose of this second set of reconstructions was to determine whether the effect of improperly choosing the regularization constant could be counteracted by increasing the number of iterations.

4.2.5 Image analysis

4.2.5.1 Mean and standard deviation

The uniform absorbing phantom was analyzed simply by measuring the mean and standard deviation of the attenuation coefficient within a $10 \times 10 \times 1 \text{ mm}^3$ region of interest located at the central axial plane, which provided initial insight into the noise-reduction properties of the OSC-TV algorithm.

4.2.5.2 Contrast to artifact + noise ratio (CANR)

For the finger phantom (phantom B) and the small field gel dosimetry dataset (phantom C), we computed the ratio of the image contrast to the combined influence of image artifacts and noise. This contrast to artifact + noise ratio (CANR) was computed for each reconstruction by measuring attenuation coefficients (in ROIs) within the high attenuation regions and in the surrounding background region. CANR was calculated using the following definition, which incorporates noise in both the background and the object regions of interest:

$$\text{CANR} = \frac{|\bar{\mu}_{\text{ROI}} - \bar{\mu}_{\text{background}}|}{\sqrt{\sigma_{\text{ROI}}^2 + \sigma_{\text{background}}^2}} \quad (4.4)$$

where $\bar{\mu}_{\text{ROI}}, \sigma_{\text{ROI}}^2$ are the mean and variance of the attenuation coefficient within the finger phantom or small field, and $\bar{\mu}_{\text{background}}, \sigma_{\text{background}}^2$ are those in the background region.

4.2.5.3 Gradient Preservation

To be useful, the reconstruction algorithm must not result in a loss of spatial information recorded in the gel. Regions of steep gradients in the image must not be “washed out”

by the image regularization step of the reconstruction method. To evaluate this, we first measured the profiles across the finger phantom (sharp gradient) in each reconstruction. The points at which a profile crossed through 95% and 5% of its maximum value were measured, and the distance between them was calculated (the “95-5% distance”). This provides a quantification of the “sharpness” of the edge in the reconstruction. For the small field dosimetry dataset, which has fields with shallower gradients, the 80-20% distances were computed. Note that we are not performing a spatial resolution test here, as we do not have a “knife” edge to generate an edge response function. Rather, we are performing this analysis to demonstrate that the use of OSC-TV in place of FBP does not alter the shape of gradients.

4.3 Results and Discussion

4.3.1 Uniform solution phantom (Phantom A)

Figure 4.2a shows central reconstruction slices of the uniform absorbing phantom obtained by filtered backprojection with a Hamming filter (left) and OSC-TV with $c = 0.5$ (right). A slice which was affected by streak artifacts due to a vessel wall imperfection was purposely chosen to highlight the artifact-reduction capability of the iterative reconstruction technique. Figure 4.2b shows line profiles through the same slice in all reconstructions, demonstrating that the OSC-TV reconstructions are considerably smoother than those obtained through FBP. The mean and standard deviation of the attenuation coefficient, measured within a $10 \times 10 \times 1 \text{ mm}^3$ ROI located at the center of the vessel, are plotted in Figure 4.2c. For OSC-TV with regularization constants of $c \geq 0.25$, the standard deviation is reduced by a factor of approximately 10 compared to FBP-Hamming, while the mean value remained constant for all reconstructions. This result demonstrates the strength of the iterative reconstruction algorithm, as it can almost entirely remove streaking artifacts asso-

ciated with imperfections in the vessel walls (e.g. vessel seams, scratches), which results in less “noisy” profiles and images. This is a key result for optical CT dosimetry, as it has been a long-standing challenge to manufacture a dosimeter vessel that performs well both optically (refractive index, imperfections) and dosimetrically (thin walls, water-like x-ray attenuation, relatively impermeable to oxygen). Furthermore, the impact of vessel imperfections, in terms of streak artifacts, increases as stray light is removed from the system [10].

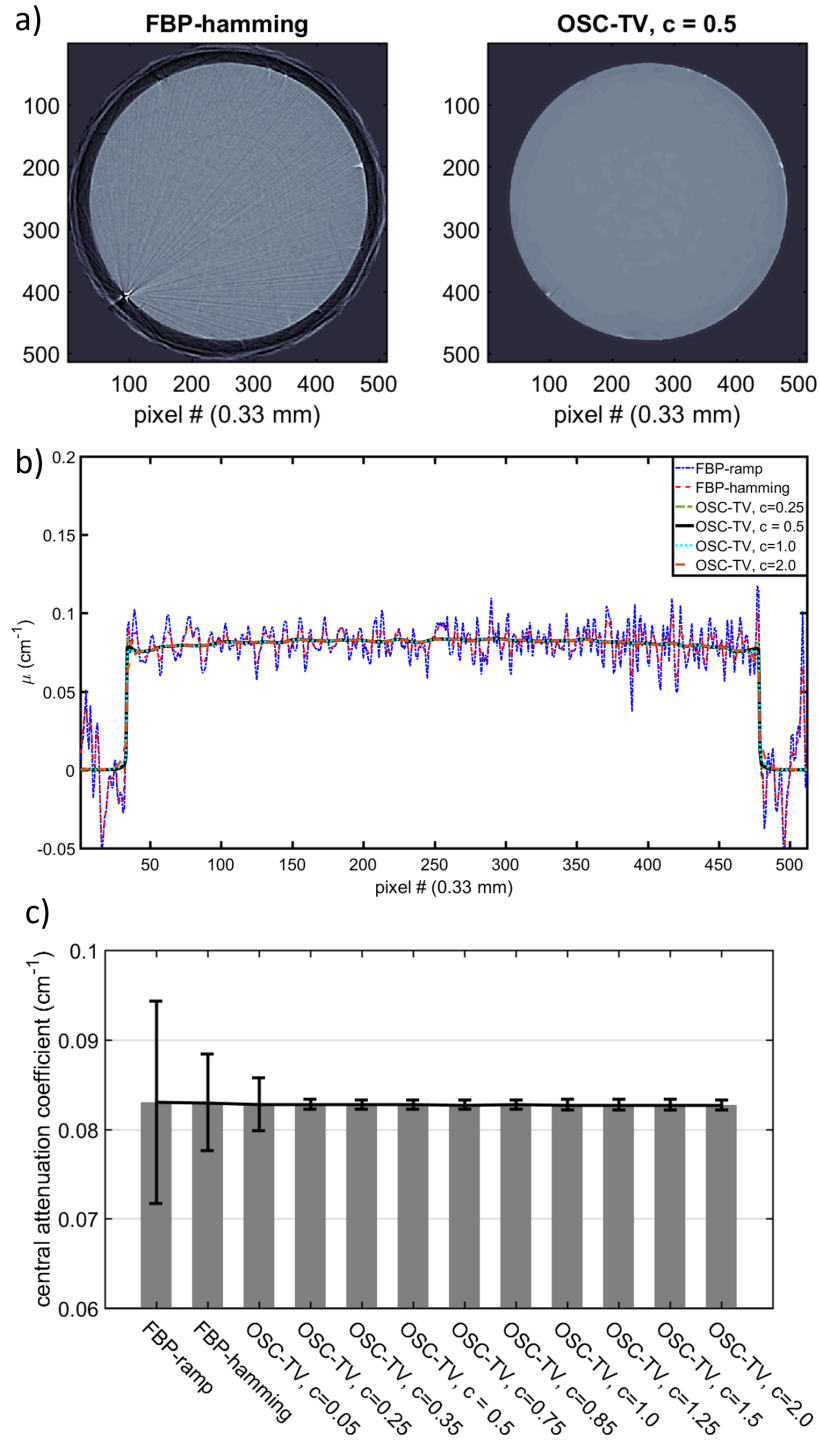


Figure 4.2: Results from the uniform absorbing solution phantom. a) reconstruction slices (window = 0.25, level = 0.125 cm^{-1}) from FBP with Hamming filter (left) and OSC-TV with $c = 0.5$ (right), showing the reduction in streak artifacts associated with vessel imperfections. b) profiles across reconstruction slices, showing the reduction in noise. For visibility, only a subset of profiles are plotted. Almost all OSC-TV profiles overlap throughout the center of the profile. c) mean and standard deviation measured within a $10 \times 10 \times 1 \text{ mm}^3$ region of interest in each reconstruction.

4.3.2 Finger Phantom (Phantom B)

4.3.2.1 Contrast to artifact + noise ratio

For this phantom, contrast to artifact + noise ratios were computed using a $5 \times 5 \times 1 \text{ mm}^3$ region of interest within the finger, and a $10 \times 10 \times 1 \text{ mm}^3$ region in the background region. CANR values are shown in the graph in Figure 4.3. The mean value varies by less than 0.5 % between FBP and OSC-TV reconstructions with $c < 2.0$, while the standard deviation is fairly constant for $0.25 \leq c \leq 1.0$. The OSC-TV algorithm achieves approximately 3-4 \times higher CANR than FBP for these regularization constants.

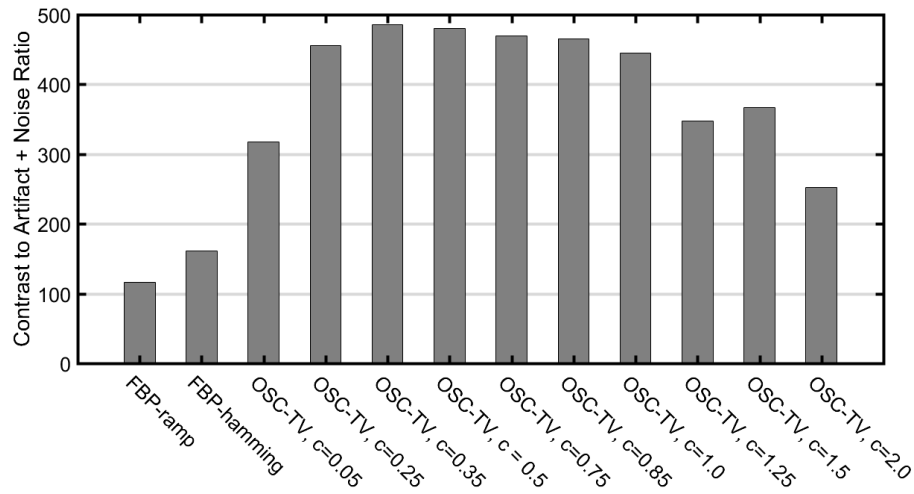


Figure 4.3: Contrast to artifact + noise ratios for reconstructions of the finger phantom (Phantom B).

4.3.2.2 Gradient sharpness

Figure 4.4a shows single profiles through the reconstructions of Phantom B. The same profiles are plotted as differences from the $c = 0.5$ reconstruction in Figure 4.4b, to highlight any differences between profiles. In most dosimetry applications, taking the average of multiple profiles would still provide sufficient spatial resolution. However, plotting single profiles accentuates the noise reduction achieved by the iterative reconstruction algorithm,

especially for the gel dosimetry dataset.

Qualitatively, OSC-TV provides a sharper edge than FBP with either ramp or Hamming filter for all regularization constants $c < 2.0$. The gradient sharpness was quantified by measuring the 95-5 distance (figure not shown). On average, OSC-TV with $c < 2.0$ resulted in a 25-33% reduction in 95-5 distance compared to the Hamming filtered FBP. Within the range of $0.25 < c < 1.75$, the 95-5 distance measured on interpolated edge profiles varied by less than 0.1 mm, which is smaller than the voxel size of the reconstruction and therefore acceptable.

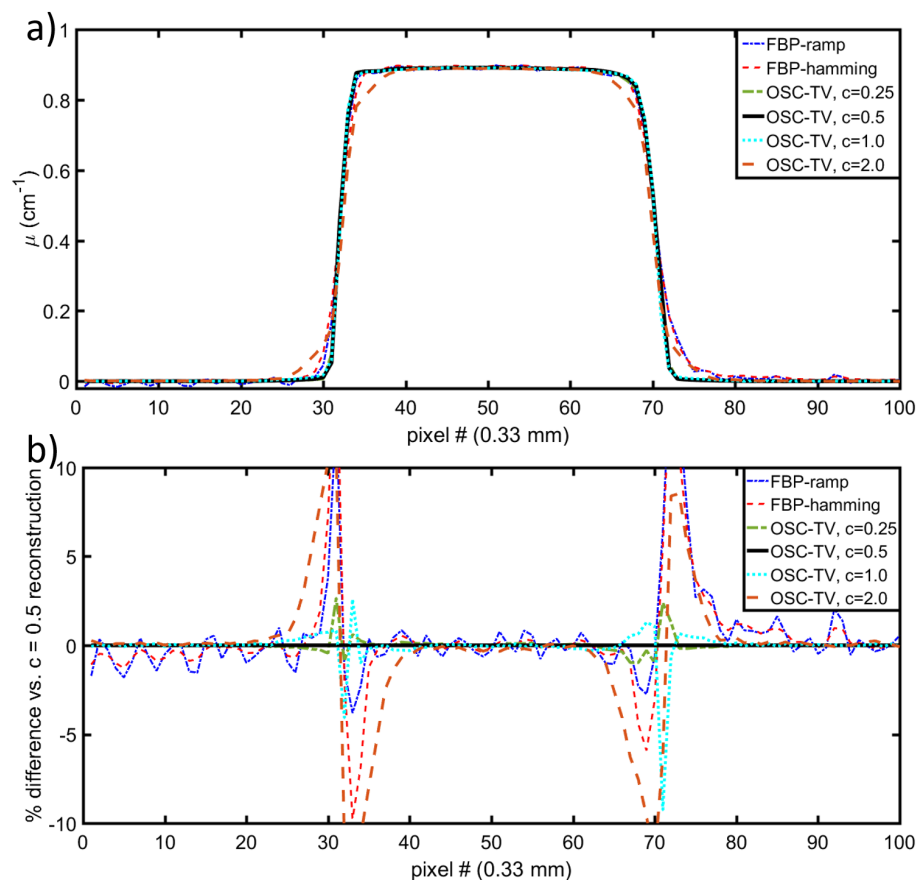


Figure 4.4: Central profiles across the finger phantom (phantom B) reconstructions. For visibility, only a subset of reconstructions are plotted. OSC-TV reconstructions with $c < 2.0$ show almost perfect overlap. b) profiles plotted as % differences from the $c = 0.5$ OSC-TV reconstruction.

The results from Phantom B show that a $3\times$ increase in contrast to noise ratio can be

achieved without a loss of sharpness in the gradient, using OSC-TV reconstruction with a regularization constant between 0.25 and 1.75. This result is encouraging, as the gradient in the phantom itself should be sharper than any encountered in external photon-beam therapy.

4.3.3 Gel dosimeter with small fields (Phantom C)

4.3.3.1 Contrast to artifact + noise ratio

Figure 4.5 summarizes the CANR values measured for each small field. The mean attenuation coefficients inside the field ROI in these slices was approximately 0.4 cm^{-1} . The background region of interest used was $10 \times 10 \times 1 \text{ mm}^3$, located away from the radiation fields, while the ROIs used to measure the signal within the field centers were $7.26 \times 7.26 \times 1 \text{ mm}^3$, $4.95 \times 4.95 \times 1 \text{ mm}^3$, $2.31 \times 2.31 \times 1 \text{ mm}^3$ and $1 \times 1 \times 1 \text{ mm}^3$ for the 3.0×3.0 , 2.0×2.0 , 1.0×1.0 and $0.6 \times 0.6 \text{ cm}$ fields, respectively.

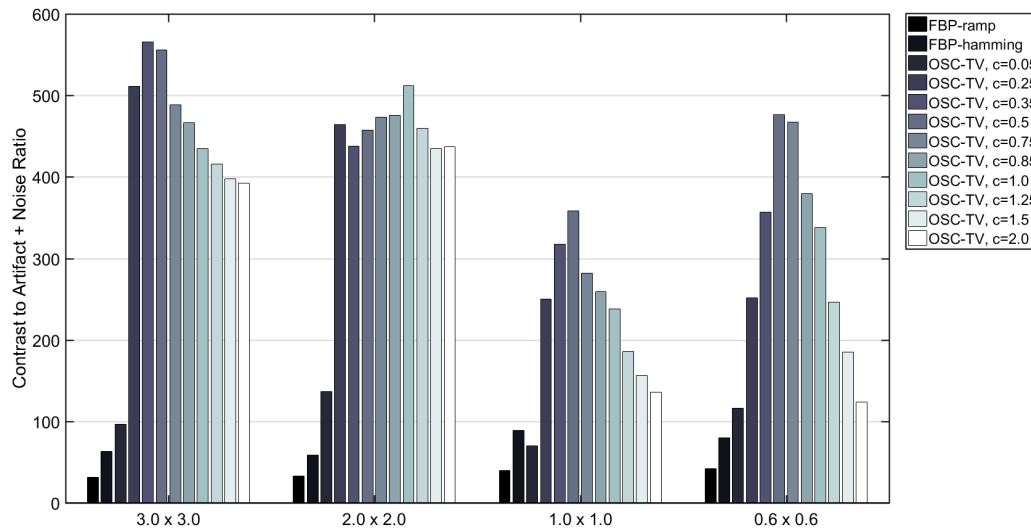


Figure 4.5: Contrast to artifact + noise ratios for the small-field gel dosimetry reconstructions.

The plots in Figure 4.5 show that the OSC-TV algorithm can provide CANR values 4-5× greater than those obtained with FBP. Regularization constant values of $0.35 \leq c \leq 0.85$ result in similar CANR values, approximately 4× higher than those obtained with Hamming-

filtered FBP. Examining the component terms of Equation 4.4 revealed that the standard deviation in the background region was most responsible for this apparent maximum in the CANR results. The background standard deviation appears to pass through a minimum value as a function of regularization constant. This analysis was performed in a slice corresponding to a depth approximately 1.5 cm below the gel surface (roughly d_{max} for the 6MV beam). Therefore, per Equation 4.4 the CANR measured here should be near its maximum. By calculating the value as a function of depth (figure not shown), it was confirmed that the measured CANR varies linearly with the mean central value in the field.

4.3.3.2 Gradient sharpness

Figure 4.6a shows single line profiles across each field size in the different reconstructions. To highlight discrepancies between profiles, differences from the $c = 0.5$ reconstruction are plotted in Figure 4.6b. Again, the OSC-TV reconstructions appear smoother than those formed via FBP. Qualitatively, the gradients appear quite similar in all reconstructions; there does not appear to be a loss of sharpness or spatial information due to regularization. This is quantified by 80-20 distance measurements for each field size (figure not shown). For $c \leq 0.5$, the difference in 80-20 distance between OSC-TV and FBP-ramp, measured from the *interpolated* profile shape, was less than 0.1 mm, which is smaller than the voxel size of the reconstruction.

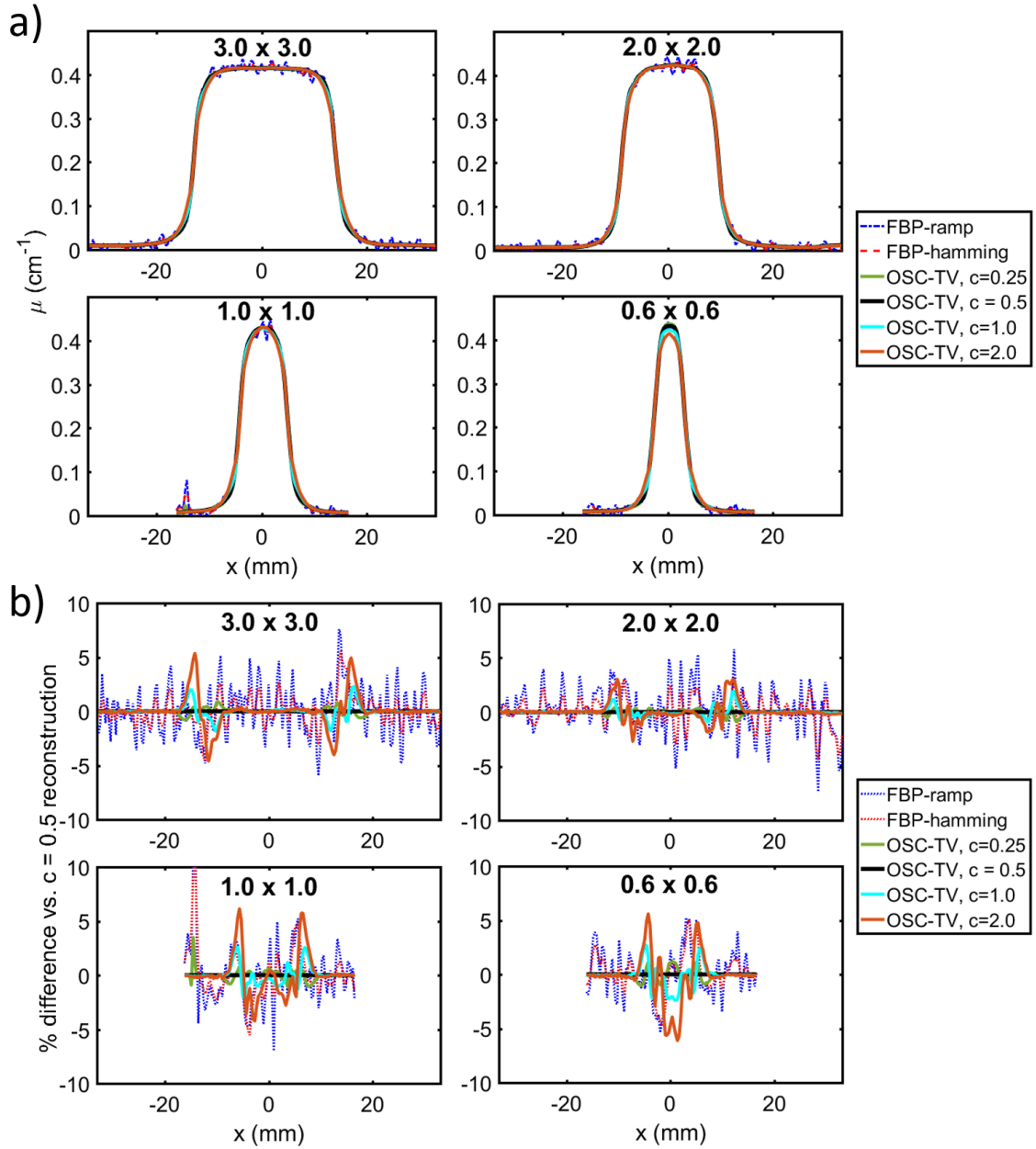


Figure 4.6: a) single line profiles through the 4 field sizes in each reconstruction. For visibility, only a subset of profiles are plotted. b) profiles plotted as % differences from the $c = 0.5$ reconstruction.

4.3.3.3 Field central attenuation coefficient value

Figure 4.7 shows the mean central value within each field (normalized to that measured in the FBP-ramp reconstruction for ease of comparison). The mean value remains unchanged for all regularization constants for the 3.0×3.0 and 2.0×2.0 cm² fields, however the 1.0×1.0 and 0.6×0.6 cm² fields exhibit a gradual decrease in mean value as the regularization aggressiveness is increased. The effect is size-dependent, as its magnitude is larger for the smaller field. We also found that allowing many more iterations of the reconstruction algorithm (up to 50) could not correct for this effect; reconstructions appeared to reach a point of convergence where subsequent iterations imparted negligible changes to the image. This result indicates that the OSC-TV reconstruction should be used carefully if a dose distribution containing features smaller than the 2.0×2.0 cm² field size (in a 15 cm diameter dosimeter), such as a small-field commissioning measurement, is to be imaged.

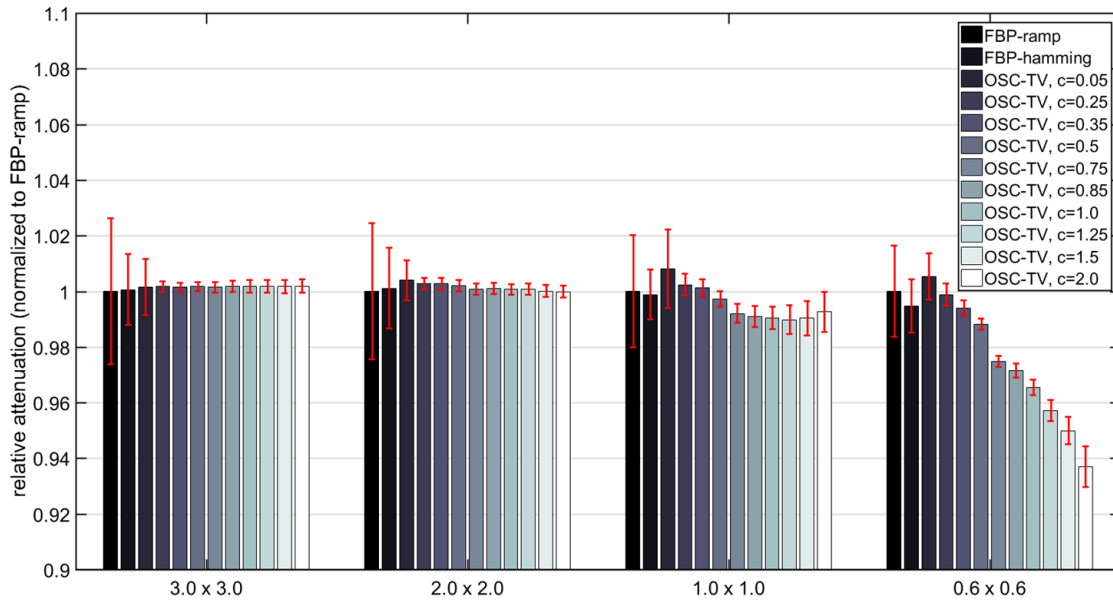


Figure 4.7: Relative mean central attenuation coefficient values for small-field reconstructions (normalized to the FBP-ramp reconstruction).

4.3.4 Investigation of mean central value drop-off

To investigate the cause of the decrease in mean central value as a function of increasing regularization constant in the smallest field ($0.6 \times 0.6 \text{ cm}^2$), reconstruction experiments were performed using a digital phantom. The phantom was a volume of $512 \times 512 \times 424$ voxels, and contained a single simulated small field. The field had a full-width at half maximum (FWHM) of 18 pixels, and was either a box function or a Gaussian function in profile with a maximum attenuation coefficient of $0.0132 \text{ pixel}^{-1}$ (equivalent to 0.4 cm^{-1} at a pixel size of 0.33 mm). 1024 projections were simulated, and zero-mean Gaussian noise with standard deviations of 0% (noise free) to 5% of the maximum intensity value was added to projection data. FBP and OSC-TV reconstructions were performed using the same parameters used to reconstruct the experimental data. The reconstructions were performed with both the box-shaped and the Gaussian small field, to determine whether the shape *and* size, or the size alone, was the driving factor for the mean value drop-off observed in the gel dosimetry dataset (Figure 4.7). Following this, 3 other square fields with widths of 93, 62, and 31 pixels were added, replicating the pattern used in the actual gel dosimetry experiment (Figure 4.1c), and the simulations were repeated, to test whether the presence of other structures in the image influenced the effect.

From the simulations, it was found that measurement noise in projection data determined the magnitude of the central value suppression in the small field reconstructions. Figure 4.8 shows the mean value within the smallest field of the digital phantom experiment, reconstructed with and without 1% Gaussian noise added to projection data, normalized against the FBP-ramp reconstruction. When reconstructing from projections with no added noise, the mean value in the smallest field dropped by 1.5% relative to the filtered backprojection reconstruction when using OSC-TV with a regularization constant value of $c = 2.0$. When zero-mean Gaussian noise with $\sigma = 1\%$ of max intensity was added, however, the value dropped by 6.5% for the same reconstruction parameters, which is similar to what

we observed in our gel dosimetry dataset. This is consistent with the TV-minimization step defined in Equation 4.2, as a noisier projection dataset will result in noisier reconstructions with a higher total variation norm, leading to an increased regularization aggressiveness in each iteration. Therefore, it is important to track the mean value in a small structure to make sure it is accurately reconstructed, especially when measurement noise is high.

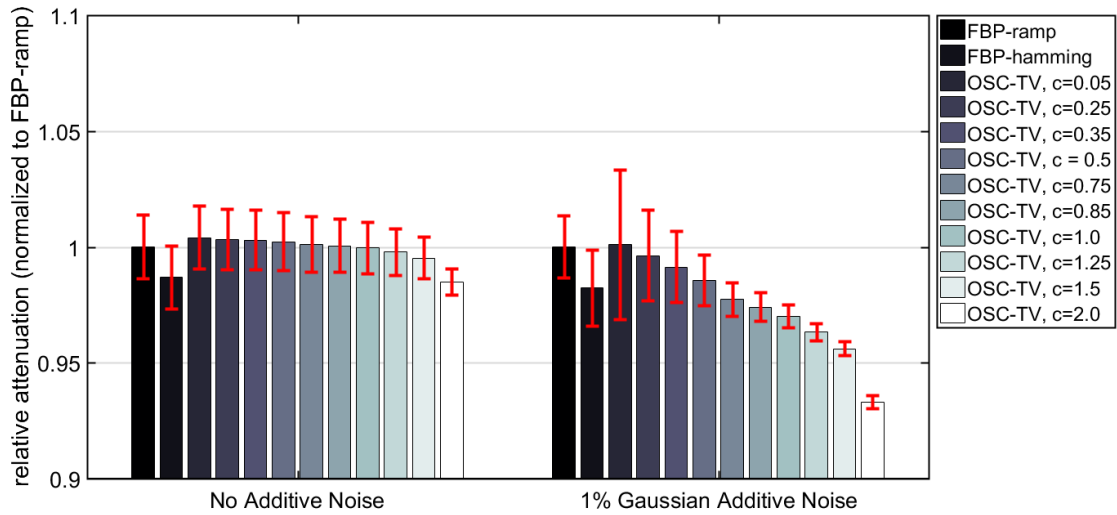


Figure 4.8: Relative mean central attenuation coefficient for a 0.6×0.6 cm square field in the digital phantom simulation, with and without 1% Gaussian noise added to projection data.

4.4 Discussion and Conclusion

Based on the results of our reconstruction study, we conclude that OSC-TV is a suitable reconstruction algorithm for gel dosimetry *via* optical CT imaging. Our phantom experiments showed that the ratio of image contrast over image artifacts and noise (CANR) can be improved by a factor of 3-5 \times , while preserving the shape of steep gradients. The OSC-TV algorithm also suppresses the effects of vessel wall imperfections such as seams and scratches, which generate considerable streaking artifacts in FBP reconstruction.

In the solution phantom experiments (phantoms A and B), the reconstruction CANR and

edge sharpness was not very sensitive to the choice of the regularization constant c in Equation 4.2; so long as the value chosen was less than $c = 2.0$, an increase in CANR of approximately $3\times$ could be achieved without losing spatial information.

In the small-field gel dosimetry dataset, the central value in the 1.0×1.0 and 0.6×0.6 cm fields were sensitive to the choice of the regularization constant, showing an overall decline as c was increased. This effect was not resolved by increasing the number of iterations of the overall OSC-TV algorithm. Additionally, note that the issue is not the absolute size of the object, but the relative size of the object compared to the field of view and voxel size. Simulation experiments showed that the noise level in projections causes this effect. After 10 iterations of OSC-TV, for $c \leq 0.35$, the mean value in all fields agreed within 0.6% with the mean value in the FBP reconstructions, and at $c = 0.25$ a CANR at least $3\times$ higher than Hamming-filtered FBP was obtained for all 4 field sizes. This specific choice of regularization constant applies to reconstructions performed with isotropic 0.33 mm voxels, on reconstructions with a field of view of 16.5 cm horizontal and 14 cm vertical. If the scanner's resolution and/or field of view are changed, this analysis should be performed again.

Most VMAT or IMRT plans delivered to a gel will produce shallower gradients and larger high dose regions than the small-field irradiations performed here. Therefore, we believe that a value of $c = 0.25$ will be acceptable for most gel dosimetry experiments performed with this scanner. Notable exceptions are small-field commissioning and stereotactic radio-surgery deliveries, which may require more careful attention. Our approach for a typical 3D dosimetry experiment will be to estimate, erring on the "sharp" side, the steepest dose gradient and/or smallest object, and choose a c -value that should not degrade these features for our scanning parameters. This can be confirmed by also reconstructing using FBP and comparing the two images.

In conclusion, we have shown that OSC-TV is a suitable algorithm for large volume 3D

dosimetry, even when small fields are present in the distribution, if care is taken in selecting an appropriate regularization constant. While we have used a radiochromic LCV gel in this study, the results are also applicable to other optical CT dosimeters such as polymer gels and PRESAGE[®], which exhibit similar artifacts. Based on our study we do not propose OSC-TV exclusively over other regularized algorithms, but we do emphasize that dosimetric comparisons (e.g. 3D gamma analysis) should be performed using iteratively reconstructed gel dosimeter data. These dose comparison assays will be more trustworthy if performed on images with reduced artifacts and noise.

4.5 Appendix: Calculation of Total Variation Gradient

The regularization process used in the reconstruction algorithm requires the calculation of the “total variation gradient”, $v_{i,j,k}$ in Equation 4.2. This refers to the change in the total variation (a scalar) as a function of changes in the individual voxel values of the image. That is, if $TV(f)$ represents the total variation of image f , then the total variation gradient is $\partial[TV(f)]/\partial f$. For a 3D image:

$$TV(f) = \sum_{i,j,k} \sqrt{(f_{i,j,k} - f_{i-1,j,k})^2 + (f_{i,j,k} - f_{i,j-1,k})^2 + (f_{i,j,k} - f_{i,j,k-1})^2}, \quad (4.5)$$

and the *local* value of the TV gradient at the voxel indexed by i, j, k is approximated as follows:

$$\begin{aligned}
 \left. \frac{\partial TV(f)}{\partial f} \right|_{i,j,k} &= \frac{3f_{i,j,k} - f_{i-1,j,k} - f_{i,j-1,k} - f_{i,j,k-1}}{\sqrt{(f_{i,j,k} - f_{i-1,j,k})^2 + (f_{i,j,k} - f_{i,j-1,k})^2 + (f_{i,j,k} - f_{i,j,k-1})^2} + \epsilon} \\
 &- \frac{f_{i+1,j,k} - f_{i,j,k}}{\sqrt{(f_{i+1,j,k} - f_{i,j,k})^2 + (f_{i+1,j,k} - f_{i+1,j-1,k})^2 + (f_{i+1,j,k} - f_{i+1,j,k-1})^2} + \epsilon} \\
 &- \frac{f_{i,j+1,k} - f_{i,j,k}}{\sqrt{(f_{i,j+1,k} - f_{i-1,j+1,k})^2 + (f_{i,j+1,k} - f_{i,j,k})^2 + (f_{i,j+1,k} - f_{i,j+1,k-1})^2} + \epsilon} \\
 &- \frac{f_{i,j,k+1} - f_{i,j,k}}{\sqrt{(f_{i,j,k+1} - f_{i-1,j,k+1})^2 + (f_{i,j,k+1} - f_{i,j-1,k+1})^2 + (f_{i,j,k+1} - f_{i,j,k})^2} + \epsilon}
 \end{aligned} \tag{4.6}$$

where ϵ is a small constant used to avoid a zero denominator. This formulation of the TV gradient is a 3D extension of the 2D example presented by Zhang *et al* [38] and Sidky *et al* [37], among others.

4.6 References

1. Gore, J. C., Ranade, M., Maryanski, M. J. & Schulz, R. J. Radiation dose distributions in three dimensions from tomographic optical density scanning of polymer gels: I. Development of an optical scanner. *Physics in Medicine and Biology* **41**, 2695 (1996).
2. Maryanski, M. J., Zastavker, Y. Z. & Gore, J. C. Radiation dose distributions in three dimensions from tomographic optical density scanning of polymer gels: II. Optical properties of the BANG polymer gel. *Physics in Medicine and Biology* **41**, 2705 (1996).
3. Kelly, R. G., Jordan, K. J. & Battista, J. J. Optical CT reconstruction of 3D dose distributions using the ferrous-benzoic-xylene (FBX) gel dosimeter. *Medical Physics* **25**, 1741 (1998).
4. Krstajic, N. & Doran, S. J. Fast laser scanning optical-CT apparatus for 3D radiation dosimetry. *Physics in Medicine and Biology* **52**, N257 (June 7, 2007).
5. Wolodzko, J. G., Marsden, C. & Appleby, A. CCD imaging for optical tomography of gel radiation dosimeters. *Medical Physics* **26**, 2508 (1999).
6. Krstajic, N. & Doran, S. J. Characterization of a parallel-beam CCD optical-CT apparatus for 3D radiation dosimetry. *Physics in Medicine and Biology* **52**, 3693 (July 7, 2007).

7. Sakhalkar, H. S. & Oldham, M. Fast, high-resolution 3D dosimetry utilizing a novel optical-CT scanner incorporating tertiary telecentric collimation. *Medical Physics* **35**, 101–111 (Jan. 2008).
8. Thomas, A. & Oldham, M. Fast, large field-of-view, telecentric optical-CT scanning system for 3D radiochromic dosimetry. *Journal of Physics: Conference Series* **250**, 012007 (Nov. 1, 2010).
9. Olding, T., Holmes, O. & Schreiner, L. J. Cone beam optical computed tomography for gel dosimetry I: scanner characterization. *Physics in Medicine and Biology* **55**, 2819–2840 (May 21, 2010).
10. Dekker, K. H., Battista, J. J. & Jordan, K. J. Stray light in cone beam optical computed tomography: II. Reduction using a convergent light source. *Physics in Medicine and Biology* **61**, 2910 (2016).
11. Low, D. A., Harms, W. B., Mutic, S. & Purdy, J. A. A technique for the quantitative evaluation of dose distributions. *Medical Physics* **25**, 656–661 (May 1, 1998).
12. Low, D. A. & Dempsey, J. F. Evaluation of the gamma dose distribution comparison method. *Medical Physics* **30**, 2455 (2003).
13. Huang, J. Y., Pulliam, K. B., McKenzie, E. M., Followill, D. S. & Kry, S. F. Effects of spatial resolution and noise on gamma analysis for IMRT QA. *Journal of Applied Clinical Medical Physics* **15** (July 8, 2014).
14. Kak, A. C. & Slaney, M. *Principles of Computerized Tomographic Imaging* Google-Books-ID: Z6RpVjb9_lwC. 335 pp. (SIAM, Jan. 2001).
15. Doran, S. J. & Yatigammana, D. N. B. Eliminating the need for refractive index matching in optical CT scanners for radiotherapy dosimetry: I. Concept and simulations. *Physics in Medicine and Biology* **57**, 665–683 (Feb. 7, 2012).
16. Rankine, L. & Oldham, M. On the feasibility of optical-CT imaging in media of different refractive index. *Medical Physics* **40**, 051701 (2013).
17. Dekker, K. H., Battista, J. J. & Jordan, K. J. Optical CT imaging of solid radiochromic dosimeters in mismatched refractive index solutions using a scanning laser and large area detector. *Medical Physics* **43**, 4585–4597 (Aug. 1, 2016).
18. Matenine, D., Mascolo-Fortin, J., Goussard, Y. & Despres, P. Evaluation of the OSC-TV iterative reconstruction algorithm for cone-beam optical CT. *Medical Physics* **42**, 6376–6386 (Nov. 1, 2015).
19. Du, Y., Wang, X., Xiang, X. & Wei, Z. Evaluation of hybrid SART + OS + TV iterative reconstruction algorithm for optical-CT gel dosimeter imaging. *Physics in Medicine and Biology* **61**, 8425 (Nov. 15, 2016).
20. Matenine, D., Goussard, Y. & Despres, P. GPU-accelerated regularized iterative reconstruction for few-view cone beam CT. *Medical Physics* **42**, 1505–1517 (Apr. 1, 2015).
21. Matenine, D., Mascolo-Fortin, J., Goussard, Y. & Despres, P. Evaluation of the OSC-TV iterative reconstruction algorithm for cone-beam optical CT. *Medical Physics* **42**, 6376–6386 (Nov. 1, 2015).
22. Olding, T., Holmes, O. & Schreiner, L. J. Cone beam optical computed tomography for gel dosimetry I: scanner characterization. *Physics in Medicine and Biology* **55**, 2819–2840 (May 21, 2010).

23. Granton, P. V., Dekker, K. H., Battista, J. J. & Jordan, K. J. Stray light in cone beam optical computed tomography: I. Measurement and reduction strategies with planar diffuse source. *Physics in Medicine and Biology* **61**, 2893 (2016).
24. Dekker, K. H., Battista, J. J. & Jordan, K. J. Scanning laser optical computed tomography system for large volume 3D dosimetry. *Physics in Medicine and Biology* **62**, 2636 (2017).
25. Babic, S., McNiven, A., Battista, J. & Jordan, K. Three-dimensional dosimetry of small megavoltage radiation fields using radiochromic gels and optical CT scanning. *Physics in Medicine and Biology* **54**, 2463–2481 (Apr. 21, 2009).
26. Shih, T.-Y. *et al.* Small-Field Measurements of 3D Polymer Gel Dosimeters through Optical Computed Tomography. *PLOS ONE* **11**, e0151300 (Mar. 14, 2016).
27. Clift, C. *et al.* Toward acquiring comprehensive radiosurgery field commissioning data using the PRESAGE/ optical-CT 3D dosimetry system. *Physics in Medicine and Biology* **55**, 1279–1293 (Mar. 7, 2010).
28. Babic, S., McNiven, A., Battista, J. & Jordan, K. Three-dimensional dosimetry of small megavoltage radiation fields using radiochromic gels and optical CT scanning. *Physics in Medicine and Biology* **54**, 2463–2481 (Apr. 21, 2009).
29. Jordan, K. J., Lindenmaier, T. & Dekker, K. H. Non-diffusing radiochromic leuco-crystal violet hydrogel dosimeter. *Journal of Physics: Conference Series* **847**, 012009 (May 2017).
30. Hudson, H. & Larkin, R. Accelerated image reconstruction using ordered subsets of projection data. *IEEE Transactions on Medical Imaging* **13** (1994).
31. Erdogan, H. & Fessler, J. A. Ordered subsets algorithms for transmission tomography. *Physics in Medicine and Biology* **44**, 2835–2851 (Nov. 1, 1999).
32. Beekman, F. J. & Kamphuis, C. Ordered subset reconstruction for x-ray CT. *Physics in Medicine and Biology* **46**, 1835–1844 (July 1, 2001).
33. Kole, J. S. & Beekman, F. J. Evaluation of the ordered subset convex algorithm for cone-beam CT. *Physics in Medicine and Biology* **50**, 613–623 (Feb. 21, 2005).
34. Sidky, E. Y. & Pan, X. Image reconstruction in circular cone-beam computed tomography by constrained, total-variation minimization. *Physics in Medicine and Biology* **53**, 4777 (Sept. 7, 2008).
35. Jorgensen, J. H. *et al.* Accelerated gradient methods for total-variation-based CT image reconstruction. *arXiv preprint arXiv:1105.4002* (2011).
36. Chen, Z., Jin, X., Li, L. & Wang, G. A limited-angle CT reconstruction method based on anisotropic TV minimization. *Physics in Medicine and Biology* **58**, 2119 (Apr. 7, 2013).
37. Sidky, E. Y., Kao, C.-M. & Pan, X. Accurate image reconstruction from few-views and limited-angle data in divergent-beam CT. *Journal of X-ray Science and Technology* **14**, 119–139 (2006).
38. Zhang, Y., Wang, Y. & Zhang, C. Total variation based gradient descent algorithm for sparse-view photoacoustic image reconstruction. *Ultrasonics* **52**, 1046–1055 (Dec. 2012).
39. Siddon, R. L. Fast calculation of the exact radiological path for a three-dimensional CT array. *Medical Physics* **12**, 252–255 (Mar. 1, 1985).

40. Xie, L. *et al.* An Effective CUDA Parallelization of Projection in Iterative Tomography Reconstruction. *PLOS ONE* **10**, e0142184 (Nov. 30, 2015).
41. Zeng, G. & Gullberg, G. Unmatched projector/backprojector pairs in an iterative reconstruction algorithm. *IEEE Transactions on Medical Imaging* **19**, 548–555 (May 2000).
42. Zeng, G. L. *Medical image reconstruction: a conceptual tutorial* OCLC: 845614149. 198 pp. (Higher Education Press, Beijing, 2010).

Chapter 5

Iterative Reconstruction in Optical CT: Mismatched refractive index scanning

This chapter is adapted from a manuscript published as “Optical CT imaging of solid radiochromic dosimeters in mismatched refractive index solutions using a scanning laser and large area detector” by Kurtis Hendrik Dekker, Jerry J. Battista and Kevin J. Jordan, *Medical Physics*, 43, 4585 (2016)¹. This article is available for reproduction under the Creative Commons Attribution License (CC-BY), as stated in Appendix B.

5.1 Introduction

5.1.1 Optical computed tomography (CT) for three-dimensional (3D) radiation dosimetry

Optical computed tomography (CT) scanning has evolved as a readout technique for three-dimensional (3D) radiation dosimetry. Optical CT dosimeters [1], consisting of either polymer gels [2] or radiochromic gels and plastics [3], undergo a local change in optical atten-

¹© Kurtis H. Dekker, Jerry J. Battista, and Kevin J. Jordan. Published by American Association of Physicists in Medicine and John Wiley & Sons, Ltd. Available under the Creative Commons Attribution Licence (<http://creativecommons.org/licenses/by/4.0/>)

uation coefficient (μ) as a function of absorbed radiation dose. The 3D dose map is then read out using a calibrated optical CT scanner. Scanner designs range from first-generation pencil beam scanners [4, 5], to fan beam [6] and cone beam [7, 8] or broad parallel beam [9–11] geometries which have decreased the scan times from hours to approximately 10 minutes for a full 3D sampling of the dosimeter.

5.1.2 PRESAGE® solid dosimeters

The PRESAGE® solid dosimeter is a polyurethane plastic containing a radiochromic leuco-dye [12, 13]. The radiological and dosimetric properties of the material have been previously reported [13–15]. Verification of radiotherapy dose distributions using PRESAGE® has been reported with various types of optical CT scanner designs [10, 15–20]. This dosimeter is a solid and thus requires no containment vessel and it can be machined, cut and drilled. Unlike hydrogel dosimeters, which are fragile and melt at approximately 303K, PRESAGE® has a much higher melting point and is very durable. Therefore it can be shipped and is available as a commercial product. These features make it potentially very attractive for optical CT dosimetry in a clinical physics setting. A disadvantage of this dosimeter, however, is its high refractive index ($n \approx 1.5$) compared to that of water ($n = 1.33$) and hydrogels ($n \approx 1.34$). Refractive index matching has historically been implemented to preserve the straight-line ray paths assumed in standard CT reconstruction algorithms. Solid plastic dosimeters necessitate the use of viscous oil-based liquids in the optical CT aquarium that contains the sample to be scanned. Mixing and filtering these liquids is a very slow process, which adds substantial time to the initial setup of a PRESAGE® dosimetry experiment. It is also difficult to remove air bubbles and particulate impurities. Rotating the dosimeter within the optical CT aquarium can create local refractive index variations, called Schlieren bands as seen in the optical projection image shown in Figure 5.1. The dynamic nature of the Schlieren bands results in projection data with a

noisy appearance, and avoiding them limits the speed of dosimeter rotation and overall scan time. Alternatively, averaging multiple images per projection while keeping fluid moving with a pump has been used with CCD systems [19], but this would prohibitively increase scan time for non-camera scanners. Lastly, oil-based liquids make cleaning the optical CT aquarium very inconvenient, and can cause degradation of some plastics used in the aquarium walls. For these reasons, work is being done to minimize the volume of viscous liquid needed for optical CT scanning through the use of “solid-tank” optical CT aquarium designs [21, 22]. However, such designs still require a small amount of high-viscosity fluid to fill the gap between the tank and the dosimeter, so rotation-induced Schlieren patterns are not eliminated, and cleaning the tank remains inconvenient. In summary, it would be advantageous if the PRESAGE® dosimeter could be scanned in an aqueous solution with a lower viscosity. This introduces a refractive index mismatch between the aquarium liquid and the dosimeter, resulting in bent ray paths that need to be considered during CT image reconstruction.

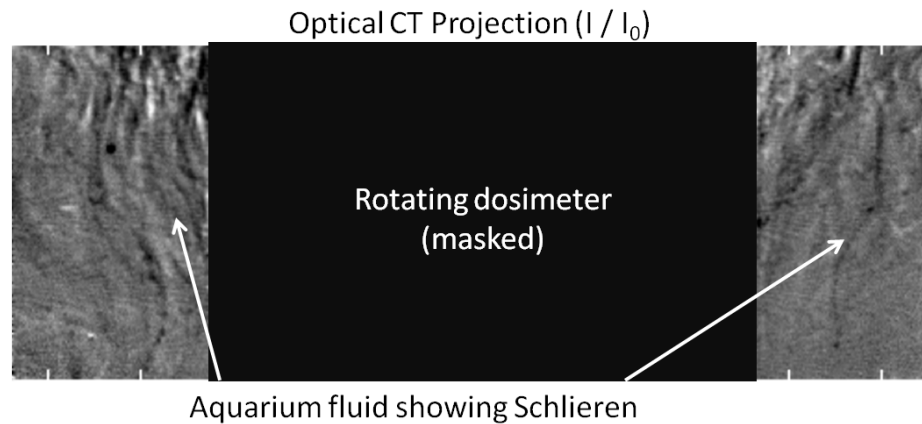


Figure 5.1: Optical CT projection acquired with a scanning laser cone-beam CT with a viscous refractive index matching liquid in the aquarium. This image is the ratio of the post-irradiation projection over the pre-irradiation projection (i.e. post-scan / pre-scan). In the aquarium liquid, Schlieren bands are clearly visible, resulting in unacceptable variable signal levels ($\pm 10\%$) through the reference liquid. These patterns change with time and therefore are different in each projection.

5.1.3 Intentionally mismatched refractive index

If the optical CT aquarium contains a liquid with a lower refractive index than the dosimeter, the dosimeter will act as a converging lens, as shown in Figure 5.2. Light rays will not travel along straight line paths from the source to the detector, violating the assumption used in x-ray and standard geometry optical CT reconstruction. In addition, there is a critical radius beyond which the dosimeter is not adequately sampled in every projection. This absence of peripheral data depends on the refractive index mismatch in the system as well as the diameter of the dosimeter [9]. Simulation studies [23, 24] have demonstrated that, using iterative CT reconstruction techniques, accurate images should be obtainable within this fully-sampled radius, if the actual paths of light rays through the dosimeter are known. The scanning-laser CT system presented by Krstajic and Doran [16], for example, has been tested for ‘in-air’ readout of PRESAGE® [25]. However the small area detector results in substantial loss of projection information. Additionally, in previous studies, the paths of light rays through the interior of the dosimeter have been calculated based on theoretical angles of refraction, without an experimental method to measure these paths during a scan. This is problematic because there may be variations in refractive index from dosimeter to dosimeter, or between different batches of the surrounding reference liquid.

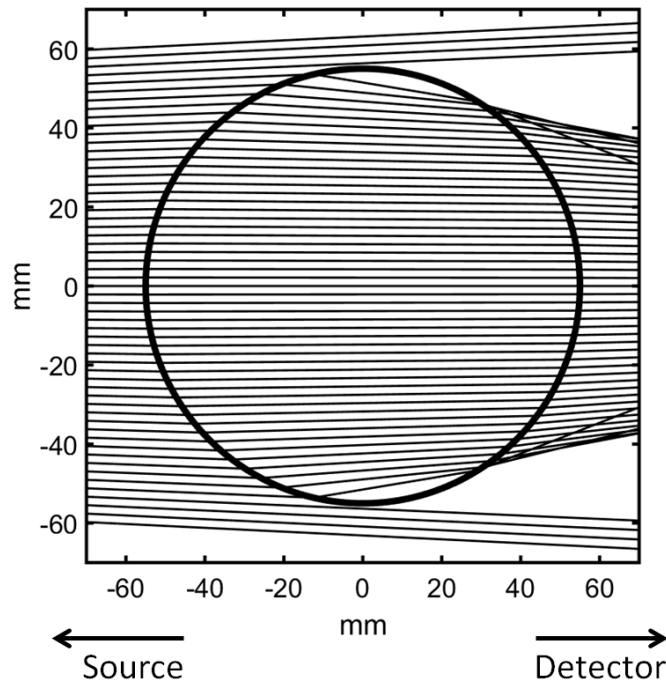


Figure 5.2: Ray-tracing simulation of refracted fan-beam light rays through an 11 cm diameter PRESAGE® solid dosimeter ($n = 1.5$) placed within a purposely mismatched refractive index media ($n = 1.41$). The plastic dosimeter acts as a converging lens.

5.1.4 Study outline

We describe an experimental method to enable optical CT imaging of solid cylindrical dosimeters placed in mismatched refractive index media. A fiducial-based technique is outlined that allows direct measurement of the paths of light rays travelling through the dosimeter. This knowledge is used to inform an iterative CT reconstruction algorithm. A proof of principle experiment using a liquid phantom is presented to demonstrate the functionality of the technique. Experiments using irradiated PRESAGE® dosimeters are then described to demonstrate application of the technique.

5.2 Methods

5.2.1 Scanning laser optical CT system

The scanning laser system used in the study is shown schematically in Figure 5.3. It was originally designed by Jordan *et al.* for large-volume 3D dosimetry and normally operates in cone-beam geometry [26] (Note: this is not the same scanner presented in Chapter 3). A helium neon laser emits a beam which is passed through a bandpass filter (10 nm bandwidth) to block plasma discharge from the laser. The beam is attenuated to approximately 10 μ W, and directed to a pair of XY galvanometer scanning mirrors (Part Number: GVS002, Thorlabs Inc.). These mirrors raster scan the beam in a cone-beam trajectory through the aquarium and dosimeter. The transmitted beam then strikes a large “catch-all” planar diffuser that scatters light into a forward cone. A fraction of this scattered light is then detected by a photomultiplier tube (PMT) held at a bias voltage of approximately 400 V DC. The PMT signal is processed through appropriate pre-amplifier and low-pass filter circuits, and is sampled at 250 kHz by a 16-bit data acquisition system (PCI-6529, National Instruments Corporation, USA). A single scan line consists of 3750 samples acquired as the laser beam is swept across the object, with a single angular sweep (approximately 14 degree arc for a 15 cm field of view) taking approximately 15 milliseconds. The scan line is down-sampled and cropped to obtain projections containing 512 equiangular spaced samples. The diffuser is large and insensitive to the angle of incidence (unlike a camera lens), so it is possible to capture almost any ray transmitted through the system, even one deflected substantially by the refractive index mismatch. This is different from a camera-based system, where mismatched refractive indices would cause a complete loss of information in large regions of projection images due to ray rejection by the imaging lens and aperture [27]. The measured intensity is dependent upon the position of the beam on the diffuser, but this is taken into account by calculating transmission as the ratio of post-irradiation

to pre-irradiation measurements. This system has a single ray – single detector property; recorded light intensities can be assigned along unique ray paths. This cannot be done using a scanner with a broad-beam light source and multi-channel detector, such as a CCD camera, as measurements taken near the central axis would be polluted by rays that were refracted inwards from the periphery (Figure 5.2).

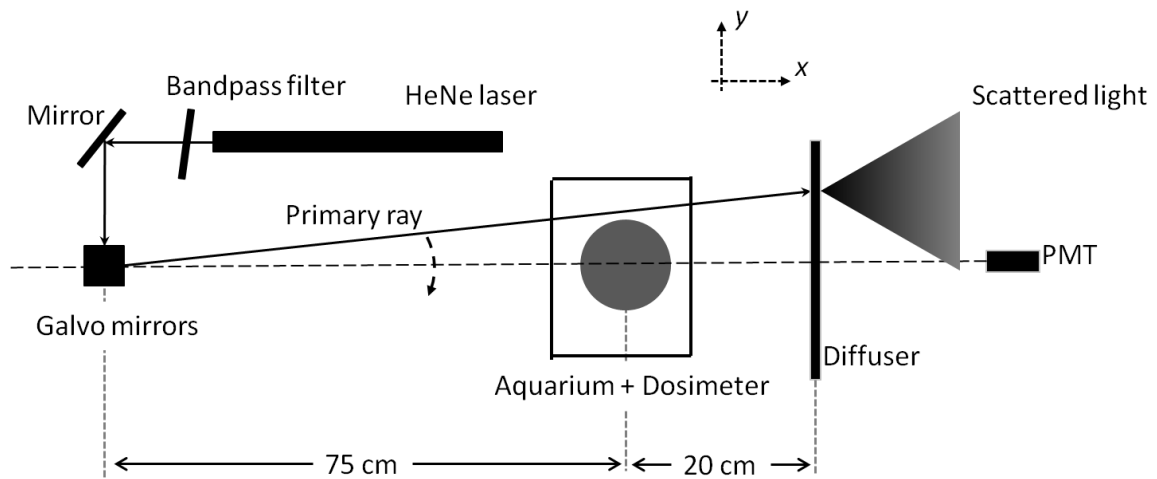


Figure 5.3: Scanning laser CT schematic, top view. A helium neon laser beam is filtered and raster-scanned in cone-beam geometry across the aquarium and dosimeter. The primary ray strikes a planar diffuser screen, which causes forward scattering of light. A fraction of this light is detected by a photomultiplier tube (PMT), and this intensity is assigned to the ray’s path determined by a fiducial marker placed on the side of the dosimeter.

For this work, the scanner from the previously-reported setup [26] was modified in the following ways. First, the original design had a secondary diffuser screen closely positioned to the PMT, in order to “flatten” the measured intensity profile in cone-beam CT projections. For this experiment, this flattening diffuser was removed. Second, the primary diffuser was moved closer to the rotation axis of the scanner, in order to capture refracted rays that would otherwise miss the diffuser due to refraction through the dosimeter. Finally, in this study we focused only on the central plane of the scanner’s imaging cone (fan beam geometry). We will discuss the extension to full 3D imaging in Section 5.3.4.

5.2.1.1 Scanning wavelengths

Due to equipment access, a 594 nm laser (Model 1677P, JDS Uniphase Corporation, USA) was used for some of the experiments in this paper, while a 633 nm Helium-Neon laser (Model HRP-050, Thorlabs Inc.) was used for others. The peak absorption of PRESAGE® is near 635 nm, but 594 nm is near 50% of peak absorption [13]. In this study, we are not attempting to characterize the sensitivity of PRESAGE®, so the wavelength switch is not an issue. Using multiple wavelengths (and therefore slightly different refractive indices) actually demonstrates a strength of our method: exact knowledge of refractive indices is not required. Table 5.1 indicates the wavelength used for each experiment in the study.

Experiment	Sections of Chapter	Laser Wavelength
Uniform solution phantom	5.2.5., 5.3.1.	594 nm
Uniform Irradiations	5.2.6.2, 5.3.2.1.	594 nm
Step-dose pattern	5.2.6.3., 5.3.2.2.	633 nm
Additional uniformity tests	5.5.1	633 nm

Table 5.1: Summary of laser wavelengths used for experiments in the study.

5.2.2 Ray path measurement

5.2.2.1 Mathematical description

Let the rotation axis of the optical CT scanner be the origin of a 2D Cartesian coordinate system, with the positive x-axis pointing along the optic axis from the light source to the detector. We restrict our attention to the central CT slice, scanned in fan-beam geometry. Let θ represent the rotation angle of the sample being scanned in the system, measured from the positive x-axis. Then, the coordinates $\langle x, y \rangle$ of a fiducial marker affixed to the wall of a rotating cylindrical sample with radius r can be described by:

$$\langle x, y \rangle = \langle r \cos(\theta), r \sin(\theta) \rangle \quad (5.1)$$

For a 360° fan-beam scan, the fiducial marker will occlude a given primary ray twice: at both its entrance to and exit from the cylinder (Figure 5.4a, 5.4b). The sample rotation angles θ_{entry} and θ_{exit} corresponding to these points can be determined from the sinogram trajectory of the fiducial (Figure 5.4c). Then, Equation 5.1 can be used to determine the corresponding Cartesian entrance and exit points $\langle x_{entry}, y_{entry} \rangle$ and $\langle x_{exit}, y_{exit} \rangle$, thus yielding the actual 2D ray trajectory through the dosimeter, assuming that the dosimeter has a uniform refractive index. This method can be compared to geometry calibration techniques used in X-ray CT [28, 29], where cylindrical phantoms with fiducials are used to determine fundamental geometry parameters for cone-beam scanners, based on the assumption of straight-line rays from source to detector. Here the problem is inverted: knowledge of the system geometry is used to measure deviations from the original straight line fan-beam ray trajectories.

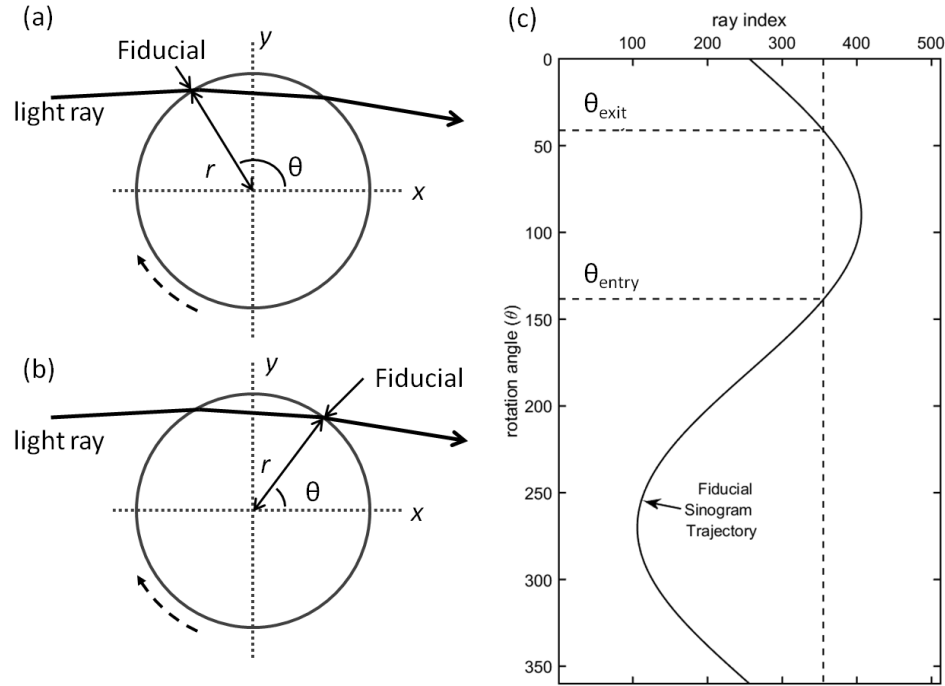


Figure 5.4: Schematic of fiducial-based ray path measurement technique. A primary ray is occluded by a fiducial marker at its entry (a) and exit (b) from the dosimeter at two different rotation angles. (c) The fiducial's sinogram trajectory, with the rotation angles corresponding to (a) and (b). By finding the intersection point between vertical “ray index lines” and the fiducial spot trajectory, the angles θ_{entry} and θ_{exit} , and thus the actual ray paths through the dosimeter, can be calculated.

5.2.2.2 Implementation in optical CT iterative reconstruction process

In this study, the ray path measurement was implemented by attaching an opaque fiducial (black vinyl tape) about 0.5 mm wide to the wall of the samples after the pre- and post-irradiation scans had been acquired, so as not to occlude the data of interest. An extra “fiducial scan” was therefore required and performed. The fiducial scan was processed using a MATLAB program to determine the path of each ray through the dosimeter. The central location of the fiducial was selected on each projection by finding a local minimum signal (since the fiducial is opaque) using the built-in *findpeaks* function in MATLAB. These ray paths are used to sort CT data into parallel-beam geometry. The technique of re-binning to correct for refraction effects is a known technique previously applied in gel

dosimetry[30] as well as biological imaging [31, 32]. Unlike these previous studies, here we are not assuming knowledge of the refractive indices. We only assume that the sample has a uniform refractive index and that the rotation angle and diameter of the cylinder are known.

5.2.3 Aquarium liquid selection

The optimal liquid for PRESAGE[®] scanning is one that is as close in refractive index as possible to the dosimeter ($n \approx 1.5$), while still maintaining a “low viscosity” condition that does not produce Schlieren effects shown in Figure 5.1 during rotation of the dosimeter. Additionally, water-soluble materials such as glycerol and propylene glycol were chosen as they are much easier to clean than oils and because our aquarium walls are not made with oil-compatible material. Mixtures of water ($n = 1.33$) and glycerol ($n = 1.47$) in various proportions were suitable.

To assess the viscosity of a given mixture, it was poured into the aquarium of a cone-beam optical CT scanner (modified Vista10, Modus Medical Devices Ltd., London, Ontario, Canada), and a 95 mm diameter vessel was inserted and rotated using a stepper motor. The video feed from the Vista scanner’s CCD camera was examined to observe rotation-induced Schlieren patterns. Experimentally, it was found that mixtures of up to 60% glycerol in water (by weight) did not produce Schlieren bands when rotating the vessel at normal scan speeds. This mixture corresponds to a refractive index of about 1.41 [33], 6% lower than the nominal refractive index of PRESAGE[®] at 1.5. Using an in-house MATLAB ray-tracing simulation, it was calculated that 92% of an 11 cm diameter PRESAGE[®] dosimeter’s radius could theoretically be fully sampled using the laser scanner with this liquid. This field of view makes good use of the available dosimeter volume, and is similar to that typically used in PRESAGE[®] dosimetry currently, since the periphery of the dosimeter is often ignored due to “edge artifacts”. For example, Thomas et al. [19] excluded the outer 7 mm of the

dosimeter from dosimetric analysis.

5.2.4 CT scanning and reconstruction

Scans were performed using 1024 equally-spaced projections spanning 360° of rotation. After down-sampling, each projection contained 512 rays. With the current, prototype system, a single plane 1024 projection scan takes approximately 15 minutes; however we are currently constructing a new fan-beam system that will be capable of acquiring a 1024 projection scan of a 20 cm x 20 cm x 15 cm (height) volume in approximately 40 minutes. Three scans were performed for each sample, a “pre-scan”, “post-scan” and the “fiducial” scan. Transmission values are calculated from the ratio of the post-scan to the pre-scan, in order to generate the sinogram data. Fiducial-measured ray paths were used to form a parallel-beam sinogram containing 512 projections equally spaced around 180° of rotation. To account for variations in laser light intensity, a normalization process similar to that used for CCD-based scanners [34] was implemented. Each projection was scaled such that the mean signal in a region containing rays that passed through only the aquarium liquid remained constant.

CT reconstruction was performed using the ASTRA Toolbox [35, 36], an open-source set of GPU-accelerated reconstruction algorithms. A basic SIRT algorithm [37] was used. Regions of the parallel-beam sinogram corresponding to the incompletely sampled portion of the dosimeter (at the periphery) were excluded from the data used to reconstruct images. Unless otherwise stated, images were reconstructed on a 512×512 grid with a 0.32 mm pixel size, using 100 iterations of the SIRT algorithm with no initial estimate image specified. No post-reconstruction averaging or smoothing was performed. On a PC equipped with an Intel(R) Core™ i7-2600 processor (Intel Corporation, Santa Clara, California, USA) and an NVIDIA GeForce GTX 780 video card (NVIDIA Corporation, Santa Clara, California, USA) the reconstruction time was approximately 0.5 seconds for a single 512

× 512 axial slice.

5.2.5 Validation of technique with a uniform solution phantom

Snell refraction depends only on the ratio of refractive indices. Therefore, it was possible to design a liquid phantom experiment to simulate the same refractive mismatch as would occur when scanning PRESAGE[®] within a 60% glycerol bath (ratio = 1.06). The purpose of this experiment was to test the refractive index mismatched scanning technique without confounding effects of possible dosimeter non-uniformities and imperfections. A perfluoroalkoxy alkane (PFA) extruded cylinder (Holscott Fluoroplastics Ltd., Lincolnshire, UK) with an inner diameter of 95 mm and wall thickness of 0.5 mm was used. A refractive index matching liquid for this cylinder was made using 9% (by weight) propylene glycol in water, which had a refractive index of approximately 1.34 [38]. It was determined that a 65% (by weight) glycerol/water solution would reproduce the refractive index ratio above. By using the 9% propylene glycol in the aquarium, refraction from the PFA vessel was eliminated, reducing this to a two-refractive index problem. Therefore, using the 65% glycerol solution inside the vessel simulates PRESAGE[®] scanning, having a high refractive index sample surrounded by a single lower index media.

For this phantom, a pre-scan was acquired, and then the phantom solution was dyed with drops of Nigrosin stain (Fisher Scientific, USA) before acquiring a post-scan. Finally, a fiducial made of black vinyl tape was attached to the wall to acquire the ray path scan. After reconstruction, the inner diameter of the phantom was used with the central transmission value to determine the “true” Beer-Lambert law attenuation value ($\mu_{Beer-Lambert}$). This value was compared to the reconstructed attenuation value (μ_{CT}) measured in a 1 cm diameter region of interest (ROI) centered 1 cm away from the rotation axis to avoid central axis artifacts sometimes present in reconstructed optical CT images.

5.2.6 PRESAGE® experiments

After the proof-of-principle solution experiment, our method was tested on PRESAGE® samples (Manufacturing batch #91, Heuris Inc., Skillman, NJ, USA). The dosimeters used had a diameter of 11 cm and a height of 10 cm. Optical CT scans and irradiations were performed at a temperature of 293K. Two different irradiation patterns were decided upon: a uniform (in axial plane) dose delivery, and a 2-level “step pattern” delivery. These models provide dose content in the incompletely sampled peripheral region of the cylinder, as well as a steep dose gradient.

5.2.6.1 Irradiation setup

PRESAGE® dosimeters were irradiated from the bottom on a decommissioned clinical Cobalt-60 irradiator (Theratron 60, Atomic Energy of Canada Limited, Chalk River, Canada). The source to surface distance (SSD) was set to 60 cm, and dosimeters were irradiated within a water tank in order to provide full scattering conditions. To achieve the two-level step dose (Section 5.2.6.3), a 4 cm thick lead block was placed just below the water tank to block roughly half of the irradiation field. The scanned plane in these experiments corresponded to a height approximately 5 cm above the bottom of the water tank. At this distance, ion chamber measurement at a radius of 6 cm (just beyond the radius of the dosimeter) was 98% of that at field center. Therefore, the dose delivered to an axial plane of the dosimeter should be uniform within 2% if no additional collimation or attenuation is added.

5.2.6.2 PRESAGE® experiment 1 - uniform dose

One dosimeter (manufactured April 2015) was irradiated to nominal doses of 1.8, 3.6, 5.4, 7.2, 9.0, 10.8, and 12.6 Gy (within the axial plane at 5 cm depth) over the course of

approximately 14 hours. Post-scans were acquired 20 minutes after each delivery, and reconstructions were performed with 0.32 mm x 0.32 mm pixels. In order to verify that the attenuation of the sample was not changing during the post-scan, the central axis transmission was examined as a function of projection number and found to remain constant. This is a valid test for a uniform or radially-symmetric attenuator. When all post-scans were complete, the fiducial marker was attached to perform the extra ray path scan. Attenuation coefficients (μ_{CT}) were measured by taking the average over 2×2 mm² regions of interest spaced every 4 mm within the fully-sampled region. These were compared against central axis calculations of the attenuation coefficient ($\mu_{Beer-Lambert}$).

5.2.6.3 PRESAGE[®] experiment 2 - step dose pattern

A second dosimeter (Manufactured September 2015) was irradiated with a “step” dose pattern. The same irradiation geometry was used. First, a nominal 1 Gy uniform dose was delivered. A post-scan was performed (as part of an experiment to test the dose response uniformity, see the chapter appendix, section 5.5.1). A second irradiation was then “added” approximately 2 hours after the initial uniform delivery, with a 4 cm thick lead block obscuring just over half of the dosimeter to create a high-dose and a low-dose region with a strong gradient between them. The post-irradiation scan was performed 20 minutes after the second irradiation. Overall, a nominal dose of 2 Gy was delivered to the high-dose region. The attenuation coefficient of PRESAGE[®] shows a temporal dependence after irradiation [15], therefore proportional dose response when comparing the low and high-dose regions in this sample was not expected. This study was not designed to examine the dosimeter’s linearity; therefore reconstructions were examined in terms of attenuation coefficients and not converted to dose maps.

In addition to a 0.32 mm pixel reconstruction, a 1 mm pixel reconstruction was also performed. This is in line with the reconstructed voxel sizes typically used for large volume

PRESAGE[®] dosimeters [15], and helped to suppress image artifacts in order to better examine large-scale features and allow comparison with previous work.

A second reconstruction was performed using the initial 1Gy irradiation as the reference scan and the “top-up” half-beam irradiation as the post-scan. The profile across the gradient in this reconstruction was compared against profiles measured in water using an Exradin A1SL ion chamber (active volume 53 mm³, Standard Imaging, Inc., Middleton, Wisconsin, USA) as well as Gafchromic EBT3 film read out using an in-house scanning point densitometer. This film scanner has a spot size of less than 1 mm and operates at a wavelength of 590 nm.

5.3 Results and Discussion

5.3.1 Phantom experiment

Figure 5.5 shows a re-sorted parallel beam sinogram projection (Figure 5.5a), as well as the reconstructed image (Figure 5.5b) and a central profile (Figure 5.5c) for the uniform liquid phantom experiment (Section 5.2.5).

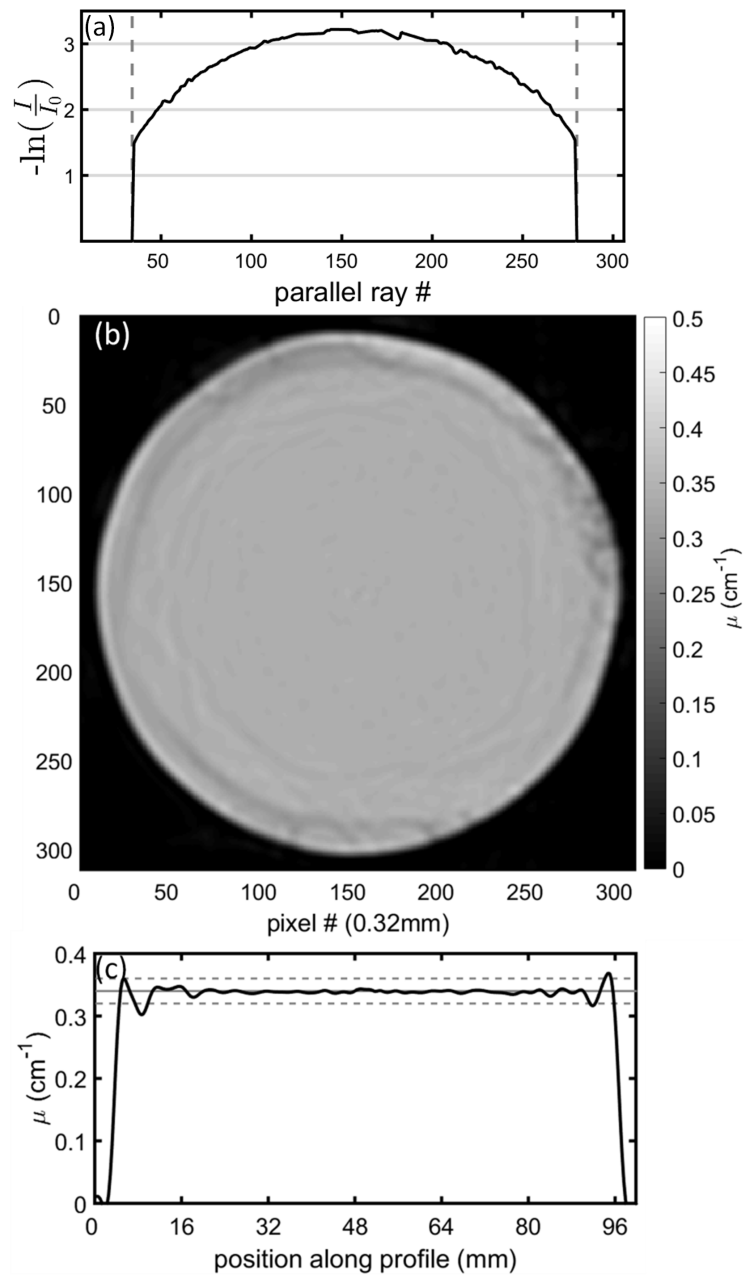


Figure 5.5: Results from the liquid phantom experiment. (a) Re-binned parallel-beam sinogram projection. Dashed vertical lines mark the edge of the completely-sampled region used in the iterative reconstruction algorithm. (b) CT reconstruction of axial slice. A ring artifact appears at the boundary between fully sampled and under-sampled radii. (c) Horizontal profile across the image in (b). The solid and dashed horizontal lines show the mean $\pm 1\sigma$ for the reference Beer-Lambert law central axis value determined along the diametric path.

The measured attenuation coefficient in the reconstructed image is $\mu_{CT} = 0.342 \pm 0.004 \text{ cm}^{-1}$, which agrees very well with the central-axis value of $\mu_{Beer-Lambert} = 0.34 \pm 0.02 \text{ cm}^{-1}$. The reconstruction remained uniform within 3% in the central 85% of the sample's radius, out to a prominent ring artifact that corresponds to the boundary between full and incomplete sampling in projection data. A similar ring has been seen in the simulation work by Doran and Yatigamana [23], and appears to be a consequence of having a non-zero change in attenuation coefficient in the incompletely-sampled region between the pre and post-scan. The results of this phantom experiment confirm that mismatched index scanning with this system geometry allows accurate optical CT reconstruction within the fully sampled radial region of the object.

5.3.2 PRESAGE[®] experiments

5.3.2.1 PRESAGE[®] experiment 1 - uniform dose

Figure 5.6 shows a representative reconstruction of the uniformly irradiated PRESAGE[®] dosimeter. The reconstruction (Figure 5.6a) and central profile (Figure 5.6b) for a nominal dose of 9 Gy are shown.

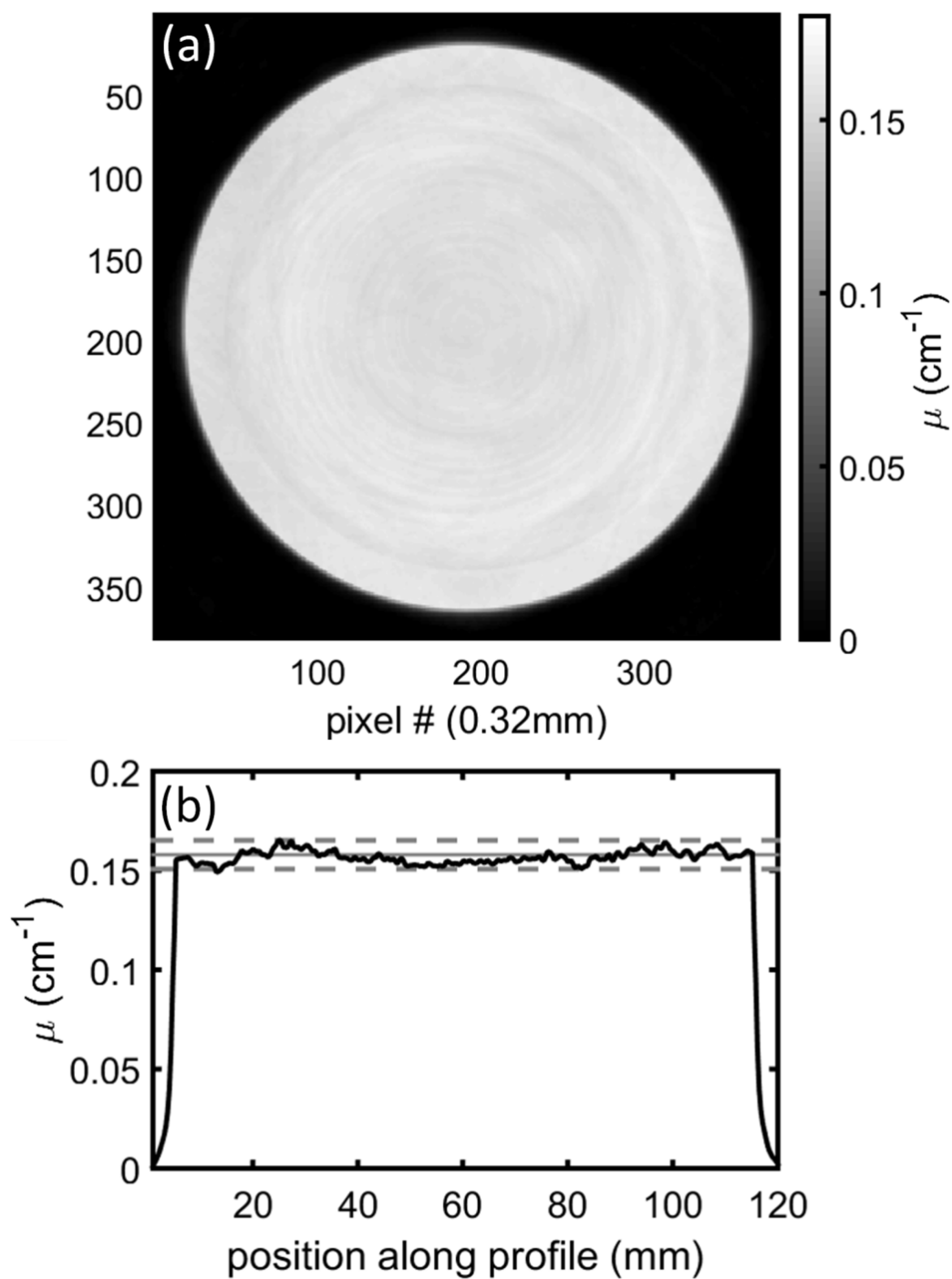


Figure 5.6: Uniformly irradiated PRESAGE® sample (9.0 Gy nominal dose). (a) Reconstructed axial slice. (b) Central profile. The reconstruction shows agreement with the central axis Beer-Lambert value (mean $\pm 1\sigma$ shown as horizontal solid and dashed lines in (b)).

As before, there is a ring in the reconstructed images that corresponds to the boundary between full and incomplete sampling of the dosimeter in projections. This is located at approximately 85% of the dosimeter’s radius, which is less than the predicted value of 92% sampling (based on ray-tracing simulations), but still provides a 9.4 cm diameter useful circular field of view within which dose distributions could be sampled accurately. The outer regions of the PRESAGE® dosimeter are frequently unused for 3D dosimetry, due to so-called “edge artifacts” caused by reflection and refraction. Thomas et al. [19] reported dosimetric analysis on PRESAGE® data ignoring the peripheral 7 mm shell. The 8 mm wide un-sampled region in this study is of similar size. Therefore, losing the use of this portion of the dosimeter is likely an acceptable tradeoff with the benefit of avoiding the drawbacks of viscous oils.

As shown in Table 5.2, reconstructed attenuation coefficients (μ_{CT}) agreed (within 1 standard deviation) with the Beer-Lambert reference value calculated along the central axis ($\mu_{Beer-Lambert}$). All reconstructions maintained this agreement within the fully sampled region. However, examining profiles such as Figure 5.6b reveals that there is some “cupping” in the reconstruction. An approximately 5% difference between the minimum and maximum response was observed in all images. This cupping effect is discussed in more detail in Section 5.3.2.3.

Nominal Dose (Gy)	μ_{CT}	$\mu_{Beer-Lambert}$
1.8	0.032 ± 0.002	0.032 ± 0.002
3.6	0.065 ± 0.001	0.065 ± 0.003
5.4	0.096 ± 0.001	0.096 ± 0.004
7.2	0.124 ± 0.006	0.127 ± 0.006
9.0	0.157 ± 0.003	0.159 ± 0.007
10.8	0.189 ± 0.003	0.190 ± 0.009
12.6	0.220 ± 0.004	0.22 ± 0.01

Table 5.2: Reconstructed attenuation coefficients (μ_{CT}) measured from eleven $2 \times 2 \text{ mm}^2$ ROIs equally spaced every 4 mm within the central, fully sampled region compared to those calculated using the Beer-Lambert law along the central axis of the dosimeter ($\mu_{Beer-Lambert}$), for the nominal doses delivered to a PRESAGE® dosimeter.

5.3.2.2 PRESAGE® experiment 2 - step-pattern irradiation

Figure 5.7 shows the reconstructed image (Figure 5.7a, 0.32 mm pixels) and central profiles (Figure 5.7b) from 0.32 mm and 1 mm pixel size reconstructions. The gradient between low and high dose regions was reconstructed with a consistent shape within the fully-sampled region. Again, cupping is present, as there appears to be approximately 5% difference in dose response from the periphery to the center of the dosimeter. This reconstruction also exhibits several additional ring artifacts, which will be discussed in Section 5.3.2.3. These effects result in data that appear “noisier” than those seen in previously published work, and are under investigation. Reconstructing at a coarser 1 mm resolution as is common in most studies performed using large PRESAGE® dosimeters, hides many of these effects.

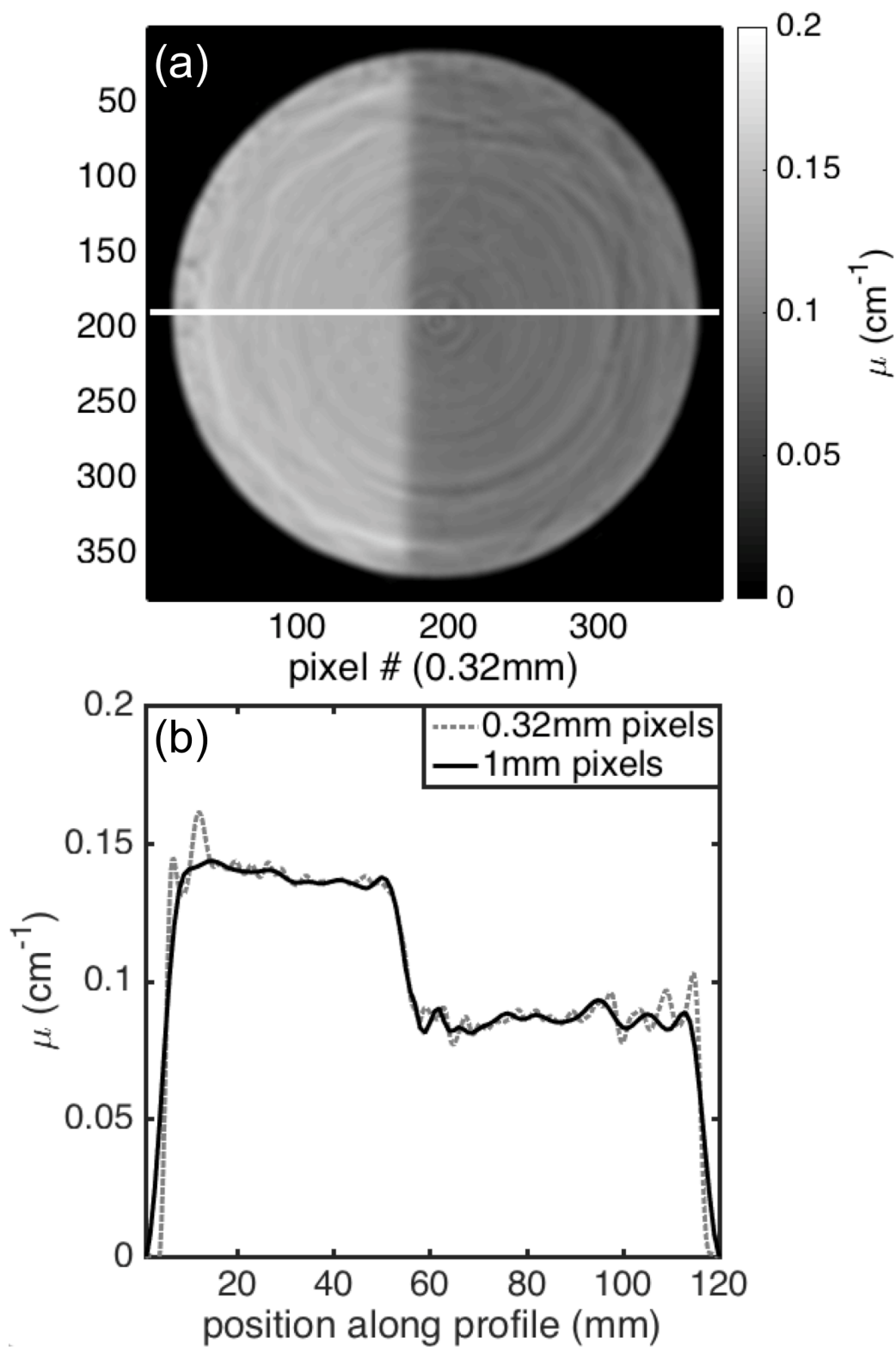


Figure 5.7: Two-level irradiation PRESAGE® experiment results (a) 0.32 mm pixel resolution reconstruction of axial slice. (b) Central line profiles from the 0.32 mm resolution reconstruction (dashed gray) and the 1 mm resolution reconstruction (solid black).

Figure 5.8 shows central profiles through the edge from the second reconstruction (using the first uniform irradiation as the pre-scan), A1SL ion chamber, and EBT3 film. The three profiles were normalized in the high-dose region and aligned using the 50% point of the gradient. The PRESAGE[®] reconstruction, film data, and ion chamber data show good agreement. These results demonstrate that the reported mismatched refractive index scanning technique is capable of acquiring accurate optical CT reconstructions in regions of steep dose gradients as would be produced in Intensity Modulated Radiation Therapy (IMRT) exposures.

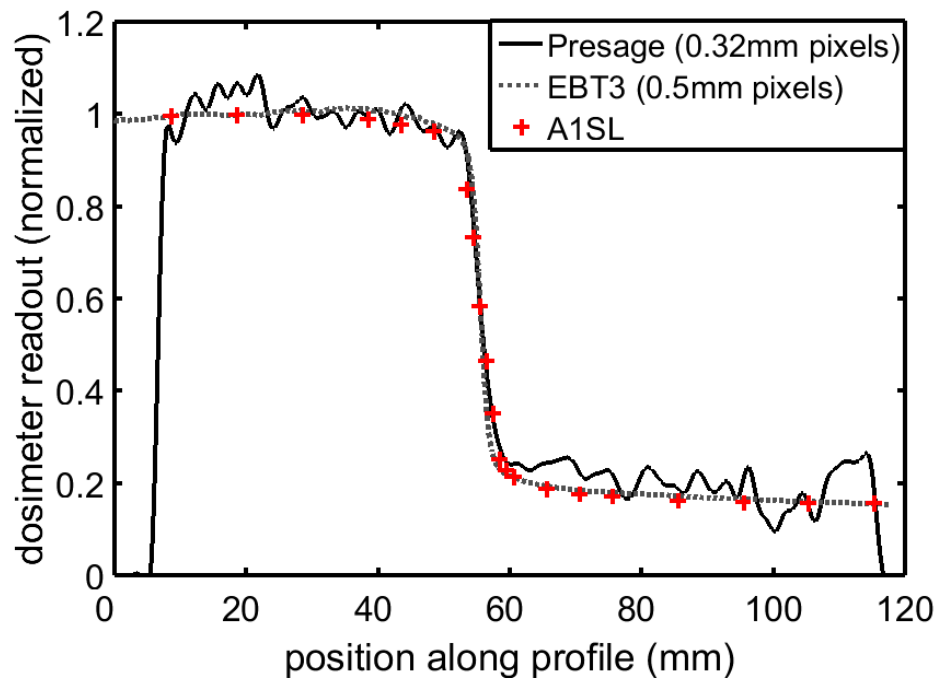


Figure 5.8: Profiles across the gradient generated by the lead block, measured by PRESAGE[®] (solid black), EBT3 film (dashed grey), and A1SL ion chamber (cross symbols). The readouts from each dosimeter (PRESAGE[®]: attenuation coefficient in cm^{-1} ; film: dose in cGy from optical density calibration data; ion chamber: charge in nC) were normalized in the center of the high dose plateau. Optical CT, film, and ion chamber measurements show good agreement in the gradient region.

5.3.2.3 PRESAGE® reconstruction artifacts and non-uniformity

The fine resolution (0.32 mm pixels) PRESAGE® images in this study exhibit more artifacts than other PRESAGE® work [10, 15, 16], and more than the uniform phantom reconstruction in this study (Figure 5.5). Large-volume PRESAGE® studies often show results obtained through filtering and down-sampling of projections, and reconstructing at 1 or 2 mm voxel sizes, to reduce noise [15, 19]. Similarly, reconstructing images in this study at 1 mm resolution (Figure 5.7b) suppresses most of the artifacts, but some of the larger features remain. An iterative reconstruction algorithm that included a total variation-based regularization was tested [39] but produced similar images, indicating that the features observed are present in the actual CT scan data. The artifacts in the PRESAGE® images here are likely caused by a combination of manufacturing imperfections in the dosimeter and error in repositioning the sample in the aquarium after radiation exposure. Streak artifacts and fluctuations in the reconstructed attenuation coefficient may be caused by refractive index inhomogeneity within the dosimeter. Unlike a CCD-based scanner, the single-channel system used here is relatively insensitive to these imperfections in that they will not cause a sharp loss of signal. However, they will still cause a small deflection of rays that can lead to transmission values being assigned along an incorrect path. The fiducial method assumes uniform refractive index within the dosimeter. If there are large fluctuations in the refractive index of PRESAGE®, techniques to map these out will be required if it is to be used for dosimetry. This fact is not specific to our scanner but applies to all forms of optical CT dosimetry. It must also be noted that the PRESAGE® samples exhibit unique patterns of optical activity, which may correlate in some way with artifacts. This effect is described in the chapter appendix (Section 5.5.2)

Ring artifacts in this experiment are not caused by bad detector elements as is normally the case in CT, as here there is only a single detector. In this scanner geometry, rings occur due to reflections and mechanical errors in sample positioning. If the dosimeter is misaligned

between the pre- and post-irradiation scans, so are reflection contributions (from dosimeter surface and back off the entry window of the aquarium) and/or transmission losses due to imperfections in the aquarium windows, leading to ring artifacts. These rings should be reduced by improving the sample positioning reproducibility. Errors in the assignment of ray paths can also cause ring artifacts (Section 5.3.3).

Of greater concern is that the PRESAGE[®] datasets appear to exhibit an intrinsic non-uniform dose response, with approximately 5% difference from minimum to maximum response. This effect appears visually as “cupping” in reconstructions, where the center of the dosimeter has a weaker response than the periphery. Additional experiments have demonstrated this effect with varying magnitude in dosimeter samples from different manufacturing batches. Reconstructions of the uniform liquid phantom did not exhibit such cupping. An ion chamber measurement of the Co-60 field at a radius of 6 cm (just beyond the radius of the dosimeter) was 98% of that at field center. This has also been found in other film and gel dosimetry experiments in our institution. The shape of the irradiation profile is the reverse of the cupping that appears in the reconstructions. Therefore, the scanning technique and radiation source have been ruled out as possible causes, indicating that the dosimeters themselves are intrinsically responding non-uniformly to dose. This result has been corroborated by discussions with the manufacturer [40], which point to poor and inconsistent heat dissipation when curing large volumes of polyurethane (an exothermic process) as the likely cause. The reader is directed to the chapter appendix (Section 5.5.2) for a description of additional experiments concerning this issue.

5.3.3 Effects of geometric errors

Ray-tracing simulations of parallel-beam CT scanning of uniform cylinders with random geometric errors in ray positioning (Gaussian-drawn, with standard deviations between 1/16th and 2 times the reconstruction pixel size) show that small errors (on the order of 1

pixel length) in ray-path geometry can also generate ring artifacts. The magnitude of these rings is larger towards the peripheral region of the dosimeter, because the change in path length through the dosimeter caused by a random shift is larger than at the center. For half-pixel errors the ring artifact magnitude is less than 2% for the full diameter of the cylinder. This sets a criterion on the required mechanical precision: one should aim for less than half-pixel uncertainties in ray path mapping. It should also be noted that the finite width of the beam in real experiments may mask some of these effects.

In this experiment, setup error in placement of the fiducial is not a major concern because the fiducial is not used for registration or for reproducibility. A full 360° fiducial-scan is acquired, so there is little concern over the initial angular positioning of the marker. The fiducial is similar in diameter to the scanning laser beam, so the detected intensity exhibits a very sharp peak when the beam falls centrally upon it; finding the local minimum signal is a robust way to locate the central point.

If mechanical imperfections in the scanner are minimal, the largest uncertainty in localization of the fiducial is related to the finite number of projections. For simplicity, the angular uncertainty in fiducial location can be approximated as half of the angular spacing between projections. The corresponding Cartesian uncertainty, by applying simple error propagation [41] to Equation 5.1 is:

$$\sigma_{x,y} = \sqrt{R^2 \sigma_\theta^2} \quad (5.2)$$

Where R is the dosimeter radius and σ_θ is the angular uncertainty. Here we have assumed that the radius is a constant, as in this technique it is set as a parameter.

For a 360° scan with 1024 projections, and a dosimeter with a radius of 55 mm, Equation 5.2 results in an uncertainty of approximately 0.165 mm, which is approximately half the reconstructed voxel size shown in this study. This means that, assuming no additional me-

chanical imperfections, our scanning parameters should be sufficient to ensure ring artifact magnitudes of less than 2%. Angular uncertainty can be reduced by acquiring more projections at finer angular resolution and by using multiple fiducials. Mechanical imperfection likely remains the dominant source of uncertainty in this experiment; however a new scanner is under construction which will have much better precision. It should be noted that for large-volume dosimetry problems, reconstructions are often performed at 1 or 2 mm voxel sizes [15, 19], which eases the precision requirement substantially.

5.3.4 Mathematical framework for 3D ray paths

The presented fiducial method can be extended to 3D ray path measurement. Consider the cylindrical object, shown in Figure 5.9, which has two fiducial lines along the wall; one vertical and one angled such that the angular separation $\Delta\theta$ between the two is a known function of the height, z :

$$\Delta\theta = f(z) \tag{5.3}$$

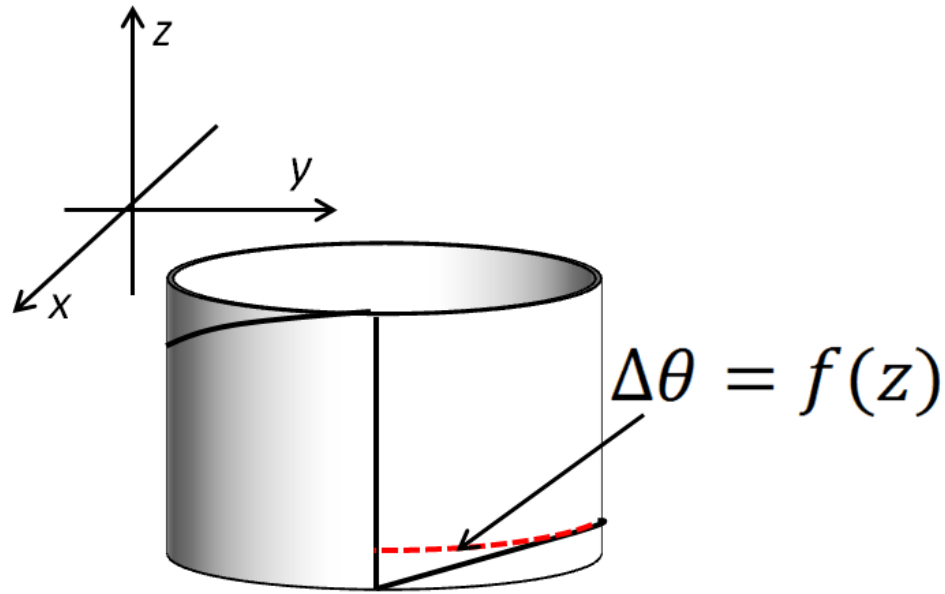


Figure 5.9: Sketch of the fiducial layout needed for ray path measurement in 3D. The z dependence of the angular separation is known.

The sinogram trajectory of the vertical line can be used to determine the x and y coordinates of the ray's trajectory using Equation 5.1 as before. Then, the angular separation between the fiducials at both entry and exit can be used to determine the z coordinates of the ray's entrance and exit point. In fact, it is not required that the object be a perfect cylinder, as long as it is rotationally symmetric and the radius as a function of height is known.

5.4 Discussion and Conclusion

This work demonstrates a new method for using mismatched refractive index optical CT scanning using a scanning laser system with a large-area detector and a fiducial-based ray-path measurement technique. The large area detector allows the capture of rays displaced by refraction through the optical system. Paired with the method of tracking ray paths with a rotating fiducial marker, this system allows one to scan a cylindrical sample with a refractive index higher than that of the surrounding aquarium fluid. The method was tested with a phantom experiment using uniform solutions, as well as a set of experiments using

the PRESAGE[®] solid dosimeter. The results indicate that the technique allows the use of water-based, low viscosity liquids in place of oils in the optical CT aquarium when scanning PRESAGE[®]. Eighty-five percent of the diameter of an 11 cm diameter dosimeter was sampled and reconstructed accurately, which provides a usable diameter of 9.4 cm for 3D radiation dosimetry. The loss of information in the peripheral 8 mm of the dosimeter's radius is not substantially more than the "edge artifacts" that have been previously described [19]. In hindsight, other laser scanner geometries that operate using a small detector, such as those reported by Gore *et al.* [4] and Babic *et al.* [42], could be modified to enable this technique as the detector position relative to the source could be optimized to detect refracted rays in each scanline.

Results presented here pertain to 2D imaging (single slice). Slice by slice and "parallel-3D" scanners are the most common format of pencil beam laser systems that have been reported for dosimetry [5, 16, 43, 44]. Extension to 3D in this case is straightforward. If the sample is truly cylindrical, only one slice is needed for the ray path measurement. For the case of cone-beam laser scanners [26], or other arbitrary scanning trajectories, we have described the fiducial layout that could be used to measure ray paths in three dimensions for rotationally symmetric objects (Section 5.3.4). The fiducial method has been applied to PRESAGE[®] dosimetry in mismatched refractive index fluids, but may also be applied in normal, matched refractive index optical CT. For example, this method could be used to validate scanner geometries or to measure geometric corrections needed for multi-wavelength scanning (since refractive index is wavelength dependent).

There are some limitations to the technique presented here. First, successful application of this approach requires accurate knowledge of the geometry of the system, and high precision in both the rotation stage and the re-positioning of the dosimeter. This is needed in all scanner geometries, but this geometry is particularly sensitive to errors that propagate through the ray path measurement technique and create artifacts (Section 5.3.3). Second, an

auxiliary “ray path measuring” scan is needed when using an opaque fiducial marker, which adds scan time to the experiment. This could be avoided using a partially transmitting fiducial mark, rather than a fully opaque one, which would eliminate the extra scan. Third, because the reconstruction software toolbox required well-defined, standard CT geometry, data was re-binned to parallel beam. However, this leads to a loss of information due to the discrete angles and radii in the re-binned sinogram. Re-binning is not required for iterative CT reconstruction in general. Thus, in future work, ray paths will be used directly with in-house iterative reconstruction code. Lastly, the PRESAGE[®] dosimeters used here are not perfect cylinders, but exhibit a slight taper from bottom to top. This results in a slightly out-of-plane path for a light ray within the dosimeter. PRESAGE[®] has been manufactured in small truly cylindrical samples [45], but scaling up to larger cylinders may be challenging. If the radius is known as a function of height, the 3D extension of the fiducial method discussed in Section 5.3.4 could be used.

Some ring artifacts are visible in the reconstructed PRESAGE[®] images, which are thought to be associated with mechanical error in re-positioning the sample. Our new laser scanner (Chapter 3) [46] has better sample positioning reproducibility, which should reduce these artifacts. More critically, an intrinsic non-uniform dose response in the PRESAGE[®] samples has been observed. The reconstructed attenuation coefficients of uniformly irradiated dosimeters increased radially from the center. Discussions with the manufacturer have suggested that excessive heat during the curing of the polyurethane plastic is the cause. This issue therefore is more likely to occur in large volume dosimeters (>1L) than in smaller samples. The manufacturing process is being modified in an attempt to alleviate this issue and extend the use of PRESAGE[®] to larger dose sampling volumes.

Despite the scanner and dosimeter limitations presented, the results obtained show promise for attaining high accuracy in larger fields of view. The ability to scan in a low-viscosity, mismatched refractive index solution circumvents the use of viscous oil-based solutions,

which eases mixing, filtering, and cleaning, and removes some restrictions on the type of materials used in aquarium construction. Also, the method improves the optical CT workflow, as it is not necessary to undergo trial-and-error refractive index matching, since the ray paths are measured directly from CT scan data for each dosimeter. These improvements would greatly improve the practicality of PRESAGE[®]-based 3D dosimetry in a clinical physics setting.

5.5 Appendix

This appendix contains the results of two additional experiments performed during the study. These experiments do not relate to the technique being presented in the paper itself, but are important in discussion of the issues that have been encountered when imaging PRESAGE[®] dosimeters.

5.5.1 PRESAGE[®] dose response non-uniformity

Throughout experiments, it was observed that large volume PRESAGE[®] dosimeters may suffer from non-uniform dose response. Specifically, there is lower dose sensitivity in the center of the dosimeter than towards the periphery. To confirm that this observed non-uniformity was dosimeter-related, and not caused by the scanner, four 11 cm diameter PRESAGE[®] dosimeters from different manufacturing batches were irradiated and imaged. Dosimeters were irradiated to uniform doses of 1 Gy. Reconstructions were performed with 1 mm pixel resolution in order to suppress other noise and artifacts to better examine the large-scale non-uniformity. Figure 5.10 shows central profiles (normalized to the central attenuation value) through these reconstructions, demonstrating the non-uniformity.

All dosimeters showed non-uniformity; however the magnitude differed between samples, ranging from a 20% (minimum to maximum) difference in the worst sample, to a 5% dif-

ference in the best samples. Due to the inconsistency in the magnitude of this effect, and the fact that the proof-of-concept uniform phantom reconstruction was flat (Section 5.3.1), the effect has been traced back to the PRESAGE[®] dosimeter itself. Additionally, performing a uniform “pre-irradiation” and using it to normalize reconstructions of subsequent irradiations results in flat profiles. This is shown in Figure 5.11, where uniform doses of (nominally) 1.1 Gy and 2.2 Gy were delivered to the same sample. The 1.1Gy irradiation is used to calculate a dose sensitivity map, which, when applied to the 2.2 Gy irradiation, results in a flat profile (in the fully-sampled region). This result indicates that the dosimeter is linear, but has spatially non-uniform sensitivity. Discussions with the dosimeter’s manufacturer suggest that this is likely caused by excessive heat generated during the casting of large volumes of polyurethane, and may be related to a high concentration of metal catalysts in the raw material. The manufacturer is working to resolve this issue [40].

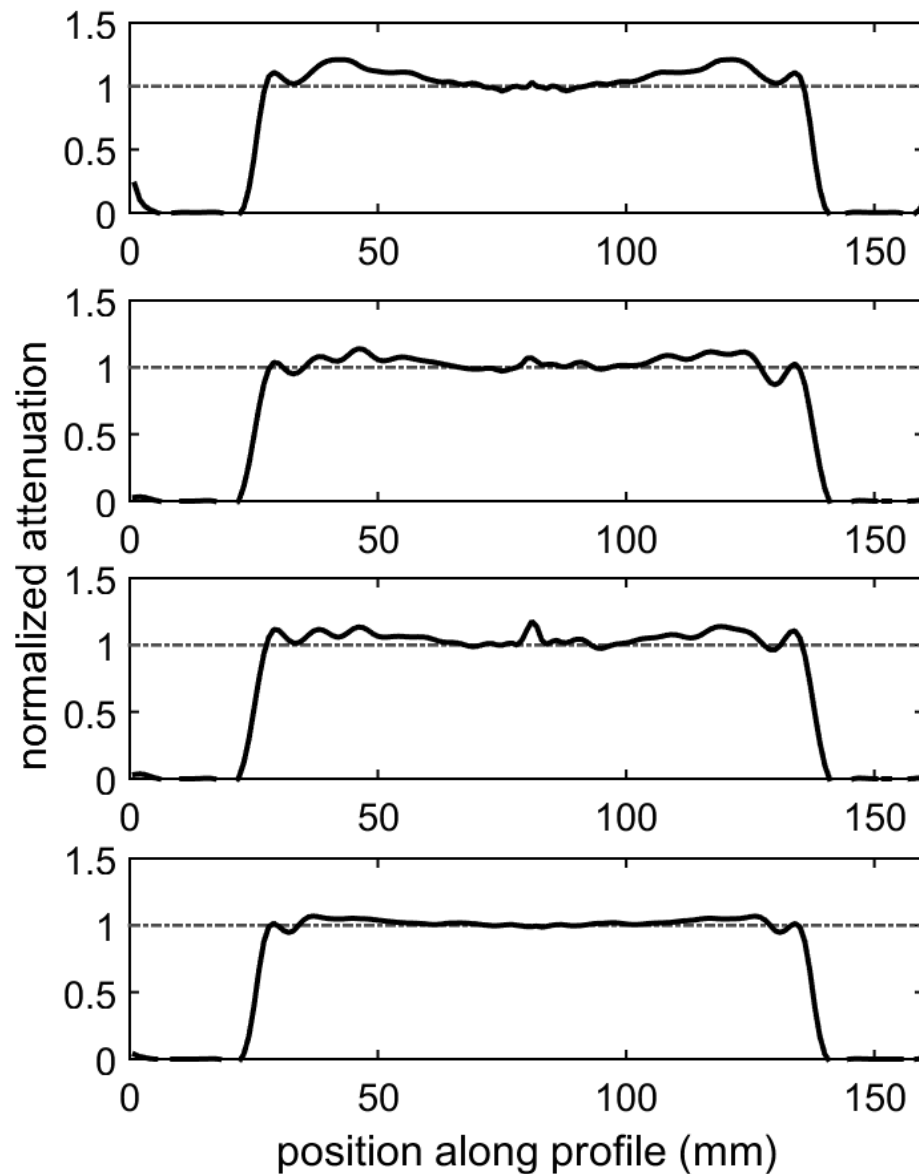


Figure 5.10: Central profiles (1 mm pixel resolution) through reconstructions of four uniformly irradiated PRESAGE[®] dosimeters manufactured in different batches, with non-uniformity in response ranging from severe (top) to moderate (bottom). The dashed grey lines in the plots indicate uniform attenuation. There is a substantial non-uniformity in some dosimeters, up to 20% difference from central to maximum response. The non-uniformity is inconsistent from batch to batch. The best dosimeters, used in the main experiments in this paper, exhibit approximately 5% non-uniformity (minimum to maximum response).

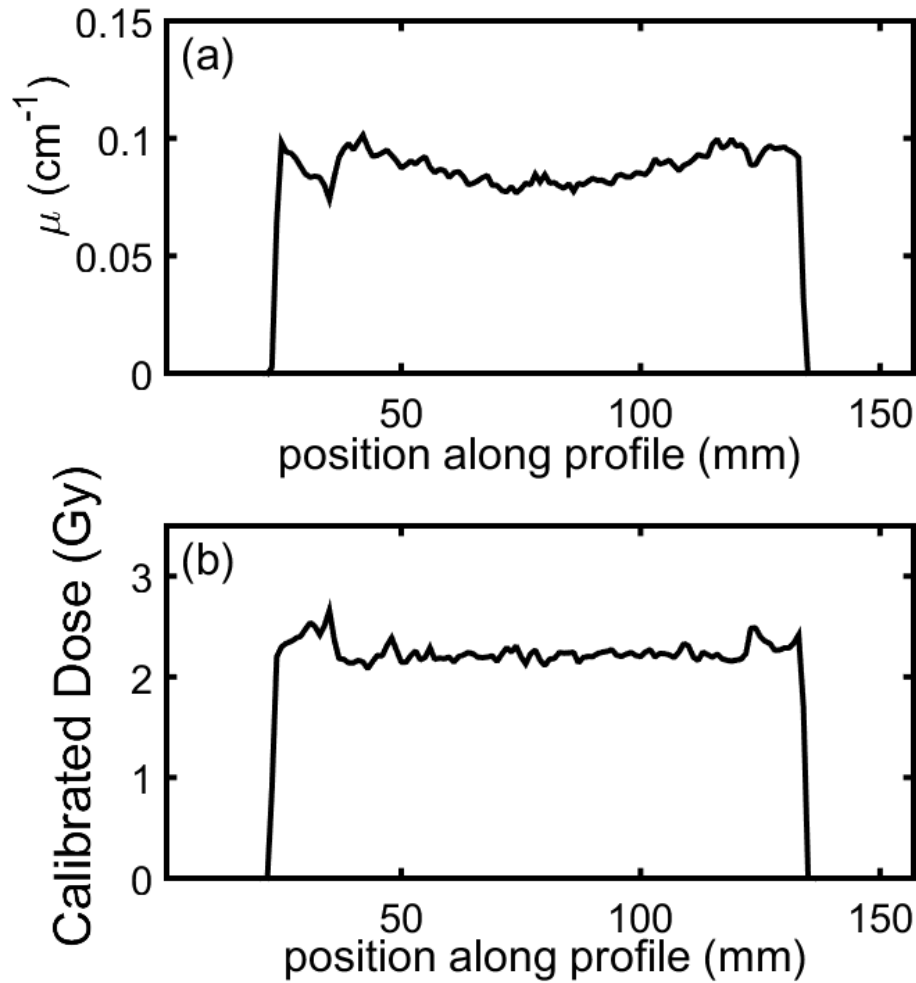


Figure 5.11: Central profile (1 mm pixel resolution) through a PRESAGE® dosimeter irradiated to a nominal dose of 2.2 Gy. (a) raw attenuation profile. (b) calibrated dose profile using a “pre-irradiation” of 1.1 Gy to create a spatial dose response map. Note that the calibrated dose profile is flat within the fully sampled region (the “spikes” in (b)), but the calibration fails outside of it. This dosimeter exhibited fairly severe non-uniformity in response.

5.5.2 PRESAGE® optical activity

In an attempt to determine the cause of artifacts in the PRESAGE® reconstructions, dosimeters were examined with polarized light to test for optical activity. The setup to probe optical activity is shown schematically in Figure 5.12a and consists of an unpolarized light source, camera, and a pair of linear polarizers oriented perpendicularly to each other. Light

is emitted from the source, and the vertically polarized component is transmitted through the first polarizer. It then travels through the aquarium filled with 100% glycerol and the PRESAGE[®] dosimeter before reaching the horizontal polarizer. If there is no optical activity, the camera will not detect any light transmitted through the system. However, if an optically active element is placed between the polarizers it will rotate the plane of polarization of the vertically polarized light, giving rise to a horizontal component to the polarization that will be transmitted through the horizontal polarizer. The camera will then detect this transmitted component. Figures 5.12b and 5.12c show the images acquired using this setup with a single vertical polarizer and with the crossed polarizers.

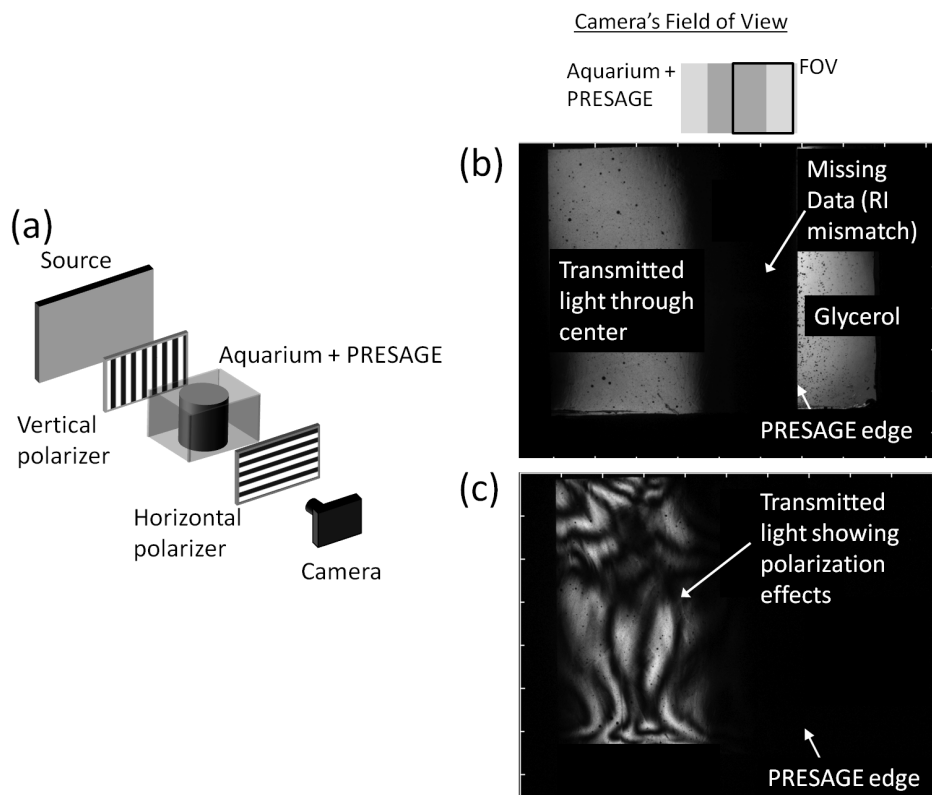


Figure 5.12: (a) Schematic of apparatus used to examine optical activity in PRESAGE[®] dosimeters. If the dosimeter is optically active, the camera will detect signal, otherwise the image will be dark. (b,c) Transmission images acquired using a single polarizer (b) and crossed polarizers (c). With crossed polarizers there is no transmission through the glycerol, indicating that it is not optically active. However, fringe patterns of transmission are visible in the light transmitted through the PRESAGE[®] dosimeter, indicating structured optical activity.

In Figure 5.12c, it can be seen that the glycerol is not optically active, as there is no transmission in the crossed polarizer case in the field of view outside the PRESAGE[®] sample. However, through the central region of the dosimeter where refraction does not cause loss of signal, patterns can be seen in the transmission image, indicating that the dosimeter has optical activity. Experimenting with different dosimeters indicates that these optical activity patterns are unique to each cylinder. Examining un-dyed polyurethane shows the same effect, which rules out the radiochromic dye as a possible cause. This non-uniform optical activity may also be related to heat dissipation during the curing process. Since a polarized light source is used to image these dosimeters in the laser scanner, it is expected that optical activity will have some effect on the measurements, as optical processes exhibit polarization dependence [47]. Additionally, if the patterns are indeed related to heat dissipation during polyurethane curing, then these features may be spatially correlated to local fluctuations in dosimetric response that are larger than the noise level in the reconstruction. Whether or not a correlation exists is under investigation.

5.6 References

1. Doran, S. J. The history and principles of chemical dosimetry for 3-D radiation fields: Gels, polymers and plastics. *Applied Radiation and Isotopes* **67**, 393–398 (Mar. 2009).
2. Baldock, C. *et al.* Polymer gel dosimetry. *Physics in Medicine and Biology* **55**, R1–R63 (Mar. 7, 2010).
3. Oldham, M. Radiochromic 3D Detectors. *Journal of Physics: Conference Series* **573**, 012006 (Jan. 12, 2015).
4. Gore, J. C., Ranade, M., Maryanski, M. J. & Schulz, R. J. Radiation dose distributions in three dimensions from tomographic optical density scanning of polymer gels: I. Development of an optical scanner. *Physics in Medicine and Biology* **41**, 2695 (1996).
5. Kelly, R. G., Jordan, K. J. & Battista, J. J. Optical CT reconstruction of 3D dose distributions using the ferrous-benzoic-xyleneol (FBX) gel dosimeter. *Medical Physics* **25**, 1741 (1998).

6. Campbell, W. G., Rudko, D. A., Braam, N. A., Wells, D. M. & Jirasek, A. A prototype fan-beam optical CT scanner for 3D dosimetry. *Medical Physics* **40**, 061712 (June 1, 2013).
7. Wolodzko, J. G., Marsden, C. & Appleby, A. CCD imaging for optical tomography of gel radiation dosimeters. *Medical Physics* **26**, 2508 (1999).
8. Olding, T., Holmes, O. & Schreiner, L. J. Cone beam optical computed tomography for gel dosimetry I: scanner characterization. *Physics in Medicine and Biology* **55**, 2819–2840 (May 21, 2010).
9. Doran, S. J. *et al.* A CCD-based optical CT scanner for high-resolution 3D imaging of radiation dose distributions: equipment specifications, optical simulations and preliminary results. *Physics in Medicine and Biology* **46**, 3191 (2001).
10. Krstajic, N. & Doran, S. J. Characterization of a parallel-beam CCD optical-CT apparatus for 3D radiation dosimetry. *Physics in Medicine and Biology* **52**, 3693 (July 7, 2007).
11. Sakhalkar, H. S. & Oldham, M. Fast, high-resolution 3D dosimetry utilizing a novel optical-CT scanner incorporating tertiary telecentric collimation. *Medical Physics* **35**, 101–111 (Jan. 2008).
12. US20040211917 A1. U.S. Classification 250/474.1, 600/3, 252/600; International Classification G01T, G01T1/00, G01T1/06, G01T1/02; Cooperative Classification G01T1/06; European Classification G01T1/06 (2004).
13. Guo, P., Adamovics, J. & Oldham, M. A practical three-dimensional dosimetry system for radiation therapy. *Medical Physics* **33**, 3962 (2006).
14. Gorjiara, T. *et al.* Investigation of radiological properties and water equivalency of PRESAGE dosimeters. *Medical Physics* **38**, 2265–2274 (Apr. 1, 2011).
15. Jackson, J., Juang, T., Adamovics, J. & Oldham, M. An investigation of PRESAGE 3D dosimetry for IMRT and VMAT radiation therapy treatment verification. *Physics in Medicine and Biology* **60**, 2217 (Mar. 21, 2015).
16. Krstajic, N. & Doran, S. J. Fast laser scanning optical-CT apparatus for 3D radiation dosimetry. *Physics in Medicine and Biology* **52**, N257 (June 7, 2007).
17. Sakhalkar, H. S., Adamovics, J., Ibbott, G. & Oldham, M. A comprehensive evaluation of the PRESAGE/optical-CT 3D dosimetry system. *Medical Physics* **36**, 71 (2009).
18. Sakhalkar, H., Sterling, D., Adamovics, J., Ibbott, G. & Oldham, M. Investigation of the feasibility of relative 3D dosimetry in the Radiologic Physics Center Head and Neck IMRT phantom using Presage/optical-CT. *Medical Physics* **36**, 3371–3377 (July 1, 2009).
19. Thomas, A., Newton, J., Adamovics, J. & Oldham, M. Commissioning and benchmarking a 3D dosimetry system for clinical use. *Medical Physics* **38**, 4846–4857 (Aug. 2011).
20. Wu, C.-S., Hoogcarpsel, S. J., Deh, K., Hsu, W.-Y. & Adamovics, J. 3-D dose verification by cone-beam optical CT scanning of PRESAGE dosimeter. *Journal of Physics: Conference Series* **444**, 012044 (June 26, 2013).
21. Chisholm, K., Miles, D., Rankine, L. & Oldham, M. Investigations into the feasibility of optical-CT 3D dosimetry with minimal use of refractively matched fluids. *Medical Physics* **42**, 2607–2614 (May 1, 2015).

22. Bache, S., Malcolm, J., Adamovics, J. & Oldham, M. Investigation of a low-cost optical-CT system with minimal refractive index-matching fluid. *Journal of Physics: Conference Series* **573**, 012052 (Jan. 12, 2015).
23. Doran, S. J. & Yatigammana, D. N. B. Eliminating the need for refractive index matching in optical CT scanners for radiotherapy dosimetry: I. Concept and simulations. *Physics in Medicine and Biology* **57**, 665–683 (Feb. 7, 2012).
24. Rankine, L. & Oldham, M. On the feasibility of optical-CT imaging in media of different refractive index. *Medical Physics* **40**, 051701 (2013).
25. US20120170049 A1. U.S. Classification 356/496; International Classification G01B11/02; Cooperative Classification G01N21/4795, G01T1/105, G01B11/02, G01M11/0257; European Classification G01T1/105, G01N21/47S, G01B11/02, G01M11/02D4 (2012).
26. Jordan, K. J., Turnbull, D. & Battista, J. J. Laser cone beam computed tomography scanner geometry for large volume 3D dosimetry. *Journal of Physics: Conference Series* **444**, 012062 (June 26, 2013).
27. Dekker, K. H., Battista, J. J. & Jordan, K. J. Stray light in cone beam optical computed tomography: II. Reduction using a convergent light source. *Physics in Medicine and Biology* **61**, 2910 (2016).
28. Cho, Y., Moseley, D. J., Siewerdsen, J. H. & Jaffray, D. A. Accurate technique for complete geometric calibration of cone-beam computed tomography systems. *Medical Physics* **32**, 968–983 (Apr. 1, 2005).
29. Xu, M., Zhang, C., Liu, X. & Li, D. Direct determination of cone-beam geometric parameters using the helical phantom. *Physics in Medicine and Biology* **59**, 5667–5690 (Oct. 7, 2014).
30. Ramm, D., Rutten, T. P., Shepherd, J. & Bezak, E. Optical CT scanner for in-air readout of gels for external radiation beam 3D dosimetry. *Physics in Medicine and Biology* **57**, 3853–3868 (June 21, 2012).
31. Jochen Birk, U., Darrell, A., Konstantinides, N., Sarasa-Renedo, A. & Ripoll, J. Improved reconstructions and generalized filtered back projection for optical projection tomography. *Applied optics* **50**, 392–398 (2011).
32. Antonopoulos, G. C. *et al.* Correction of image artifacts caused by refractive index gradients in scanning laser optical tomography in. SPIE BiOS (International Society for Optics and Photonics, Mar. 12, 2014), 894907–894907–6.
33. Hoyt, L. F. New Table of the Refractive Index of Pure Glycerol at 20°C. *Industrial & Engineering Chemistry* **26**, 329–332 (Mar. 1934).
34. Olding, T. & Schreiner, L. J. Cone-beam optical computed tomography for gel dosimetry II: imaging protocols. *Physics in Medicine and Biology* **56**, 1259 (Mar. 7, 2011).
35. Palenstijn, W. J., Batenburg, K. J. & Sijbers, J. Performance improvements for iterative electron tomography reconstruction using graphics processing units (GPUs). *Journal of structural biology* **176**, 250–253 (2011).
36. Van Aarle, W. *et al.* The ASTRA Toolbox: A platform for advanced algorithm development in electron tomography. *Ultramicroscopy* **157**, 35–47 (Oct. 2015).
37. Gilbert, P. Iterative methods for the three-dimensional reconstruction of an object from projections. *Journal of Theoretical Biology* **36**, 105–117 (July 1972).

38. MacBeth, G. & Thompson, A. R. Densities and Refractive Indexes for Propylene Glycol-Water Solutions. *Analytical Chemistry* **23**, 618–619 (1951).
39. Matenine, D., Goussard, Y. & Despres, P. GPU-accelerated regularized iterative reconstruction for few-view cone beam CT. *Medical Physics* **42**, 1505–1517 (Apr. 1, 2015).
40. Adamovics, J. *Private Email Communication* E-mail. Sept. 1, 2015.
41. Taylor, J. R. *An Introduction to Error Analysis: The Study of Uncertainties in Physical Measurements* 356 pp. (University Science Books, Jan. 1997).
42. Babic, S., Battista, J. & Jordan, K. Three-Dimensional Dose Verification for Intensity-Modulated Radiation Therapy in the Radiological Physics Centre Head-and-Neck Phantom Using Optical Computed Tomography Scans of Ferrous Xylenol-Orange Gel Dosimeters. *International Journal of Radiation Oncology - Biology - Physics* **70**, 1281–1291 (Mar. 15, 2008).
43. Oldham, M., Siewerdsen, J. H., Kumar, S., Wong, J. & Jaffray, D. A. Optical-CT gel-dosimetry I: Basic investigations. *Medical Physics* **30**, 623–634 (Apr. 1, 2003).
44. Maryanski, M. J., Zastavker, Y. Z. & Gore, J. C. Radiation dose distributions in three dimensions from tomographic optical density scanning of polymer gels: II. Optical properties of the BANG polymer gel. *Physics in Medicine and Biology* **41**, 2705 (1996).
45. Doran, S. J. *et al.* Establishing the suitability of quantitative optical CT microscopy of PRESAGE radiochromic dosimeters for the verification of synchrotron microbeam therapy. *Physics in Medicine and Biology* **58**, 6279 (Sept. 21, 2013).
46. Dekker, K. H., Battista, J. J. & Jordan, K. J. Scanning laser optical computed tomography system for large volume 3D dosimetry. *Physics in Medicine and Biology* **62**, 2636 (2017).
47. Hecht, E. *Optics* 698 pp. (Addison-Wesley, 2002).

Chapter 6

Applications of Optical CT: Small Field Dosimetry

In this chapter, the new optical CT scanner developed in Chapter 3 and the reconstruction algorithms described in Chapter 4 are applied to the problem of small field dosimetry. This serves to demonstrate that the developments presented in this thesis have indeed improved the accuracy and precision of optical CT scanning to the point where clinically-relevant tasks can be performed.

The gel dosimetry work in this chapter was performed by Kurtis H. Dekker, Kevin J. Jordan, and Sydney Bell. Gel preparation was performed by KJJ and SB. Irradiations were performed by KJJ, KHD, and SB. Optical CT imaging and data analysis was performed by KHD. In addition, Monte Carlo simulations that had been previously performed by Matt Mulligan were utilized for comparison to gel data.

6.1 Background: Small Field Dosimetry

The definition of a “small field” in radiation therapy and dosimetry is somewhat subjective. As a rule of thumb, a square field size of less than $3 \times 3 \text{ cm}^2$ is often considered to be a small field that requires some care in both dose calculation and measurement [1]. Bassinet

et al. state that megavoltage photon beams are considered “small fields” when either of the following statements are true [2]:

- The field dimensions are such that the electrons set in motion at the field center have sufficient lateral range to reach the beam edges (energy dependent). This leads to a disruption in lateral charged particle equilibrium (CPE).
- The collimating device (Jaws, Multi-leaf collimators, etc) is set to an aperture that is smaller than the physical source itself, leading to more complicated field penumbrae.

Currently, linear accelerators equipped with multileaf collimators (MLCs) or dedicated circular apertures, are able to deliver field sizes down to approximately 4-6 mm across. At these small field sizes, charged particle equilibrium is lost because secondary electrons generated within the beam have an average lateral travel distance larger than half the field size. This means that secondary electrons leaving a volume at the center of beam are not being replaced at the same rate, a phenomenon that is known as Lateral Electron Disequilibrium. This leads to a dramatic drop in central axis dose for small fields compared to larger fields [3]. If one plots the central axis dose of a 6MV photon beam as a function of field size, the precipitous fall-off in dose for fields smaller than approximately 1 cm becomes clear. Due to the fact that these small fields are 1) physically small, 2) have no “flat” central portion, and 3) have steep dose gradients, it is challenging to accurately measure central axis doses and beam profiles using point detectors, either due to the relatively large volume of the detector [3, 4], or because it is difficult to achieve precise alignment along the central axis [5]. Additionally, small fields exhibit lateral electron disequilibrium throughout their entire profile, and point detectors will perturb this disequilibrium significantly if they contain material that is highly non-equivalent to water [1].

Despite the difficulties associated with small field dosimetry, it is a necessary task. Kairn *et al.* demonstrated that if an inappropriate measurement strategy (one more suited to large fields) was used to measure small field output factors, isocentre dose errors of up to 3.3

% could be observed in routine stereotactic radiotherapy or radiosurgery treatment fields less than 9 mm across [6]. Furthermore, they found substantial dose errors, up to 11 %, in complicated treatment fields wherein MLC leaves are separated by less than 12 mm. Therefore, they recommended that small field dosimetry must be performed carefully if fields (or MLC leaf gaps in IMRT) less than 15 mm across are clinically used.

6.1.1 Measuring small fields with gels

A gel dosimeter has several advantages for measuring small radiation fields. First, it is uniform and nearly water-equivalent and thus lateral electron equilibrium (or disequilibrium) is not perturbed. Second, as a large, isotropic-resolution, integrating dosimeter, exact alignment when performing the measurement is less critical, because the exact field center can be located when processing data. Third, gel dosimeters allow a single radiation exposure to capture an entire small field dose distribution (to a certain depth, typically ~10-15 cm), which reduces the amount of machine time required to characterize a given field size. Finally, depending on the field sizes, multiple beams can even be delivered to the same gel dosimeter for improved efficiency.

The challenges associated with small field dosimetry in gels historically have been associated with diffusion of radiochromic dyes and with stray light in the optical CT imaging systems. Diffusion causes the dose gradients delivered to lose spatial integrity. In small fields, the central axis dose can even be degraded by this diffusion. Stray light in diffuser-source broad-beam optical CT has been shown to artificially suppress attenuation coefficients in small objects [7, 8]. However, with the planar scanner (chapter 3) and the modified broad-beam source (chapter 2) developed in this dissertation, we have reduced the stray light contribution in optical CT considerably to minimize this limitation. Additionally, the leuco-crystal-violet dosimeter using sodium dodecyl sulfate as the surfactant (LCV-SDS) exhibits a very low diffusion rate [9]. Thus, we now have the tools to enable

accurate small field measurements in gel dosimeters.

This chapter describes a small-field dosimetry experiment performed in our cancer center using LCV-SDS gel with the prototype planar scanning laser system (chapter 3). We present relative dose factors (RDFs), percent depth dose (PDD) curves, and lateral beam profiles for jaw-defined small fields (0.6×0.6 cm - 3×3 cm) at 6MV, delivered on a Varian 21iX linear accelerator. We compare our gel dosimetry measurements to Monte Carlo simulations performed using EGS-nrc [10]. The parameters used in these simulations had been previously tuned such that they matched measurements made using an ion chamber, and thus the Monte Carlo simulation should be a fairly accurate representation of the delivered dose. These simulation parameters were *not* altered for this experiment.

6.2 Small Field Dosimetry Experiment

6.2.1 Gel preparation

The LCV-SDS gel dosimeter was prepared according to the method described by Jordan *et al.* [9], using (by weight) 5% gelatin (300 bloom, porcine, Sigma Aldrich), 95 % water, 1 mM SDS, 1 mM LCV and (initially) 25 mM trichloroacetic acid. To make the batch of gel, about 10% of the water was used to dissolve the TCAA and LCV, and the remainder to dissolve gelatin. Gelatin was added slowly to water at 293K to avoid clumping. 1mM hydrogen peroxide was added to the gelatin/water mixture to sterilize it, and it was stirred at 328 degrees K for approximately 5 hours. The gelatin/water/peroxide mixture was left at room temperature overnight, and then brought back up to 328K the next day for another 5 hours. The purpose of these heating periods was to consume peroxide from the system prior to adding the radiochromic dye, in order to reduce the pre-irradiation conversion of leuco dye to the coloured form. The level of peroxide in the gel was periodically checked by adding approximately 1 mL of gel to 3 mL of Ferrous Xylenol Orange (FX) solution

and checking for colour change either visually or by absorption spectrometer measurement (water reference).

Once the peroxides were consumed, the gel was cooled to 305K and the LCV + TCAA solution was added, with stirring and exposure to room air for reoxygenation. The gel was then poured into the desired 15 cm diameter vessel and stored overnight in a refrigerator at approximately 277K. Unfortunately, the next day (irradiation day), the gel was found to be opalescent (cloudy appearance). This is a phenomenon that had been reported by Babic *et al.* [11], and occurs when the concentration of the trichloroacetic acid is too low. The reason that this occurred in this gel preparation is because we had modified our previously standard 4% gelatin to 5% gelatin in order to achieve a stronger hydrogel for the large dosimeter volume, but had neglected to add additional TCAA to compensate.

To remedy the error, the gel was re-melted (at 308K) in the 15 cm vessel and more acid was added, bringing the concentration of TCAA up to 30 mM. This removed the opalescent appearance. The gel was then transferred to a water bath at 292K, shielded from light, and left at rest for approximately 4 hours before being scanned on the optical CT scanner (time from re-cast to first irradiation was approximately 5 hours). As we discuss later in section 6.4, pouring and using the gel on the same day actually provides the best datasets when using this dosimeter.

6.2.2 Irradiation

Irradiation was performed using the 6MV photon beam on a Varian 21iX linear accelerator. 6MV photons were chosen as they were the lowest energy available on the machine. The lower the energy, the smaller the field size before a loss of lateral charged particle equilibrium occurs. Thus, using the definition in Section 6.1, 6MV “small fields” are smaller than those at higher energies, representing a more challenging imaging task for the optical CT scanner.

Jaw-defined fields of (nominally) 3.0×3.0 , 2.0×2.0 , 1.0×1.0 , and 0.6×0.6 cm² were delivered in the pattern shown in Figure 6.1. The gel dosimeter was placed within a water tank and was irradiated from the top (SSD = 90 cm), with the surface exposed to air. The monitor units delivered for each field were calculated from empirically determined output factors (from previous film measurements) such that approximately 20 Gy would be deposited at a depth of 10 cm in each field.

6.2.3 Optical CT imaging

The optical CT dataset contained 1024 two-dimensional projections of size 750×560 , acquired using the planar laser scanner (Chapter 3) operating with a 594 nm Helium-Neon laser. The projection pixel size was 0.25 mm in both horizontal and vertical directions. Reconstructions were performed at 0.33 mm voxel resolution using in-house CUDA implementations of FBP (hamming filter) and OSC-TV (10 iterations, 20 TV-minimization iterations, and $c = 0.25$). For dosimetric analyses, the OSC-TV reconstructions were used, after confirming that the mean attenuation value at the center of the smallest field was not degraded by this choice of reconstruction algorithm (Chapter 4).

6.3 Small Fields Analysis

Figure 6.1 shows axial, sagittal and coronal slices through a reconstruction for the small-field dosimetry experiment.

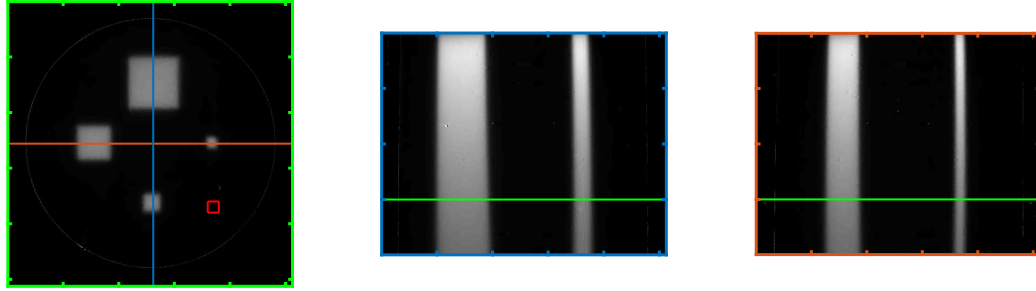


Figure 6.1: Small-field gel dosimetry dataset. Axial (10 cm depth), sagittal and coronal slices of the reconstruction (OSC-TV) are shown. Reconstruction matrix size was $512 \times 512 \times 400$ voxels (0.33 mm isotropic). Window/level = $0.25/0.5 \text{ cm}^{-1}$. The red square outlined in the left panel (side length = 10 mm) is a region of interest used to measure background auto-oxidation.

In the small field dosimetry dataset, a cubic region of interest of size $10 \times 10 \times 10 \text{ mm}^3$, located away from the delivered beams (indicated by the red box in Figure 6.1), was used to quantify background signal due to auto-oxidation between the pre- and post-scan. This value was subtracted from the 3D attenuation coefficient images.

6.3.1 Measured field size

At a depth of 10 cm in the gel data, 30, 18, 9, or 3 line profiles in both the X and Y directions (“crossline” and “inline” directions, using clinical physics terminology) were averaged for the 3×3 , 2×2 , 1×1 and $0.6 \times 0.6 \text{ cm}$ fields, respectively. These measurements are reported in column 2 of table 6.1. It can be seen that the field sizes measured in the gel (by taking the full-width at half-max of the small fields) match fairly well with the nominal field sizes, varying by no more than 0.6 mm.

At small field sizes, the output factor is strongly dependent on field size, and therefore it is important that field size be verified in each small field experiment. This highlights a strength of using integrating dosimeters, such as gels, for small field dosimetry, as the field size can be measured simultaneously with the central axis dose.

6.3.2 Relative dose factors (RDFs)

Since we did not have an independent calibration gel to enable “absolute” dose measurement for this experiment, we computed Relative Dose Factors (RDFs) using the $3 \times 3 \text{ cm}^2$ field as the reference. This was defined as the ratio of central axis attenuation coefficients (normalized by the number of Monitor Units delivered) at 10 cm depth for the field size in question compared to the 3×3 field.

Field	Measured Field Size ($X \times Y$, cm)	Averaging ROI Size (mm)	RDF (vs 3×3)
3×3 , 21iX, jaw-defined	2.97×3.06	$10 \times 10 \times 2$	1.000
2×2 , 21iX, jaw-defined	1.99×2.02	$6 \times 6 \times 2$	0.946
1×1 , 21iX, jaw-defined	1.00×1.02	$3 \times 3 \times 2$	0.815
0.6×0.6 , 21iX, jaw-defined	0.61×0.66	$1 \times 1 \times 2$	0.627

Table 6.1: Measured FWHM field sizes (10 cm depth) and relative dose factors (vs. 3×3 field) for small fields (6 MV).

Output factors for Varian linear accelerators measured by point detectors have been reported in studies making use of small ion chambers, diamond detectors, and plastic scintillators. Table 6.2 displays comparisons between our RDFs (relative to the 3×3 field) and those derived from studies where measurements were performed at $\text{SSD} = 90 \text{ cm}$ and $d = 10 \text{ cm}$.

Study	Relative Dose Factor (vs. 3×3)		Detector Used
	1×1	2×2	
Beirholm <i>et al.</i> 2014 [12]	0.825 ± 0.005	0.953 ± 0.002	Scintillator (DTU ME40)
Beirholm <i>et al.</i> 2014 [12]	0.835 ± 0.005	0.951 ± 0.001	MicroDiamond (PTW60003)
Beirholm <i>et al.</i> 2014 [12]	N/A	0.950 ± 0.003	Ion Chamber (PTW31014)
Russo <i>et al.</i> 2016 [13]	0.83 ± 0.02	0.95 ± 0.01	MicroDiamond (PTW60019)
Mancosu <i>et al.</i> 2017 [14]	0.83 ± 0.02	0.95 ± 0.02	Scintillator (Exradin W1)
LCV gel (Trial 1)	0.82 ± 0.01	0.95 ± 0.01	15 cm gel, laser CT
LCV gel (Trial 2)	0.81 ± 0.01	0.95 ± 0.01	15 cm gel, laser CT
LCV gel (Trial 3)	0.81 ± 0.01	0.95 ± 0.01	15 cm gel, laser CT

Table 6.2: Relative Dose Factors (3×3 reference) for 6MV photons, measured at $\text{SSD} = 90 \text{ cm}$ and $d = 10 \text{ cm}$. Results from 3 trials of the gel dosimetry experiment, performed using different batches of LCV-SDS, are included (bold font). External study results have been calculated from reported output factors for 3×3 , 2×2 , and $1 \times 1 \text{ cm}^2$ field sizes, where available.

It should be noted that the irradiation parameters were not completely identical for all of the studies. For example, Russo *et al.* [13] combined results from TrueBeam and Clinac accelerators, while Beierholm *et al.* [12] only reported TrueBeam data. Additionally, in Mancosu *et al.* [14], fields were shaped using MLCs, while in Russo *et al.* they were shaped using the MLCs with jaws following the MLC apertures. In contrast, in our work and in Beirholm *et al.*, fields were shaped using the linear accelerator jaws. While these differences may introduce some additional variation between studies, on average the results appear quite consistent with each other. Our RDF values agree with those calculated from reported Relative Output Factors (using a $10 \times 10 \text{ cm}^2$ reference) within 1-2 % in most cases, which is a very encouraging result.

6.3.3 Field profiles and percent depth dose curves

The field profiles (X and Y) measured at 10 cm depth, as well as central axis percent depth dose (PDD) curves, are plotted in Figures 6.2 and 6.3. Profiles and PDDs obtained from Monte Carlo simulations (EGSnrc [10]) are also plotted. Datasets were normalized to each other at a depth of 5 cm for each field size. This depth was chosen as it corresponded to the center of the gel, relatively far from the air interface at the top, to avoid normalizing in a region potentially perturbed by oxygen permeation.

The input parameters used in the Monte Carlo simulation were informed by various measurements made previously on accelerators in the London Regional Cancer Program, using various point and planar dosimeters, and therefore should closely represent the beam characteristics. However, it is important to note that Monte Carlo simulations are not experimental datasets, and actual measurements should take precedent where available.

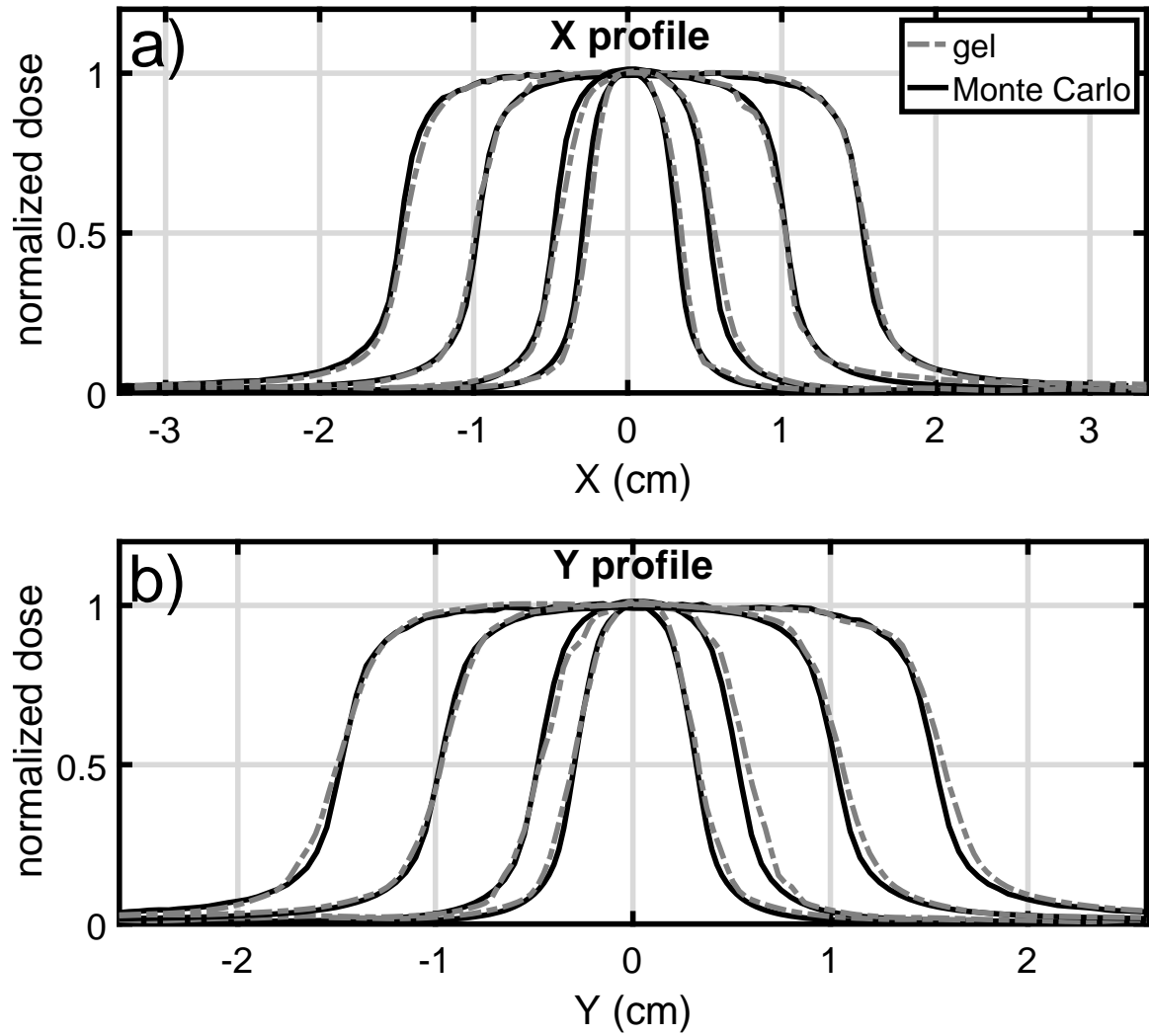


Figure 6.2: Gel and Monte Carlo beam profiles at 10 cm depth for small fields (Varian 21iX, 6MV, jaw-defined fields). Profiles plotted here are normalized to the *gel*. For visibility, error bars are not included.

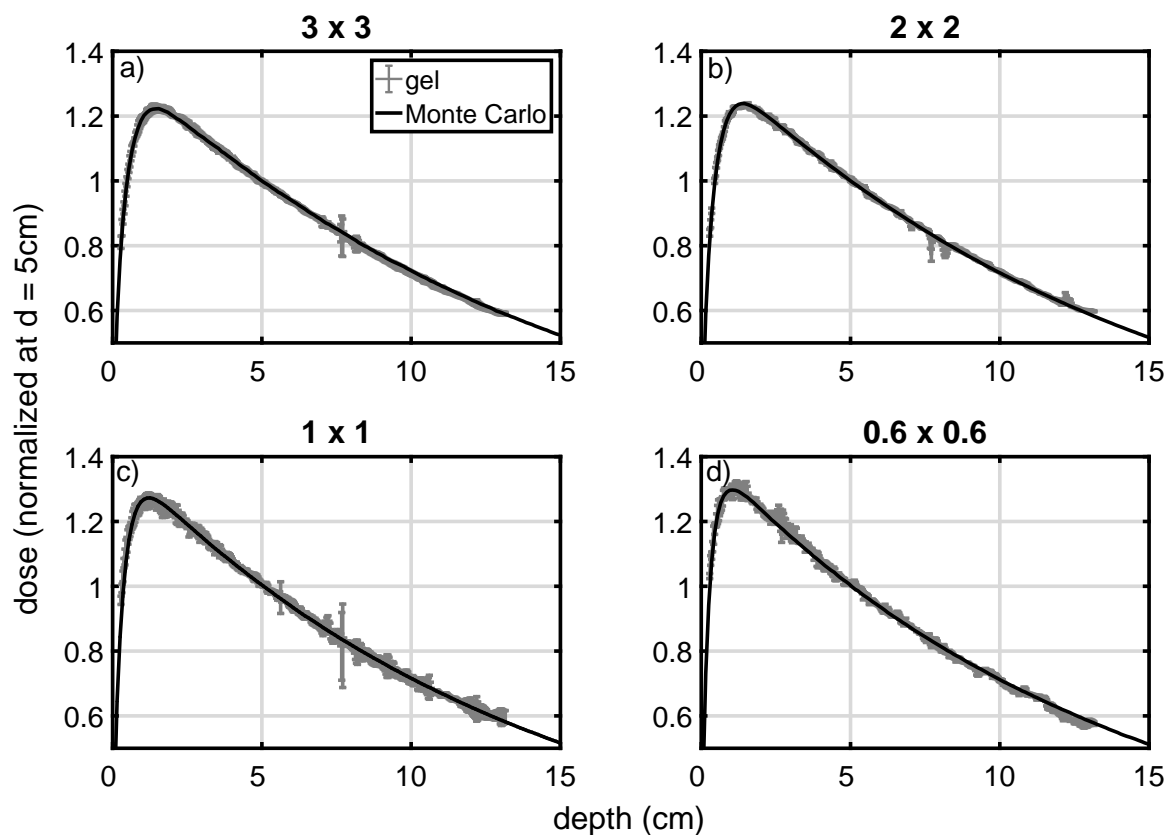


Figure 6.3: Gel and Monte Carlo Percent Depth Dose curves for small fields (Varian 21iX, 6MV, jaw-defined fields). Doses have been normalized at the field center at 5 cm depth. Large spikes in the magnitude of error bars correspond to ring artifacts in the reconstruction.

The gel PDD curves occasionally show deviations as large as 5 - 10 % compared to Monte Carlo simulation. However, if the reconstruction is visually examined, these larger deviations can be seen to correspond to artifacts such as rings or occasionally to bubbles in the gel. If the reconstruction slices containing such artifacts are disregarded, the maximum discrepancy between the gel and Monte Carlo data is less than 2 % for all of the PDD curves. In most cases, it is possible to identify and remove ring artifacts, by interpolation of projection images, without loss of information. The X and Y profiles (at depth of 10 cm, SAD100) also appear very similar to the Monte Carlo simulation, although there are small field size discrepancies as noted in Table 6.1. In addition, the field edges for the X profiles are slightly sharper than those in the Y profiles in the gel measurement due to the position offset of the X and Y jaws in the treatment unit (Y jaws are above X jaws) which was not modeled in the Monte Carlo simulation.

Overall, the small field gel dosimetry results for the 21iX linear accelerator show very good agreement with Monte Carlo simulations performed using input parameters that were previously empirically determined for that machine (and not further adjusted for the experiments reported here). This result indicates that gel dosimetry can be used to obtain reliable commissioning-style measurements of small radiation fields.

6.4 Gel Preparation Insights

The gel preparation error described in Section 6.2.1 forced us to melt and re-cast our gel dosimeter on the same day as irradiation. While this had the unfortunate effect of generating a very dark gel dosimeter (initial transmission was approximately 2% relative to water), it led to the discovery of a gel aging effect occurring near the gel-air interface.

Subsequent experiments performed with gel dosimeters that had been stored in a refrigerator for between 1 and 3 days after casting produced percent depth dose curves that did not

agree as well with Monte Carlo simulation (or point measurement spot checks). Figure 6.4 shows the $3 \times 3 \text{ cm}^2$ field percent depth dose curves (normalized at 5 cm depth) obtained from Monte Carlo simulation and 3 different gel dosimetry experiments. The first gel experiment shown in this plot is the same one shown in the previous plots, and provides the best agreement with the Monte Carlo simulation. The second experiment was performed using a gel that had been stored in the fridge for 1 day, and the third using a gel stored for 3 days.

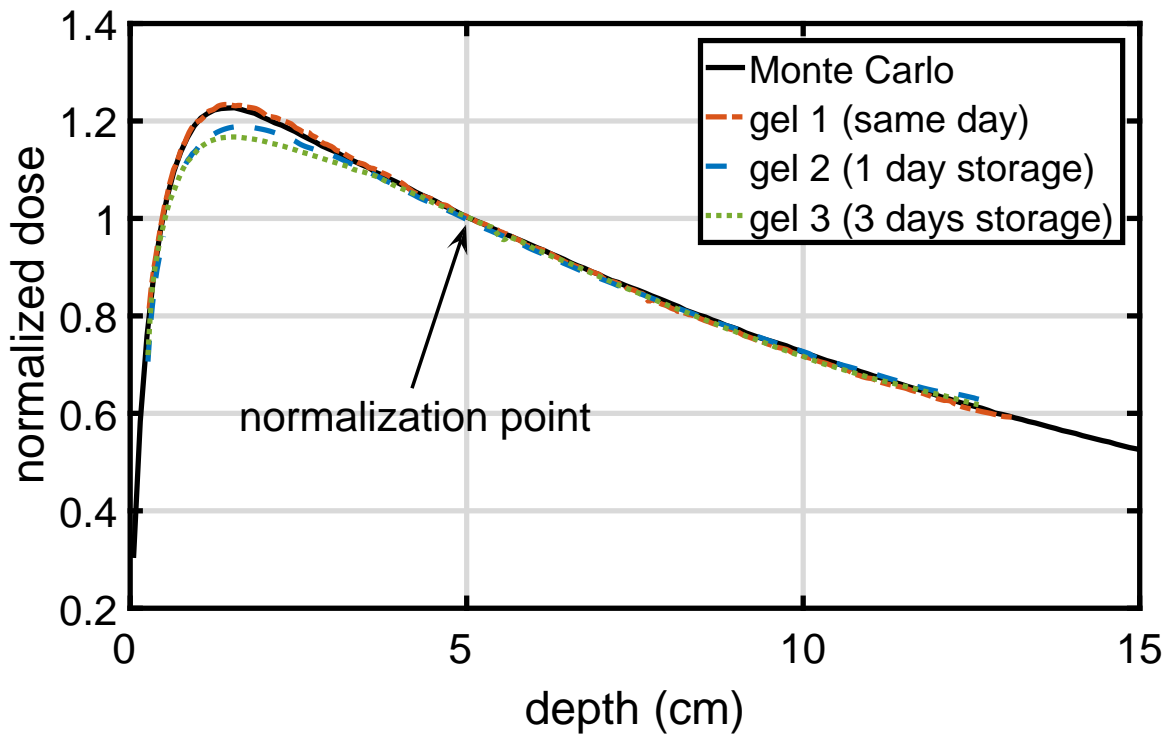


Figure 6.4: $3 \times 3 \text{ cm}^2$ field percent depth dose curves obtained from Monte Carlo simulation and 3 iterations of the small field gel dosimetry experiment with different gel storage times. Doses have been normalized at 5 cm depth (the most trustworthy region of the gel). For visibility, error bars on gel measurements have not been included.

From this figure, we can see that storing the gel prior to irradiation appears to degrade the results. The gel stored for 1 day underestimates the dose at d_{max} by approximately 2-3%, while the gel stored for 4 days under-reports by approximately 5%, when normalizing the PDDs in the center of the gels (5 cm depth). The dose fall-off portion of the gel-measured PDD beyond about 3 cm depth appears to agree well with Monte Carlo in all

cases. Prompted by these results, we investigated the uniformity of dosimeter response as a function of gel storage history. Our preliminary results indicate that the response of the gel dosimeter within an axial slice is uniform, however there is a non-uniformity in the response as one approaches the top surface of the gel. Specifically, there is a drop in sensitivity within the first few cm of the gel. We believe that this is related to either oxygen permeation or a different gelation / drying condition near the air interface, as gels were only covered (not sealed air-tight) during storage and an air gap was present between the lid and the gel surface.

We are currently performing further investigation into gel chemistry and storage effects, to avoid this phenomenon. However, it should be noted that with the current methods, the gel appears to be uniform in response beyond the first 2-3 cm even when stored for up to 3 days. Therefore, it should be acceptable for many clinical applications where the dose can be primarily deposited in the central portion of the dosimeter. In cases such as the small fields presented here, a uniform (or well-known) dose distribution could be delivered in order to assess the sensitivity as a function of height within the gel prior to performing the experiment of interest. Alternatively, the gel preparation can be finalized the morning of the experiment. If the gelatin and water have already been mixed and the peroxides have been cleared, then the addition of the SDS and LCV+TCAA solution can be performed relatively quickly (≤ 1 hour), and the gel cooling time is comparable to the time it takes to bring a gel from the refrigerator temperature to room temperature. Therefore, while this is less convenient than storing gels in the fridge, it is not infeasible in most cases.

6.5 Discussion and Conclusions

We have demonstrated the use of 3D gel dosimeters to perform small-field radiation dosimetry in a clinical physics environment. The ability to measure both field size and

central axis dose simultaneously allows for an improved confidence in dosimetry as it removes one source of uncertainty, especially for field sizes producing lateral electron disequilibrium. As well, we were able to measure field profiles (at any depth), relative dose factors, and percent depth dose curves for 4 field sizes within a single gel dosimeter with one irradiation session. Since point dosimeters are difficult to use for small fields due to setup uncertainties, the fact that we are able to use a 3D integrating dosimeter, instead of combining results from multiple dosimeters and exposures, is very attractive. When using a fresh gel dosimeter (cast in vessels the same day as irradiations), our field profiles and percent depth dose curves agreed very well with Monte Carlo simulations. As well, for the 1×1 and 2×2 fields, our relative dose factors (3×3 reference) were consistent with those derived from published literature values [12–14].

Obtaining this level of agreement between the gel, Monte Carlo simulations, and published data demonstrates that the scanner described in this thesis has enabled accurate, clinically-relevant 3D dosimetry using radiochromic gels for beam conditions that are difficult with other types of dosimeters. Moving forward, small field dosimetry performed in gels, spot-checked with planar (films or slabs of gels) and point (ion chambers or diodes) dosimeters, will be used to determine or verify the correct parameters for Monte Carlo simulations and other software-based dosimetry verification systems. Small-field dosimetry is important with the increasing trend towards multi-focal stereotactic radiosurgery of small brain metastases [15, 16]. Finally, there is academic interest in grid therapy in our institution, for which the dosimetry of small (≈ 5 mm square) fields is required. Therefore, gel dosimetry will play a role in future developments of radiotherapy techniques.

6.6 References

1. Das, I. J., Ding, G. X. & Ahnesjo, A. Small fields: Nonequilibrium radiation dosimetry. *Medical Physics* **35**, 206–215 (Jan. 1, 2008).

2. Bassinet, C. *et al.* Small fields output factors measurements and correction factors determination for several detectors for a CyberKnife and linear accelerators equipped with microMLC and circular cones. *Medical Physics* **40**, 071725 (2013).
3. Bjärngard, B. E., Tsai, J.-S. & Rice, R. K. Doses on the central axes of narrow 6-MV x-ray beams. *Medical Physics* **17**, 794–799 (Sept. 1, 1990).
4. Laub, W. U. & Wong, T. The volume effect of detectors in the dosimetry of small fields used in IMRT. *Medical Physics* **30**, 341–347 (Mar. 1, 2003).
5. Li, S., Rashid, A., He, S. & Djajaputra, D. A new approach in dose measurement and error analysis for narrow photon beams (beamlets) shaped by different multileaf collimators using a small detector. *Medical Physics* **31**, 2020–2032 (June 22, 2004).
6. Kairn, T., Charles, P., Crowe, S. B. & Trapp, J. V. Effects of inaccurate small field dose measurements on calculated treatment doses. *Australasian Physical & Engineering Sciences in Medicine* **39**, 747–753 (Sept. 2016).
7. Babic, S., McNiven, A., Battista, J. & Jordan, K. Three-dimensional dosimetry of small megavoltage radiation fields using radiochromic gels and optical CT scanning. *Physics in Medicine and Biology* **54**, 2463–2481 (Apr. 21, 2009).
8. Granton, P. V., Dekker, K. H., Battista, J. J. & Jordan, K. J. Stray light in cone beam optical computed tomography: I. Measurement and reduction strategies with planar diffuse source. *Physics in Medicine and Biology* **61**, 2893 (2016).
9. Jordan, K. J., Lindenmaier, T. & Dekker, K. H. Non-diffusing radiochromic leuco-crystal violet hydrogel dosimeter. *Journal of Physics: Conference Series* **847**, 012009 (May 2017).
10. Kawrakow, I. Accurate condensed history Monte Carlo simulation of electron transport. I. EGSnrc, the new EGS4 version. *Medical Physics* **27**, 485–498 (Mar. 1, 2000).
11. Babic, S., Battista, J. & Jordan, K. Radiochromic leuco dye micelle hydrogels: II. Low diffusion rate leuco crystal violet gel. *Physics in Medicine and Biology* **54**, 6791–6808 (Nov. 21, 2009).
12. Beierholm, A. R. *et al.* *Reference dosimetry and small-field dosimetry in external beam radiotherapy: Results from a Danish intercomparison study* (DTU Nutech, 2014).
13. Russo, S. *et al.* Small field output factors evaluation with a microDiamond detector over 30 Italian centers. *Physica Medica* **32**, 1644–1650 (Dec. 2016).
14. Mancosu, P. *et al.* Dosimetric characterization of small fields using a plastic scintillator detector: A large multicenter study. *Physica Medica* **41**, 33–38 (Sept. 2017).
15. Brown, P. D. *et al.* Postoperative stereotactic radiosurgery compared with whole brain radiotherapy for resected metastatic brain disease (NCCTG N107C/CEC-3): a multicentre, randomised, controlled, phase 3 trial. *The Lancet Oncology* **18**, 1049–1060 (Aug. 1, 2017).
16. Li, J. & Brown, P. D. The Diminishing Role of Whole-Brain Radiation Therapy in the Treatment of Brain Metastases. *JAMA Oncology* **3**, 1023–1024 (Aug. 1, 2017).

Chapter 7

Conclusions and Future Direction

7.1 Summary of Contributions and Limitations

This dissertation has advanced the field of 3D radiation dosimetry by improving upon the quantitative accuracy, precision, and practicality of radiochromic gel dosimetry. We approached the problem both instrumentally, designing and building new scanners to reduce stray light, and computationally, by evaluating the use of iterative CT reconstruction techniques. Finally, we demonstrated the utility of optical CT gel dosimetry through small field commissioning measurements.

7.1.1 Stray light reduction: new optical CT scanner designs

In Chapter 2, we demonstrated a method to improve the accuracy of CCD-based cone-beam optical CT through the use of a convergent light source in place of a diffuse light source. This modification reduced stray light contributions from 25% of total signal to approximately 4% when imaging gel dosimeters, and consequently doubled the previously reported range of attenuation coefficients that could accurately be probed [1]. Furthermore, our convergent source design has been incorporated into a new version of the commercially-available scanner (VistaTM, ModusQA, London, Canada). We are currently in the process

of characterizing this scanner, which can image objects up to 16 cm in diameter. Initial results indicate excellent accuracy (within 3% agreement between CT and narrow-beam Beer-Lambert law calculation) for both absorbing *and* scattering solutions with central axis transmission as low as 2%, when the scanner is operated using a small light source. The standard VistaTM 15 cm diameter vessels are a problem when using the small source, as the optical quality is quite low, leading to artifacts. If a better vessel can be identified, this scanner will be an excellent option for 3D dosimetry.

In Chapter 3, we described the design and construction of a laser optical CT system that can accurately image 15 cm diameter, 12 cm high cylindrical gel dosimeters at a spatial resolution of 0.33 mm (isotropic), in approximately 30 minute scan times. The scanner was designed to maintain accuracy by minimizing the detected scattered and stray light signals, without excessively compromising speed. This was accomplished by illuminating the gel with a single scanned pencil beam, and using a small area detector. We characterized the device in terms of spatial resolution, signal to noise ratio, accuracy, precision and linearity using a variety of large volume absorbing and scattering phantoms, as well as for small absorbing phantoms placed within scattering media. Excellent linearity and agreement (within 2% or less) was found between the scanner and independent attenuation measurements over a large transmission range (90+% to $\leq 2\%$) in all configurations, even when the amount of scatter present in the volumetric phantom was well beyond that typically seen in radiochromic gels ($\mu_{scatter} \approx 0.05 \text{ cm}^{-1}$). This scanner has become a “reference standard” system, as it is our best performing in terms of stray light rejection. However, one limitation is that it is slower to scan than the camera-based cone beam systems. This could be improved in the future if the custom lens aquarium design can be extended from an acylindrical shape to an aspheric shape, as this would allow us to replace translation stages with a 2-axis galvanometer mirror system.

7.1.2 Iterative CT reconstruction: Noise reduction and refractive index mismatched optical CT

We explored iterative CT reconstruction techniques and demonstrated their applicability to optical CT-based dosimetry. In Chapter 4, we examined the noise and artifact reduction capability of the OSC-TV algorithm [2] in the context of radiochromic gel dosimetry. We concluded that roughly 3-5x improvement in contrast-to-noise ratio could be achieved without losing spatial information when imaging in a small-field dosimetry experiment. We also presented a caveat to would-be users of iterative CT reconstruction algorithms in terms of the quantitative accuracy of attenuation coefficients in small objects during the de-noising step of algorithms. These investigations of iterative CT reconstruction in the gel dosimetry context should lead to an increased utility of optical CT scanning by reducing the impact of imperfect optics (dosimeter vessels, aquarium windows, etc.) on image quality. The cost of this improvement is that care must be taken in selecting a correct regularization parameter in the reconstruction algorithm. Additionally, the approach could be improved by determining a method to terminate the iterative algorithm at an optimal time, rather than using a set number of iterations, which would improve speed and image quality.

In Chapter 5, we examined the feasibility of optical CT scanning in the case of refractive index mismatch between the dosimeter and surrounding aquarium liquid. This study showed that when using iterative CT algorithms to reconstruct images, a solid plastic dosimeter, such as PRESAGE[®], could be scanned without the use of oil-based matching liquids, experimentally validating the conclusions of previous computer simulations in the literature [3, 4]. The avoidance of oils is a major step forward in practicality, as non-oil solutions are much more convenient to work with in a clinical or research setting. Accurate optical CT reconstruction was demonstrated within a central sub-volume of the cylindrical dosimeter, the radius of which depends on the refractive index mismatch between the dosimeter and surrounding medium. The experimental ray-path measurement technique we described re-

laxes the requirement for accurate refractive index measurement, and has applicability in other aspects of optical CT scanning (e.g. confirming parallel beam geometry, measuring fan-beam divergence, etc.). Limitations of this technique arise from the need for an additional "fiducial scan" to perform ray path measurement, as well as an increased sensitivity to sample positioning errors between pre- and post-scans. The auxiliary scan issue could be addressed in the future by the use of semi-transparent fiducials, and the sample positioning errors could potentially be addressed by the use of dual-wavelength scanning to eliminate the pre-scan, if the refractive index at the two wavelengths is not too great [5].

7.1.3 Utility of optical CT dosimetry: Small field measurements

Finally, in Chapter 6, we demonstrated the clinical utility of our optical CT scanner by performing one of the most difficult dosimetry tasks: small-field beam measurement. Our small-field gel measurements showed excellent agreement with 3D Monte Carlo simulations. The fact that gels can be used for small field commissioning measurements represents a potential for time saving, as it is possible to capture all of the parameters needed for treatment planning (output factor, beam profiles at various depths, percent depth dose curves) in a single exposure, rather than acquiring many individual point measurements with 1D detectors. As well, multiple beams can be deposited in the same gel dosimeter, further accelerating the process. Based on our results, we believe that commissioning data for at least four field sizes below $3 \times 3 \text{ cm}^2$ could be acquired within approximately 2 hours, with only spot-check point detector measurements required for validation.

7.1.4 Summary of results

Overall, this dissertation has brought optical CT based 3D radiation dosimetry to a point where it can be applied clinically to obtain trustworthy results in a practical fashion. Im-

provements were made in both optical scanner design, to reduce the contribution of non-primary light in measurements, as well as in implementation of iterative reconstruction algorithms, which improved image quality and enabled non-standard CT geometry to be used for imaging. With our scanners, we now achieve optical CT reconstructed attenuation coefficients that agree with independent measurements within $\sim 1\%$ (laser scanner, Chapter 3) to $\sim 3\%$ (cone beam scanner, Chapter 2). The use of iterative reconstruction improves contrast to noise ratios by a factor of approximately 5. Furthermore, when applying our laser scanner to gel dosimetry, we obtained agreement between gel and Monte Carlo simulation within $\sim 2\%$. These results were obtained within reasonable scan times of approximately 30 minutes.

At this stage, we believe that if applied correctly, gel dosimetry has the potential to save considerable time in certain tasks such as small field commissioning, and it is perhaps the most appropriate way to truly verify the highly complex multifocal dose distributions that are gaining in popularity, especially in the brain. Some of the technical developments presented in this thesis have been adopted by commercial partners (convergent cone beam source, iterative reconstruction for gels), and the in-house scanning laser system is now a reference standard for 3D dosimetry at our institution, to which we compare other scanner designs and which we use for evaluation of different gel dosimeters.

7.2 Remaining Limitations and Future Directions in Optical CT Dosimetry

At the end of this dissertation, we believe that we have brought the imaging and image processing/reconstruction portion of optical CT dosimetry up to a clinically acceptable standard. However, it is prudent to highlight some of the limitations of our work as well as optical CT dosimetry in general, and to provide some potential avenues for future research and development. At this stage, it is our belief that the main limitation on 3D dosimetry is

no longer the optical CT imaging system, but 1) the dosimeter vessels, and 2) the chemical dosimeter material itself (preparation and storage).

7.2.1 Gel dosimeter vessels

Vessels remain a considerable issue in gel dosimetry. They must be of high optical quality, first and foremost, to achieve the required image quality in optical CT. However, it is also important to consider the impact of the vessel on dose deposition as well as gel dosimeter chemistry. Plastic vessels are used in place of glass because they exhibit better dosimetric properties (physical density, electron density similar to tissue). However, they are typically of lower optical quality than glass, and with the reduction of scattered light in our optical scanners, optical imperfections become more visible and create more artifacts in images. To combat this, our lab has worked to develop custom-made vessels from thin sheets of plastic, which have been quite effective for most of our experiments. Iterative CT reconstruction greatly suppresses artifacts in our reconstructions as well. However, some artifacts remain, specifically due to the seam in our vessels.

7.2.2 Gel dosimeter chemistry

The second and more critical consideration for optical CT dosimetry is the dosimeter material itself. No “best” gel dosimeter has been identified by the 3D dosimetry community. Most of the recent gel work in our lab, including the gel results presented in this dissertation, has been performed using the leuco crystal violet (LCV) dosimeter using sodium dodecyl sulfate (SDS) surfactant [6]. This LCV-SDS gel dosimeter has provided excellent results, but there are some limitations. First, we have observed that this gel dosimeter provides best results when it is made on the day of the irradiation. This requires foresight in planning gel dosimetry experiments, particularly when using large volume dosimeters, as

it takes roughly 5 hours for a 15 cm diameter ($\sim 2.5\text{L}$) gel to cool to room temperature after pouring. Storing gels (in the refrigerator) results in a non-uniform response wherein the first 2-3 cm below the top (air surface) of the gel exhibit an under-response of approximately 2% (after 1 day) to 5 % (after 4 days). This effect appears to be tied to the air interface, and is theorized to be caused by either oxygen permeation or the difference in moisture content of the gel near the surface. We are currently investigating approaches to minimize this effect in order to allow longer-term storage of gels without perturbing accuracy.

Second, while the LCV dosimeter is reusable through melting and re-casting, its initial colour becomes darker each time, reducing the dynamic range when scanning. We have successfully used our in-house laser scanner for at least 2 uses of a 15 cm LCV gel, followed by subsequent recycling of the gel in smaller volumes, which reduces the amount of fresh gel that must be prepared. However, the ideal dosimeter would be “erasable”, in the sense that its radiation-induced attenuation could be reversed. We are investigating methylene blue based gels, which have been previously studied, as they may be reversible, and could be stored at room temperature. Methylene blue, a photosensitizer [7], was first proposed for radiation dosimetry (in solution form) as early as the 1950s [8]. The main limitation in these gels has been oxygen sensitivity and the creation of a re-sealable optical CT vessel. This is required because the re-setting process for methylene blue gels consists of opening the vessel to allow oxygen to enter the system and reverse the radiation-induced change, followed by photo-bleaching to consume the oxygen and make the gel sensitive again. If an oxygen-impermeable, re-sealable vessel could be manufactured, methylene blue gels would be very attractive due to their re-usability.

Finally, the sensitivity of the LCV-SDS dosimeter is considerably lower than that of the Ferrous Xylenol Orange gels (FXG), which are still in use by many researchers. These FXG dosimeters still exhibit a relatively high diffusion rate, requiring fast scanners. However, some recent work from other researchers suggests that the addition of the amino acid

glycine prevents diffusion in FXG dosimeters [9]. If this result can be replicated, FXG would likely be the dosimeter of choice in our lab, as it has a sensitivity approximately $10\times$ higher than LCV gels, allowing dosimetry of conventional single-fraction doses (≤ 2 Gy). Furthermore, we are currently attempting to image large volume FXG dosimeters (15 cm diameter) using the new VistaTM scanner, as it uses green light (more linear FXG response than yellow light) and can acquire full 3D datasets in approximately 2 minutes, which is fast enough to mitigate “during-scan” diffusion effects. In order to image FXG at large volumes with green light, intensity compensation of the light source is needed, as the initial attenuation is quite high. Thus, we have developed a method to create low cost, object-specific source compensators by printing greyscale images onto transparent films using a laser printer. This is described in Appendix A.

In summary, gel dosimeter chemistry is still very much an active area of research. With the developments in this thesis, we believe that the readout mechanism has now reached a point where it is very robust and accurate, which will allow us to focus on identifying the best gel dosimeters for given tasks.

7.2.3 Clinical applications and developments

While work is ongoing into the above limitations, it would be unfair to say that they are currently *preventing* gel dosimetry from being used. In Chapter 6, we demonstrated that optical CT imaging, using our scanner and a fresh gel dosimeter, achieves excellent results in small-field commissioning measurements. This gives us confidence in moving forward with clinical applications such as dosimetry of multi-focal stereotactic radiosurgery plans, which feature multiple small targets spread across a large volume. We have begun work on this type of treatment validation. In addition, we plan to apply gel dosimetry to motion-managed treatments, as a way to evaluate the effectiveness of respiratory gating for radiotherapy. The gel would be moved during radiation exposure to mimic a moving tumour,

and then read out to assess if gating was properly timed.

The use of gel dosimetry in machine commissioning is under investigation for a wider scope of clinical applications. We believe that small field beam commissioning measurements could be performed using our laser scanner and LCV-SDS gel, with a few spot checks performed by point dosimeters for validation. This would eliminate a large number of measurements currently made using a scanning point detector in a large water tank. Evaluation of our gels and scanners for small-field commissioning is underway. In terms of clinically-focused technical research, gel dosimetry can contribute to the development of grid or beamlet therapy techniques by providing the verification that these complex treatment plans can be delivered. This should avoid the need to apply an inefficient combination of dosimeters that requires merging and reconciliation of different datasets. It is hoped that the developments reported in this dissertation will improve the accuracy and efficiency of clinical dosimetry protocols used for radiotherapy techniques of the present and future.

7.3 References

1. Olding, T., Holmes, O. & Schreiner, L. J. Cone beam optical computed tomography for gel dosimetry I: scanner characterization. *Physics in Medicine and Biology* **55**, 2819–2840 (May 21, 2010).
2. Matenine, D., Goussard, Y. & Despres, P. GPU-accelerated regularized iterative reconstruction for few-view cone beam CT. *Medical Physics* **42**, 1505–1517 (Apr. 1, 2015).
3. Rankine, L. & Oldham, M. On the feasibility of optical-CT imaging in media of different refractive index. *Medical Physics* **40**, 051701 (2013).
4. Doran, S. J. & Yatigammana, D. N. B. Eliminating the need for refractive index matching in optical CT scanners for radiotherapy dosimetry: I. Concept and simulations. *Physics in Medicine and Biology* **57**, 665–683 (Feb. 7, 2012).
5. Ramm, D. A fast dual wavelength laser beam fluid-less optical CT scanner for radiotherapy 3D gel dosimetry I: design and development. *Phys. Med. Biol.* (2018).
6. Jordan, K. J., Lindenmaier, T. & Dekker, K. H. Non-diffusing radiochromic leuco-crystal violet hydrogel dosimeter. *Journal of Physics: Conference Series* **847**, 012009 (May 2017).

7. Ginimuge, P. R. & Jyothi, S. Methylene Blue: Revisited. *Journal of Anaesthesiology, Clinical Pharmacology* **26**, 517–520 (2010).
8. Lafuente, B., Goldblith, S. & Proctor, B. Some further studies on the application of methylene blue in aqueous solution as a dosimeter for intense beams of high-energy radiation. *The International Journal of Applied Radiation and Isotopes* **3**, 119–124 (Jan. 1958).
9. Babu, S. S., Singh, I. R., Poornima, C. & Ravindran, B. Enhancing the longevity of three-dimensional dose in a diffusion-controlled Fricke gel dosimeter. *Journal of Cancer Research and Therapeutics* **11**, 580 (2015).

Appendix A

Fixed, object-specific intensity compensation for cone beam optical CT radiation dosimetry

This chapter is adapted from a technical note published as “Fixed, object-specific intensity compensation for cone beam optical CT radiation dosimetry” by Kurtis Hendrik Dekker, Rubin Hazarika, Matheus A. Silveira, and Kevin J. Jordan, *Physics in Medicine and Biology*, 63, 06NT02 (2018)¹. Permission to reproduce this article was granted by IOP Publishing, and is provided in Appendix B.

A.1 Introduction

A.1.1 Optical CT Dosimetry

Optical computed tomography (CT) scanning of radiochromic [1] or polymer [2] gel dosimeters provides truly three-dimensional (3D) measurement of absorbed ionizing radiation dose. A large variety of optical CT systems have been reported over the last two decades, ranging from scanning laser devices [3–7] to broad parallel-beam [8–11] or

¹© Institute of Physics and Engineering in Medicine. Reproduced by permission of IOP Publishing. All rights reserved.

cone beam [12, 13] scanners. Commercially, the laser-based OCTOPUS (MGS Research Inc., Madison, CT, USA) and cone beam VistaTM (ModusQA, London, Ontario, Canada) are available. Scanners based on a single pencil beam and small area detector geometry are fundamentally more accurate than broad-beam scanners, as they exhibit a greater ability to reject non-primary (stray) light rays [7]. However, broad-beam CCD-based scanners are generally more robust and faster, as they have fewer moving parts and can acquire 2D projection images of the full field of view (FOV). In this note, we focus on the cone beam geometry. Previously, we presented a modification of the VistaTM optical CT scanner that reduced the stray light contribution in typical gelatin-based dosimeter imaging from approximately 25% to about 4% [14]. This greatly improved the accuracy and usable attenuation range of the scanner for imaging radiochromic gels (absorption-based contrast).

A.1.2 Intensity compensation in cone beam optical CT

Many radiochromic gel dosimeters exhibit a relatively high initial attenuation coefficient. For a 10 cm diameter cylindrical volume, it is not uncommon to observe an initial transmission of less than 20% (relative to water) along the diameter. This has been seen in both ferrous xylenol-orange [15] and leuco crystal violet [16] gels. When acquiring projection images using a CCD camera, the light source intensity and CCD integration time (shutter speed) are set such that the full range of the sensor is utilized without saturating any parts of the image, as saturated pre-irradiation projection images will not provide correct reference intensities for calculation of post-irradiation transmission and subsequent CT reconstruction. For most dosimeters, irradiation causes an increase in optical attenuation coefficient, thus a high initial attenuation of many gels can result in all of the actual dosimetry being performed within the bottom 10 - 20 % of the camera's dynamic range, resulting in sub-optimal signal-to-noise ratio and image quality. This problem becomes more pronounced

as dosimeter size is increased, due to longer path-lengths through the gel.

Because optical CT dosimeters are typically imaged within a tank or aquarium filled with a refractive index matching solution (to prevent refraction of light rays and preserve standard CT geometry), attenuating dyes can be added to the matching liquid [17–19]. This brings the matching liquid attenuation to a similar level to that of the unirradiated dosimeter, resulting in more uniform intensity in pre-irradiation projections. Employing solutions with a broad absorption spectrum minimizes spectral artifacts when imaging with non-monochromatic sources [20]. However, in our experience the stability of dyes in aqueous solutions is often an issue. Some dyes, such as nigrosin, are sensitive to pH, and change colour as carbon dioxide dissolves into the solution from the air. Other dyes are stable in water, but precipitate when propylene glycol or glycerol is added to the solution for refractive index matching (e.g. patent blue, carbon black + surfactant emulsions). Some dyes (e.g. nigrosin) precipitate onto plastic (vessels) but not onto glass (aquarium windows), which is difficult to correct for analytically). Solutions such as ferric xylenol orange in sulfuric acid are very stable, but the acid damages anti-reflective coatings on aquarium windows.

In general, if the solution is not stable, a change in liquid attenuation between pre- and post-irradiation scans, can occur which perturbs measurement of the radiation induced *change* in optical attenuation of the gel. This may be associated with precipitation onto dosimeter vessels or the aquarium windows, changing the transmission of these surfaces. The proper correction for these effects depends on which of these has occurred, or, more likely, the magnitude of each effect in combination. Therefore, it would be preferable to avoid the use of dyed liquid in the optical CT scanner, and instead modulate the intensity profile of the incoming light.

A possible alternative to modifying the attenuation of the aquarium liquid is to perform high dynamic range imaging through the use of multiple exposures with different integra-

tion times [21]. This imaging technique was used by Thomas *et al.* to image PRESAGE® dosimeters using a CCD-based telecentric optical CT scanner [11]. However, when imaging gel dosimeters, which have more scatter than PRESAGE®, this method may break down as scatter contributions that were below the detection limit of the scanner at one integration time become detectable at longer times. Campbell *et al.* used multiple integration times when imaging polymer gel dosimeters; however, their scanner featured an array of photodiodes, each with its own physical collimator, which greatly reduced scatter acceptance [22]. In our case, we are using a broad-beam, camera-based system to image objects that exhibit scatter, thus high dynamic range imaging will not be as effective as modulating the incoming light intensity.

Instead of changing aquarium liquid or performing high dynamic range imaging, we propose modifying the intensity profile of the light source to compensate for the object's initial attenuation. Here, we modulate the incoming light such that there is a higher intensity in the image center (rays passing through the dosimeter center) than towards the periphery (rays passing through shorter chord lengths or through liquid alone). As before, the aim is to reduce the detected signal intensity towards the dosimeter periphery / outside the vessel relative to the central axis signal, which allows the use of a longer integration time and/or brighter illumination source to achieve higher overall signal through the dosimeter without saturating images. We have previously examined the use of discrete strips of attenuating film placed in front of the optical CT aquarium, but the resulting sharp edges in source intensity profiles created strong ring artifacts in reconstructed images. Thus, in this note, we propose a method to generate smoothly-varying source compensator gradients. This approach is analogous to the commonly-used bowtie filter in x-ray CT scanners [23]. Grayscale-printed transparency films have previously been used in the context of optical CT for performing ultraviolet light exposures [24], however here we use them as an element in the optical imaging system.

A.1.3 Study Outline

In this note, we demonstrate a simple, inexpensive method to produce intensity compensators for a CCD-based optical cone beam CT scanner using a conventional laser printer and transparent films. We describe the methodology used to generate compensator profiles, and present results from imaging a solution phantom with attenuation representative of typical radiochromic gels, in order to show that the technique does not perturb image quality or introduce artifacts.

A.2 Materials and Methods

A.2.1 Optical CT Scanner

Figure A.1 shows a top-view schematic of the modified Vista10 optical CT scanner (ModusQA, London, Canada). The scanner consists of a light source, aquarium and rotational stage, and a scientific camera (DR2-BW, Point Grey Research, Inc., Canada) equipped with a 2/3" diameter, 16 mm focal length lens (HF 16HA-1B, Fujinon Corporation, China) set to an aperture of $f/4$. The camera captures 12-bit images of 640×480 pixels, which are saved in a 16 bit unsigned integer format. The original large diffuser light box was previously replaced with a small, bandpass-filtered light emitting diode (LED, 535 nm central wavelength) + diffuser source (5 mm diameter) and a large Fresnel lens (catalogue #32-595, Edmund Optics, Barrington, NJ, USA) in order to reduce the contribution of stray light and improve the scanner's accuracy [14]. In this note, we describe the addition of a source intensity compensator (Position ii, Figure A.1) to the system.

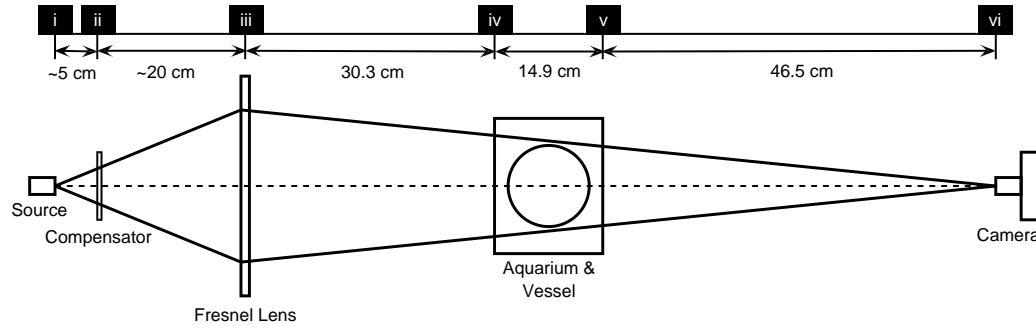


Figure A.1: Top view schematic of the modified VistaTM optical CT scanner. The positions of the light source (i), intensity compensator (ii), Fresnel lens (iii), aquarium entrance aperture (iv), aquarium exit aperture (v) and camera (vi) are shown. Positions of the light source and compensator were adjustable, so only approximate distances are provided in this figure. A convergent cone of image forming primary rays is generated by the Fresnel lens focusing the light from the small LED + diffuser source.

A.2.2 Intensity Compensators

A variety of intensity compensators were generated by printing grayscale patterns onto transparent films (overhead projector transparencies, 3M Company, Austin, TX, USA) using a laser printer (HP Color LaserJet 5550dtn, Hewlett-Packard Company, Palo Alto, CA, USA). All printing was performed with the “print grayscale” option selected, at 600 dots per inch (highest available), and with all other settings at default values.

A.2.2.1 Transmission vs. grayscale value

Before printing intensity compensators, the relationship between grayscale value and optical transmission was established by imaging a printed test strip pattern using the modified Vista10 scanner. The test pattern consisted of ten 2 cm wide \times 10 cm high regions, printed from a bitmap image file with gray levels ranging from 25-250 (where, in the 8 bit unsigned integer representation, 0 represents black and 255 represents white) in steps of 25. An air image was acquired, followed by an image taken with the test pattern located at the scanner’s axis of rotation, in order to generate an air-referenced transmission image. Average transmission values for each gray level were calculated by averaging over a 1 cm

$\times 5$ cm region of interest within the center of each strip. A power-law function was fit to the transmission vs. grayscale data points.

A.2.2.2 Parabolic grayscale profile compensator

As an initial test of source compensation, we generated a simple parabolic grayscale profile, as shown in Figure A.2b. A 1000 x 750 pixel bitmap image was formed by replicating this gradient, and printed at both 8×6 cm and at 18×13.5 cm on transparent films. Transmission images (relative to air) were acquired of the larger compensator placed at the optical CT scanner's rotation axis (between positions iv and v, Figure A.1), and of the smaller compensator placed on the source side of the Fresnel lens, approximately 5 cm from the face of the diffuser (Position ii, Figure A.1). These images are shown in Figure A.3.

A.2.2.3 Object-specific compensator

We performed a proof of principle experiment using an object-specific static compensator (profile shown in Figure A.2b). This was done by acquiring a reference image of a water-filled aquarium, followed by an image of a uniform solution phantom (11 cm diameter custom-made vessel). A transmission image was calculated, and its complementary image (i.e. $1 - \text{Transmission}$) was used to calculate grayscale values using the fit derived in section A.2.2.1. The resulting grayscale compensator image was smoothed using an averaging filter with a kernel size of 11x11 pixels to remove any sharp features. Finally, the compensator was printed at a size of $8 \text{ cm} \times 6 \text{ cm}$ and positioned approximately 6 cm from the optical CT scanner's LED + diffuser source. It should be noted that the compensator was positioned in a flat orientation; however, in the future it may be better to design a curved frame, since the image-forming rays are emitted in a cone from the small diffuser source. Additionally, we performed a test using two layered printouts of the object-specific

compensator, to achieve greater attenuation values.

A.2.3 Solution phantom imaging with compensated source

To verify the efficacy of source compensation, we performed optical CT scanning experiments using an 11 cm diameter solution phantom. The solution consisted of approximately 10% (by weight) propylene glycol in water, and was dyed using Nigrosin stain (Fisher Scientific, USA). In these experiments, the solution used for the pre-scan had an initial attenuation coefficient of approximately 0.2 cm^{-1} , corresponding to approximately 12% initial transmission (relative to water) in the 11 cm diameter vessel, which is a common starting point when imaging FXG dosimeters using green light. The post-scan solution had an attenuation coefficient of approximately 0.4 cm^{-1} , corresponding to about 1.5% transmission.

Projection images of the reference solution phantom were acquired with no compensator as well as with the parabolic and object-specific compensators in place. The distance between compensator and diffuser source (Positions i and ii in Figure A.1) was varied such that the 50% point in the compensator's resulting intensity gradient (see Figure A.3) was roughly lined up with the vessel wall in projection images. Profiles across these projection images are plotted in Figure A.4a.

For both the parabolic and object-specific compensators, optical CT scanning was performed using 1024 projections, and images were reconstructed at $0.25 \times 0.25 \times 0.25 \text{ mm}^3$ voxels using in-house GPU-accelerated implementations of the Feldkamp-Davis-Kress (FDK) algorithm [25] with a Hamming filter, as well as the Ordered Subsets Convex Algorithm with Total Variation minimization (OSC-TV) [26, 27].

A.3 Results and Discussion

A.3.1 Transmission of printed compensators

A.3.1.1 Relationship between grayscale value and transmission

Figure A.2a shows the measured transmission (relative to air) of 3M brand transparencies as a function of grayscale value printed on the HP 5550dtn. A power law was fit to the data ($r^2 = 0.99$), resulting in a grayscale-dependent transmission value given by

$$T = 0.82 \left(\frac{G}{255} \right)^{3.44} \quad (\text{A.1})$$

where T is the transmission of the printout and G is the grayscale value, given as an unsigned 8-bit integer. This function was subsequently used to generate compensator profiles from transmission images. From these results, it appears that grayscale values below approximately 100 result in similar transmission values ($\sim 1.5\%$ relative to air). This was later confirmed by transmission measurements with grayscale values from 0-50. Additionally, further experiments showed that the transmission of grayscale values ≥ 250 was the same as that of a film without any printing, setting an upper bound on usable values to achieve modulation.

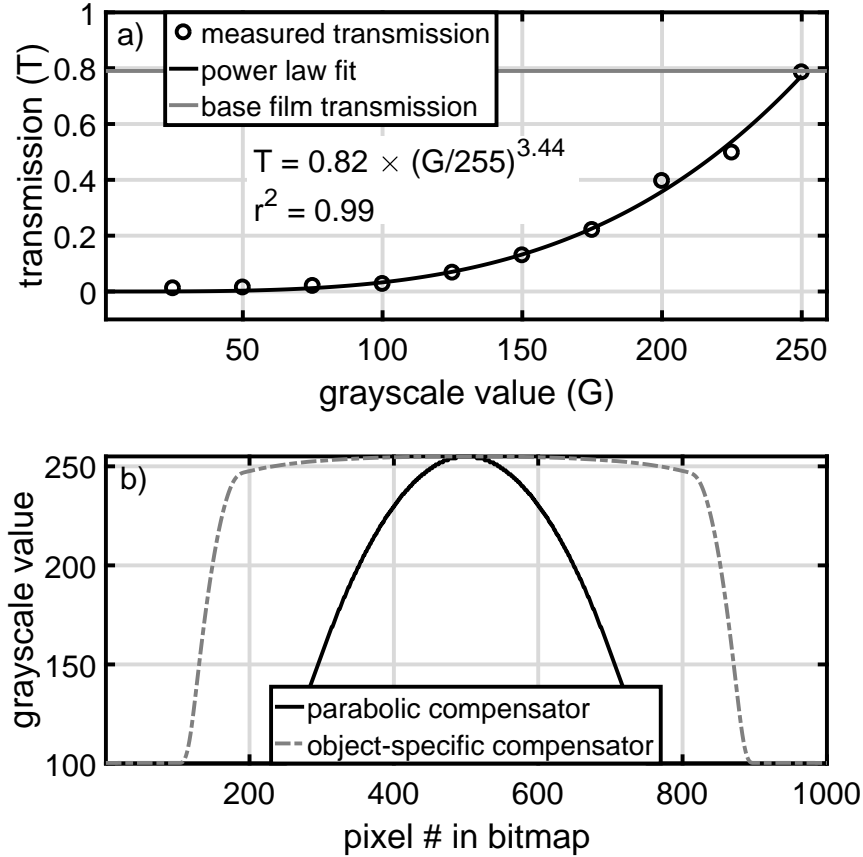


Figure A.2: a) Average transmission values (averaged over $1 \text{ cm} \times 5 \text{ cm}$ ROI) of laser-printed test strips on overhead transparencies, measured at the scanner's rotation axis (in focus). The transmission of the base film (no printing) is also shown (solid gray line). b) Central horizontal profiles across bitmap image files used to print the parabolic (solid black) and object-specific (dashed gray) compensators.

A.3.1.2 Parabolic-profile compensators

Figure A.3 shows transmission images and profiles (air reference) for the large ($18 \text{ cm} \times 13.5 \text{ cm}$) and small ($8 \text{ cm} \times 6 \text{ cm}$) parabolic-profile compensators described in section A.2.2.2. For comparison, we also included a calculation of the expected transmission profile for the large compensator placed at the scanner rotation axis, using the model fit shown in Figure A.2a, along with the observed grayscale threshold value described in section A.3.1.1. The image of the large compensator placed at the scanner's rotation axis (in focus) (Figure A.3a) shows that the printed compensator contains many high spatial frequency features, related to both innate film defects and printing artifacts, superimposed

on the transmission gradient. However, acquiring images using the smaller compensator placed on the source side of the Fresnel lens (Location ii in Figure A.1) shows a similar transmission gradient but without the high frequency structures (Figure A.3b). This is reflected in the central horizontal profiles plotted in Figure A.3c. The profiles have a similar overall shape, but the high frequency structures in (a) give the appearance of a “noisy” transmission profile. Note that we do not have fine enough resolution to observe the binary dot pattern that forms the “grayscale” image, and that when we refer to printing artifacts we mean the streak patterns visible in Figure A.3a.

It can also be seen that placing at the source side of the lens results in less intensity reduction in the darkest regions of the images. This is likely due to the relative sizes of the compensator gradient and the diffuser light source. In this case, a 5 mm diameter circular aperture was placed in front of the diffuser, which was previously found to achieve a good balance between quantitative accuracy and dosimeter vessel imperfection-related artifacts [14]. Therefore, some of the image forming rays that contribute in those regions of the image may pass through the lighter gradient region rather than the dark areas of the compensator. It is hypothesized that using a smaller source diameter would result in a lower intensity detected in these regions. Additionally, it may be necessary to stack multiple compensators in order to achieve sufficiently low intensity towards the edge of projections when scanning very dark objects, as shown in Figure A.4a.

The transmission profiles have a flat top, which is consistent with the gray value threshold of 250 that was previously observed. This threshold is likely a physical limitation of the printer; however, additional print settings could be explored in the future. It should be noted that while the compensator itself was designed with a parabolic grayscale gradient, the transmission profile was not expected to be parabolic, based on the non-linear relationship shown in Figure A.2a. In Figure A.3c, a calculated profile is shown for the case where the compensator is placed at the aquarium rotation axis plane. This calculated profile

agrees very well with the experimental measurement. Overall, these results indicate that compensators should be placed on the source side of the scanner's Fresnel lens, to avoid introducing artifacts into CT reconstructions. When this was done, we did not observe features that would produce the ring artifacts previously seen using discrete compensator strips.

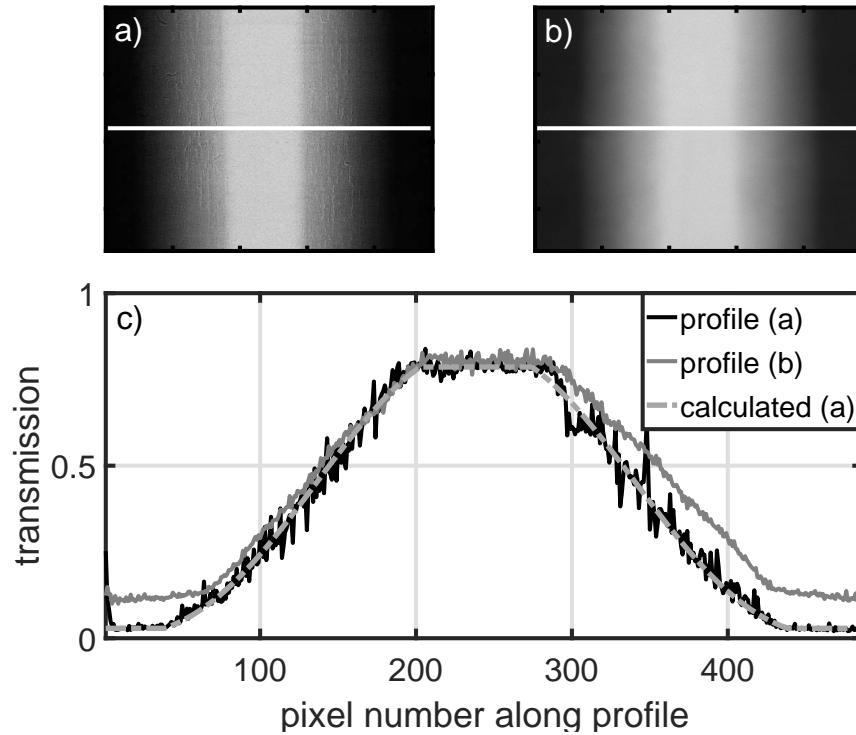


Figure A.3: Transmission (air reference) images of laser-printed parabolic-profile compensators. a) large compensator located at scanner rotation axis (in focus). b) small compensator located 6cm from light source (out of focus). c) indicated profiles through (a) and (b), as well as the expected transmission profile for (a). Note that the compensator in (b) is slightly offset from the center of the field of view; this was corrected prior to performing optical CT imaging experiments.

A.3.2 Solution phantom with compensated source

Figure A.4a shows horizontal profiles across projection images taken of the solution phantom with the 0.2 cm^{-1} attenuating reference liquid, acquired with no compensator, with the parabolic compensator, and with the object-specific compensator. It can be clearly seen, by

looking at the regions of the profile that fall outside the vessel, that the use of compensators greatly reduces the range of detected intensity values in the pre-irradiation images. In this example, the ratio of detected intensities through the vessel center to that through the liquid regions was reduced from approximately $1/8$ with no compensator, to about $2/5$ using the parabolic compensator, $1/4$ using the object-specific compensator, and $2/3$ using the 2-layer object-specific compensator. This means that the camera integration time (shutter speed) or the LED source brightness can be increased, without saturating images, allowing optical CT imaging to be performed in the middle of the camera's range rather than the bottom 10-20%.

Reconstructing the 0.4 cm^{-1} attenuating liquid, relative to the 0.2 cm^{-1} liquid, showed no image artifacts that could be attributed to the compensator itself. A representative reconstruction slice and profile are shown in Figure A.4b and A.4c. The OSC-TV reconstructed image exhibited flatness (within $\pm 1\%$) within the central 95% of the vessel's radius, beyond which there was a bright ring associated with a loss of about 2 mm of data due to refractive index mismatch between the vessel wall, interior solution, and aquarium liquid.

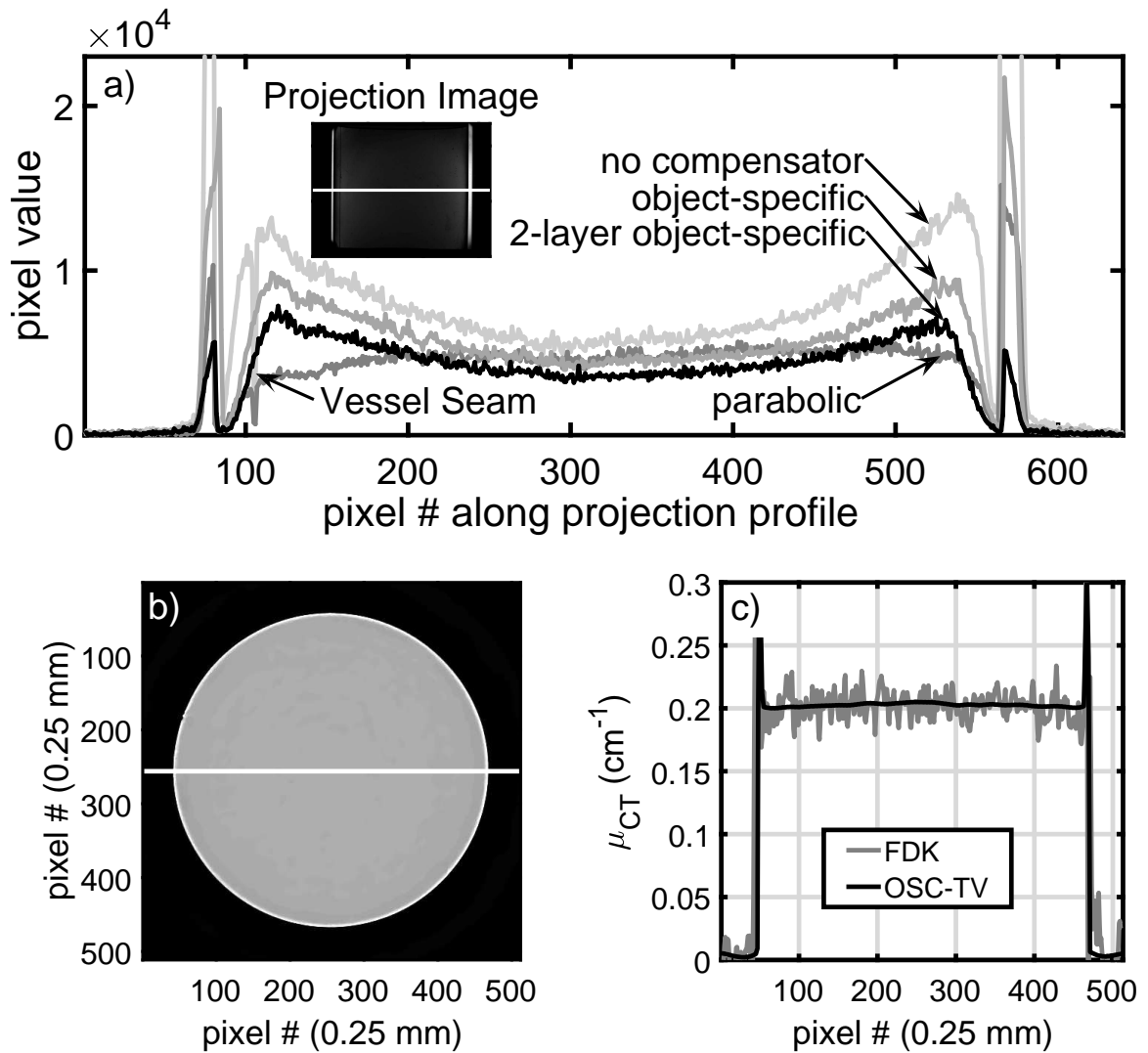


Figure A.4: a) Horizontal profiles across single projection images of the reference solution phantom with no compensator, object-specific, 2-layer object-specific, and parabolic compensators. Note that the signal value in the “no compensator” profile reaches approximately 6×10^4 in the regions outside the vessel, which has been cut off in this plot. Also note that the vessel was rotated such that the seam was not visible in the latter 2 profiles. b) Reconstruction slice (OSC-TV, 0.25 mm voxels) of the solution phantom scanned using the parabolic compensator. c) Central horizontal profiles (FDK and OSC-TV) across the reconstructions, along line indicated in (b).

A.4 Discussion and Conclusions

In this note, we have demonstrated that cone beam optical CT source compensation can be achieved by printing grayscale patterns onto transparent film. We created both generic as well as object-specific compensators for a small-source + converging lens system. Placing the compensators on the *source* side of the system's converging lens (and beyond the focus of the imaging lens) allows the high spatial frequency structures of the printed compensator to be filtered out by the optical system, avoiding artifacts in CT reconstructions. Thus, the low optical quality of the transparency films and printer output do not negatively impact the optical CT system.

In this study, we only addressed the problem of compensating for a uniformly-attenuating cylindrical object, such as a dosimeter prior to irradiation. However, most gel dosimeters remain linear over a much larger dose range than is typically utilized in an optical CT experiment and could potentially be used again if enough signal could be obtained in transmission imaging. Therefore, the compensator technique presented here may enable multiple uses of the same gel dosimeter. This could be further extended by generating a “compromise” object-specific compensator from the average of several transmission projections from different angles, and/or by simulating expected transmission projections using the previous optical CT reconstruction. This approach would be particularly useful in dosimeters that have previously been irradiated with an arc delivery, such as a VMAT plan. Furthermore, it may be possible to make use of a small liquid-crystal or organic LED display to dynamically change the source intensity pattern as a function of projection angle, similar to Fluence Field Modulated CT (FFMCT), an active research area in x-ray imaging [28–30].

The current technique, printing fixed compensators, is accessible and inexpensive, as most institutions will have access to a printer, and transparent films are still readily available from office supply retailers for a low cost. Source compensation will result in improved signal

to noise ratio in projection images, and will increase the dynamic range of the optical CT scanner, enabling darker objects to be scanned. In the future, we will use this approach to enable imaging of large (15 cm diameter) ferrous xylenol orange gel dosimeters with green light, which was previously challenging due to high initial attenuation.

A.5 References

1. Oldham, M. Radiochromic 3D Detectors. *Journal of Physics: Conference Series* **573**, 012006 (Jan. 12, 2015).
2. Baldock, C. *et al.* Polymer gel dosimetry. *Physics in Medicine and Biology* **55**, R1–R63 (Mar. 7, 2010).
3. Gore, J. C., Ranade, M., Maryanski, M. J. & Schulz, R. J. Radiation dose distributions in three dimensions from tomographic optical density scanning of polymer gels: I. Development of an optical scanner. *Physics in Medicine and Biology* **41**, 2695 (1996).
4. Maryanski, M. J. & Ranade, M. K. *Laser microbeam CT scanning of dosimetry gels in Medical Imaging 2001* (International Society for Optics and Photonics, 2001), 764–774.
5. Van Doorn, T., Bhat, M., Rutten, T. P., Tran, T. & Costanzo, A. A fast, high spatial resolution optical tomographic scanner for measurement of absorption in gel dosimetry. *Australasian Physics & Engineering Sciences in Medicine* **28**, 76–85 (June 2005).
6. Krstajić, N. & Doran, S. J. Fast laser scanning optical-CT apparatus for 3D radiation dosimetry. *Physics in Medicine and Biology* **52**, N257 (June 7, 2007).
7. Dekker, K. H., Battista, J. J. & Jordan, K. J. Scanning laser optical computed tomography system for large volume 3D dosimetry. *Physics in Medicine and Biology* **62**, 2636 (2017).
8. Doran, S. J. *et al.* A CCD-based optical CT scanner for high-resolution 3D imaging of radiation dose distributions: equipment specifications, optical simulations and preliminary results. *Physics in medicine and biology* **46**, 3191 (2001).
9. Krstajic, N. & Doran, S. J. Characterization of a parallel-beam CCD optical-CT apparatus for 3D radiation dosimetry. *Physics in Medicine and Biology* **52**, 3693 (July 7, 2007).
10. Sakhalkar, H. S. & Oldham, M. Fast, high-resolution 3D dosimetry utilizing a novel optical-CT scanner incorporating tertiary telecentric collimation. *Medical Physics* **35**, 101–111 (Jan. 2008).
11. Thomas, A. & Oldham, M. Fast, large field-of-view, telecentric optical-CT scanning system for 3D radiochromic dosimetry. *Journal of Physics: Conference Series* **250**, 012007 (Nov. 1, 2010).

12. Wolodzko, J. G., Marsden, C. & Appleby, A. CCD imaging for optical tomography of gel radiation dosimeters. *Medical Physics* **26**, 2508 (1999).
13. Jordan, K. & Battista, J. Linearity and image uniformity of the VistaTM optical cone beam scanner. *Journal of Physics: Conference Series* **56**, 217 (Dec. 1, 2006).
14. Dekker, K. H., Battista, J. J. & Jordan, K. J. Stray light in cone beam optical computed tomography: II. Reduction using a convergent light source. *Physics in Medicine and Biology* **61**, 2910 (2016).
15. Kelly, R. G., Jordan, K. J. & Battista, J. J. Optical CT reconstruction of 3D dose distributions using the ferrous–benzoic–xylenol (FBX) gel dosimeter. *Medical Physics* **25**, 1741 (1998).
16. Babic, S., Battista, J. & Jordan, K. Radiochromic leuco dye micelle hydrogels: II. Low diffusion rate leuco crystal violet gel. *Physics in Medicine and Biology* **54**, 6791–6808 (Nov. 21, 2009).
17. Babic, S., Battista, J. & Jordan, K. Three-Dimensional Dose Verification for Intensity-Modulated Radiation Therapy in the Radiological Physics Centre Head-and-Neck Phantom Using Optical Computed Tomography Scans of Ferrous Xylenol–Orange Gel Dosimeters. *International Journal of Radiation Oncology • Biology • Physics* **70**, 1281–1291 (Mar. 15, 2008).
18. Alqathami, M., Blencowe, A., Geso, M. & Ibbott, G. Characterization of novel water-equivalent PRESAGE[®] dosimeters for megavoltage and kilovoltage x-ray beam dosimetry. *Radiation Measurements* **74**, 12–19 (Mar. 2015).
19. Doran, S. *et al.* Issues involved in the quantitative 3D imaging of proton doses using optical CT and chemical dosimeters. *Physics in Medicine and Biology* **60**, 709 (Jan. 21, 2015).
20. Jordan, K. & Battista, J. A stable black-refractive-index-matching liquid for optical CT scanning of hydrogels. *Journal of Physics: Conference Series* **164**, 012045 (May 1, 2009).
21. Robertson, M. A., Borman, S. & Stevenson, R. L. *Dynamic range improvement through multiple exposures* in *Proceedings 1999 International Conference on Image Processing (Cat. 99CH36348)* Proceedings 1999 International Conference on Image Processing (Cat. 99CH36348). **3** (1999), 159–163 vol.3.
22. Campbell, W. G., Rudko, D. A., Braam, N. A., Wells, D. M. & Jirasek, A. A prototype fan-beam optical CT scanner for 3D dosimetry. *Medical Physics* **40**, 061712 (June 1, 2013).
23. Mail, N., Moseley, D. J., Siewerdsen, J. H. & Jaffray, D. A. The influence of bowtie filtration on cone-beam CT image quality. *Medical Physics* **36**, 22–32 (Jan. 1, 2009).
24. Rahman, A. T. A. *et al.* Sophisticated test objects for the quality assurance of optical computed tomography scanners. *Physics in Medicine & Biology* **56**, 4177 (2011).
25. Feldkamp, L. A., Davis, L. C. & Kress, J. W. Practical cone-beam algorithm. *JOSA A* **1**, 612–619 (1984).
26. Matenine, D., Mascolo-Fortin, J., Goussard, Y. & Després, P. Evaluation of the OSC-TV iterative reconstruction algorithm for cone-beam optical CT. *Medical Physics* **42**, 6376–6386 (Nov. 1, 2015).

27. Dekker, K. H., Battista, J. J. & Jordan, K. J. Technical Note: Evaluation of an iterative reconstruction algorithm for optical CT radiation dosimetry. *Medical Physics* **44**, 6678–6689 (Nov. 14, 2017).
28. Bartolac, S., Graham, S., Siewerdsen, J. & Jaffray, D. Fluence field optimization for noise and dose objectives in CT. *Medical Physics* **38**, S2–S17 (S1 July 1, 2011).
29. Szczykutowicz, T. P. & Mistretta, C. A. Experimental realization of fluence field modulated CT using digital beam attenuation. *Physics in Medicine & Biology* **59**, 1305 (2014).
30. Stayman, J. W. *et al.* Fluence-Field Modulated X-ray CT using Multiple Aperture Devices. *Proceedings of SPIE—the International Society for Optical Engineering* **9783** (Feb. 27, 2016).

Appendix B

Copyright Releases

B.1 Permission to reproduce content in Chapters 1-3

Mon 19/06/17 5:34 AM

To: Kurtis Dekker [REDACTED]

Dear Kurtis Dekker,

Thank you for your email and for taking the time to seek this permission.

Regarding:

Kurtis H Dekker et al 2016 Phys. Med. Biol. 61 2910

Kurtis H Dekker et al 2017 Phys. Med. Biol. 62 2636

Figure 1 (Patrick V Granton et al 2016 Phys. Med. Biol. 61 2893)

When you transferred the copyright in your article to IOP, we granted back to you certain rights, including the right to include the Final Published Version of the article within any thesis or dissertation. Please note you may need to obtain separate permission for any third party content you included within your article.

Please include citation details, "© Institute of Physics and Engineering in Medicine. Reproduced by permission of IOP Publishing. All rights reserved" and for online use, a link to the Version of Record.

The only restriction is that if, at a later date, your thesis were to be published commercially, further permission would be required.

Please let me know if you have any further questions.

In the meantime, I wish you the best of luck with the completion of your dissertation.

Kind regards,

Contact Details

E-mail: [REDACTED]

For further information about copyright and how to request permission: <http://iopscience.iop.org/page/copyright>

Please see our Author Rights Policy <http://iopublishing.org/author-rights/>

Please note: We do not provide signed permission forms as a separate attachment. Please print this email and provide it to your publisher as proof of permission.

Please note: Any statements made by IOP Publishing to the effect that authors do not need to get permission to use any content where IOP Publishing is not the publisher is not intended to constitute any sort of legal advice. Authors must make their own decisions as to the suitability of the content they are using and whether they require permission for it to be published within their article.

B.2 Permission to reproduce content in Chapter 4

JOHN WILEY AND SONS LICENSE TERMS AND CONDITIONS

Apr 06, 2018

This Agreement between kurtis dekker ("You") and John Wiley and Sons ("John Wiley and Sons") consists of your license details and the terms and conditions provided by John Wiley and Sons and Copyright Clearance Center.

License Number	4264231019922
License date	Jan 08, 2018
Licensed Content Publisher	John Wiley and Sons
Licensed Content Publication	Medical Physics
Licensed Content Title	Technical Note: Evaluation of an iterative reconstruction algorithm for optical CT radiation dosimetry
Licensed Content Author	Kurtis H. Dekker, Jerry J. Battista, Kevin J. Jordan
Licensed Content Date	Nov 14, 2017
Licensed Content Pages	12
Type of Use	Dissertation/Thesis
Requestor type	Author of this Wiley article
Format	Print and electronic
Portion	Full article
Will you be translating?	No
Title of your thesis / dissertation	High-performance optical computed tomography for accurate three-dimensional radiation dosimetry
Expected completion date	Apr 2018
Expected size (number of pages)	250
Requestor Location	kurtis dekker

Publisher Tax ID	EU826007151
Total	0.00 CAD
Terms and Conditions	

TERMS AND CONDITIONS

This copyrighted material is owned by or exclusively licensed to John Wiley & Sons, Inc. or one of its group companies (each a "Wiley Company") or handled on behalf of a society with which a Wiley Company has exclusive publishing rights in relation to a particular work (collectively "WILEY"). By clicking "accept" in connection with completing this licensing transaction, you agree that the following terms and conditions apply to this transaction (along with the billing and payment terms and conditions established by the Copyright Clearance Center Inc., ("CCC's Billing and Payment terms and conditions"), at the time that you opened your RightsLink account (these are available at any time at <http://myaccount.copyright.com>).

Terms and Conditions

- The materials you have requested permission to reproduce or reuse (the "Wiley Materials") are protected by copyright.

- You are hereby granted a personal, non-exclusive, non-sub licensable (on a stand-alone basis), non-transferable, worldwide, limited license to reproduce the Wiley Materials for the purpose specified in the licensing process. This license, **and any CONTENT (PDF or image file) purchased as part of your order**, is for a one-time use only and limited to any maximum distribution number specified in the license. The first instance of republication or reuse granted by this license must be completed within two years of the date of the grant of this license (although copies prepared before the end date may be distributed thereafter). The Wiley Materials shall not be used in any other manner or for any other purpose, beyond what is granted in the license. Permission is granted subject to an appropriate acknowledgement given to the author, title of the material/book/journal and the publisher. You shall also duplicate the copyright notice that appears in the Wiley publication in your use of the Wiley Material. Permission is also granted on the understanding that nowhere in the text is a previously published source acknowledged for all or part of this Wiley Material. Any third party content is expressly excluded from this permission.
- With respect to the Wiley Materials, all rights are reserved. Except as expressly granted by the terms of the license, no part of the Wiley Materials may be copied, modified, adapted (except for minor reformatting required by the new Publication), translated, reproduced, transferred or distributed, in any form or by any means, and no derivative works may be made based on the Wiley Materials without the prior permission of the respective copyright owner. **For STM Signatory Publishers clearing permission under the terms of the [STM Permissions Guidelines](#) only, the terms of the license are extended to include subsequent editions and for editions in other languages, provided such editions are for the work as a whole in situ and does not involve the separate exploitation of the permitted figures or extracts**, You may not alter, remove or suppress in any manner any copyright, trademark or other notices displayed by the Wiley Materials. You may not license, rent, sell, loan, lease, pledge, offer as security, transfer or assign the Wiley Materials on a stand-alone basis, or any of the rights granted to you hereunder to any other person.
- The Wiley Materials and all of the intellectual property rights therein shall at all times remain the exclusive property of John Wiley & Sons Inc, the Wiley Companies, or their respective licensors, and your interest therein is only that of having possession of and the right to reproduce the Wiley Materials pursuant to Section 2 herein during the continuance of this Agreement. You agree that you own no right, title or interest in or to the Wiley Materials or any of the intellectual property rights therein. You shall have no rights hereunder other than the license as provided for above in Section 2. No right, license or interest to any trademark, trade name, service mark or other branding ("Marks") of WILEY or its licensors is granted hereunder, and you agree that you shall not assert any such right, license or interest with respect thereto
- NEITHER WILEY NOR ITS LICENSORS MAKES ANY WARRANTY OR REPRESENTATION OF ANY KIND TO YOU OR ANY THIRD PARTY, EXPRESS, IMPLIED OR STATUTORY, WITH RESPECT TO THE MATERIALS OR THE ACCURACY OF ANY INFORMATION CONTAINED IN THE MATERIALS, INCLUDING, WITHOUT LIMITATION, ANY IMPLIED WARRANTY OF MERCHANTABILITY, ACCURACY, SATISFACTORY QUALITY, FITNESS FOR A PARTICULAR PURPOSE, USABILITY, INTEGRATION OR NON-INFRINGEMENT AND ALL SUCH WARRANTIES ARE HEREBY EXCLUDED BY WILEY AND ITS LICENSORS AND WAIVED BY YOU.
- WILEY shall have the right to terminate this Agreement immediately upon breach of this Agreement by you.
- You shall indemnify, defend and hold harmless WILEY, its Licensors and their respective directors, officers, agents and employees, from and against any actual or threatened claims, demands, causes of action or proceedings arising from any breach of this Agreement by you.
- IN NO EVENT SHALL WILEY OR ITS LICENSORS BE LIABLE TO YOU OR ANY OTHER PARTY OR ANY OTHER PERSON OR ENTITY FOR ANY SPECIAL, CONSEQUENTIAL, INCIDENTAL, INDIRECT, EXEMPLARY OR PUNITIVE DAMAGES, HOWEVER CAUSED, ARISING OUT OF OR IN CONNECTION WITH THE DOWNLOADING, PROVISIONING, VIEWING OR USE OF THE MATERIALS REGARDLESS OF THE FORM OF ACTION, WHETHER FOR BREACH OF CONTRACT, BREACH OF WARRANTY, TORT, NEGLIGENCE, INFRINGEMENT OR OTHERWISE (INCLUDING, WITHOUT LIMITATION, DAMAGES BASED ON LOSS OF PROFITS, DATA, FILES, USE, BUSINESS OPPORTUNITY OR CLAIMS OF THIRD PARTIES), AND WHETHER OR NOT THE PARTY HAS BEEN ADVISED OF THE POSSIBILITY OF SUCH DAMAGES. THIS LIMITATION SHALL APPLY NOTWITHSTANDING ANY FAILURE OF ESSENTIAL PURPOSE OF ANY LIMITED REMEDY PROVIDED HEREIN.
- Should any provision of this Agreement be held by a court of competent jurisdiction to be illegal, invalid, or unenforceable, that provision shall be deemed amended to achieve as nearly as possible the same economic effect as the original provision, and the legality, validity and enforceability of the remaining provisions of this Agreement shall not be affected or impaired thereby.

- The failure of either party to enforce any term or condition of this Agreement shall not constitute a waiver of either party's right to enforce each and every term and condition of this Agreement. No breach under this agreement shall be deemed waived or excused by either party unless such waiver or consent is in writing signed by the party granting such waiver or consent. The waiver by or consent of a party to a breach of any provision of this Agreement shall not operate or be construed as a waiver of or consent to any other or subsequent breach by such other party.
- This Agreement may not be assigned (including by operation of law or otherwise) by you without WILEY's prior written consent.
- Any fee required for this permission shall be non-refundable after thirty (30) days from receipt by the CCC.
- These terms and conditions together with CCC's Billing and Payment terms and conditions (which are incorporated herein) form the entire agreement between you and WILEY concerning this licensing transaction and (in the absence of fraud) supersedes all prior agreements and representations of the parties, oral or written. This Agreement may not be amended except in writing signed by both parties. This Agreement shall be binding upon and inure to the benefit of the parties' successors, legal representatives, and authorized assigns.
- In the event of any conflict between your obligations established by these terms and conditions and those established by CCC's Billing and Payment terms and conditions, these terms and conditions shall prevail.
- WILEY expressly reserves all rights not specifically granted in the combination of (i) the license details provided by you and accepted in the course of this licensing transaction, (ii) these terms and conditions and (iii) CCC's Billing and Payment terms and conditions.
- This Agreement will be void if the Type of Use, Format, Circulation, or Requestor Type was misrepresented during the licensing process.
- This Agreement shall be governed by and construed in accordance with the laws of the State of New York, USA, without regards to such state's conflict of law rules. Any legal action, suit or proceeding arising out of or relating to these Terms and Conditions or the breach thereof shall be instituted in a court of competent jurisdiction in New York County in the State of New York in the United States of America and each party hereby consents and submits to the personal jurisdiction of such court, waives any objection to venue in such court and consents to service of process by registered or certified mail, return receipt requested, at the last known address of such party.

WILEY OPEN ACCESS TERMS AND CONDITIONS

Wiley Publishes Open Access Articles in fully Open Access Journals and in Subscription journals offering Online Open. Although most of the fully Open Access journals publish open access articles under the terms of the Creative Commons Attribution (CC BY) License only, the subscription journals and a few of the Open Access Journals offer a choice of Creative Commons Licenses. The license type is clearly identified on the article.

The Creative Commons Attribution License

The [Creative Commons Attribution License \(CC-BY\)](#) allows users to copy, distribute and transmit an article, adapt the article and make commercial use of the article. The CC-BY license permits commercial and non-

Creative Commons Attribution Non-Commercial License

The [Creative Commons Attribution Non-Commercial \(CC-BY-NC\) License](#) permits use, distribution and reproduction in any medium, provided the original work is properly cited and is not used for commercial purposes.(see below)

Creative Commons Attribution-Non-Commercial-NoDerivs License

The [Creative Commons Attribution Non-Commercial-NoDerivs License](#) (CC-BY-NC-ND) permits use, distribution and reproduction in any medium, provided the original work is properly cited, is not used for commercial purposes and no modifications or adaptations are made. (see below)

Use by commercial "for-profit" organizations

Use of Wiley Open Access articles for commercial, promotional, or marketing purposes requires further explicit permission from Wiley and will be subject to a fee.

Further details can be found on Wiley Online Library <http://olabout.wiley.com/WileyCDA/Section/id-410895.html>

Other Terms and Conditions:

B.3 Permission to reproduce content in Chapter 5




[Home](#)
[Account Info](#)
[Help](#)



Title: Optical CT imaging of solid radiochromic dosimeters in mismatched refractive index solutions using a scanning laser and large area detector

Author: Kurtis H. Dekker, Jerry J. Battista, Kevin J. Jordan

Publication: Medical Physics

Publisher: John Wiley and Sons

Date: Nov 30, 2016

© 2016 The Authors. Published by American Association of Physicists in Medicine and John Wiley & Sons Ltd.

Logged in as:
kurtis dekker
Account #:
[REDACTED]

[LOGOUT](#)

Welcome to RightsLink

This article is available under the terms of the **Creative Commons Attribution License (CC BY)** (which may be updated from time to time) and permits use, distribution and reproduction in any medium, provided that the Contribution is properly cited.

For an understanding of what is meant by the terms of the Creative Commons License, please refer to **Wiley's Open Access Terms and Conditions**.

Permission is not required for this type of reuse.

Wiley offers a professional reprint service for high quality reproduction of articles from over 1400 scientific and medical journals. Wiley's reprint service offers:

- Peer reviewed research or reviews
- Tailored collections of articles
- A professional high quality finish
- Glossy journal style color covers
- Company or brand customisation
- Language translations
- Prompt turnaround times and delivery directly to your office, warehouse or congress.

[CLOSE WINDOW](#)

Copyright © 2017 Copyright Clearance Center, Inc. All Rights Reserved. [Privacy statement](#). [Terms and Conditions](#).
Comments? We would like to hear from you. E-mail us at [\[REDACTED\]](#)

B.4 Permission to reproduce content in Appendix A

From: Permissions [REDACTED]
Sent: March 26, 2018 6:38 AM
To: Kurtis Dekker
Subject: Re: Permission to reproduce material within thesis - PMB 63 06NT02

Dear Kurtis Dekker,

Thank you for your email and for taking the time to seek this permission.

When you transferred the copyright in your article to Institute of Physics and Engineering in Medicine, you were granted back certain rights, including the right to include the Final Published Version of the article within any thesis or dissertation. Please note you may need to obtain separate permission for any third party content you included within your article.

Please include citation details, "© Institute of Physics and Engineering in Medicine. Reproduced with permission. All rights reserved" and for online use, a link to the Version of Record.

The only restriction is that if, at a later date, you wanted your thesis/dissertation to be published commercially, further permission would be required.

I wish you the best of luck with the completion of your thesis/dissertation.

Kind regards,

Please note: We do not provide signed permission forms as a separate attachment. Please print this email and provide it to your publisher as proof of permission.

Please note: Any statements made by IOP Publishing to the effect that authors do not need to get permission to use any content where IOP Publishing is not the publisher is not intended to constitute any sort of legal advice. Authors must make their own decisions as to the suitability of the content they are using and whether they require permission for it to be published within their article.

Appendix C

Curriculum Vitae

Kurtis Hendrik Dekker

Ph.D. Candidate in Medical Biophysics

Education

- 2013–2018 **Ph.D., CAMPEP Clinical M.Sc., Medical Biophysics**
The University of Western Ontario (UWO), London, ON, Canada,
 Supervisors: Kevin Jordan, Ph.D.; Jerry Battista, Ph.D.
 Thesis Title: “High performance optical computed tomography for accurate three-dimensional radiation dosimetry”.
 Projected Completion Date: April 2018.
- 2009–2013 **B.Sc.(Honours), Physics, Astrophysics Specialization**
Queen’s University, Kingston, ON, Canada.

Peer Reviewed Journal Articles (6)

- 2018 **K. H. Dekker**, R. Hazarika, M. A. Silveira, and K. J. Jordan, “Fixed, object-specific intensity compensation for cone beam optical CT radiation dosimetry,” *Physics in Medicine & Biology*, vol. 63, no. 6, 06NT02, Mar. 2018.
- 2017 **K. H. Dekker**, J. J. Battista, and K. J. Jordan, “Technical note: Evaluation of an iterative reconstruction algorithm for optical CT radiation dosimetry,” *Medical Physics*, vol. 44, no. 12, pp. 6678–6689, Nov. 2017.
- K. H. Dekker**, J. J. Battista, and K. J. Jordan, “Scanning laser optical computed tomography system for large volume 3d dosimetry,” *Physics in Medicine and Biology*, vol. 62, no. 7, 2636–2657. **Featured in the PMB Highlights of 2017**, Mar. 2017.
- 2016 **K. H. Dekker**, J. J. Battista, and K. J. Jordan, “Optical CT imaging of solid radiochromic dosimeters in mismatched refractive index solutions using a scanning laser and large area detector,” *Medical Physics*, vol. 43, no. 8, 4585–4597. **Selected as an Editor’s Choice Publication**, Aug. 2016.
- K. H. Dekker**, J. J. Battista, and K. J. Jordan, “Stray light in cone beam optical computed tomography: II. Reduction using a convergent light source,” *Physics in Medicine and Biology*, vol. 61, no. 7, pp. 2910–2925, Mar. 2016.
- P. V. Granton, **K. H. Dekker**, J. J. Battista, and K. J. Jordan, “Stray light in cone beam optical computed tomography: I. Measurement and reduction strategies with planar diffuse source,” *Physics in Medicine and Biology*, vol. 61, no. 7, pp. 2893–2909, Mar. 2016.

Peer Reviewed Conference Proceedings (5)

- 2017 **K. H. Dekker**, J. J. Battista, and K. J. Jordan, "Fan-beam scanning laser optical computed tomography for large volume dosimetry," in *Journal of Physics: Conference Series*, vol. 847, May 2017, p. 012 008.
- K. J. Jordan, T. Lindenmaier, and **K. H. Dekker**, "Non-diffusing radiochromic leuco-crystal violet hydrogel dosimeter," in *Journal of Physics: Conference Series*, vol. 847, May 2017, p. 012 009.
- K. J. Jordan and **K. H. Dekker**, "Active heating of large gel dosimeters," in *Journal of Physics: Conference Series*, vol. 847, May 2017, p. 012 050.
- 2015 **K. H. Dekker**, J. J. Battista, and K. J. Jordan, "Towards Optical CT scanning of radiochromic 3d dosimeters in mismatched refractive index solutions," in *World Congress on Medical Physics and Biomedical Engineering, June 7-12, 2015, Toronto, Canada*, D. A. Jaffray, Ed., vol. 51, Springer International Publishing, 2015, pp. 716–719.
- K. J. Jordan, **K. H. Dekker**, and J. J. Battista, "Stray light reduction in optical computed tomography using a convergent cone-beam source," in *Journal of Physics: Conference Series*, vol. 573, Jan. 2015, p. 012 033.

Awards and Honours

- 2016–2018 **Alexander Graham Bell Canada Graduate Scholarship (Doctoral)**
Natural Sciences and Engineering Research Council of Canada (NSERC).
- November 2016 **Top 3 Oral Presentation**
9th International Conference on 3D Dosimetry (IC3DDose), Galveston, TX, USA.
- June 2015 **Best Presentation Award of the International Organization for Medical Physics (IOMP) and Jack Cunningham Award of the Canadian Organization of Medical Physicists (COMP/OCPM)**
J R Cunningham Young Investigator Symposium, World Congress on Medical Physics and Biomedical Engineering 2015, Toronto, ON, Canada.
- 2013–2014 **Queen Elizabeth II Graduate Scholarship in Science and Technology**
The University of Western Ontario, London, ON, Canada.
- 2009–2013 **Dean's Honour List**
Queen's University, Kingston, ON, Canada.
- 2009–2013 **Queen Elizabeth II Aiming for the Top Scholarship**
Queen's University, Kingston, ON, Canada.
- 2011 **Harold E. Johns Studentship in Medical Physics**
Southlake Regional Health Centre, Newmarket, ON, Canada.
- 2009–2010 **Principal's Entrance Scholarship**
Queen's University, Kingston, ON, Canada.

Conference Presentations and Abstracts (9)

- July 2017 **K. H. Dekker**, J. J. Battista and K. J. Jordan, "Laser source compensator for optical CT imaging of gel dosimeters". *Poster Presentation at the 63rd Annual Scientific Meeting of the Canadian Organization of Medical Physicists*, Ottawa, ON, Canada
- March 2017 **K. H. Dekker**, J. J. Battista and K. J. Jordan, "Evaluation of an iterative reconstruction algorithm for optical CT dosimetry of small radiation fields". *Oral Presentation at the 15th Imaging Network Ontario Symposium*, London, ON, Canada
- November 2016 **K. H. Dekker**, J. J. Battista and K. J. Jordan, "Fan-beam scanning laser optical computed tomography for large volume dosimetry". *Oral Presentation at the 9th International Conference on 3D Dosimetry (IC3DDose)*, Galveston, TX, USA
- March 2016 K. J. Jordan, **K. H. Dekker** and J. J. Battista, "Development of improved gel dosimeter vessels for low stray light optical CT scanners". *Oral Presentation at the 14th Imaging Network Ontario Symposium*, Toronto, ON, Canada
- June 2015 **K. H. Dekker**, J. J. Battista and K. J. Jordan, "Towards optical CT scanning of radiochromic 3D dosimeters in mismatched refractive index solutions". *Oral Presentation at the World Congress on Medical Physics and Biomedical Engineering 2015*, Toronto, ON, Canada
- June 2015 L. Kaci, **K. H. Dekker**, C. Versnick, J. Dietrich, K. Jordan, J. Miller and J. J. Battista, "A Desktop optical scanner for teaching the principles of computed tomography (CT)". *Oral Presentation at the World Congress on Medical Physics and Biomedical Engineering 2015*, Toronto, ON, Canada
- March 2015 **K. H. Dekker**, T. Villani, N. Crider, M. Johnson, J. J. Battista and K. J. Jordan, "Optical computed tomography for skeletal imaging in an optically-cleared mouse". *Poster Presentation at London Health Research Day 2015 (London, Canada)*. *Oral and Poster Presentation at the 13th Imaging Network Ontario Symposium*, London, ON, Canada
- L. Kaci, **K. H. Dekker**, C. Versnick, J. Dietrich, K. Jordan, J. Miller and J. J. Battista, "Clinically relevant laboratory experiments for the DeskCATTM educational CT scanner". *Poster Presentation at the 13th Imaging Network Ontario Symposium*, London, ON, Canada
- March 2014 **K. H. Dekker**, J. J. Battista and K. J. Jordan, "Characterization of refractive index artifacts in fan beam optical CT through primary ray tracing". *Poster presentation at London Health Research Day 2014 (London, Canada) and the 12th Imaging Network Ontario Symposium*, Toronto, ON, Canada

Campus and Departmental Talks (1)

April 2016 **K. H. Dekker**, J. J. Battista and K. J. Jordan, "3D Dosimetry using optical computed tomography (CT): Designing a high-performance scanner". *Invited Student Presentation at the 25th annual A.C. Burton Day, Department of Medical Biophysics, The University of Western Ontario, London, ON, Canada*

Relevant Experience

- 2013–present **Ph.D. and Clinical Physics M.Sc. Candidate**
Department of Medical Biophysics, The University of Western Ontario, London, ON, Canada.
 Development of optical computed tomography systems for 3D radiation dosimetry
- Sept–Dec 2014, **Quality Assurance Assistant**
 May–Aug 2016 *London Regional Cancer Program, London, ON, Canada.*
 Weekly mechanical and dosimetric output measurements for Varian linear accelerators
- Jan–May 2014 **Lab Course Design (Special Topics Course)**
The University of Western Ontario, London, ON, Canada.
 Development of lab exercises implemented in a new course in the Medical Biophysics department, to teach the principles of medical imaging using "desktop" systems
- May–Aug 2012 **Summer Student, Radiation Physics**
University Health Network - Princess Margaret Hospital, Toronto, ON, Canada.
 Development of software tools for image analysis during radiotherapy cancer treatments, aimed towards adaptive radiotherapy research
- June–Aug 2011 **Summer Student, Medical Physics**
Southlake Regional Health Centre, Newmarket, ON, Canada.
 Development of image processing software for quality assurance of radiotherapy equipment
 Development and testing of prototype surface-tracking apparatus and software

Skills

- Programming and Analysis MATLAB, C, CUDA C/C++, Python, Bash, Mathematica, Excel
- Technical and Scientific Numerical Simulation, Mathematical Modelling, Tomographic Reconstruction, Optical Design, Basic Electronics, Instrument Construction
- Clinical Linear Accelerator Operation (Varian), Radiation Dosimetry

Professional Memberships

- Canadian Organization of Medical Physicists (COMP) - *Student Member*
 American Association of Physicists in Medicine (AAPM) - *Student Member*